

University of Bath



PHD

Micro- and nanogap based biosensors

Hammond, Jules

Award date:
2017

Awarding institution:
University of Bath

[Link to publication](#)

General rights

Copyright and moral rights for the publications made accessible in the public portal are retained by the authors and/or other copyright owners and it is a condition of accessing publications that users recognise and abide by the legal requirements associated with these rights.

- Users may download and print one copy of any publication from the public portal for the purpose of private study or research.
- You may not further distribute the material or use it for any profit-making activity or commercial gain
- You may freely distribute the URL identifying the publication in the public portal ?

Take down policy

If you believe that this document breaches copyright please contact us providing details, and we will remove access to the work immediately and investigate your claim.

Download date: 22. May. 2019

Micro- and nanogap based biosensors.

Jules Lloyd Hammond

A thesis submitted for the degree of Doctor of Philosophy
University of Bath
Department of Electronic and Electrical Engineering
May 2017

COPYRIGHT

Attention is drawn to the fact that copyright of this thesis rests with the author. A copy of this thesis has been supplied on condition that anyone who consults it is understood to recognise that its copyright rests with the author and that they must not copy it or use material from it except as permitted by law or with the consent of the author.

I have so much to say to you
that I am afraid I shall tell you nothing.
— Fyodor Dostoyevsky

To my father.

Acknowledgements

Firstly I would like to thank both my supervisors, Dr. Pedro Estrela and Prof. Frank Marken. The support and guidance throughout my entire PhD has been far beyond what I could have hoped for, and for that I am grateful. Whilst the past few years have been challenging, they have also transformed me into a better person.

It was very fortunate that I was able to work within both the Estrela and Marken research groups, and I am thankful for both the professional and personal support received from others. It has always been interesting to think that people may never know of their importance to your perception of life—fleeting moments, so pertinent now. I would like to thank some of the many people that I have had the opportunity to work with: Andrew Gross, Benjamin Metcalfe, Chris Lewins, Jonathan Storey, Shrey Pathak, Zhugen Yang, Sunil Arya, Nikhil Bhalla, Nello Formisano, Pawan Jolly, Pavel Zhurauski, Caleb Wong, Şerife Üstüner, Alex Beasley, Jonathan Graham-Harper-Cater, Emmanuel Le Boulbar, Sara Dale, Grace Lewis, Elena Madrid and James Weber.

A special mention must go to Dr. Siva Sivaraya and Dr. Mark Rosamond, both of whom assisted with the nanofabrication and provided counsel and plenty of patience in the facilities at both the University of Bath and the University of Leeds, respectively.

I am also grateful for Leeds EPSRC Nanoscience and Nanotechnology (LENNF) accepting my application to work with Dr. Mark Rosamond (and grant holders Prof. Rik Brydson & Prof. Edmund Linfield). Finally I thank EPSRC for providing the doctoral training award (DTA) to finance this PhD.

May 2017

J. L. Hammond

Abstract

Biosensors are used for the detection of a range of analytes for applications in healthcare, food production, environmental monitoring and biodefence. However, many biosensing platforms are large, expensive, require skilled operators or necessitate the analyte to be labelled. Direct electrochemical detection methods present a particularly attractive platform due to the simplified instrumentation when compared to other techniques such as fluorescence-based biosensors. With modern integrated circuit capabilities electrochemical biosensors offer greater suitability for monolithic integration with any necessary signal processing circuitry.

This thesis explores micro- and nanogap devices for both redox cycling and dielectric spectroscopy sensing mechanisms. By using two electrodes with interelectrode separation down to distances in the micro- and nanometre scale, several benefits can be realised. Firstly the close proximity of the two electrodes significantly reduces the interdiffusion time. This allows an electroactive species to be rapidly shuttled across the gap and switched between reduced and oxidised states. The result is feedback amplification of the amperometric response, increasing the signal. The second benefit is that the screening effect caused by electric double layers at the electrode–electrolyte interface is reduced due to the electric double layers occupying a larger fraction of the sensing volume. This significantly improves the sensor suitability for dielectric spectroscopy by increasing the potential drop across the bilayer.

These two sensing mechanisms are demonstrated using a large area dual-plate microgap device for the detection of two different analytes. Utilising the first mode, detection of cysteine–cystine, an important redox couple involved in the signalling mechanism for the regulation of protein function, interaction and localisation is shown. The microgap device is then used for dielectric spectroscopy sensing of a mannose-specific uropathogenic *Escherichia coli* strain whilst also demonstrating the effect of ionic concentration on the capacitive response.

The response of these devices is highly dependent on the interelectrode separation as well as the surface area of the electrodes. However, fabrication of large-area nanogap devices

presents a significant challenge. This meant that careful optimisation and the development of novel techniques was necessary. This work reports the design, fabrication and characterisation of both a vertical and a horizontal coplanar large area nanogap device. The vertical nanogap device is fabricated using an inductively-coupled plasma reactive ion etching process to create a channel in a silicon substrate. A lower electrode is then optically patterned in the channel before anodically bonding a second identical electrode patterned on glass directly above. The horizontal nanogap device uses a different approach, utilising a state-of-the-art electron-beam lithography system to create a long serpentine nanogap with passivation to reduce fringing effects. The design allows the electron-beam lithography step to be substituted with nanoimprint lithography to reduce cost and improve throughput. Both of these devices have integrated microfluidic channels and provide a capacity for relatively high-throughput production.

Keywords: biosensor, sensor, large-area, microgap, nanogap, electrochemical, redox cycling, generator–collector, dielectric spectroscopy, capacitance, electric double layer

Contents

Acknowledgements	i
Abstract	iii
List of Figures	vii
List of Tables	xv
List of Abbreviations	xix
List of Symbols	xxi
1 Introduction	1
1.1 Background	1
1.2 Motivation	3
1.2.1 Progression of generator–collector systems	5
1.2.2 Trend towards nanogap devices	6
1.3 Aim	10
1.4 Overview of the thesis	10
References	21
2 Theory	23
2.1 Overview of the sensing systems	23
2.2 Principles of electrochemistry	24
2.2.1 Kinetics	26
2.2.2 Mass transport	27
2.2.3 Voltammetry	29
2.2.4 Redox cycling	31
2.3 The electrode–electrolyte interface	35
2.3.1 Overlapping electric double layers	38
2.3.2 Capacitance of the electric double layer	40
2.4 Self-assembled monolayers for capacitive sensing	42
References	47

3	Pilot Tests with a Dual-Plate Microgap Sensor	49
3.1	Microgap sensor	50
3.1.1	Microgap sensor fabrication	50
3.1.2	Microgap sensor characterisation	52
3.2	Electrochemical redox cycling with a microgap sensor	53
3.2.1	The cysteine–cystine redox couple	53
3.2.2	Experimental information	57
3.2.3	Results	58
3.2.4	Discussion	67
3.3	Dielectric spectroscopy measurements with a microgap sensor	69
3.3.1	Detection of <i>Escherichia coli</i>	69
3.3.2	Experimental information	70
3.3.3	Results	73
3.3.4	Discussion	80
	References	89
4	Fabrication of a Large Area Vertical Coplanar Nanogap Device	91
4.1	Present fabrication techniques for vertical nanogap devices	93
4.2	Alternative fabrication techniques for vertical nanogap devices	96
4.2.1	SU-8 as a sacrificial layer/adhesive	96
4.2.2	Wafer bonding	97
4.2.3	Prototype device and pilot tests for anodic bonding	100
4.3	Revised fabrication process	105
4.3.1	Substrate preparation	107
4.3.2	Silicon etching	108
4.3.3	Passivation layer	112
4.3.4	Electrode layers	116
4.3.5	Anodic bonding	118
4.4	Simulation	122
4.4.1	Microfluidics	122
4.4.2	Electroanalysis	128
4.5	Electrical characterisation	131
4.6	Discussion	132
	References	141
5	Fabrication of a Large Area Horizontal Coplanar Nanogap Device	143
5.1	Present fabrication techniques for horizontal nanogap devices	144
5.2	Fabrication process	150
5.2.1	Overview	150
5.2.2	Electrode layer	152
5.2.3	Passivation layer	154
5.2.4	Etch processes for defining device geometry and electrical access	157
5.2.5	Microfluidic layer	158

5.3	Simulation	160
5.3.1	Effect of the passivation layer on device performance	161
5.4	Electrical characterisation	163
5.5	Oligonucleotide detection by dielectric spectroscopy sensing	166
5.5.1	Peptide nucleic acids as a probe layer	166
5.5.2	Experimental information	168
5.5.3	Results	169
5.6	Discussion	174
	References	185
6	Summary and Outlook	187
6.1	Summary	187
6.2	Outlook	189
	References	191
	Appendices	193
A	Trialled Fabrication Methods for Vertical Coplanar Nanogaps	195
A.1	Unexposed SU-8 as a sacrificial layer	195
A.2	SU-8 as an adhesive layer	198
B	Trialled Fabrication Methods for Horizontal Coplanar Nanogaps	201
B.1	Focused ion beam milling	201
B.2	Improving ma-N 2403/glass adhesion	204
B.3	Patterning of a nanoimprint lithography silicon master	205
C	Simulation of the Horizontal Coplanar Nanogap Device	211
C.1	Electrostatics	211
C.2	Microfluidics	214
	References	217

List of Figures

1.1	Diagrammatic representation of a biosensor.	3
2.1	Free energy plot for a simple, single electron reduction of species 'O'	26
2.2	Voltage waveform (a) and cyclic voltammogram (b) for a system containing a single working electrode.	30
2.3	Diagram depicting the principle of redox cycling between generator and collector electrodes.	31
2.4	Voltage waveform (a) and cyclic voltammogram (b) for a generator–collector system.	33
2.5	Simplified illustration of the electric double layer at the electrode–electrolyte interface.	35
2.6	Plot showing effect of ionic strength on thickness of electric double layer.	38
2.7	Plot showing normalised potential distributions for electrode separations of k^{-1} , $2k^{-1}$, $5k^{-1}$ and $10k^{-1}$. Zero distance represents the centre point of the gap.	40
3.1	3D exploded diagram of the microgap sensor showing glass substrates, metallic electrodes (highlighted) and epoxy layers.	49
3.2	Fabrication process of the microgap sensor. (a): A 5 mm central region of gold is passivated using Kapton [®] tape. (b): The exposed gold is etched in <i>aqua regia</i> solution before oxidising the remaining titanium in a furnace. (c): Epoxy is applied to both electrodes and the two halves brought into contact and bonded under pressure using a mechanical press. (d): The bonded device is cut with a diamond saw along the cut line shown in (c2), this maximises the width of overlapping electrodes. The surface is then mechanically polished using various grits of silicon carbide paper and alumina slurry. (e): Piranha solution is used to etch the epoxy forming the microgap cavity. Finally conductive adhesive copper tape is attached to the top of the sensor to provide simplified electrical connections.	51
3.3	SEM images showing interelectrode spacing of the microgap sensor for (a) an $\approx 800\ \mu\text{m}$ and (b) a $\approx 40\ \mu\text{m}$ section.	52
3.4	Molecular diagrams of (a) L-cysteine and (b) L-cystine	53
3.5	Molecular diagram showing zwitterionic form of L-cysteine.	56

List of Figures

3.6	Cyclic voltammogram showing the oxidative sweeps of 1 mM cysteine (RSH) and 1 mM cystine (RSSR) at a 1 mm gold electrode in purged 0.1 M PBS, pH 7.0, at a scan rate of 100 mV·s ⁻¹	58
3.7	Cyclic voltammogram showing the reductive sweep of 1 mM cystine (RSSR) at a 1 mm gold electrode in purged 0.1 M PBS, pH 7.0, at a scan rate of 100 mV·s ⁻¹	59
3.8	Cyclic voltammogram showing the effect of collector potential (ϕ_c) on the collector current response for 1 mM cysteine in 0.1 M PBS, pH 7.0 at a scan rate of 25 mV·s ⁻¹	60
3.9	Cyclic voltammogram demonstrating how the collector potential affects the generator current response for 1 mM cysteine in 0.1 M PBS, pH 7.0, at a scan rate of 25 mV·s ⁻¹	61
3.10	Cyclic voltammogram showing the effect of collector potential (ϕ_c) on the collector current response for 1 mM cystine in 0.1 M PBS, pH 7.0, at a scan rate of 25 mV·s ⁻¹	61
3.11	Cyclic voltammogram showing the effect of increasing concentration of cysteine (RSH) on the generator current in 0.1 M PBS, pH 7.0, at a scan rate of 25 mV·s ⁻¹ and the collector held at -0.85 V <i>vs.</i> SCE.	62
3.12	Cyclic voltammogram showing the effect of increasing concentration of cysteine (RSH) on the collector current in 0.1 M PBS, pH 7.0, at a scan rate of 25 mV·s ⁻¹ and collector held at -0.85 V <i>vs.</i> SCE.	63
3.13	Plot showing dose response of cysteine (RSH) at the collector with the collector held at -0.85 V <i>vs.</i> SCE in 0.1 M PBS, pH 7.0, at a scan rate of 25 mV·s ⁻¹ . Error bars indicate $\pm\sigma$, $n = 5$. Linear regression constants: 140.28 and +2.464.	63
3.14	Cyclic voltammogram showing the effect increasing concentration of cystine (RSSR) on the generator current in 0.1 M PBS, pH 7.0, at a scan rate of 25 mV·s ⁻¹ and the collector held at 0.60 V <i>vs.</i> SCE.	64
3.15	Cyclic voltammogram showing the effect of increasing concentration of cystine (RSSR) on the collector current in 0.1 M PBS, pH 7.0, at a scan rate of 25 mV·s ⁻¹ and the collector held at 0.60 V <i>vs.</i> SCE.	65
3.16	Plot showing dose response of cystine (RSSR) at the collector with the collector held at 0.60 V <i>vs.</i> SCE in 0.1 M PBS, pH 7.0, at a scan rate of 25 mV·s ⁻¹ . Error bars indicate $\pm\sigma$, $n = 5$. Linear regression constants: 140.17 and -0.168.	65
3.17	Plot showing combined dose response of both cysteine and cystine at the collector, collector held at 0.60 V <i>vs.</i> SCE in 0.1 M PBS, pH 7.0, at a scan rate of 25 mV·s ⁻¹ . Error bars indicate $\pm\sigma$, $n = 5$	67
3.18	Diagram illustrating the expected biorecognition stack after the addition of the specific bacteria.	70
3.19	Barchart showing the relative capacitance change (%) after SAM immobilisation. Error bars indicate $\pm\sigma$, $n = 5$	73
3.20	Capacitance spectra of Electrode A after SAM formation in (a) 100 μ M PBS, (b) 1 mM PBS and (c) 10 mM PBS.	74
3.21	Frequency profile for Electrode A in 100 μ M PBS.	76

3.22	Frequency profile for Electrode A in 1 mM PBS.	77
3.23	Frequency profile for Electrode A in 10 mM PBS.	77
3.24	Set of barcharts showing the capacitance change (%) for different electrodes after immobilisation of sugar and bacteria in 100 μ M, 1 mM and 10 mM PBS. Error bars indicate $\pm\sigma$, $n = 5$	79
3.25	SEM images showing gold surfaces after immobilisation of different molecules used for the sugar–bacteria affinity capture assay.	80
4.1	3D exploded diagram of the vertical coplanar nanogap device showing silicon substrate, silicon nitride and electrode layers (highlighted) and glass substrate.	91
4.2	Diagram demonstrating some of the geometries used to obtain vertical nanogaps: (a) use of a sacrificial layer within a mesa structure then angled deposition; (b) etching a sacrificial layer to create a deep undercut; (c) formation of nanopores with plane-recessed disc electrodes using nanosphere templates; and (d) etching a sacrificial layer to form an encapsulated cavity.	93
4.3	Diagram demonstrating the mechanism of silicon–glass anodic bonding.	98
4.4	Calculated critical channel heights (h_c) for a range of channel widths (w).	99
4.5	Fabrication process of the prototype vertical nanogap sensor. (a): A Cr layer is patterned by lift-off photolithography on the silicon substrate to act as an etch mask for KOH etching a submicron channel. (b): The Cr mask is removed in Cr etchant then a stack of $\text{SiO}_2/\text{Ti}/\text{Au}$, forming the passivation and electrode layers, is deposited using electron-beam evaporation and patterned using lift-off photolithography. (c): On a separate borosilicate glass substrate an identical stack of $\text{SiO}_2/\text{Ti}/\text{Au}$ is also patterned using lift-off lithography. (d): Finally the two halves of the device are anodically bonded.	101
4.6	Optical image showing one of the prototype devices after unsuccessful anodic bonding.	103
4.7	Comparison of the geometry for (a) the prototype and (b) the revised design.	105
4.8	Fabrication process of the vertical nanogap sensor. (a): A photoresist layer is patterned on a silicon substrate to provide an etch mask before inductively-coupled plasma reactive ion etching a submicron channel. (b): A silicon nitride passivation layer is grown using plasma-enhanced chemical vapour deposition (PECVD) before patterning the lower metallic electrodes using lift-off photolithography. (c): On a separate borosilicate glass substrate the upper electrodes are patterned using lift-off photolithography. (d): Finally the two halves of the device are pretreated and anodically bonded.	106
4.9	3D diagram showing the prepared (a) silicon and (b) glass substrates.	107
4.10	3D diagram showing the substrate (a) before and (b) after channel formation.	108
4.11	Channel depth as a function of time for SF_6/O_2 ICP-RIE. Error bars indicate $\pm\sigma$, $n = 5$	110
4.12	Profilometer data showing the 900 nm deep silicon channel.	112

List of Figures

4.13	3D diagram showing the substrate (a) before and (b) after patterning the silicon nitride passivation layer.	112
4.14	Optical images showing the buffered oxide etched SiN _x passivation layer after photoresist removal: (a) without defects; (b) and with minor edge defects caused by undercutting of the photoresist mask.	114
4.15	Profilometer data showing a 900 nm silicon channel with a 110 nm silicon nitride passivation layer.	115
4.16	3D diagrams showing (a) the silicon substrate after patterning the lower electrode and (b) the glass substrate after patterning the upper electrode.	116
4.17	Optical images of the lift-off mask showing: (a) the transition to contact pad; (b) connection to the sensing electrode; (c) transition of the connect; and (d) the auxiliary electrode.	117
4.18	Optical images of the vertical nanogap device after prebonding: (a) alignment marks; (b) visible darker prebonded area on raised silicon section; (c) connect wire between contact pad and electrode; and (d) misalignment of the main sensing electrodes.	118
4.19	Current profile for glass–silicon anodic bonding at 225 V, 250 °C.	120
4.20	Images showing a completed vertical coplanar nanogap device. Left: Photograph showing an entire device. Top-right: microscope image with a microfluidic inlet/outlet and alignment marks visible. Bottom-right: Microscope image with increased magnification showing the misalignment at the sensing electrodes.	121
4.21	Diagram representing a typical hydraulic circuit.	125
4.22	Simulated results for microfluidic flow: (a) surface velocity; (b) normalised pressure contours with proportional velocity arrows; and (c) the utilised mesh for the simulations.	127
4.23	Simulated electrochemical response for Fc(MeOH) ₂ : (a) cyclic voltammogram (10 mV·s ⁻¹) for a 500 nm nanogap; (b) effect of the interelectrode distance (x) on the limiting current density; (c) concentration profile of c_{red} at I_{lim} ; and (d) concentration profile of c_{ox} at I_{lim}	130
4.24	I-V traces for vertical nanogap device filled with air for backside connection modes: (1) solder paste; (2) coiled wire with solder paste; and (3) coiled wire.	131
4.25	Capacitance profile for a 500 nm vertical nanogap device filled with air for the frequency range 1 kHz to 500 kHz.	132
5.1	3D exploded diagram of the horizontal nanogap device showing glass substrate, electrode layer (highlighted) and the SU-8 passivation & microfluidic layers.	143
5.2	Diagram demonstrating some of the fabrication techniques used to obtain horizontal nanogaps: (a) use of oblique-angle deposition with microchannels acting as a shadowmask [33]; (b) oxidation of a metallic layer to create an overhanging self-aligned mask [34]; (c) milling through a metallic layer with a Ga ⁺ focused ion beam [35]; and (d) use of a focused electron beam to pattern a bilayer of positive tone electron-beam resists to create the desired lift-off profile.	145

5.3	Diagram showing the horizontal nanogap device (cross section not to scale).	150
5.4	Fabrication process of the horizontal nanogap sensor. (a): Electron-beam lithography (EBL) is used to pattern the electrode layers by lift-off method. (b) A thin SU-8 layer is deposited and blanket exposed to form a passivation layer. An aluminium hard mask, patterned with a second EBL lift-off mask, is used to pattern the thin SU-8 layer by reactive ion etching (RIE). (c) A series of wet and dry etching steps are used to define the device geometry and provide access to electrical contact pads. (d) Finally a thick SU-8 layer is optically patterned to provide a microfluidic layer.	151
5.5	3D diagram showing the (a) glass substrate and (b) patterned electrode layers.	152
5.6	3D diagram showing the sample with (a) just the electrode layer and (b) both the electrode and passivation layers.	154
5.7	SEM images showing the second ma-N 2403 layer after development.	155
5.8	SEM images showing the electrode and passivation layers after lift-off (Figure 5.4, view (b).): (a) A $\approx 12\ \mu\text{m}$ straight section of the serpentine. (b) Measurements of the separation of both the electrode and passivation layers.	156
5.9	3D diagram showing the sample (a) before and (b) after patterning the microfluidic layer.	158
5.10	Microscope images showing a completed device: (a) The bow-tie-shaped sensor with contact pads and central microfluidic channel visible. (b) A close-up showing the serpentine microfluidic channel with funnelled inlet/outlet.	160
5.11	Annotated diagram depicting exposed top surface of the nanogap electrodes.	160
5.12	Simulated current response and surface concentration plots demonstrating the effect of undesirable lateral etching of the passivation layer.	162
5.13	Simulated limiting current density for (a) increasing lateral etch distance and (b) increasing passivation height.	163
5.14	Measured I-V responses in air for a prototype and a batch of five horizontal nanogap devices.	164
5.15	Capacitance profiles for the frequency range 1 kHz to 1 MHz in (a) air and in (b) 10 mM PBS.	164
5.16	Current response in 10 mM phosphate buffer, 2.7 mM KCl, 137 mM NaCl, pH 7.4, with and without the addition of $50\ \mu\text{M Fc}(\text{CH}_2\text{OH})_2$ at a scan rate of $2.5\ \text{mV}\cdot\text{s}^{-1}$. In both cases the collector is held at 0.0 V <i>vs.</i> Ag/AgCl.	165
5.17	Diagram illustrating the physical displacement occurring after oligonucleotide hybridisation.	166
5.18	Molecular diagram comparing DNA and PNA structures.	167
5.19	Capacitance spectra showing the dose response for: (a) & (b) complementary and (c) & (d) non-complementary single-stranded DNA.	172
5.20	Relative percentage change in capacitance at 25 kHz for increasing concentrations of complementary and non-complementary single-stranded DNA. Error bars represent the measurement error calculated using Equation 3.10, for 5 measurements of each device at each stage in the experiment.	173

List of Figures

A.1	Fabrication process based on SU-8 as a sacrificial layer. (a): First a lower metallic electrode is patterned using lift-off photolithography. (b): A diluted (500 nm) SU-8 layer is spincoated and exposed, but not fully cross-linked, acting as a sacrificial layer. (c): The top metallic electrode is ‘blanket’ deposited before patterning a thicker (2-30 μm) SU-8 layer that simultaneously acts as an etch mask for the top electrode as well as improving structural integrity. (d): Any remaining SU-8 that is not cross-linked (e.g. within the confined nanogap) is developed overnight.	197
A.2	Fabrication process based on SU-8 as an adhesive layer. (a): Metallic electrodes are first patterned on identical quartz substrates using lift-off photolithography. (b): A diluted (1 μm) SU-8 layer is spincoated on one of the substrates and exposed to UV. (c): The second half of the device is aligned before applying force and/or heat during one of the cross-linking stages to bond the two halves. . . .	200
B.1	Fabrication process based on FIB milling. (a): A ma-N 2403 resist is patterned by EBL on top of a Ti/Au/SU-8 stack. (b): A Ti hard mask is then patterned by lift-off and the exposed SU-8 dry etched using either RIE or ICP-RIE. (c): The top Ti layer and underlying SU-8 are used as a mask to mill a nanogap into the Ti/Au electrode layer. (d): After FIB milling the Ti hard mask is removed in diluted HF.	202
B.2	SEM images showing the result of etching the SU-8 passivation layer with RIE for: (a) a wide channel and (b) a narrow channel.	202
B.3	SEM images showing the result of etching the SU-8 passivation layer with ICP-RIE for: (a) a wide channel and (b) a narrow channel.	203
B.4	SEM images showing the results of FIB milling for decreasing sizes of nanogaps.	203
B.5	SEM images showing the results of dose tests ($600 \mu\text{C}\cdot\text{cm}^{-2}$) for approximately (a) 200 nm, (b) 100 nm, (c) 80 nm and (d) 50 nm nanogaps.	204
B.6	Microscope images of: (a) the nanogap serpentine and (b) a zoomed view showing the ‘halo’ effect caused by cross-linking of the PMMA adhesion layer.	205
B.7	Proposed nanoimprint lithography process. (a): First a XR-1541-006 resist is patterned using EBL to act as an etch mask. (b): The silicon is then dry etched and the resist removed to produce the master. An intermediate stamp is then created in PDMS (c): The PDMS stamp is then used to imprint a bilayer consisting of an imprint resist (e.g., Mr-UVcur06 [micro resist technology]) and a lift-off resist (e.g., PMGI/LOR [MicroChem]). (d): The residual resist is then removed using ICP/ICP-RIE with an O_2 chemistry whilst also generating the undercut required for lift-off. (e): A stack of Ti/Au/ SiO_2 can then be deposited using electron-beam lithography without breaking vacuum. (f) Finally lift-off is performed in a suitable solvent (e.g. Remover PG [MicroChem]) to create the nanogap structure.	207
B.8	SEM images showing: (a) two straight sections of the 200 nm nanogap serpentine connected by an arc and (b) measurement of the 200 nm nanogap serpentine. .	208

B.9	SEM images showing measurement of (a) 50 nm straight sections and (b) 50 nm arcs.	208
C.1	Contour (a) and streamline (b) plots for the horizontal nanogap device with top surface of electrodes partially exposed in air.	212
C.2	Contour (a) and streamline (b) plots for the horizontal nanogap device with top surface of electrodes completely passivated in air.	212
C.3	Contour (a) and streamline (b) plots for the horizontal nanogap device with top surface of electrodes partially exposed in PBS.	213
C.4	Contour (a) and streamline (b) plots for the horizontal nanogap device with top surface of electrodes completely passivated in PBS.	213
C.5	Simulated surface velocities for (a) a flow rate of $18.41 \text{ nL}\cdot\text{min}^{-1}$ and (b) mesh used for the microfluidic simulations.	215
C.6	Surface velocity plots for flow rates of (a) $18.41 \text{ nL}\cdot\text{min}^{-1}$ and (b) $1.29 \mu\text{L}\cdot\text{min}^{-1}$	215

List of Tables

1.1	Examples of biosensor elements.	3
1.2	Typical criteria for assessing biosensor performance.	4
1.3	Progression of generator–collector systems and key milestones in their application.	7
2.1	Parameters used for the simulation of a simple redox cycling process in a micro-gap generator–collector system.	33
2.2	Calculated Debye lengths for a monovalent electrolyte with a range of ionic concentrations.	38
3.1	Selection of electrodes used for the electrochemical detection of cysteine and cystine (lower portion) with their metrics.	55
3.2	Combinations of sugars and bacteria immobilised on the different electrodes for the dielectric spectroscopy study.	70
3.3	Sequence of key experimental steps for the capacitive sensing of sugar–bacteria interactions.	72
3.4	Calculated capacitance per unit area for the self-assembled monolayer at a frequency of 1 kHz in different PBS concentrations.	75
3.5	Ratios of specific to non-specific signals at a frequency of 1 kHz in different PBS concentrations.	78
4.1	Process parameters for the prototype device fabrication.	102
4.2	Process parameters for etching the channel in silicon.	111
4.3	ICP-RIE parameters used to characterise the effect of etch duration.	111
4.4	PECVD parameters for SiN _x deposition.	113
4.5	Process parameters for patterning the SiN _x passivation layer.	114
4.6	Process parameters for patterning the lower and upper electrodes.	117
4.7	Process parameters for silicon–glass anodic bonding.	119
4.8	Anodic bonding parameters and respective device yield.	121
4.9	Hydraulic resistances of fluidic circuit components.	125
4.10	Expected flow rates of 0.25 m tubing using a 5-350 mbar vacuum pump.	126
4.11	Simulated flow velocities at the sensor surface.	128
4.12	Parameters used to simulate the effect of interelectrode distance on limiting current density.	129

List of Tables

5.1	Process parameters for patterning the electrode layer.	153
5.2	ICP-RIE parameters used for low-pressure SU-8 etching.	155
5.3	Process parameters for patterning the passivation layer.	157
5.4	Process parameters for the sequence of etch processes to define device geometry and provide electrical access.	158
5.5	Process parameters for patterning the microfluidic layer.	159
5.6	Sequence of key experimental steps for the capacitive sensing of PNA–DNA interactions.	170
A.1	Process parameters for the fabrication of a vertical nanogap device using SU-8 as a sacrificial layer.	196
A.2	Process parameters for the fabrication of a vertical nanogap device using SU-8 as an adhesive layer.	199
B.1	Process steps for EBL patterning the NIL silicon master.	208
B.2	Optimised ICP-RIE parameters for etching vertical sidewalls in silicon.	209
C.1	Parameters used for electrostatic simulations.	211

List of Abbreviations

AC	alternating current
ALD	atomic layer deposition
BC	boundary condition
CFU	colony-forming unit
CMC	<i>N</i> -Cyclohexyl- <i>N'</i> -(2-morpholinoethyl)carbodiimide metho- <i>p</i> -toluenesulfonate
CMP	chemical mechanical polishing
CV	cyclic voltammetry <i>or</i> cyclic voltammogram
DC	direct current
DI	deionised
DLW	direct laser writer
DMSO	dimethyl sulfoxide
DNA	deoxyribonucleic acid
DPN	dip-pen nanolithography
ds	double-stranded
EBL	electron-beam lithography
EDC	<i>N</i> -(3-Dimethylaminopropyl)- <i>N'</i> -ethylcarbodiimide hydrochloride
EDL	electric double layer
EDTA	ethylenediaminetetraacetic acid
EG	ethylene-glycol
ETA	ethanolamine
FIA	fluorescence immunoassay
FIB	focused ion beam
GAL	2-Acetamido-2-deoxy- α -D-glucopyranose
GNDU	ground unit
HMDS	hexamethyldisilane
HPLC	high-performance liquid chromatography
HSQ	hydrogen silsesquioxane
IC	integrated circuit

List of Abbreviations

ICP	inductively-coupled plasma
IDA	interdigitated array
IDE	interdigitated electrode
IPA	isopropyl alcohol
LER	line edge roughness
LMM	laser micromachining
MALDI-TOF MS	matrix-assisted laser desorption/ionisation time-of-flight mass spectrometry
MANN	α -D-mannose
MEMS	microelectromechanical systems
MCH	6-mercapto-1-hexanol
μTAS	micro total analysis systems
NIL	nanoimprint lithography
NHS	N-Hydroxysuccinimide
NMP	N-Methyl-2-pyrrolidone
OPG	ordinary pyrolytic graphite
oxPTMs	oxidative post-translational modifications (oxPTMs)
PBS	phosphate-buffered saline
PDMS	polydimethylsiloxane
PEC	proximity effect correction
PEG	polyethylene-glycol
PECVD	plasma-enhanced chemical vapour deposition
POC	point-of-care
PNA	peptide nucleic acid
QCM	quartz crystal microbalance
RE	reference electrode
RIE	reactive ion etching
RNS	reactive nitrogen species
ROS	reactive oxygen species
RT	room temperature
RRDE	rotating ring–disk electrode
SAM	self-assembled monolayer
SCE	saturated calomel electrode
SECM	scanning electrochemical microscope
SMU	source measure unit
SOI	silicon-on-insulator
ss	single-stranded
TMAH	tetramethylammonium hydroxide
WE	working electrode

List of Symbols

A	area	$[\text{m}^2]$
A	frequency factor	$[\text{s}^{-1}]$
$c_{i,0}$	concentration of ions of type ' i ' at the electrode surface	$[\text{mol}\cdot\text{m}^{-3}]$
$c_{i,b}$	concentration of ions of type ' i ' in bulk solution	$[\text{mol}\cdot\text{m}^{-3}]$
\mathbf{D}	electric displacement field	$[\text{C}\cdot\text{m}^{-2}]$
D_i	diffusion coefficient for ions of type ' i '	$[\text{m}^2\cdot\text{s}^{-1}]$
E	Young's modulus	$[\text{Pa}]$
E_{eq}	equilibrium potential	$[\text{V}]$
E°	standard electrode potential	$[\text{V}]$
\mathbf{E}	electric field vector	$[\text{V}\cdot\text{m}^{-1}]$
F	Faraday constant	$[\text{C}\cdot\text{mol}^{-1}]$
G	standard Gibbs free energy	$[\text{kJ}\cdot\text{mol}^{-1}]$
ΔG^\ddagger	standard Gibbs free energy of activation	$[\text{kJ}\cdot\text{mol}^{-1}]$
i_0	exchange current	$[\text{A}]$
j	flux	$[\text{mol}\cdot\text{m}^{-2}\cdot\text{s}^{-1}]$
j_i	flux of species of type ' i '	$[\text{mol}\cdot\text{m}^{-2}\cdot\text{s}^{-1}]$
j_d	diffusive flux	$[\text{mol}\cdot\text{m}^{-2}\cdot\text{s}^{-1}]$
j_m	migratory flux	$[\text{mol}\cdot\text{m}^{-2}\cdot\text{s}^{-1}]$
k_0	standard heterogeneous rate constant	$[\text{m}\cdot\text{s}^{-1}]$
k_i°	standard heterogeneous rate constant for species of type ' i '	$[\text{m}\cdot\text{s}^{-1}]$
k_B	Boltzmann constant	—
\mathbf{L}	characteristic length	$[\text{m}]$
l	length	$[\text{m}]$
\overline{M}_w	mass-average molar mass	$[\text{kg}\cdot\text{mol}^{-1}]$
m_s	spin quantum number	—
N_A	Avogadro constant	$[\text{mol}^{-1}]$
$n_{i,b}$	number density of ions of type ' i ' per unit volume of bulk solution	$[\text{m}^{-3}]$
n_b	number density of ions per unit volume of bulk solution	$[\text{m}^{-3}]$

List of Symbols

P	pressure	[Pa]
P_e	electrostatic pressure	[V·m ⁻¹]
pK _a	negative logarithm of acid dissociation constant	—
pH	negative logarithm of molar proton concentration	—
Q	volumetric flow rate	[m ³ ·s ⁻¹]
q	elementary charge	[C]
R_h	hydraulic resistance	[Pa·s·m ⁻³]
T	absolute temperature	[K]
T_m	duplex melting temperature	[K]
\mathbf{u}	velocity vector	[m·s ⁻¹]
x	interelectrode distance	[m]
z	charge number	—
<hr/>		
α_i	activity coefficient for species of type ' i '	—
α_a	anodic transfer coefficient	—
α_c	cathodic transfer coefficient	—
Γ	amplification factor	—
γ	surface energy density	[J·m ⁻²]
δ	Nernst diffusion layer thickness	[m]
ϵ_0	permittivity of free space	[F·m ⁻¹]
ϵ_r	relative permittivity	—
ϵ'_r	real part of relative permittivity	—
ϵ''_r	imaginary part of relative permittivity	—
η	polarisation overpotential	[V]
η_c	collection efficiency	—
λ_D	Debye length	[m]
μ	dynamic viscosity	[m ² ·s ⁻¹]
μ_i	mobility of ions of type ' i '	[mol·s·kg ⁻¹]
ρ	electric charge density	[C·m ⁻³]
σ	electrical conductivity	[S·m ⁻¹]
ϕ	electric potential	[V]
ϕ_0	electrode surface potential	[V]
ω	angular frequency	[rad·s ⁻¹]

1 Introduction

A biosensor can be considered of being comprised of two key parts, the biomolecular recognition part and the transduction part. In recent years the field of microelectromechanical systems (MEMS) has seen the emergence of a subset family of devices termed micro total analysis systems (μ TAS). These devices combine a miniaturised sensor platform with microfluidic sample delivery [1]. Electrochemical detection has favourable attributes for these applications as the necessary signal processing circuitry can be easily integrated.

Direct electrochemical detection methods are of particular interest. Such systems are often referred to as 'label-free' electrochemical sensors and benefit from avoiding the need for an expensive and time consuming labelling step. These devices offer the capacity to be low cost, compact, portable, and have the potential to provide analytical results within a few minutes for a range of applications [2].

1.1 Background

It was as early as the 18th century that pioneers such as Luigi Galvani and Alessandro Volta were conducting electrochemical experiments [3, 4]. Galvani's work centred around what he called 'animal electricity', studying the contraction of a dead frog's muscles when applying static charge. Volta instead believed the galvanism was caused by the metal contacts and this disagreement led him to develop the first battery, termed a voltaic pile. This was used by Anthony Carlisle and William Nicholson to demonstrate the electrolysis of water [5]. Some years later Michael Faraday published his accounts of his research in electricity [6], in which he described the now conventional terms: electrode, anode, cathode, electrolyte, ion, anion and cation. Such was the importance of Faraday's work, charge-transfer reactions occurring at the electrode surface are termed 'Faradaic' reactions.

However, it would take over one century before electrochemistry would be utilised for biologi-

cal sensing. In 1962 Leland Clark Jr. and Champ Lyons inadvertently created the first glucose biosensor by demonstrating how blood oxygen content could be monitored using the enzyme glucose oxidase and an electrochemical oxygen probe [7]. But it was the work by Cass *et al.* [8] in developing a redox mediated glucose sensor, capable of determining glucose levels in a drop of blood that revolutionised the field.

Glucose sensing has demonstrated how biosensing can become both socially and economically successful with the technology now assisting an estimated 285 million people worldwide afflicted with diabetes, with the figure expected to reach around 440 million by 2030 [9]. The market is estimated to be worth around \$26 billion by 2021 [10]. Much of this success can be attributed to the patient now having the ability to perform self-monitoring of blood glucose levels using a point-of-care (POC) device. This allows the patient to regularly check and track their blood glucose levels for more effective diabetes management.

Despite the success of glucose biosensing there remain many challenges before biosensors become a ubiquitous part of our daily lives. The consumer electronics industry has continued to push the capabilities of fabrication, lowering costs to the point that mobile electronic devices have now morphed into multifunctional devices with extraordinary capability. Yet commercially available tools for biosensing are often so expensive that they are resigned to the most affluent medical centres, hospitals or laboratories. For example, high-performance liquid chromatography (HPLC) paired with mass spectrometry often forms the pinnacle of analytical performance. Yet the size, high capital investment, maintenance costs and the requirement of highly-trained technicians mean they are unlikely to ever be used for POC biosensing applications.

Fluorescence-based sensors have also demonstrated high sensitivity and selectivity [11] and allow simultaneous detection of a range of biological targets in the form of a fluorescence immunoassay (FIA). Here the hybridisation between an immobilised antigen and a fluorophore-labelled antibody target (in either direct or indirect formats) can be quantitatively determined by the fluorescence signal. However, this technique does suffer from a key drawback; the fluorescent labelling step is both expensive and time-consuming and the optical transduction requires complex apparatus which is presently difficult to miniaturise.

Biosensors use a form of transduction element to detect the presence of analyte within a sample matrix. A diagrammatic representation of a biosensor is depicted in Figure 1.1, with its main elements described in Table 1.1. Transduction methods include electrochemical, gravimetric, optical, piezoelectric and pyroelectric. However, of all the transduction methods, it is the electrochemical transduction that best lends itself to low-cost miniaturised devices.

Electrochemical transduction can be split into three main subsets: amperometric, the measurement of current; impedimetric, the measurement of impedance and potentiometric, the measurement of potential. These measurements offer greater suitability for monolithic chip

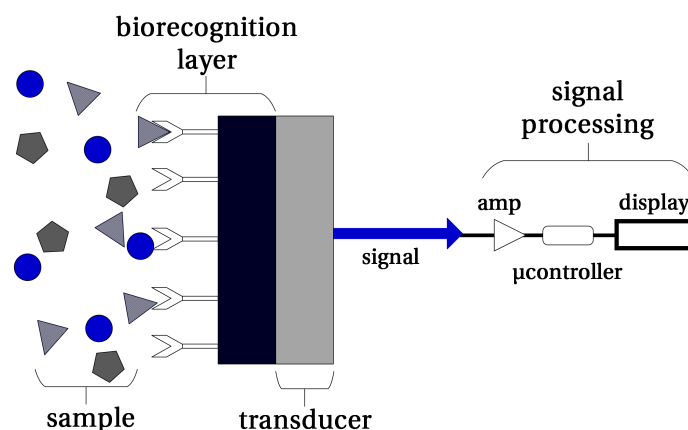


Figure 1.1: Diagrammatic representation of a biosensor.

integration with signal processing circuitry. Direct electrical techniques also benefit from not requiring an expensive and time-consuming labelling step, making them more amenable to large-scale manufacturing and thus the development of low-cost POC devices.

Table 1.1: Examples of biosensor elements.

Biomolecular recognition elements	Transduction methods	Analytes
Antibodies	Electrochemical	Disease biomarkers
Proteins	Gravimetric	Drugs and their metabolites
Enzymes	Optical	Environmental pollutants
Nucleic acids	Piezoelectric	Industrial chemicals
Organelles	Pyroelectric	Physiological markers
Peptides		Toxins
Boronic acids		

1.2 Motivation

Important areas for the development of biosensors are to improve the sensitivity and selectivity, as well as improving the clinical relevance and commercial viability of such devices through miniaturisation, affordability and ease of use. The typical criteria for a biosensor are summarised in Table 1.2.

Table 1.2: Typical criteria for assessing biosensor performance.

Criteria	Remarks
Selectivity	Describes the ability of the biosensor to discriminate the analyte in complex media
Sensitivity	Provides the ratio of output signal for a measured stimulus
Limit of detection/quantification	Defined as the lowest quantity of an analyte that can be reliably detected, usually calculated as 3/10 times the standard deviation divided by the slope of the regression line
Reliability	The device should act with predictable performance
Dynamic range	Describes the range between the largest and smallest levels that can be detected
Cost	This is fundamental to the economic viability of the product
Availability	Promotes market uptake
Sample preparation	Minimising the requirement for sample preparation often reduces time, cost and complexity of a device
Complexity of use	Simple operation can significantly reduce the risk of user error.
Size/portability	For many applications the device must be small enough to be easily transported, stored and deployed; this is especially true for point-of-care and rapid response devices

Some approaches to improve electrochemical sensor performance include the use of enzymes, electrocatalysts and redox cycling. The enzymatic approach provides the advantage that a group of analytes can be detected (e.g. substrates, products and inhibitors) and the enzyme is not consumed in the reaction and therefore can be used continuously. A major drawback is that the stability of the enzyme over prolonged durations in a range of media can limit applications.

For electrocatalytic systems a catalyst is used to mediate the charge transfer between analyte and the electrode (which may in fact be the electrocatalyst). Electrocatalysts lower the activation energy for the reaction without altering the reaction equilibrium whilst also lowering the excess energy consumed due to the activation barriers of a redox reaction. Often an electrocatalyst can be very reaction-specific and can suffer from degradation.

Redox cycling involves the use of two closely spaced electrodes in what is known as a 'generator-collector' configuration. The potentials of the generator and collector electrodes are set such that an analyte can be repeatedly cycled between a reduced and oxidised state. This leads to a single molecule contributing to the current response on each reaction, effectively amplifying the sensor response. Here the challenge is to minimise the interelectrode spacing to reduce time for interdiffusion, as well as providing sufficient surface area for the electrochemical reactions.

Dielectric spectroscopy is a direct electrochemical technique gaining importance as a label-free detection tool for monitoring biomolecular binding events. Sensing involves recording a dielectric spectra of an applied electrical signal across a wide frequency range. The dielectric properties of the system are very complex involving dipole relaxation, ionic relaxation, atomic polarisation and electronic polarisation. However, by monitoring the capacitance changes in the interfacial region (*i.e.*, electrode–biomolecular–electrolyte) can be detected. A small interelectrode spacing means that the electric double layers occupy an increased fraction of the sample volume, mitigating screening effects and increasing sensitivity. Whilst larger surface areas allow increased immobilisation of the recognition probe.

1.2.1 Progression of generator–collector systems

Numerous geometries of generator–collector systems have been studied over a period of several decades. A timeline showcasing some of the key work is provided in Table 1.3. Initial forms of generator–collector systems were not strictly used for redox cycling as the product of the reaction at the collector often diffused or, in the case of hydrodynamic systems, was forced into the bulk solution. In later incarnations both electrodes share both roles of generator and collector in order to amplify the signal. The earliest form of generator–collector electrodes was the rotating ring–disk electrode (RRDE). The rotation of the electrode induces convective flow which moves radially over the generator electrode surface and out towards the collector ring electrode. The first RRDE was used by Frumkin and Nekrasov in 1959 for the reduction of oxygen in alkaline solution [12]. Albery *et al.* contributed significant work on RRDEs for over two decades from 1966 [13] to 1989 [14], refining the theory and developing new applications.

In the 1960s the group of Reilley also produced generator–collector systems whereby the interelectrode distance was adjusted using a micrometer positioner [15–18] to create thin-layer cells. At a similar time Gerischer and coworkers pioneered double channel flow electrodes [19], whereby solution flows over an upstream generator electrode and the product is detected at the downstream collector electrode. In the absence of flow these devices form dual-microband systems, relying on diffusion between the electrodes and were used effectively by Williams *et al.* [20].

As microfabrication processes became more widespread, the ability to pattern electrodes by photolithography resulted in the emergence of interdigitated arrays (IDAs) of electrodes. IDAs were first described by Sanderson & Anderson [21] in 1985 and developed further to improve miniaturisation and explore applications by Bard [22, 23], Chidsey [24], Aoki [25] and Niwa [26–29]. Other significant progression in the use of IDAs has been to achieve submicron interelectrode separation, first reported by Ueno *et al.* [30] and burying the IDAs in microfluidic [31] and nanofluidic [32] channels to improve efficiency.

One of the breakthrough applications of a generator–collector system to arise was scanning

electrochemical microscopy (SECM). SECM-like measurements were first performed by Engstrom *et al.* by using a micropositioning device to place a microelectrode perpendicular to the diffusion layer of a macro electrode [33]. However, it wasn't until 1989 that the term SECM was introduced by Bard *et al.* who refined the work of Engstrom, describing the generator-collector mode relative to the z direction [34] as well as the procedure for obtaining 3D scans and topographic information of conducting and insulating surfaces, the process that is most associated with SECM today [35]. This approach was utilised by Fan & Bard in 1995 for the detection of single molecules [36].

Dual-cylinder microelectrodes were introduced by Seddon *et al.* in 1994 [37], with the first dual-disc electrodes later used by Matysik [38] in 1997. Whilst the idea of dual-hemisphere electrodes was discussed in 1999 [39], it was not until 2008 that a method to fabricate the electrodes would be developed by the Marken group [40]. These were then exploited by Rassaei *et al.* for a range of sensing applications including the detection of glucose [41].

In the last few decades, advanced microfabrication techniques has allowed the fabrication of more complex structures such as micro- and nanopores. In 1999 Henry & Fritsch developed a bottom-up fabrication technique for the formation of a gold/polyimide/gold micropore [42]. In 2006 nanoparticles were used by Neugebauer *et al.* to create a nanoporous device [43]. Many novel devices with a range of geometries have been reported by the groups of Lemay [32, 44–46], Wolfrum [32, 45–47] and Matsue [48, 49] that include nanofluidic cavities [44, 46], crossbar arrays [48], IDAs buried in nanofluidic channels [32], dual-plate nanocavities [45], nanoporous structures [47] and ring–ring nanocavities [49].

1.2.2 Trend towards nanogap devices

The spectacular advance in the development and application of integrated-circuit (IC) technology, driven by the consumer electronics industry, has seen the resulting capabilities exploited by the academic community. Modern microfabrication techniques have allowed feature sizes of structures to be decreased to the micro- and nanometre scale with high controllability and reproducibility. Techniques primarily involve thin-film deposition/growth, etching and lithographic patterning. These processes provide the ability to incorporate electrodes, fluidic channels and integrated circuits (ICs) all within a single device.

Given the importance device geometry plays in the effectiveness of redox cycling and other electrochemical sensors, it comes as no surprise that there has been a trend to fabricate electrodes with submicron interelectrode spacing. Such devices are often termed 'nanogap' sensors and their inherent scale make them particularly suited to the detection of biomolecules (amino acids, lipids, oligonucleotides, proteins, *etc.*). It is important to highlight that detection of larger biological targets (bacteria, cells, *etc.*) are often restricted due to their size ($>1\ \mu\text{m}$).

Table 1.3: Progression of generator–collector systems and key milestones in their application.

Year	Type	Remarks	Reference & Group
1959	RRDE	First generator–collector system	Frumkin <i>et al.</i> [12]
1965	TLC	Use of a micrometer to create a TLC	Anderson & Reilley [15]
1965	DCFE	First DCFE system	Gerischer <i>et al.</i> [19]
1973	TLC	Detailed theoretical expressions for TLCs	Hubbard & Peters [50]
1985	IDA	Studied steady-state currents of redox markers	Sanderson & Anderson [21]
1986	IDA	Coupled redox simulations with experiments	Bard <i>et al.</i> [22]
1986	IDA	Use of redox-active polymer with an IDA	Chidsey <i>et al.</i> [24]
1986	SECM	First SECM-like experiments	Engstrom [33]
1988	IDA	Quantitative analysis of redox markers	Aoki <i>et al.</i> [25] [Tabei]
1989	IDA	Fabricated a vertically separated IDA	Niwa [26] <i>et al.</i> [Tabei]
1989	SECM	First use of the term ‘SECM’	Bard <i>et al.</i> [34]
1989	SECM	Performed 3D surface scans with a SECM	Kwak & Bard [35]
1990	IDA	Studied effect of geometry on system response	Niwa <i>et al.</i> [27] [Tabei]
1991	IDA	Diffusion measurements using an IDA	Nishihara <i>et al.</i> [51]
1991	IDA	First biomolecular detection using an IDA	Niwa <i>et al.</i> [28] [Tabei]
1991	DCFE	Simulations of collector efficiencies of DCFEs	Fisher & Compton [52]
1994	dual-cylinder	First dual-cylinder system	Seddon <i>et al.</i> [37]
1995	SECM	First single molecule detection	Fan & Bard [36]
1997	dual-microband	Flowless DCFE for diffusion-based studies	Williams <i>et al.</i> [20]
1997	dual-disc	First use of a dual-disc system	Matysik [38]
1999	recessed microdisc	Recessed microdisc geometry	Henry & Fritsch [42]
1999	dual-hemisphere	Simulation of dual-hemisphere geometry	Fulian <i>et al.</i> [39] [Fisher]
2003	STM	Single molecule resistance measurements	Xu & Tao [53]
2003	IDA	Fabrication of high aspect ratio IDAs	Honda <i>et al.</i> [54]
2003	IDA	Submicron separation by EBL	Finot <i>et al.</i> [55]
2004	IDA	Submicron separation by NIL	Beck <i>et al.</i> [56]
2006	recessed nanodisc	Use of a nanoparticle template	Neugebauer <i>et al.</i> [43]
2007	IDE	Contained an IDA in a microchannel	Dam <i>et al.</i> [31]
2007	nanofluidic cavity	Detection of concentration fluctuations	Zevenbergen <i>et al.</i> [44] [Lemay]
2008	STM	Single molecule charge transfer measurements	Li <i>et al.</i> [57]
2008	TLC	Single molecule detection with a Pt–Hg TLC	Sun & Mirkin [58]
2008	crossbar array	Demonstration of a crossbar array	Lin <i>et al.</i> [48] [Matsue]
2009	IDA	Contained an IDA in nanochannels	Goluch <i>et al.</i> [32] [Wolfrum & Lemay]
2008	dual-hemisphere	First use of dual-hemisphere electrodes	French <i>et al.</i> [40] [Marken]
2009	ring-recessed disc	Simulation of ring-recessed disc electrodes	Menshykau <i>et al.</i> [59] [Compton]
2010	dual-hemisphere	Demonstrated glucose detection	Rassaei & Marken [41]
2010	plane-recessed disc	First plane-recessed disc electrodes	Menshykau <i>et al.</i> [60] [Compton]
2010	nanocavity	Dopamine detection with a vertical nanogap	Kätelhön <i>et al.</i> [45] [Lemay & Wolfrum]
2011	nanoporous	Use of a nanoporous oxide template	Hüske & Wolfrum [47]
2011	nanofluidic cavity	Single molecule stochastic detection	Zevenbergen <i>et al.</i> [46] [Wolfrum & Lemay]
2012	nanofluidic cavity	Adsorption found to be a limiting factor	Kang <i>et al.</i> [61] [Lemay]
2013	dual-plate	Developed epoxy-based dual-plate fabrication	Dale <i>et al.</i> [62] [Compton & Marken]
2014	nanofluidic cavity	Enzymatic detection in a vertical nanogap	Rassaei <i>et al.</i> [63] [Lemay]
2015	nanocavity ring–ring	Demonstrated embryoid detection	Kanno <i>et al.</i> [49] [Matsue]

Key: DCFE = dual-channel flow electrode, EBL = electron-beam lithography, IDA = interdigitated array, NIL = nanoimprint lithography, RRDE = rotating ring–disc electrode, SECM = scanning electrochemical microscopy, STM = scanning tunneling microscopy, TLC = thin-layer cell

By using electrodes separated by a nanogap, very large electric fields ($>100 \text{ kV}\cdot\text{m}^{-1}$) can be established using fairly modest applied potentials ($<100 \text{ mV}$). For biosensing applications the analyte is often within an ionic matrix and as a consequence the electric field will decay exponentially with increasing distance from the electrode due to the formation of an electric double layer. Enhancement of the electric field provides improved dynamic range and therefore better ability to distinguish properties. Furthermore, these strong electric fields can be applied whilst ensuring that the potentials are low enough that electrolysis does not occur. It is important to stress that for extremely high electric fields ($>0.5 \text{ V}\cdot\text{nm}^{-1}$) biomolecules may exhibit an adverse response, such as irreversible conformation or malfunction [64, 65].

Nanogap sensors therefore provide a highly sensitive platform for the interrogation of biomolecules whilst minimising sample volume and allow a wide range of electrical behaviours to be observed. There are two distinct types of nanogap devices that have emerged. The first are those that are used for the interrogation of biomolecules, often consisting of sharp triangular point-like electrodes with minute interelectrode distances to match that of the target molecule and minimal contact area for improved selectivity. The geometry of such devices results in poor redox amplification and complicated fringing effects. The second type are those that are employed for electrochemical sensing applications, where both the submicron interelectrode distance and relatively large surface area lead to improved performance.

As early as 1974 Aviram and Ratner [66] predicted that individual molecules would in future be used in circuit devices. This drive towards molecular electronics as well as single-molecule interrogation has resulted in a vast amount of research on nanogap devices aimed at trapping single molecules. Consequently the majority of early nanogap devices are in the form of horizontal coplanar point-like junctions with lengths of less than $1 \mu\text{m}$. Again, this geometry results in nonplanar electric fields that complicate electrochemical detection and minute surface areas that limit biomolecular probe loading. However, many of the fabrication techniques developed can still be exploited to fabricate larger surface areas.

Early forms of nanogaps were predominantly horizontal coplanar devices and fabrication techniques include: atomic layer deposition (ALD) with adhesive tape planarisation [67, 68], chemical-mechanical polishing [69], deep-ultraviolet lithography with silylation [70], dip-pen nanolithography [71], direct chemical synthesis [72], electrochemical synthesis [73], electromigration [74–76], electron-beam lithography, [77, 78], electroplating [79], focused ion beam (FIB) milling [80–83], mechanical break junctions [84, 85], molecular lithography [86], molecular rulers [87, 88], oblique-angle [89] and double oblique-angle evaporation [90], on-wire lithography [91], oxidative plasma ablation [92] and transfer printing [93].

The earliest vertical coplanar nanogaps appear in the late 1980s and existed in the guise of the SECM [33, 34]. In more recent years new methods to fabricate vertical coplanar nanogaps have emerged and these include: etching recesses into sidewalls of metallic layers [94], etching sacrificial layers [44, 46, 95, 96], molecular-beam epitaxy [97], nanosphere lithography [43, 98]

and nanoskiving [99]. Naturally as microfabrication facilities and processing equipment have become more accessible there has been a growing number of researchers working on nanogap devices. As a consequence there are several recent comprehensive reviews [100–103] covering the fabrication and applications of nanogap sensors.

Considering devices suited for electrochemical redox cycling sensing applications (*i.e.*, $<50\text{ }\mu\text{m}$ interelectrode spacing and relatively large surface area), the most widely reported devices are the class of interdigitated arrays (IDAs) with horizontally orientated nanogaps. For these devices the fabrication technique of choice remains electron-beam lithography. Most of these devices do not have any form of passivation on the top surface of the electrode. In the case of redox cycling applications this means there are large electrode areas exposed to the sample volume that do not provide a linear diffusion path. Furthermore, unless the electrodes are contained in a micro- or nanofluidic channel (to limit sensing volume) there can be a large loss of diffusive flux into the bulk solution, reducing the amplification factor. In order to maximise the sensitivity the residence time of molecules inside the detection volume should be maximised, while the spacing between the electrodes (x) is minimised. For capacitive-based biosensors the sensitivity can be hampered by the fringe electric fields and an exposed top surface without volume containment would remove any benefits of confining the electric double layers of the opposing electrodes.

In more recent years there has been a growing number of vertical nanogap devices to emerge. The most popular method for producing vertical nanogaps has been to etch a sacrificial layer that exists between two metallic layers. The popularity of this method is most likely due to the excellent control of layer deposition/growth and well characterised etching processes now available. However, the method is not without its pitfalls. For cavities etched in sidewalls the structural integrity and stability of the overhanging electrode limits the distance that can be etched and thus the surface area that can be achieved. For encapsulated cavities with micro- nanofluidic access, complete removal of the sacrificial layer and residues becomes extremely difficult for large areas without causing collapse. Without judicious choice of material or geometry any residual stress in the top electrode can lead to buckling, altering the interelectrode spacing along the nanochannel.

It is important to highlight that for sensing applications simply minimising the interelectrode separation is not always suitable. Many of the reported devices to date provide enough amplification to detect a few hundred molecules, but the minuscule sensing volume limits their molar sensitivity, which is more important in many applications. For instance, a nanofluidic redox cycling sensor with length of $100\text{ }\mu\text{m}$, width of $2\text{ }\mu\text{m}$ and 100 nm interelectrode separation, coupled to a bulk reservoir with an analyte concentration of 100 fM contains approximately 0.0012 molecules within the sensing volume. By increasing the length and width of the electrodes the total sensing volume increases, providing a greater likelihood of a molecule being present between the electrodes, and therefore detected.

Chapter 1. Introduction

To summarise, electrochemical nanogap devices offer an exciting prospect for sensitive and selective label-free sensing applications. Benefits include low sample and reagent volumes, low power consumption and the ability to create large electric fields with modest applied potentials. Modern microfabrication processes have allowed continued downscaling of the transducer element and offers the possibility to incorporate micro- and/or nanofluidics with ICs into a single chip to provide a μ TAS solution. However, there are remaining challenges involved in the fabrication of large surface area nanogap devices.

1.3 Aim

The aim of this thesis is to explore the design and fabrication of large surface area nanogap biosensors with ideal geometry for both redox cycling and dielectric spectroscopy sensing applications. Maintaining ideal parallel-plate geometry presents a significant challenge but is paramount in providing a linear diffusion path, reduced loss of diffusive flux to bulk solution and minimising fringe electric fields. The approach is two-fold: keep interelectrode spacing to the nanometre regime to ensure both reduced interdiffusion time and to mitigate the screening effect from the electric double layer; as well as provide a relatively large surface area, increasing the electroactive sensing volume and therefore detection probability.

1.4 Overview of the thesis

Using a microgap sensor, both redox-cycling and dielectric spectroscopy sensing techniques are introduced. Next, the design and fabrication methods for two new large-area vertical and horizontal coplanar nanogap geometries are reported. The horizontal coplanar nanogap device is then used to demonstrate oligonucleotide detection by monitoring capacitance changes caused by the reformation of the electric double layer following hybridisation.

Chapter 2 reviews the necessary theory in order to better understand the potential benefits of nanogap systems. This includes: an overview of operating a pair of electrodes in generator-collector configuration and its advantages; the nature of the electric double layer formed at a polarised electrode in an electrolyte, and the effects of bringing two electrodes into close proximity; the capacitance of the electric double layer; and finally the importance of the self-assembled monolayer for affinity-based biosensing applications.

Chapter 3 describes the fabrication of a dual-plate microgap sensor and results of studies of both the detection of the cysteine–cystine redox couple by redox cycling and detection of an *E coli*. strand by performing dielectric spectroscopy sensing.

Chapter 4 introduces the design, fabrication and characterisation of a large-area vertical copla-

nar nanogap device using a novel fabrication technique that combines an inductively-coupled plasma reactive ion etch with anodic bonding of silicon and borosilicate glass substrates.

Chapter 5 covers the design, fabrication and characterisation of a large-area horizontal coplanar nanogap device using a state-of-the-art electron-beam lithography system. The geometry maximises the surface area of the device by utilising a serpentine geometry whilst maintaining dimensions that permit a wide range of microfluidic flowrates. The device is then used for dielectric spectroscopy sensing of PNA–DNA binding events

Chapter 6 provides a retrospective summary of the completed work, discussion of the two direct electrochemical sensing techniques and an outlook on future applications and research directions for large area nanogap devices.

References

- [1] D. R. Reyes, D. Iossifidis, P.-A. Auroux, and A. Manz. Micro Total Analysis Systems. 1. Introduction, Theory, and Technology. *Analytical Chemistry*, 74(12):2623–2636, 2002.
- [2] J. Wang. Electrochemical biosensors: Towards point-of-care cancer diagnostics. *Biosensors and Bioelectronics*, 21(10):1887–1892, 2006.
- [3] L. Galvani. De viribus electricitatis in motu muscularis commentarius. *De Bononiensi Scientiarum et Artium Instituto atque Academia Commentarii*, 7:363–418, 1791.
- [4] A. Volta. On the Electricity Excited by the Mere Contact of Conducting Substances of Different Kinds. *Philosophical Transactions of the Royal Society of London*, 90:403–431, 1800.
- [5] W. Nicholson and A. Carlisle. Account of the new Electrical or Galvanic Apparatus of Sig. Alex. Volta, and Experiments performed with the same. *Journal of Natural Philosophy, Chemistry and the Arts*, 4(September):179–187, 1801.
- [6] M. Faraday. Experimental Researches in Electricity. *Philosophical Transactions of the Royal Society of London*, 124:77–122, 1834.
- [7] L. C. Clark Jr. and C. Lyons. Electrode systems for continuous monitoring in cardiovascular surgery. *Annals Of The New York Academy Of Sciences*, 102(1):29–45, 1962.
- [8] A. E. G. Cass, G. Davis, G. D. Francis, H. A. O. Hill, W. J. Aston, I. J. Higgins, E. V. Plotkin, L. D. L. Scott, and A. P. F. Turner. Ferrocene-mediated enzyme electrode for amperometric determination of glucose. *Analytical Chemistry*, 56(4):667–671, 1984.
- [9] J. E. Shaw, R. A. Sicree, and P. Z. Zimmet. Global estimates of the prevalence of diabetes for 2010 and 2030. *Diabetes Research and Clinical Practice*, 87(1):4–14, 2010.
- [10] Zion Market Research. Global Diabetes Care Devices Market: By Device Type, Applications, Size, Growth and Forecast 2015-2021. Technical report, 2016.
- [11] T. Li, W. Hu, and D. Zhu. Nanogap Electrodes. *Advanced Materials*, 22(2):286–300, 2010.

References

- [12] A. Frumkin, L. Nekrasov, B. Levich, and J. Ivanov. Die anwendung der rotierenden scheibenelektrode mit einem ringe zur untersuchung von zwischenprodukten elektrochemischer reaktionen. *Journal of Electroanalytical Chemistry*, 1(1):84–90, 1959.
- [13] W. J. Albery. Ring-disc electrodes. Part 1.—A new approach to the theory. *Transactions of the Faraday Society*, 62:1915–1919, 1966.
- [14] W. J. Albery and A. R. Mount. Ring Disk Electrodes 24.— Studies of Counterion Fluxes at a Thionine-Coated Electrode. *Journal of the Chemical Society-Faraday Transactions I*, 85(11):3717–3724, 1989.
- [15] L. B. Anderson and C. N. Reilley. Thin-layer electrochemistry: use of twin working electrodes for the study of chemical kinetics. *Journal of Electroanalytical Chemistry*, 10:538–552, 1965.
- [16] L. B. Anderson and C. N. Reilley. Thin-layer electrochemistry: steady-state methods of studying rate processes. *Journal of Electroanalytical Chemistry*, 10(4):295–305, 1965.
- [17] D. M. Oglesby, S. H. Omang, and C. N. Reilley. Thin Layer Electrochemical Studies Using Controlled Potential or Controlled Current. *Analytical Chemistry*, 37(11):1312–1316, 1965.
- [18] B. McDuffie and C. N. Reilley. Twin-electrode thin-layer electrochemistry. Kinetics of second-order disproportionation of uranium(V) by decay of steady-state current. *Analytical Chemistry*, 38(13):1881–1887, 1966.
- [19] H. Gerischer, I. Mattes, and R. Braun. Elektrolyse im strömungskanal: Ein verfahren zur untersuchung von reaktionen und zwischenprodukten. *Journal of Electroanalytical Chemistry*, 10(5):553–567, 1965.
- [20] D. E. Williams, K. Ellis, A. Colville, S. J. Dennison, G. Laguillo, and J. Larsen. Hydrodynamic modulation using vibrating electrodes: Application to electroanalysis. *Journal of Electroanalytical Chemistry*, 432(1-2):159–169, 1997.
- [21] D. G. Sanderson and L. B. Anderson. Filar electrodes : Steady-state currents and spectroelectrochemistry at twin interdigitated electrodes. *Analytical Chemistry*, 57(12):2388–2393, 1985.
- [22] A. J. Bard, J. A. Crayston, G. P. Kittlesen, T. V. Shea, and M. S. Wrighton. Digital simulation of the measured electrochemical response of reversible redox couples at microelectrode arrays: consequences arising from closely spaced ultramicroelectrodes. *Analytical Chemistry*, 58(11):2321–2331, 1986.
- [23] T. V. Shea and A. J. Bard. Digital simulation of homogeneous chemical reactions coupled to heterogeneous electron transfer and applications at platinum/mica/platinum ultramicroband electrodes. *Analytical Chemistry*, 59(17):2101–2111, 1987.

-
- [24] C. E. Chidsey, B. J. Feldman, C. Lundgren, and R. W. Murray. Micrometer-spaced platinum interdigitated array electrode: fabrication, theory, and initial use. *Analytical Chemistry*, 58(3):601–607, 1986.
- [25] K. Aoki, M. Morita, O. Niwa, and H. Tabei. Quantitative analysis of reversible diffusion-controlled currents of redox soluble species at interdigitated array electrodes under steady-state conditions. *Journal of Electroanalytical Chemistry and Interfacial Electrochemistry*, 256(2):269–282, 1988.
- [26] O. Niwa, M. Morita, and H. Tabei. Fabrication and characteristics of vertically separated interdigitated array electrodes. *Journal of Electroanalytical Chemistry*, 267(1-2):291–297, 1989.
- [27] O. Niwa, M. Morita, and H. Tabei. Electrochemical behavior of reversible redox species at interdigitated array electrodes with different geometries: consideration of redox cycling and collection efficiency. *Analytical Chemistry*, 62(5):447–452, 1990.
- [28] O. Niwa, M. Morita, and H. Tabei. Highly sensitive and selective voltammetric detection of dopamine with vertically separated interdigitated array electrodes. *Electroanalysis*, 3(3):163–168, 1991.
- [29] O. Niwa, Y. Xu, H. B. Halsall, and W. R. Heineman. Small-volume voltammetric detection of 4-aminophenol with interdigitated array electrodes and its application to electrochemical enzyme immunoassay. *Analytical Chemistry*, 65(11):1559–63, 1993.
- [30] K. Ueno, M. Hayashida, J.-Y. Ye, and H. Misawa. Fabrication and electrochemical characterization of interdigitated nanoelectrode arrays. *Electrochemistry Communications*, 7(2):161–165, 2005.
- [31] V. A. T. Dam, W. Olthuis, and A. van den Berg. Redox cycling with facing interdigitated array electrodes as a method for selective detection of redox species. *The Analyst*, 132(4):365–370, 2007.
- [32] E. D. Goluch, B. Wolfrum, P. S. Singh, M. A. G. Zevenbergen, and S. G. Lemay. Redox cycling in nanofluidic channels using interdigitated electrodes. *Analytical and Bioanalytical Chemistry*, 394(2):447–456, 2009.
- [33] R. C. Engstrom, M. Weber, D. J. Wunder, R. Burgess, and S. Winquist. Measurements within the diffusion layer using a microelectrode probe. *Analytical Chemistry*, 58(4):844–848, 1986.
- [34] A. J. Bard, F.-R. F. Fan, J. Kwak, and O. Lev. Scanning Electrochemical Microscopy. Introduction and Principles. *Analytical Chemistry*, 61(2):132–138, 1989.
- [35] J. Kwak and A. J. Bard. Scanning electrochemical microscopy. Apparatus and two-dimensional scans of conductive and insulating substrates. *Analytical Chemistry*, 61(17):1794–1799, 1989.

References

- [36] F.-R. F. Fan and A. J. Bard. Electrochemical detection of single molecules. *Science*, 267(5199):871–874, 1995.
- [37] B. J. Seddon, C. F. Wang, W. Peng, and X. Zhang. Dual-cylinder Microelectrodes Part 2. — Steady-state Generator and Collector Electrode Currents. *Journal of the Chemical Society, Faraday Transactions*, 90(4):605–608, 1994.
- [38] E.-M. Matysik. Voltammetric characterization of a dual-disc microelectrode in stationary solution. *Electrochimica Acta*, 42(20-22):3113–3116, 1997.
- [39] Q. Fulian, N. A. Williams, and A. C. Fisher. Computational electrochemistry: three-dimensional boundary element simulations of double electrode geometries. *Electrochemistry Communications*, 1(3–4):124–127, 1999.
- [40] R. W. French, A. M. Collins, and F. Marken. Growth and application of paired gold electrode junctions: evidence for nitrosonium phosphate during nitric oxide oxidation. *Electroanalysis*, 20(22):2403–2409, 2008.
- [41] L. Rassaei and F. Marken. Pulse-voltammetric glucose detection at gold junction electrodes. *Analytical Chemistry*, 82(17):7063–7067, 2010.
- [42] C. S. Henry and I. Fritsch. Microfabricated Recessed Microdisk Electrodes: Characterization in Static and Convective Solutions. *Analytical Chemistry*, 71(3):550–556, 1999.
- [43] S. Neugebauer, U. Müller, T. Lohmüller, J. P. Spatz, M. Stelzle, and W. Schuhmann. Characterization of nanopore electrode structures as basis for amplified electrochemical assays. *Electroanalysis*, 18(19-20):1929–1936, 2006.
- [44] M. A. G. Zevenbergen, D. Krapf, M. R. Zuiddam, and S. G. Lemay. Mesoscopic Concentration Fluctuations in a Fluidic Nanocavity Detected by Redox Cycling. *Nano Letters*, 7(2):384–388, 2007.
- [45] E. Kätelhön, B. Hofmann, S. G. Lemay, M. A. G. Zevenbergen, A. Offenhäusser, and B. Wolfrum. Nanocavity redox cycling sensors for the detection of dopamine fluctuations in microfluidic gradients. *Analytical Chemistry*, 82(20):8502–8509, 2010.
- [46] M. A. G. Zevenbergen, P. S. Singh, E. D. Goluch, B. L. Wolfrum, and S. G. Lemay. Stochastic sensing of single molecules in a nanofluidic electrochemical device. *Nano Letters*, 11(7):2881–2886, 2011.
- [47] M. Hüske and B. Wolfrum. Fabrication of a nanoporous dual-electrode system for electrochemical redox cycling. *Physica Status Solidi (A) Applications and Materials Science*, 208(6):1265–1269, 2011.
- [48] Z. Lin, Y. Takahashi, Y. Kitagawa, T. Umemura, H. Shiku, and T. Matsue. An addressable microelectrode array for electrochemical detection. *Analytical Chemistry*, 80(17):6830–6833, 2008.

- [49] Y. Kanno, K. Ino, H. Shiku, and T. Matsue. A local redox cycling-based electrochemical chip device with nanocavities for multi-electrochemical evaluation of embryoid bodies. *Lab on a Chip*, 15(23):4404–4414, 2015.
- [50] A.T. Hubbard and D.G. Peters. Electrochemistry in thin layers of solution. *CRC Critical Reviews in Analytical Chemistry*, 3(2):201–242, 1973.
- [51] H. Nishihara, F. Dalton, and R. W. Murray. Interdigitated Array Electrode Diffusion Measurements in Donor- Acceptor Solutions in Polyether Electrolyte Solvents. *Analytical Chemistry*, 63(24):2955–2960, 1991.
- [52] A. C. Fisher and R. G. Compton. Double-channel electrodes: Homogeneous kinetics and collection efficiency measurements. *Journal of Applied Electrochemistry*, 21(3):208–212, 1991.
- [53] B. Xu and N. J. Tao. Measurement of Single-Molecule Resistance by Repeated Formation of Molecular Junctions. *Science*, 301(5637):1221–1223, 2003.
- [54] N. Honda, K. Emi, T. Katagiri, T. Irita, S. Shoji, H. Sato, T. Homma, T. Osaka, M. Saito, J. Mizuno, and Y. Wada. 3-D comb electrodes for amperometric immuno sensors. In *12th International Conference on Solid-State Sensors, Actuators and Microsystems.*, pages 1132–1135. IEEE, 2003.
- [55] E. Finot, E. Bourillot, R. Meunier-Prest, Y. Lacroute, G. Legay, M. Cherkaoui-Malki, N. Latruffe, O. Siri, P. Braunstein, and A. Dereux. Performance of interdigitated nanoelectrodes for electrochemical DNA biosensor. *Ultramicroscopy*, 97(1-4):441–449, 2003.
- [56] M. Beck, F. Persson, P. Carlberg, M. Graczyk, I. Maximov, T. G. I. Ling, and L. Montelius. Nanoelectrochemical transducers for (bio-) chemical sensor applications fabricated by nanoimprint lithography. *Microelectronic Engineering*, 73-74:837–842, 2004.
- [57] C. Li, I. Pobelov, T. Wandlowski, A. Bagrets, A. Arnold, and F. Evers. Charge transport in single Au |alkanedithiol | Au Junctions: Coordination geometries and conformational degrees of freedom. *Journal of the American Chemical Society*, 130(17):19, 2008.
- [58] P. Sun and M. V. Mirkin. Electrochemistry of individual molecules in zeptoliter volumes. *Journal of the American Chemical Society*, 130(26):8241–8250, 2008.
- [59] D. Menshykau, F. J. del Campo, F. X. Muñoz, and R. G. Compton. Current collection efficiency of micro- and nano-ring-recessed disk electrodes and of arrays of these electrodes. *Sensors and Actuators B: Chemical*, 138(1):362–367, 2009.
- [60] D. Menshykau, M. Cortina-Puig, F. J. del Campo, F. X. Muñoz, and R. G. Compton. Plane-recessed disk electrodes and their arrays in transient generator–collector mode: The measurement of the rate of the chemical reaction of electrochemically generated species. *Journal of Electroanalytical Chemistry*, 648(1):28–35, 2010.

References

- [61] S. Kang, K. Mathwig, and S. G. Lemay. Response time of nanofluidic electrochemical sensors. *Lab on a Chip*, 12(7):1262, 2012.
- [62] S. E. C. Dale, C. E. Hotchen, and F. Marken. Generator-collector electroanalysis at tin-doped indium oxide-epoxy-tin-doped indium oxide junction electrodes. *Electrochimica Acta*, 101:196–200, 2013.
- [63] L. Rassaei, K. Mathwig, S. Kang, H. A. Heering, and S. G. Lemay. Integrated biodetection in a nanofluidic device. *ACS Nano*, 8(8):8278–8284, 2014.
- [64] P. Ojeda-May and M. E. Garcia. Electric Field-Driven Disruption of a Native β -Sheet Protein Conformation and Generation of a Helix-Structure. *Biophysical Journal*, 99(2):595–599, 2010.
- [65] D. Jarukanont, J. T. S. Coimbra, B. Bauerhenne, P. A. Fernandes, S. Patel, M. J. Ramos, and M. E. Garcia. Biomolecular structure manipulation using tailored electromagnetic radiation: a proof of concept on a simplified model of the active site of bacterial DNA topoisomerase. *Physical Chemistry Chemical Physics*, 16(39):21768–21777, 2014.
- [66] A. Aviram and M. A. Ratner. Molecular rectifiers. *Chemical Physics Letters*, 29(2):277–283, 1974.
- [67] X. Chen, H.-R. Park, M. Pelton, X. Piao, N. C. Lindquist, H. Im, Y. J. Kim, J. S. Ahn, K. J. Ahn, N. Park, D.-S. Kim, and S.-H. Oh. Atomic layer lithography of wafer-scale nanogap arrays for extreme confinement of electromagnetic waves. *Nature Communications*, 4:2361, 2013.
- [68] A. Cui, Z. Liu, H. Dong, F. Yang, Y. Zhen, W. Li, J. Li, C. Gu, X. Zhang, R. Li, and W. Hu. Mass Production of Nanogap Electrodes toward Robust Resistive Random Access Memory. *Advanced Materials*, 28(37):8227–8233, 2016.
- [69] C. Lee, E.-H. Yang, N. V. Myung, and T. George. A Nanochannel Fabrication Technique without Nanolithography. *Nano Letters*, 3(10):1339–1340, 2003.
- [70] A. E. Cohen and R. R. Kunz. Large-area interdigitated array microelectrodes for electrochemical sensing. *Sensors and Actuators, B: Chemical*, 62(1):23–29, 2000.
- [71] R. D. Piner, J. Zhu, F. Xu, S. Hong, and C. Mirkin. "Dip-Pen" Nanolithography. *Science*, 283:661–663, 1999.
- [72] T. Jain, Q. Tang, T. Bjørnholm, and K. Nørgaard. Wet chemical synthesis of soluble gold nanogaps. *Accounts of Chemical Research*, 47(1):2–11, 2014.
- [73] J. H. Kim, H. Moon, S. Yoo, and Y. K. Choi. Nanogap electrode fabrication for a nanoscale device by volume-expanding electrochemical synthesis. *Small*, 7(15):2210–2216, 2011.

-
- [74] J. Park, A. N. Pasupathy, J. I. Goldsmith, C. Chang, Y. Yaish, J. R. Petta, M. Rinkoski, J. P. Sethna, H. D. Abruña, P. L. McEuen, D. C. Ralph, H. D. Abruña, P. L. McEuen, and D. C. Ralph. Coulomb blockade and the Kondo effect in single-atom transistors. *Nature*, 417(6890):722–725, jun 2002.
- [75] A. K. Mahapatro, S. Ghosh, and D. B. Janes. Nanometer scale electrode separation (nanogap) using electromigration at room temperature. *IEEE Transactions on Nanotechnology*, 5(3):232–236, 2006.
- [76] M. Ito, K. Morihara, T. Toyonaka, K. Takikawa, and J.-I Shirakashi. High-throughput nanogap formation by field-emission-induced electromigration. *Journal of Vacuum Science & Technology B, Nanotechnology and Microelectronics: Materials, Processing, Measurement, and Phenomena*, 33(5):051801, 2015.
- [77] Th. Weimann, P. Hinze, H. Scherer, and J. Niemeyer. Fabrication of a metallic single electron tunneling transistor by multilayer technique using lithography with a scanning transmission electron microscope. *Microelectronic Engineering*, 46(1):165–168, 1999.
- [78] M. A. Guillorn, D. W. Carr, R. C. Tiberio, E. Greenbaum, and M. L. Simpson. Fabrication of dissimilar metal electrodes with nanometer interelectrode distance for molecular electronic device characterization. *Journal of Vacuum Science & Technology B: Microelectronics and Nanometer Structures*, 18(3):1177, 2000.
- [79] A. F. Morpurgo, C. M. Marcus, and D. B. Robinson. Controlled fabrication of metallic electrodes with atomic separation. *Applied Physics Letters*, 74(14):2084–2086, 1999.
- [80] T. Nagase, T. Kubota, and S. Mashiko. Fabrication of nano-gap electrodes for measuring electrical properties of organic molecules using a focused ion beam. *Thin Solid Films*, 438-439(3):374–377, 2003.
- [81] T. Blom, K. Welch, M. Strømme, E. Coronel, and K. Leifer. Fabrication and characterization of highly reproducible, high resistance nanogaps made by focused ion beam milling. *Nanotechnology*, 18(28):285301, 2007.
- [82] A. Cui, Z. Liu, H. Dong, Y. Wang, Y. Zhen, W. Li, J. Li, C. Gu, and W. Hu. Single grain boundary break junction for suspended nanogap electrodes with gapwidth down to 1-2 nm by focused ion beam milling. *Advanced Materials*, 27(19):3002–3006, 2015.
- [83] R. Hatsuki, A. Honda, M. Kajitani, and T. Yamamoto. Nonlinear electrical impedance spectroscopy of viruses using very high electric fields created by nanogap electrodes. *Frontiers in Microbiology*, 6:940, 2015.
- [84] J. Moreland and J. W. Ekin. Electron tunneling into superconducting filaments using mechanically adjustable barriers. *Applied Physics Letters*, 47(2):175–177, 1985.
- [85] M. A. Reed. Conductance of a Molecular Junction. *Science*, 278(5336):252–254, 1997.

References

- [86] G. S. McCarty, B. Moody, and M. K. Zachek. Enhancing electrochemical detection by scaling solid state nanogaps. *Journal of Electroanalytical Chemistry*, 643(1-2):9–14, 2010.
- [87] A. Hatzor and P. Weiss. Molecular rulers for scaling down nanostructures. *Science*, 291(5506):1019–1020, 2001.
- [88] V. M. Serdio V., T. Muraki, S. Takeshita, D. E. Hurtado S, S. Kano, T. Teranishi, and Y. Majima. Gap separation-controlled nanogap electrodes by molecular ruler electroless gold plating. *RSC Advances*, 5(28):22160–22167, 2015.
- [89] S. Kubatkin, A. Danilov, M. Hjort, J. Cornil, J.-L. Brédas, N. Stuhr-Hansen, P. Hedegård, and T. Bjørnholm. Single-electron transistor of a single organic molecule with access to several redox states. *Nature*, 425(6959):698–701, 2003.
- [90] Y. Naitoh, K. Tsukagoshi, K. Murata, and W. Mizutani. A Reliable Method for Fabricating sub-10 nm Gap Junctions Without Using Electron Beam Lithography. *e-Journal of Surface Science and Nanotechnology*, 1:41–44, 2003.
- [91] L. Qin. On-Wire Lithography. *Science*, 309(5731):113–115, 2005.
- [92] X. Guo, M. Myers, S. Xiao, M. Lefenfeld, R. Steiner, G. S. Tulevski, J. Tang, J. Baumert, F. Leibfarth, J. T. Yardley, M. L. Steigerwald, P. Kim, and C. Nuckolls. Chemoresponsive monolayer transistors. *Proceedings of the National Academy of Sciences of the United States of America*, 103(31):11452–11456, 2006.
- [93] O. Fakhr, P. Altpeter, K. Karrai, and P. Lugli. Easy Fabrication of Electrically Insulating Nanogaps by Transfer Printing. *Small*, 7(17):2533–2538, 2011.
- [94] S. Strobel, K. Arinaga, A. Hansen, and M. Tornow. A silicon-on-insulator vertical nanogap device for electrical transport measurements in aqueous electrolyte solution. *Nanotechnology*, 18(29):295201, 2007.
- [95] D.-Y. Jang, Y.-P. Kim, H.-S. Kim, S.-H. Ko Park, S.-Y. Choi, and Y.-K. Choi. Sublithographic vertical gold nanogap for label-free electrical detection of protein-ligand binding. *Journal of Vacuum Science & Technology B: Microelectronics and Nanometer Structures*, 25(2):443–447, 2007.
- [96] M. I. Schukfeh, L. Sepunaru, P. Behr, W. Li, I. Pecht, M. Sheves, D. Cahen, and M. Tornow. Towards nanometer-spaced silicon contacts to proteins. *Nanotechnology*, 27(11):115302, 2016.
- [97] R. Krahne, A. Yacoby, H. Shtrikman, I. Bar-Joseph, T. Dadosh, and J. Sperling. Fabrication of nanoscale gaps in integrated circuits. *Applied Physics Letters*, 81(4):730–732, 2002.
- [98] C. Ma, N. M. Contento, L. R. Gibson, and P. W. Bohn. Redox cycling in nanoscale-recessed ring-disk electrode arrays for enhanced electrochemical sensitivity. *ACS Nano*, 7(6):5483–5490, 2013.

-
- [99] P. Pourhossein and R. C. Chiechi. Fabricating Nanogaps by Nanoskiving. *Journal of Visualized Experiments*, (75):e50406, 2013.
- [100] R. L. McCreery and A. J. Bergren. Progress with Molecular Electronic Junctions: Meeting Experimental Challenges in Design and Fabrication. *Advanced Materials*, 21(43):4303–4322, 2009.
- [101] Z. Li, Y. Wang, J. Wang, Z. Tang, J. G. Pounds, and Y. Lin. Rapid and Sensitive Detection of Protein Biomarker Using a Portable Fluorescence Biosensor Based on Quantum Dots and a Lateral Flow Test Strip. *Analytical Chemistry*, 82(16):7008–7014, 2010.
- [102] X. Chen, Z. Guo, G. M. Yang, J. Li, M. Q. Li, J. H. Liu, and X. J. Huang. Electrical nanogap devices for biosensing. *Materials Today*, 13(11):28–41, 2010.
- [103] A. Cui, H. Dong, and W. Hu. Nanogap Electrodes towards Solid State Single-Molecule Transistors. *Small*, 11(46):6115–6141, 2015.

2 Theory

This chapter provides an overview of the fundamentals of electrochemistry, highlighting certain key aspects that apply to nanogap transducers for electrochemical sensing applications. Firstly the two main sensing mechanisms are briefly described before exploring the principle of electrochemical reactions occurring at electrodes. The limiting factors of the electrochemical reaction are discussed and the concept of using voltammetry to assess whether they are kinetically or mass-transport limited is introduced. The process of redox cycling with a generator–collector system in order to improve the system response is then demonstrated.

Next the theory of the electric double layer formed at the electrode–electrolyte interface is introduced and the effect of the ionic strength of the electrolyte demonstrated. Attention is then drawn to the effect of overlapping electric double layers, which can be present in nanogap systems. The capacitance of the electric double layer is explored before finally discussing the importance of self-assembled monolayers for capacitive biosensing applications.

2.1 Overview of the sensing systems

Redox cycling

Redox cycling involves polarising two closely spaced electrodes such that an electroactive analyte is repeatedly cycled between a reduced and oxidised state. In a conventional electrochemical cell, analyte may be lost to the bulk solution and undergo further irreversible reactions. However, when the interelectrode spacing is below that of the Nernst diffusion layer thickness (δ), typically $1\text{ }\mu\text{m}$ to $50\text{ }\mu\text{m}$, the time for interdiffusion is reduced sufficiently such that an individual molecule can contribute to the current response on each reaction as it shuttles across the gap. This effectively amplifies the signal response and improves the sensitivity of the system.

Dielectric spectroscopy

Dielectric spectroscopy is gaining importance as a label-free technique for monitoring biomolecular interactions. Molecules within the sensing volume respond differently depending on the frequency of the perturbing oscillatory field. This allows relaxation processes occurring over a wide range of characteristic times (from approximately 10^{-12} s to 10^3 s) to be investigated, revealing information about electron transfer, atomic bonds and molecular motions. The sensing strategy is to detect changes in the dielectric properties and charge distribution at the sensor surface by monitoring the electrical capacitance. These changes occur as a result of binding events at the recognition layer and reorganisation of the electric double layer formed at the interface. For nanogap systems the electric double layers occupy an increased fraction of the sample volume, mitigating screening effects and increasing sensitivity.

2.2 Principles of electrochemistry

Electrochemistry is the study of factors that affect the transfer of charge between the interfaces of phases, for example, between two metallic electrodes separated by an electrolyte solution. Often the term ‘electrochemical cell’ is used to describe the collection of interfacial boundaries. The electrostatic potential across an interface within the electrochemical cell, for instance $\phi_m - \phi_s$, is an indicator of the ability to transfer charge between them. Information on these interfacial regions can be deduced by monitoring and analysing the charge transfer and potential between them.



Within the electrochemical cell two half-cell reactions take place, one at each of the two electrodes. In order to perform analysis, one of these half-cell reactions is usually controlled, through the use of a reference electrode (RE). The RE is an electrode with steady phases that provide a stable reference potential. Any changes in charge transfer can then be considered to be caused by the other half-cell reaction occurring at the other electrode, named the working electrode (WE).

At equilibrium the electric potential of the electrode is described by the Nernst equation:

$$E_{\text{eq}} = E^{\circ} + \frac{RT}{nF} \ln \frac{\alpha_{\text{ox}}}{\alpha_{\text{red}}} \quad (2.1)$$

Where E° is the standard electrode potential and α_{ox} and α_{red} are the activities of the oxidised and reduced species at the electrode surface. If the activity coefficients of the two species can be considered equal, they may be replaced by values of concentrations.

In order to drive an electrolysis reaction an electric potential must be applied such that an overpotential (η) is formed, where η is the difference between the applied electrode potential E and the cell equilibrium potential E_{eq} , ($E - E_{\text{eq}}$). As the overpotential develops, the Fermi level within the lattice of the metal electrode will change. With a sufficient change in the Fermi level, electron transfer at the interfacial region becomes thermodynamically viable and oxidative or reductive reactions will ensue. These processes are termed 'Faradaic' processes because they obey Faraday's law*. There are also other processes whereby the interfacial region undergoes changes (*e.g.*, the development of an adlayer or charging of the electric double layer) that can cause transient external currents without any electron transfer across the interface and these processes are termed 'non-Faradaic' processes.

By controlling the potential of the WE with respect to the RE and recording the resulting current, one can yield information about the interfacial boundary and hence the Faradaic and non-Faradaic processes occurring. This broad technique is termed voltammetry and is discussed in greater detail later. The current, i [A], is determined by the number of electrons involved in the reaction, n , the Faraday constant, F [$\text{C}\cdot\text{mol}^{-1}$], the electrode area, A [m^2], and the flux of the analyte at the interfacial boundary, j [$\text{mol}\cdot\text{m}^{-2}\cdot\text{s}^{-1}$], as shown by the following equation:

$$i = nFAj \quad (2.2)$$

The flux is of primary concern and describes the rate of the reaction, comprising of the electron transfer heterogeneous rate constant, k_0 [$\text{m}\cdot\text{s}^{-1}$], which describes the electron transfer kinetics and the concentration of analyte at the electrode–electrolyte interface, $c_{i,0}$ [$\text{mol}\cdot\text{m}^{-3}$], which is dependent on the mass transport of analyte to the interface:

$$j = k_0 c_{i,0} \quad (2.3)$$

*The reaction of 1 mole of electroactive species from one oxidation state to another involves 96,485 coulombs.

Chapter 2. Theory

The slowest process will consequently become the reaction rate-determining process. However, in general, the factors that influence the reaction rate include:

- concentration of analyte and other species within the bulk solution;
- concentration of analyte and other species at the interfacial boundary;
- mass transport (diffusion, convection and migration) of species from bulk solution to the interfacial boundary;
- other chemical reactions occurring within the electrolyte;
- and other electrode reactions (adsorption, electrodeposition, *etc.*).

2.2.1 Kinetics

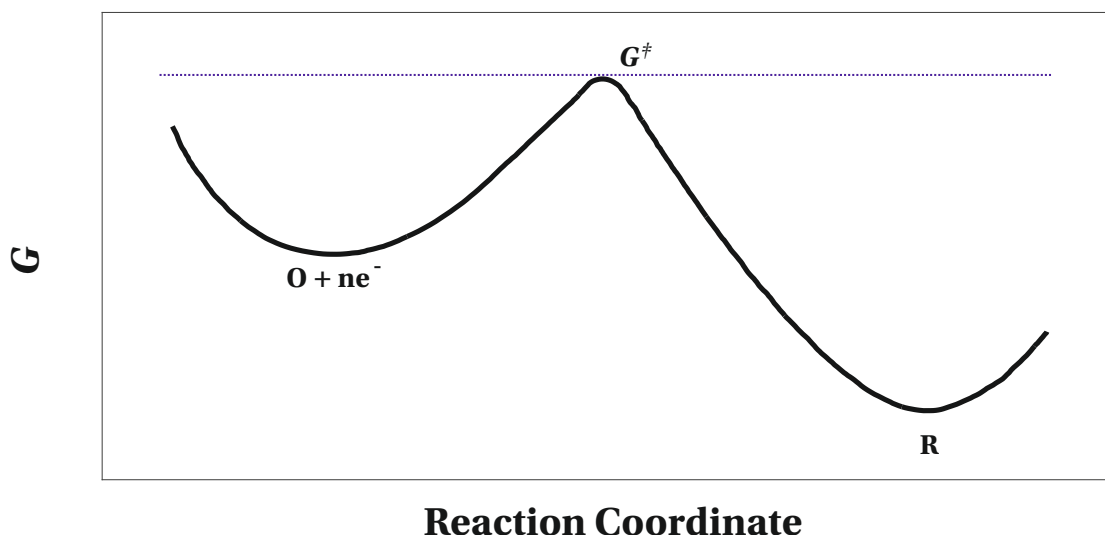


Figure 2.1: Free energy plot for a simple, single electron reduction of species 'O' .

Electron transfer reactions can be described by the transition state model shown in Figure 2.1, occurring via a path that involves reactants $O + e^-$ overcoming an energy barrier (transition state), en route to forming products R . Transition state theory then defines the rate of the reduction reaction as:

$$k_{\text{red}} = A \exp\left(\frac{-\Delta G_{\text{red}}^\ddagger}{RT}\right) \quad (2.4)$$

Where $\Delta G_{\text{red}}^\ddagger$ is the standard Gibbs free energy of activation [$\text{kJ}\cdot\text{mol}^{-1}$] and A is the frequency factor, describing the frequency of collisions at the electrode surface with correct orientation.

The important thing to note is that the applied potential at the electrode, ϕ_m , and consequent potential of the solution, ϕ_s , will alter the free energies of the reactants (G_{red}^\ddagger), products (G_{ox}^\ddagger) and transition state (G^\ddagger). This leads to the potential dependence of the kinetics of the electrode reaction. For simplicity these complex relationships are often simplified using standard constants k_i° [$\text{m}\cdot\text{s}^{-1}$] such that the rate constants at other potentials can be expressed as follows:

$$k_{\text{red}} = k_{\text{red}}^\circ \exp\left(\frac{-\alpha_c F \eta}{RT}\right) \quad (2.5)$$

and

$$k_{\text{ox}} = k_{\text{ox}}^\circ \exp\left(\frac{\alpha_a F \eta}{RT}\right) \quad (2.6)$$

Given the net current for the reaction can be simply expressed as: $i = i_a + i_c$, therefore:

$$i = FA(k_{\text{ox}}c_{\text{red}} - k_{\text{red}}c_{\text{ox}}) \quad (2.7)$$

By substituting Equations 2.5 and 2.6 into Equation 2.7 the Butler–Volmer equation is derived, describing the net current:

$$i = i_0 \left[\exp\left(\frac{\alpha_a F \eta}{RT}\right) c_{\text{red}} - \exp\left(\frac{-\alpha_c F \eta}{RT}\right) c_{\text{ox}} \right] \quad (2.8)$$

Where i_0 is the exchange current [A]. There are several important factors to consider here: the net current response is formed of both anodic and cathodic contributions and if the magnitude of both the anodic and cathodic contributions are equal, the net current will be zero; the exchange current density is directly proportional to the heterogeneous rate constant, k_0 , and therefore provides an indicator of the kinetics of the system; and finally both the anodic and cathodic current responses are exponentially dependent on the potential as well as being dependent on the concentration of the reduced and oxidised species, respectively.

2.2.2 Mass transport

In order for electrolysis to occur the reactant molecules must be present at the electrode–electrolyte interface. Therefore the reaction will be dependent on the rate at which molecules

Chapter 2. Theory

are brought to or from the electrode through mass transport. The key transport processes are convection, diffusion and migration.

Convection

Convection is the movement caused by a mechanical force acting on a solution. Natural convection includes the movement caused by thermal or density gradients within the solution and can significantly affect studies performed with large electrodes. Forced convection includes stirring or pumping the solution. For microfluidic systems the flow regime is often laminar and therefore the velocity vector \mathbf{u} [$\text{m}\cdot\text{s}^{-1}$] is well defined. The change in concentration can then be given by:

$$\frac{\partial c_i}{\partial t} = -u_x \frac{\partial c_i}{\partial x} \quad (2.9)$$

Diffusion

Diffusion of a species is dependent on a concentration gradient and Fick's law describes the relationship between the analyte concentration, c_i [$\text{mol}\cdot\text{m}^{-3}$], analyte diffusion coefficient, D_i [$\text{m}^2\cdot\text{s}^{-1}$], time, t [s], and the diffusion field's Cartesian directions, x , y and z .

$$\frac{\partial c_i}{\partial t} = D_i \frac{\partial^2 c_i}{\partial x^2} + D_i \frac{\partial^2 c_i}{\partial y^2} + D_i \frac{\partial^2 c_i}{\partial z^2} \quad (2.10)$$

If the diffusion can be considered planar the equation can be simplified to a single dimension:

$$\frac{\partial c_i}{\partial t} = D_i \frac{\partial^2 c_i}{\partial x^2} \quad (2.11)$$

The diffusional flux, j_d [$\text{mol}\cdot\text{m}^{-2}\cdot\text{s}^{-1}$], of analyte at a given point can then be written as:

$$j_d = -D_i \frac{\partial c_i}{\partial x} \quad (2.12)$$

Migration

Applied potentials at the electrode within the electrochemical cell leads to the formation of an electric double layer and a subsequent potential drop at the electrode–electrolyte interface. Ions within the electrolyte experience electrostatic forces leading to movement to or from the electrode.

This migratory flux, j_m , is proportional to the concentration of the ion, c_i , the electric field, ϕ , and the mobility of the ion, μ_i :

$$j_m \propto -\mu_i c_i \frac{\partial \phi}{\partial x} \quad (2.13)$$

High concentrations of supporting electrolyte are often used to ensure the formation of very small electric double layers, mitigating migration effects.

Transport-limited reaction

For transport-limited reactions the Nernst model that describes an estimated diffusion layer thickness (δ), typically 1 μm to 50 μm , as a result of extrapolating the steady state concentration gradient allows the flux of species perpendicular to the electrode due to linear diffusion to be described as:

$$j = \frac{i}{nFA} = D_i \frac{c_{i,b} - c_{i,0}}{\delta} \quad (2.14)$$

Given a sufficient overpotential, all the transported electroactive species are consumed by the electrolysis reaction and $c_{i,0} \rightarrow 0$. By combining with Equation 2.2 it can be seen that a steady-state limiting current will be reached for transport-limited reactions:

$$I_{\text{lim}} = \frac{D_i n F A c_{i,b}}{\delta} \quad (2.15)$$

2.2.3 Voltammetry

Voltammetry is the study of an electrochemical cell's current as a function of an applied voltage. Variants include: cyclic, squarewave, differential pulse, staircase, and stripping. Possibly the most common is cyclic voltammetry, which was pioneered by Nicholson and Shain in 1964 [1]. Here an electrochemical cell is perturbed with a low-frequency triangular voltage waveform.

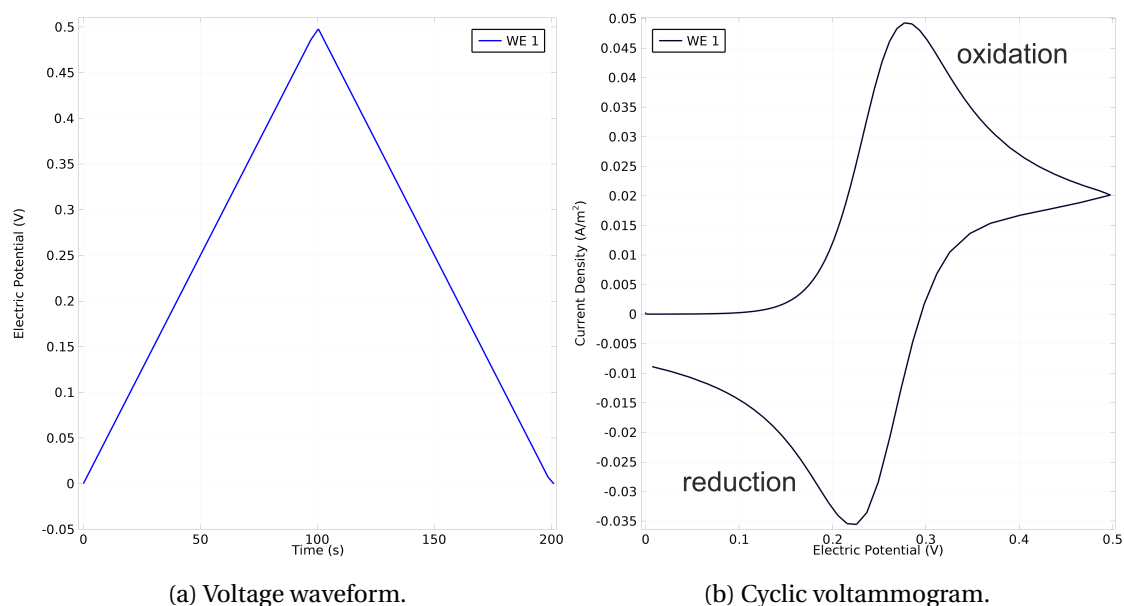


Figure 2.2: Voltage waveform (a) and cyclic voltammogram (b) for a system containing a single working electrode.

By analysing the current response, detailed information on the concentration of electroactive species, molecular reactions, diffusion and electron transfer characteristics can be gleaned. A typical perturbing signal and resulting current response for a reversible electroactive species are shown in Figures 2.2a and 2.2b, respectively.

It can be seen that as the potential is ramped up, an overpotential (η) is imposed and current rapidly increases as reactant at the electrode surface undergoes oxidation to form product. Throughout this process the concentration of surface reactant decreases and the concentration of surface product increases, causing an ever larger concentration gradient to be formed.

The surface reactant eventually becomes completely depleted and an anodic peak current is reached (i_{pa}); reactant must now travel from bulk solution to the electrode surface and the current begins to fall. The potential is then ramped back down, causing the reverse, reductive, reaction and a corresponding cathodic peak (i_{pc}) is observed.

By monitoring the derivative of the current, information about the system can be revealed: the rate of change of current prior to i_p is governed by electron transfer kinetics and the rate of change of current following i_p is governed by mass transport.

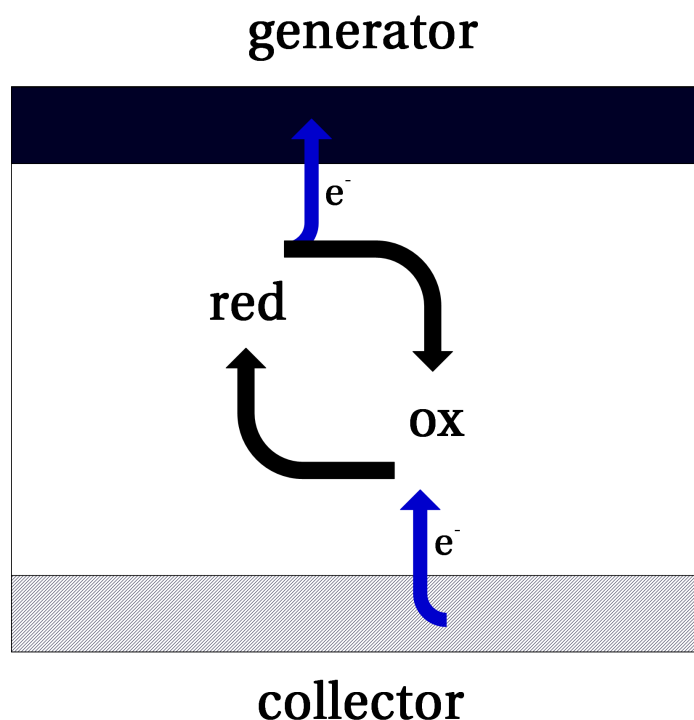


Figure 2.3: Diagram depicting the principle of redox cycling between generator and collector electrodes.

2.2.4 Redox cycling

One method to overcome the rapid depletion of analyte at the electrode–electrolyte interface is to perform redox cycling using what is referred to as a ‘generator–collector’ system. By introducing a second working electrode with an independently controlled potential (through the use of a bipotentiostat), the second working electrode can be held at a potential such that ‘generated’ product is ‘collected’ and converted to another species, preferably back to the reactant. If the reactant can be regenerated the analyte can again contribute to the signal.



When the interelectrode separation is below that of the Nernst diffusion layer thickness (δ), it results in overlapping diffusion fields. The interdiffusion time is now significantly faster, meaning molecules effectively shuttle between the two electrodes. With such a system an

analyte can be repeatedly switched between reduced and oxidised states. The significance is that a single molecule now contributes to the Faradaic current response on each reaction, and is less likely to undergo tertiary reactions, amplifying the sensor response and providing a diffusion-limited response. Figure 2.3 depicts the redox cycling process between generator and collector electrodes. In this example the reduced species is oxidised at the generator and reduced at the collector.

When referring to redox cycling systems, rather than use the parameter δ , it is convenient to define an explicit parameter for interelectrode spacing, x . The average shuttling time for a single molecule to diffuse across this distance can then be defined as:

$$T_s = \frac{x^2}{2D} \quad (2.16)$$

Where T_s is the average shuttling time of the molecule [s], D_i is the diffusion coefficient of the molecule in question [$\text{m}^2 \cdot \text{s}^{-1}$] and x is the interelectrode distance [m]. From this the average current contribution of a single molecule shuttling between the two electrodes that can transfer n elementary charges (q) can be evaluated as:

$$I_s = \frac{nq}{2T_s} = \frac{nqD_i}{x^2} \quad (2.17)$$

In order to demonstrate the amplification effect of redox cycling, the electrochemical response of an example system, in this case 1,1'-ferrocenedimethanol ($\text{Fc}(\text{CH}_2\text{OH})_2$), with $20 \mu\text{m}$ interelectrode spacing is now presented. The simulation settings were identical to those used to illustrate the cyclic voltammogram in Figure 2.2b apart from the addition of the second electrode held at a static reducing potential. Simulation parameters for the example are provided in Table 2.1. The voltage waveforms for both the generator (performing a standard cyclic voltammetry sweep with respect to the RE) and collector (held at a constant voltage with respect to the RE) are shown in Figure 2.4a shows.

Figure 2.4b shows that the reactions at both electrodes reach a diffusion-limited, steady-state current of approximately $0.25 \text{ A} \cdot \text{m}^{-2}$, which is around 50 times higher than the $0.005 \text{ A} \cdot \text{m}^{-2}$ achieved for the single electrode [Figure 2.2]. The steady-state current of the generator-collector system provides an analytical signal independent of time (for typical applications this can be achieved within milliseconds) and can be easily measured from the cyclic voltammogram.

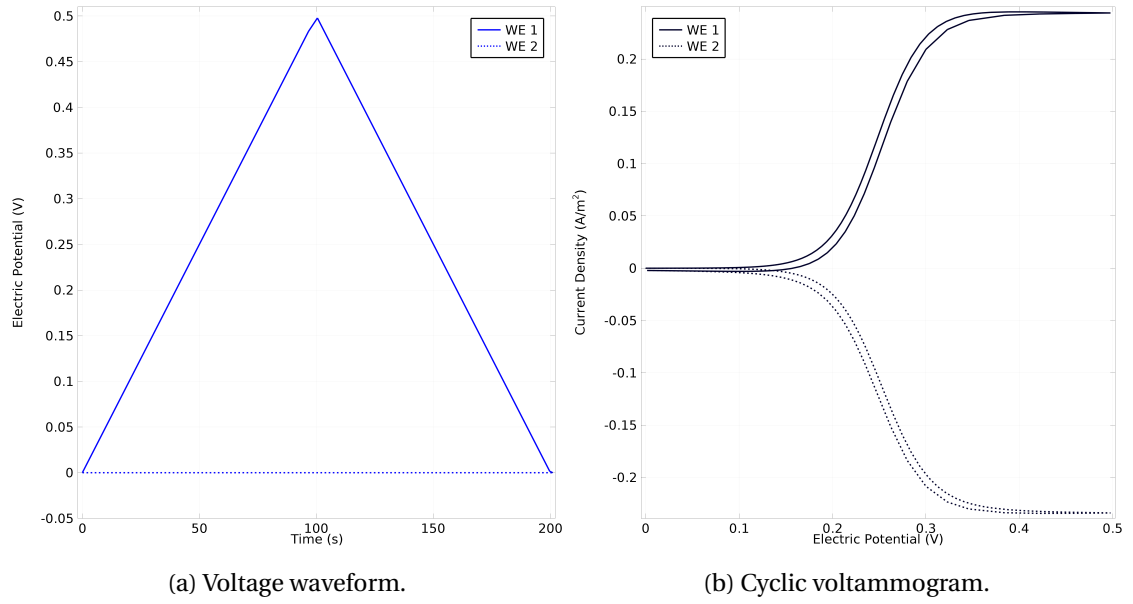


Figure 2.4: Voltage waveform (a) and cyclic voltammogram (b) for a generator–collector system.

Table 2.1: Parameters used for the simulation of a simple redox cycling process in a microgap generator–collector system.

α_c	0.49
α_a	0.51
$c_{\text{red},b}$	$0.05 \text{ mol}\cdot\text{m}^{-3}$
$c_{\text{ox},b}$	$0.0 \text{ mol}\cdot\text{m}^{-3}$
D_{red}	$6.7 \times 10^{-10} \text{ m}^2\cdot\text{s}^{-1}$
D_{ox}	$6.7 \times 10^{-10} \text{ m}^2\cdot\text{s}^{-1}$
E_{eq}	$0.251 \text{ V vs. Ag/AgCl}$
F	$96485 \text{ C}\cdot\text{mol}^{-1}$
k_0	$0.06 \text{ m}\cdot\text{s}^{-1}$
R	$8.31 \text{ J}\cdot\text{K}^{-1}$
T	293.15 K
ν	$5 \text{ mV}\cdot\text{s}^{-1}$
x	$20 \text{ }\mu\text{m}$

Redox cycling metrics

It is useful to have an indicator of the quality of geometrical confinement of the system. The collector efficiency, η_c , of the redox cycling process is expressed as the ratio of the current at the collector electrode, I_c , to the current at the generator electrode, I_g . However, its use can be problematic due to its dependence on the concentration profile of species in the solution and the temporal nature of redox cycling.

$$\eta_c = \left| \frac{I_c}{I_g} \right| \quad (2.18)$$

Another useful metric is the amplification factor (Γ), describing the amplification of the sensor operating in redox cycling mode (I_{rc}), where both electrodes are active, versus operating in standard mode (I_{nrc}), where only a single electrode is active. This parameter is useful as it isolates the response due to molecules involved in the redox reaction from background processes. This can be considered a metric of the selective enhancement.

$$\Gamma = \left| \frac{I_{rc}}{I_{nrc}} \right| \quad (2.19)$$

There are several other advantages that can be realised through the use of generator–collector systems. Further to the signal amplification achieved from the development of a feedback current, other benefits include: discrimination of interferents such as ascorbates [2] or oxygen [3]; improved selectivity due to the two separately applied potentials, allowing the redox system to be effectively switched on or off [4, 5]; a steady-state response; and a collector response less susceptible to electric double layer charging effects.

2.3 The electrode–electrolyte interface

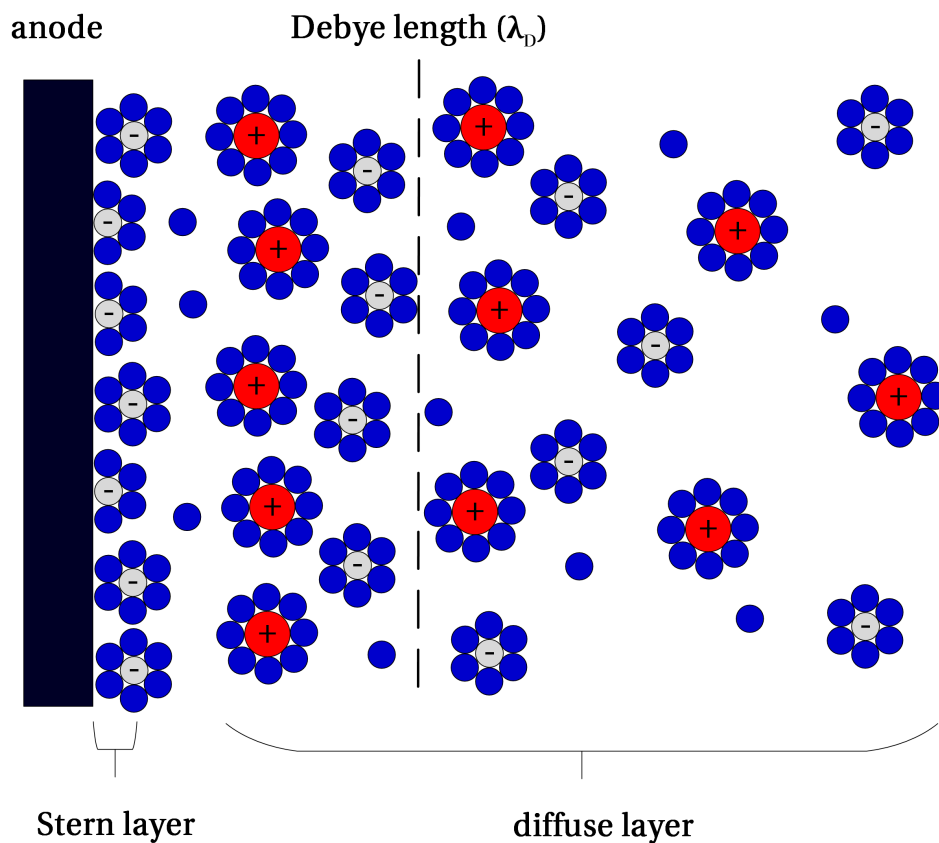


Figure 2.5: Simplified illustration of the electric double layer at the electrode–electrolyte interface.

When a metallic electrode is polarised within an electrolyte, solvated ions form what is termed the electric double layer (EDL). The theoretical model of this electrode–electrolyte interface has evolved over a period spanning more than one century. Hermann von Helmholtz was the first to hypothesise on the nature of this interface in 1879 [6], realising that some ions must reside at the surface in order to balance the electrode's surface charge.

In later years both Louis-Georges Gouy in 1910 [7] and David Chapman in 1913 [8] presented models to account for mobile ions within the electrolyte, forming what is now termed the 'diffuse layer'. They recognised that the charge distribution was dependant on both the electrode potential and ionic strength, and that the diffuse layer could be described by a Boltzmann distribution due to their Brownian motion and electrostatic interactions. It was not until 1924 that the Helmholtz and Gouy–Chapman models would be combined by Otto Stern [9]. Finally in 1947 David Grahame [10] proposed the presence of specifically adsorbed ions at the metal surface due to forces other than electrostatic interaction.

Chapter 2. Theory

In this section the fundamentals of the electric double layer will be explored, specifically looking at the effect of different ionic concentration and overlapping diffusion layers. First, several assumptions must be made to better understand the complex behaviour at the electrode-electrolyte interface. Considering an infinite, uniformly charged planar surface, the potential is related to the charge density by Poisson's equation:

$$\frac{\partial^2 \phi}{\partial x^2} = -\frac{\rho}{\epsilon_0 \epsilon_r} \quad (2.20)$$

Considering the ions as point charges, their distribution at the interface is determined by both the temperature and the energy required (w_i) to bring an ion from an infinite distance to a point at which the potential is ϕ . This distribution is given by Boltzmann's equation:

$$n_i = n_{i,b} \exp\left(\frac{-w_i}{k_B T}\right) \quad (2.21)$$

Where $n_{i,b}$ is the number density of ions of type ' i ' per unit volume in the bulk electrolyte, k_B is Boltzmann's constant and T is the absolute temperature [K].

The volume charge density, ρ [$\text{C}\cdot\text{m}^{-3}$], can then be defined as:

$$\rho = \sum_i n_{i,b} z_i q \exp\left(\frac{-z_i q \phi}{k_B T}\right) \quad (2.22)$$

Combining with the Poisson equation, we arrive at the Poisson–Boltzmann equation:

$$\frac{\partial^2 \phi}{\partial x^2} = -\frac{1}{\epsilon_0 \epsilon_r} \sum_i n_{i,b} z_i q \exp\left(\frac{-z_i q \phi}{k_B T}\right) \quad (2.23)$$

Considering only low potentials, where $|z_i q \phi| \ll k_B T$, the exponential can be expanded retaining only the first and second terms, this is called the Debye–Hückle approximation:

$$\frac{\partial^2 \phi}{\partial x^2} = -\frac{1}{\epsilon_0 \epsilon_r} \sum_i n_{i,b} z_i q - \sum_i \frac{n_{i,b} z_i^2 q^2 \phi}{k_B T} \quad (2.24)$$

Respecting preservation of electroneutrality: $\sum_i n_{i,b} z_i q = 0$, the equation simplifies to:

$$\frac{\partial^2 \phi}{\partial x^2} = \sum_i \frac{n_{i,b} z_i^2 q^2}{\epsilon_0 \epsilon_r k_B T} \phi \quad (2.25)$$

At this point the Debye–Hückel parameter (k) can be observed:

$$\frac{\partial^2 \phi}{\partial x^2} \simeq k^2 \phi \quad (2.26)$$

Given that the number density is related to concentration by $n_i = N_A c_i$, the Debye length can be expressed as:

$$k^{-1} \simeq \sqrt{\frac{\epsilon_0 \epsilon_r k_B T}{\sum_i N_A c_i z_i^2 q^2}} \quad (2.27)$$

The symbol k^{-1} is normally reserved to denote the Debye length for a monovalent electrolyte and a more generalised symbol (λ_D) is used ordinarily. In order to visualise the effect of electrolyte concentration on the Debye length and EDL, the electric potential (ϕ) can be analytically calculated and plotted versus the perpendicular distance from the electrode surface, with varying electrolyte ionic concentrations $I = \frac{1}{2} \sum_i c_i z_i^2$ using the equation:

$$\phi = \phi_0 \exp(-kx) \quad (2.28)$$

With boundary conditions of $\phi = 0$ at $x = \infty$ and $\phi = \phi_0 = 10$ mV at $x = 0$.

The calculated Debye lengths for a monovalent electrolyte are listed in Table 2.2.

The calculated potentials in Figure 2.6 show that for certain ionic strengths of electrolytes a double layer of several hundreds of nanometres is viable. Therefore a pair of electrodes separated by a nanogap will have EDLs that either occupy a significant proportion of the volume or have overlapping electric double layers. The implication of this is that molecules within a nanogap are often subject to more homogeneous conditions than traditional macroscale electrode systems and sensitivity should be improved.

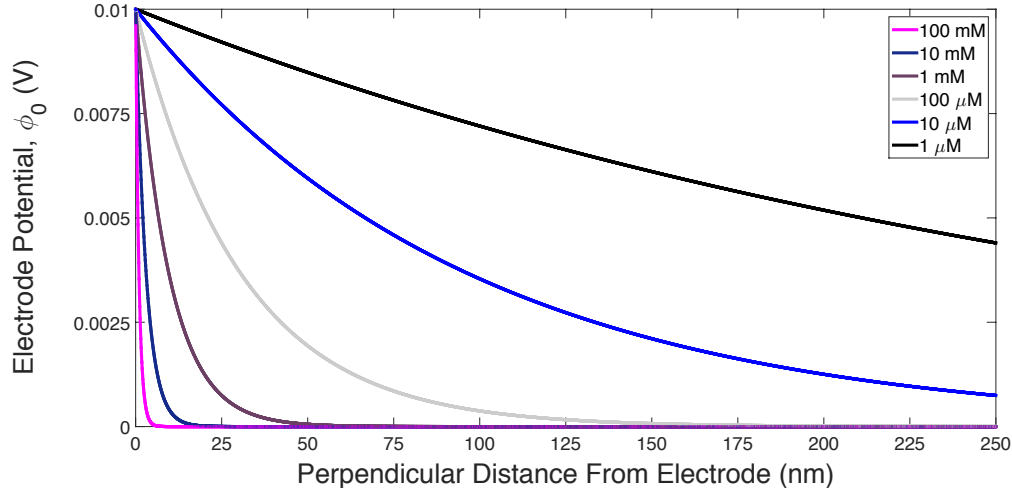


Figure 2.6: Plot showing effect of ionic strength on thickness of electric double layer.

Table 2.2: Calculated Debye lengths for a monovalent electrolyte with a range of ionic concentrations.

Ionic strength	Debye length (nm)
1 M	0.3045
100 mM	0.9630
10 mM	3.0451
1 mM	9.6295
100 μ M	30.451
10 μ M	96.295
1 μ M	304.51

2.3.1 Overlapping electric double layers

In order to further investigate the effect of overlapping double layers, the Poisson–Boltzmann equation must be reconsidered. When $|z_i q \phi| \geq k_B T$, the Debye–Hückel approximation becomes invalid and Equation 2.23 is rewritten as[†]:

$$\frac{\partial^2 \phi}{\partial x^2} = -\frac{1}{\epsilon_0 \epsilon_r} \left[n_b z q \exp\left(\frac{-z q \phi}{k_B T}\right) - n_b z q \exp\left(\frac{z q \phi}{k_B T}\right) \right] \quad (2.29)$$

[†]For a symmetrical electrolyte, *i.e.*, $|z_i| = |z_+| = |z_-| = z$

Rearranging the equation gives:

$$\frac{\partial^2 \phi}{\partial x^2} = \frac{n_b z q}{\epsilon_0 \epsilon_r} \left[\exp\left(\frac{z q \phi}{k_B T}\right) - \exp\left(\frac{-z q \phi}{k_B T}\right) \right] \quad (2.30)$$

Using the hyperbolic sine relation the equation can be simplified to:

$$\frac{\partial^2 \phi}{\partial x^2} = \frac{2 n_b z q}{\epsilon_0 \epsilon_r} \left[\sinh\left(\frac{z q \phi}{k_B T}\right) \right] \quad (2.31)$$

This can be solved to yield:

$$\tanh\left(\frac{z q \phi}{4 k_B T}\right) = \tanh\left(\frac{z q \phi_0}{4 k_B T}\right) \exp(-k x) \quad (2.32)$$

With low electrode potentials $\tanh(x) \simeq x$ the equation simplifies to Equation 2.28 just as per the Debye–Hückel approximation. However, at a large distance from an electrode of high potential, $\tanh(x) \simeq 1$ and the equation simplifies to:

$$\phi = \frac{4 k_B T}{z q} \exp(-k x) \quad (2.33)$$

This shows that at large distances from an electrode of high potential, the experienced potential is independent of the electrode surface potential and instead dictated by the term $\frac{4 k_B T}{z q}$.

Solving Equation 2.32 analytically, a normalised potential distribution can be plotted for various electrode separation distances, described as multiples of their EDL distance [Figure 2.7].

The potential response described by Equation 2.32 for electrode potentials provides a far greater potential decay close to the electrode surface whilst maintaining the exponential decay in the farfield. Nevertheless, the Gouy–Chapman model is an equilibrium, mean-field, point-charge formulation and consequently neglects solvent and ion dynamics. This can lead to infinitely high concentrations for large surface potentials. There are numerous methods to provide a limit to the ion concentration at the electrode surface, such as the inclusion of a Stern layer as described in the following section.

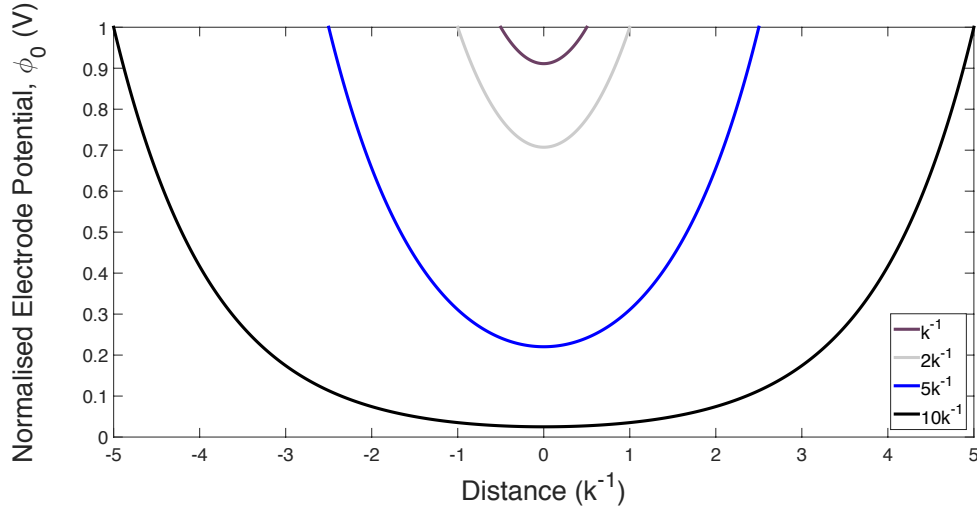


Figure 2.7: Plot showing normalised potential distributions for electrode separations of k^{-1} , $2k^{-1}$, $5k^{-1}$ and $10k^{-1}$. Zero distance represents the centre point of the gap.

2.3.2 Capacitance of the electric double layer

The capacitor is able to store charge when a voltage is applied across it. This relation is given by:

$$C = \frac{dq}{dV} \quad (2.34)$$

The capacitance for a parallel plate capacitor with two electrodes each of area A , separated by a distance of x with dielectric permittivity ϵ can be ordinarily described as:

$$C = \frac{\epsilon_0 \epsilon_r A}{x} \quad (2.35)$$

Considering the EDL storing charge due to an applied electrode potential (ϕ_0) and expressing as capacitance per unit area:

$$C'' = -\frac{q''}{\phi_0} \quad (2.36)$$

Debye–Hückel approximation

Starting with a Debye–Hückel approximation (valid for symmetric electrolytes at low applied electrode potentials), the EDL acts like a parallel capacitor with a separation of λ_D . The potential distribution at the electrode surface can therefore be evaluated as:

$$\left. \frac{\partial \phi}{\partial x} \right|_{\text{surface}} = -\frac{\phi_0}{\lambda_D} \quad (2.37)$$

And assuming that the surface and EDL charges are balanced:

$$\left. \frac{\partial \phi}{\partial x} \right|_{\text{surface}} = -\frac{q''_{\text{surface}}}{\epsilon_0 \epsilon_r} = \frac{q''_{\text{EDL}}}{\epsilon_0 \epsilon_r} \quad (2.38)$$

Rearranging produces two identities:

$$q''_{\text{surface}} = \frac{\epsilon_0 \epsilon_r}{\lambda_D} \phi_0 \quad (2.39)$$

and

$$q''_{\text{EDL}} = -\frac{\epsilon_0 \epsilon_r}{\lambda_D} \phi_0 \quad (2.40)$$

And so the capacitance can be defined as:

$$C'' = -\frac{q''_{\text{EDL}}}{\phi_0} = \frac{\epsilon_0 \epsilon_r}{\lambda_D} \quad (2.41)$$

Poisson–Boltzmann approximation

The Poisson–Boltzmann model improves on the Debye–Hückel model by correctly predicting the capacitance for small applied potentials. The hyperbolic sine solution to the Poisson–Boltzmann equation predicts the charge in the electric double layer with symmetric electrolyte

as:

$$q_{\text{EDL}}'' = -\frac{\epsilon_0 \epsilon_r \phi_0}{\lambda_D} \left[\frac{2k_B T}{z\phi_0} \sinh\left(\frac{z\phi_0}{2k_B T}\right) \right] \quad (2.42)$$

Rearranging and using the identity $C'' = -q'' \phi_0^{-1}$, we arrive at a Poisson–Boltzmann expression for the capacitance per unit area:

$$C_{\text{EDL}}'' = \frac{\epsilon_0 \epsilon_r}{\lambda_D} \left[\cosh\left(\frac{z\phi_0}{2k_B T}\right) \right] \quad (2.43)$$

Stern modified Poisson–Boltzmann approximation

As previously discussed, a downfall of the Poisson–Boltzmann model is its point-charge approximation. This can be improved by introducing the Stern modification to stipulate a region of condensed ions with permittivity ϵ_S and thickness λ_S . Thus the capacitance of the EDL can now be given by the series combination:

$$\frac{1}{C_{\text{EDL}}''} = \frac{1}{\frac{\epsilon_0 \epsilon_r}{\lambda_D} \left[\cosh\left(\frac{z\phi_0}{2k_B T}\right) \right]} + \frac{1}{\frac{\epsilon_S}{\lambda_S}} \quad (2.44)$$

The Stern modification provides a limiting case for $\phi_0 \rightarrow \infty$ of $C_{\text{EDL}}'' \rightarrow \epsilon_S \lambda_S^{-1}$. Typical values for modelling the Stern layer are $\epsilon_S = 6\text{--}30$ and $\lambda_S = 1\text{--}10 \text{ \AA}$.

2.4 Self-assembled monolayers for capacitive sensing

Many biosensors require the use of a biorecognition layer to detect affinity reactions such as the formation of an antibody–antigen complex. Affinity-based sensors are an attractive proposition as they are able to determine the analyte with no or very little sample preparation. A problem associated with label-free affinity biosensors is non-specific binding, as there is often no discrimination between the measured signal from specific and non-specific interactions. If such a distinction is to be realised the transducer has to be sensitive to conformational changes of the binding site or changes in charge distribution around this site after binding. It is therefore imperative to consider the design and immobilisation of the biorecognition layer when implementing a capacitive biosensor.

The total capacitance of the system can be considered as the combination of capacitances in

2.4. Self-assembled monolayers for capacitive sensing

series as demonstrated by Equation 2.45. It is important to note that this makes the assumption that each layer covers the total electrode area. Here C_{tot} is the total equivalent capacitance, C_{ins} represents the insulating layer used to minimise unwanted charge transfer, C_{rec} represents the probe layer and any bound molecules and finally C_{EDL} represents the capacitance of the electric double layer. It is evident that the lowest capacitance will dominate the total capacitance, therefore the capacitance of the insulating layer should be made as high as possible in order to enhance detection of binding events.

$$\frac{1}{C_{\text{tot}}} = \frac{1}{C_{\text{ins}}} + \frac{1}{C_{\text{rec}}} + \frac{1}{C_{\text{EDL}}} \quad (2.45)$$

Gold is widely chosen as an electrode material in biosensing applications, in part due to its biocompatibility, stability and ability to incorporate into microfabrication processes. It is well reported that alkanethiols spontaneously produce robust and well-organised structures on gold [11–13] and this gold–alkanethiol system has since been adopted for a range of biosensing applications [14, 15]. Often a self-assembled monolayer (SAM) is created by immobilising a mix of thiol-modified probes (*e.g.*, oligonucleotides) and shorter thiol spacers. This provides a mechanism to control the surface density of the probe and maximise the efficacy of the affinity reaction by reducing lateral steric hindrance. The spacer helps to displace any non-specific interactions between the probe and the gold surface during SAM assembly, improving the number of available reaction sites.

In the case of the capacitive biosensor, if the initial SAM does not provide sufficient insulation, electron transfer may occur either through permeation of the layer, charge transfer at defect sites or electron tunnelling through the monolayer, all leading to reduced sensitivity. The transfer resistance is described to be exponentially proportional to the SAM thickness [11, 16]. For alkanethiols with more than 8 CH₂ groups (> 1 nm) tunnelling is greatly reduced and the insulation is significantly improved [16, 17]. The insulating properties of alkanethiols with 8–15 CH₂ groups has been studied in detail by Boubour *et al.* using impedance spectroscopy [18]. Results showed little variation in the impedance of the different lengths with a typical value of $1 \times 10^5 \Omega \cdot \text{cm}^2$. Binding of alkanethiols is maximised on Au (111) surface, prominent in evaporated Au films and preferentially formed during low-temperature (100 °C annealing) [19], providing a maximum density of $\approx 4.5 \times 10^{14}$ molecules per square centimetre, requiring a minimum concentration of $\approx 1 \mu\text{M}$ to form a dense SAM [20].

Moving focus to the recognition layer, it may not always be possible to co-immobilise a thiol-terminated probe with an insulating thiol spacer. In these cases it can be useful to utilise carboxyl (–COOH) groups to allow covalent bonding (after activation) to amine (–NH₂) groups present on the surfaces of proteins. Importantly, activation with the use of either *N*-Cyclohexyl-*N'*-(2-morpholinoethyl)carbodiimide metho-*p*-toluenesulfonate (CMC) or *N*-(3-Dimethylaminopropyl)-*N'*-ethylcarbodiimide hydrochloride (EDC) has been shown not to

interfere with the insulating properties of the initial SAM [21].

In order to improve efficacy of binding events spacers can be used to provide extra distance between the hybridisation portion of the probe and the anchor site. The use of ethylene-glycol (EG) groups to form polyethylene-glycol (PEG) linkers are of particular interest as they have been shown to provide excellent results for capacitive sensing applications [22]. Conventional hydrocarbon linkers form highly hydrophobic surfaces [23], whereas a PEG linker provides a highly hydrophilic surface [24]. The hydrophilic nature of the PEG linker results in a decrease of non-specific interactions at the probe. It has been suggested that the reduced interference from the linker is a result of the compact arrangement of water molecules around the EG sites [25].

References

- [1] R. S. Nicholson and I. Shain. Theory of Stationary Electrode Polarography. Single Scan and Cyclic Methods Applied to Reversible, Irreversible, and Kinetic Systems. *Analytical Chemistry*, 36(4):706–723, 1964.
- [2] B. Wolfrum, M. Zevenbergen, and S. Lemay. Nanofluidic redox cycling amplification for the selective detection of catechol. *Analytical Chemistry*, 80(4):972–977, 2008.
- [3] M. A. Hasnat, A. J. Gross, S. E. C. Dale, E. O. Barnes, R. G. Compton, and F. Marken. A dual-plate ITO-ITO generator-collector microtrench sensor: surface activation, spatial separation and suppression of irreversible oxygen and ascorbate interference. *The Analyst*, 139(3):569–75, 2013.
- [4] A. J. Gross, S. Holmes, S. E. C. Dale, M. J. Smallwood, S. J. Green, C. Peter W., N. Benjamin, P. G. Winyard, and F. Marken. Nitrite/nitrate detection in serum based on dual-plate generator-collector currents in a microtrench. *Talanta*, 131:228–235, 2015.
- [5] H. R. Zafarani, K. Mathwig, S. G. Lemay, E. J. R. Sudhölter, and L. Rassaei. Modulating Selectivity in Nanogap Sensors. *ACS Sensors*, 1(12):1439–1444, 2016.
- [6] H. Helmholtz. Studien über electrische Grenzsichten. *Annalen der Physik*, 243(7):337–382, 1879.
- [7] L.-G. Gouy. Sur la constitution de la charge électrique à la surface d’un électrolyte. *Journal de Physique Théorique et Appliquée*, 9(1):457–468, 1910.
- [8] D. L. Chapman. A contribution to the theory of electrocapillarity. *Philosophical Magazine Series 6*, 25(148):475–481, 1913.
- [9] O. Stern. Zur Theorie der Elektrolytischen Doppelschicht. *Zeitschrift für Elektrochemie*, 30:508–516, 1924.
- [10] D. C. Grahame. The Electrical Double Layer and the Theory of Electrocapillarity. *Chemical Reviews*, 41(3):441–501, 1947.
- [11] M. D. Porter, T. B. Bright, D. L. Allara, and C. E. D. Chidsey. Spontaneously Organized Molecular Assemblies. 4. Structural Characterization of n-Alkyl Thiol Monolayers on

References

- Gold by Optical Ellipsometry, Infrared Spectroscopy, and Electrochemistry. *Journal of American Chemical Society*, 109(6):3559–3568, 1987.
- [12] C. D. Bain, E. B. Troughton, Y. T. Tao, J. Evall, G. M. Whitesides, and R. G. Nuzzo. Formation of monolayer films by the spontaneous assembly of organic thiols from solution onto gold. *Journal of the American Chemical Society*, 111(1):321–335, 1989.
- [13] C. D. Bain, J. Evall, and G. M. Whitesides. Formation of monolayers by the coadsorption of thiols on gold: variation in the head group, tail group, and solvent. *Journal of the American Chemical Society*, 111(18):7155–7164, 1989.
- [14] Th. Wink, S. J. van Zuilen, A. Bult, and W. P. van Bennekom. Self-assembled Monolayers for Biosensors. *The Analyst*, 122(4):43R–50R, 1997.
- [15] N. K. Chaki and K. Vijayamohanan. Self-assembled monolayers as a tunable platform for biosensor applications. *Biosensors and Bioelectronics*, 17(1-2):1–12, 2002.
- [16] C. Miller, P. Cuendet, and M. Graetzel. Adsorbed ω -hydroxy thiol monolayers on gold electrodes: evidence for electron tunneling to redox species in solution. *The Journal of Physical Chemistry*, 95(2):877–886, 1991.
- [17] F. Schreiber. Structure and growth of self-assembling monolayers. *Progress in Surface Science*, 65(5-8):151–256, 2000.
- [18] E. Boubour and R. B. Lennox. Insulating Properties of Self-Assembled Monolayers Monitored by Impedance Spectroscopy. *Langmuir*, 16(9):4222–4228, 2000.
- [19] J. R. White. Annealing behaviour of thin evaporated gold films. *Thin Solid Films*, 22(1):23–35, 1974.
- [20] J. C. Love, L. A. Estroff, J. K. Kriebel, R. G. Nuzzo, and G. M. Whitesides. Self-Assembled Monolayers of Thiolates on Metals as a Form of Nanotechnology. *Chemical Reviews*, 105(4):1103–1170, 2005.
- [21] V. M. Mirsky, M. Riepl, and O. S. Wolfbeis. Capacitive monitoring of protein immobilization and antigen–antibody reactions on monomolecular alkylthiol films on gold electrodes. *Biosensors and Bioelectronics*, 12(9-10):977–989, 1997.
- [22] S. Carrara, V. Bhalla, C. Stagni, L. Benini, A. Ferretti, F. Valle, A. Gallotta, B. Riccò, and B. Samorì. Label-free cancer markers detection by capacitance biochip. *Sensors and Actuators B: Chemical*, 136(1):163–172, 2009.
- [23] R. Smith and C. Tanford. Hydrophobicity of Long Chain n-Alkyl Carboxylic Acids, as Measured by Their Distribution Between Heptane and Aqueous Solutions. *Proceedings of the National Academy of Sciences*, 70(2):289–293, 1973.
- [24] M. J. Kao, D. C. Tien, C. S. Jwo, and T. T. Tsung. The study of hydrophilic characteristics of ethylene glycol. *Journal of Physics: Conference Series*, 13:442–445, 2005.

- [25] E. Ostuni, L. Yan, and G. M. Whitesides. The interaction of proteins and cells with self-assembled monolayers of alkanethiolates on gold and silver. *Colloids and Surfaces B: Biointerfaces*, 15(1):3–30, 1999.

3 Pilot Tests with a Dual-Plate Microgap Sensor

This chapter investigates the use of a microgap sensor for both direct electrochemical detection of the cysteine–cystine redox couple as well as the detection of *E. coli* using dielectric spectroscopy. The work demonstrates the advantages provided by the micrometre interelectrode spacing in both sensing modes with practical applications.

The microgap sensor is based on the use of an epoxy to provide a strong bond between two opposing metallic electrodes as well as acting as a sacrificial layer. The interelectrode spacing is controlled through the viscosity of the epoxy and the applied force whilst bonding. A cavity between the electrodes is formed using a chemical wet etch process which simultaneously cleans the electrode surface. Interelectrode distances from 50 μm down to 2.0 μm were achieved with cavity depths of between 50 μm and 100 μm . The typical electroactive surface area for this type of device was around $2.5 \times 10^{-7} \text{ m}^2$.

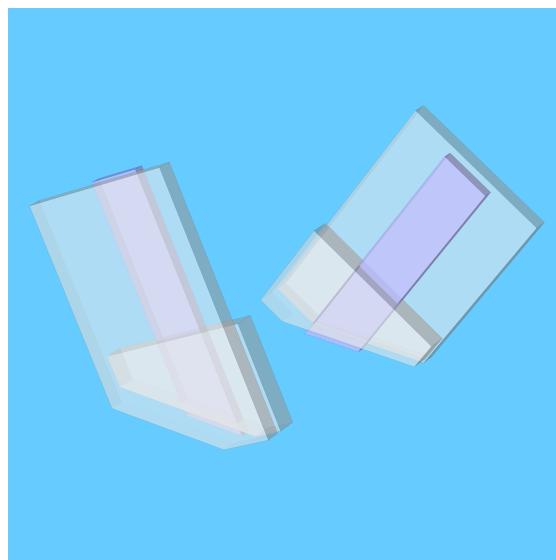


Figure 3.1: 3D exploded diagram of the microgap sensor showing glass substrates, metallic electrodes (highlighted) and epoxy layers.

3.1 Microgap sensor

3.1.1 Microgap sensor fabrication

The device is depicted at key points in the fabrication process with brief descriptions in Figure 3.2. First borosilicate glass slides coated with a <5 nm Ti adhesion layer and 100 nm Au layer [Sigma Aldrich] were cut into 10 mm × 25 mm strips using a diamond saw [Buehler Isomet 1000] in cutting fluid [Buehler Cool 3]. These were cleaned in acetone then isopropyl alcohol (IPA) with 5 minutes ultrasonic agitation before rinsing in IPA and drying with N₂. The electrodes were defined by passivating 5 mm central strips with Kapton[®] tape and etching the unpassivated gold with *aqua regia* solution (HNO₃:HCl, 1:3, vol.) for 3 minutes before immediately neutralising in deionised (DI) water. The electrodes were then placed in a tube furnace at 500 °C for 1 hour to oxidise any remaining Ti.

Next epoxy [Gurit SP 106] was prepared (resin:hardener, 1:10, vol.), mixed for 5 minutes and left to partially cure for a further 50 minutes. The lower sections of each electrode were then coated with epoxy and two opposing electrodes overlapped to form a 'V', placed between Teflon[®] sheets and compressed with a mechanical press applying around 10 kN·m⁻² of pressure (16-24 h). The electrodes were then cut across the centre of overlap to create a flat base. Next the base was polished with increasing grades of SiC polishing paper (240 grit to 800 grit) [Buehler] then diamond lapping films (15 µm to 1 µm) [Buehler] followed with 0.3 µm alumina slurry [Buehler]. In order to create the electrochemical junction, a cavity was etched in the epoxy at the lower region of the electrodes in Piranha solution (H₂SO₄:H₂O₂, 3:1, vol.) for 5 minutes with 50% ultrasonic agitation. The Piranha solution simultaneously etches away the epoxy and cleans the gold surface. The reaction was neutralised by placing the electrodes in DI water then rinsing with DI water for 1 minute. The electrodes were left partially submerged in IPA for at least 15 minutes to help remove any remaining residues. Finally conductive adhesive copper tape was applied to the top of each electrode for simplified electrical connection to the bipotentiostat.

Some control over the interelectrode spacing was achieved by controlling the epoxy density, pre-cure time and the applied pressure during bonding. For a gap of approximately 6 µm, the epoxy density of the 10:1 mix was 1.15 kg·m⁻³ (resin = 1164 kg·m⁻³, hardener = 1008 kg·m⁻³), the total pre-cure time was 55 minutes and the applied pressure was ≈10 kN·m⁻². The interelectrode spacing was most sensitive to the epoxy density and least sensitive to the applied pressure. Achieving smaller interelectrode distances was challenging with many fabricated devices demonstrating electrical short-circuits. Some of these devices could be recovered by cutting above the initial cut-line and etching a new cavity, however interelectrode distances below about 20 µm provided poor yields (≈20%). A typical yield for larger gaps was around 50%.

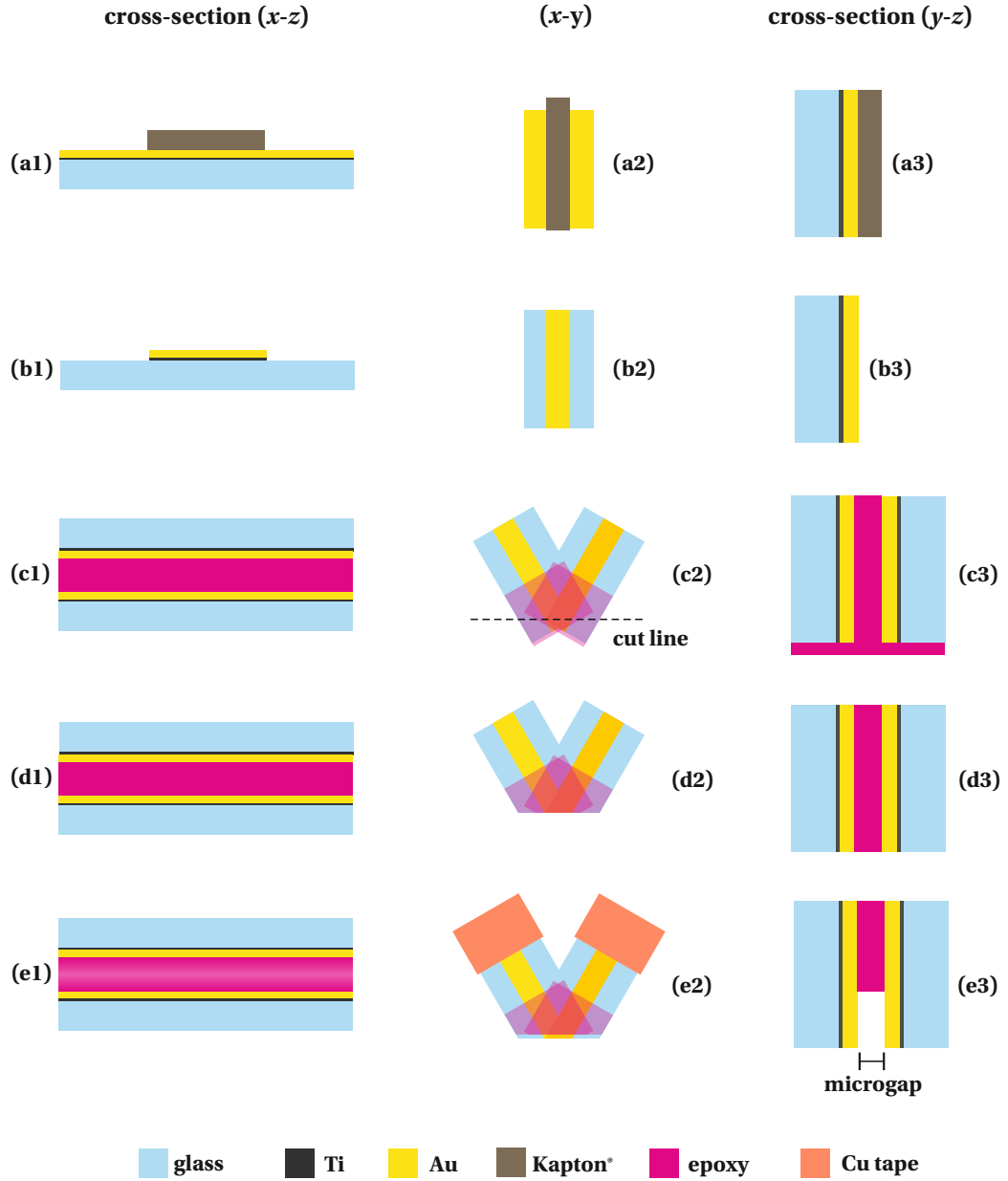


Figure 3.2: Fabrication process of the microgap sensor. (a): A 5 mm central region of gold is passivated using Kapton[®] tape. (b): The exposed gold is etched in *aqua regia* solution before oxidising the remaining titanium in a furnace. (c): Epoxy is applied to both electrodes and the two halves brought into contact and bonded under pressure using a mechanical press. (d): The bonded device is cut with a diamond saw along the cut line shown in (c2), this maximises the width of overlapping electrodes. The surface is then mechanically polished using various grits of silicon carbide paper and alumina slurry. (e): Piranha solution is used to etch the epoxy forming the microgap cavity. Finally conductive adhesive copper tape is attached to the top of the sensor to provide simplified electrical connections.

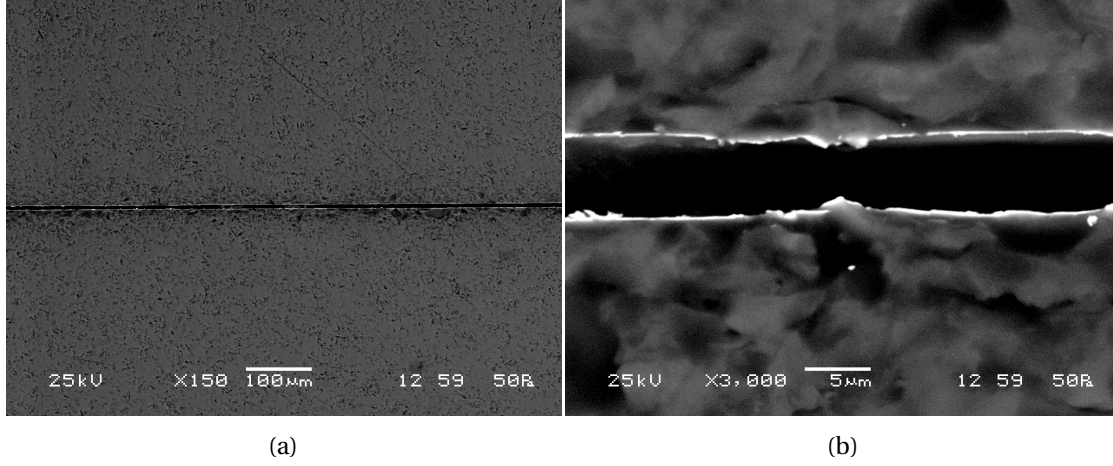


Figure 3.3: SEM images showing interelectrode spacing of the microgap sensor for (a) an $\approx 800 \mu\text{m}$ and (b) a $\approx 40 \mu\text{m}$ section.

3.1.2 Microgap sensor characterisation

The interelectrode spacing for the device used to complete the redox cycling studies was determined as $5.71 \mu\text{m} \pm 0.38 \mu\text{m}$ using a scanning electron microscope (SEM) [JEOL SEM6480LV] and measuring acquired images at several points with ImageJ, an image processing toolkit. Figures 3.3a and 3.3b show the microgap at different levels of magnification.

The sensor's electroactive area was determined by performing cyclic voltammetry with a redox marker (1 mM ferri-/ferrocyanide $[\text{Fe}(\text{CN})_6]^{3-/4-}$ in 0.1 M KCl as a supporting electrolyte) and monitoring the diffusion controlled limiting current. Using Equation 3.1 [1] with the recorded collector limiting current $I_{\text{lim}} = -3.46 \mu\text{A}$, $n = 1$, diffusion coefficients of D_{red} for $\text{K}_4\text{Fe}(\text{CN})_6 = 6.67 \times 10^{-10} \text{ m}^2 \cdot \text{s}^{-1}$, and D_{ox} for $\text{K}_3\text{Fe}(\text{CN})_6 = 7.26 \times 10^{-10} \text{ m}^2 \cdot \text{s}^{-1}$ [1], A is the electrode area, c_0 is the concentration of ferrocyanide (1 mM), and δ is the Nernst diffusion layer thickness, which is substituted by the interelectrode distance (x).

$$I_{\text{lim},D} = \frac{2nFAc_0}{\delta} \frac{D_{\text{red}} \times D_{\text{ox}}}{D_{\text{red}} + D_{\text{ox}}} \quad (3.1)$$

The electrode area is calculated to be $\approx 2.95 \times 10^{-7} \text{ m}^2$ and with a $\approx 5 \text{ mm}$ width, the trench depth is estimated to be $\approx 60 \mu\text{m}$. With a $\approx 6 \mu\text{m}$ interelectrode gap, the aspect ratio is approximately 10. The volume of solution within the sensor can then be calculated by multiplying the electrode area with the interelectrode spacing, yielding a value of $\approx 1.7 \times 10^{-12} \text{ m}^3$ ($\approx 1.7 \text{ nL}$).

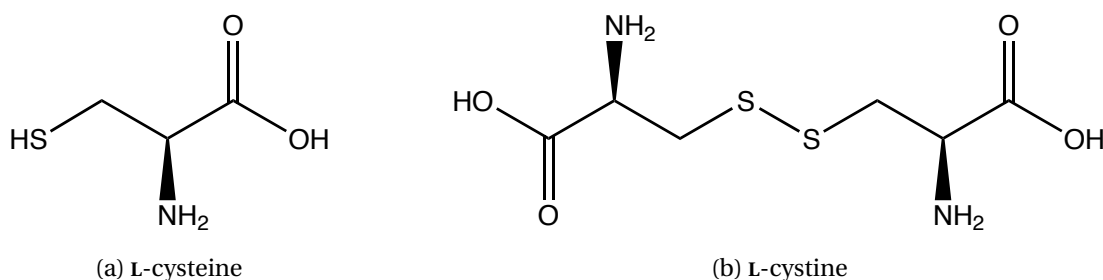


Figure 3.4: Molecular diagrams of (a) L-cysteine and (b) L-cystine

3.2 Electrochemical redox cycling with a microgap sensor

3.2.1 The cysteine–cystine redox couple

To test the feasibility of the device as a biosensor, the cysteine–cystine couple was investigated as an analyte [Figure 3.4]. Cysteine is an α -amino acid found in many natural proteins and physiological media. Cystine, the oxidised dimer of cysteine, provides a modality for cross-linking via the disulphide bonds, fundamental in defining the primary, secondary and tertiary structure of proteins. The sulfhydryl group ($-\text{SH}$) of cysteine is partially deprotonated at physiological pH, decreasing its pK_a and ultimately enhancing its reactivity [2]. This leads to increased formation of reversible oxidative post-translational modifications (oxPTMs). These oxPTMs are induced by reactive nitrogen species/reactive oxygen species (RNS/ROS) [3]. Levels of RNS and ROS are related to nitrosative and oxidative stress, both leading to cellular damage. These oxPTMs act like a binary switch providing a signalling mechanism for the regulation of protein function, interaction and localisation [4, 5].

Formation of disulphide bonds can occur spontaneously *in vitro* by the oxidation of two cysteine residues coupled with the reduction of an appropriate acceptor such as oxygen. In the case of oxygen as an acceptor, a transition metal or flavin moiety is required to overcome the kinetically sluggish, yet thermodynamically viable reaction. Whereas *in vivo* thiol–disulfide redox cycling is catalysed by thiol oxidases and disulfide reductases in the lumen of endoplasmic reticulum in eukaryotic cells and the periplasmic space of prokaryotic cells [6].

Typical concentrations of cysteine in blood plasma approximately range between $200\ \mu\text{M}$ and $400\ \mu\text{M}$ [7–9]. In urine it is the oxidised species, cystine, which is most commonly present with concentrations varying from around $50\ \mu\text{M}$ to $200\ \mu\text{M}$ [10–12]. Both cysteine and cystine can be useful as medical indicators in human diseases such as rheumatoid arthritis and Alzheimer's disease whereby the cysteine–cystine metabolism regulates the glutathione and thioredoxin pathways [13]. Elevated levels of cystine is an indicator of cystinuria which leads to significant morbidity in affected patients due to the recurrent formation of kidney stones [14].

The electrochemical detection of the cysteine–cystine redox couple offers advantages of be-

ing more affordable, easier to miniaturise as well as providing fast and sensitive detection when compared to colourimetric/spectrometric [15] or liquid chromatography/mass spectroscopy [16] techniques. However, in particular for thiols and disulfides, very few analytical procedures have been developed due to the complexity of these redox systems. For example: direct oxidation of cysteine at bare solid electrodes provides a poor voltammetric response and is only marginally improved with nanostructured electrocatalysts [17]. Reduction of cystine requires strong negative potentials, encouraging the use of metallic electrodes of high hydrogen overpotentials such as Sn, Pb, Zn, or Hg, often with very acidic conditions. Both the oxidative and reductive processes are kinetically slow [18] and both molecules demonstrate complex adsorption processes [19].

The majority of previous work has focussed on the oxidation of cysteine and has been demonstrated with a variety of electrode types [Table 3.1], many utilising complex electrocatalysts to provide sensitivity. There has been comparatively little work on the reduction of the dimer, cystine. Hanging mercury drop electrodes [20,21] and lead electrodes [22] have been used using acidic conditions to shift the reduction potential (E_{pc}) to less negative values. Whereas Zagal *et al.* adsorbed vitamin B12 on an ordinary pyrolytic graphite (OPG) electrode to achieve linear detection from 1 mM to 10 mM [23]. Almost a decade later Mimica *et al.* refined this work by immobilising 5'-deoxyadenosyl cobalamin (coenzyme B₁₂) on the OPG electrode, improving the linear range of detection down to 500 μ M to 2 mM [24]. More recently Shaidarova *et al.* modified a carbon-paste electrode with a cobalt(II) phthalocyanine (CoPC) catalyst to achieve a linear range of 50 μ M to 1 mM [25].

Whilst there has been several successful demonstrations of cysteine and cystine detection, the majority of these have used exotic electrodes or immobilised catalysts, as shown by Table 3.1. The motivation for using a dual-plate gold–gold microgap sensor is to try and demonstrate how a simple platform can be used for direct electrochemical detection of the cysteine–cystine redox couple down to physiologically relevant levels.

Electrochemical reaction mechanism

Cysteine oxidation has been shown to proceed (depending on electrode and applied potential) in a two-step multi electron pathway via cystine to produce cysteic acid as a final product [41–44]. First the thiol moiety forms a free radical, providing a mechanism for the amino acid to adsorb to the gold surface [Reaction R3.1], then the oxidation of adsorbed cysteine on gold is believed to occur as per Reaction R3.2. This process will occur concomitantly with gold surface oxidation in aqueous buffer at pH 7.0 [45], adding a further level of complexity to analytical detection.

3.2. Electrochemical redox cycling with a microgap sensor

Table 3.1: Selection of electrodes used for the electrochemical detection of cysteine and cystine (lower portion) with their metrics.

Electrode	Technique	Linear Range	LoD	Remarks	Reference
Manganese dioxide carbon (MnO ₂)-C nanostructure codeposited with a chitosan hydrogel on GCE	CA	0.5-680 μ M	22 nM	0.2 M BSB, pH 7.8	Xiao <i>et al.</i> [26]
Brilliant-blue-modified poly(diallyldimethylammonium chloride) nafion-coated GCE	RD CA	10-100 μ M	0.5 μ M	0.1 M NaCl, pH 1.5, 600 rpm, purged	Chen <i>et al.</i> [27]
Oxovanadium(IV)-N,N'-bis(salicylidene)ethylenediamine modified GCE	LSV	0.1-1 mM	—	0.1 M KCl, purged	Sonkar <i>et al.</i> [28]
Fluorosurfactant (Zonyl-FSO)-modified gold electrode	CV	\approx 10-200 μ M	0.5 μ M	0.15 M PBS, pH 7.0, stirred	Chen <i>et al.</i> [29]
Platinum-modified chemical vapour deposited carbon nanotubes on graphite electrode	CA	0.5-100 μ M	0.3 μ M	67 mM PBS, pH 7.4, stirred	Fei <i>et al.</i> [30]
Carbon paste electrode modified with N,N'-ethylenebis(salicylideneiminato) oxovanadium(IV) complex	CA	0.24-2.3 mM	170 μ M	0.1 M KCl, pH 5.0, stirred	Teixeira <i>et al.</i> [31]
Cobalt tetra-2-mercaptopyrimidylphthalocyanine (CoTMPyr-Pc)-modified GCE	CV	1.5-25 μ M	1.5 μ M	0.1 M PBS, pH 4.0, purged	Obirai <i>et al.</i> [32]
Sol-gel constructed ceramic electrode modified with Ru[(tpy)(bpy)Cl]PF ₆ complex	RD FI CA	5-685 μ M	2 μ M	0.1 M PB, pH 2.0, 3000 rpm, purged	Salimi <i>et al.</i> [33]
Silicon electrode coated with microwave plasma-assisted chemical vapour deposited boron-doped polycrystalline diamond	LSV	1-200 μ M	0.9 μ M	0.5 M KHCO ₃ , pH 9.0, purged	Spătaru <i>et al.</i> [34]
Mercury-modified silver electrode with [His-Cu] ²⁺ complex	P	10 μ M-20 mM	10 μ M	55 mM PBS, pH 7.4, stirred	Drożdż <i>et al.</i> [35]
Lead phthalocyanine incorporated-poly(vinylchloride) membrane-coatedpyrolytic graphite electrode	P	1 μ M-50 mM	1 μ M	0.01 M PBS, pH 8.5	Shahrokian <i>et al.</i> [36]
Copper-zinc superoxide dismutase (SOD1) co-immobilised with horseradish peroxidase on polypyrrole-platinum electrode	CV	50-500 μ M	10 μ M	0.1 M PBS, pH 7.0	Dharmapandian <i>et al.</i> [37]
Ordered mesoporous carbon-modified GCE	CA	18 μ M-2.5 mM	2.0 nM	0.1 M PBS, pH 2.0, stirred, purged	Zhou <i>et al.</i> [38]
Ordinary pyrolytic graphite disk electrode with immobilised 5'-deoxyadenosyl cobalamin (coenzyme B ₁₂)	CV	1-4 mM	—	Tris-HCl, pH 7.4, purged	Mimica <i>et al.</i> [24]
GCE modified with (ferrocenyl-methyl)trimethylammonium	CA	50 μ M - 6 mM	—	0.1 M Na ₂ SO ₄ , purged	Gao <i>et al.</i> [39]
Copper-doped polymeric chitosan film on GCE	CV	2-55 μ M	1.4 μ M	PB, pH 7.0, purged	Martínez-Huitle <i>et al.</i> [40].
Cobalt(II) phthalocyanine (CoPC) modified carbon paste electrode	CV	0.1-10 mM	100 μ M	0.1 M NaOH, pH 7.0, purged	Shaidarova <i>et al.</i> [25]
Hanging mercury drop electrode	CV	116 μ M-1 mM	—	50 mM PB, pH 7, purged	Monterroso-Marco & López-Ruiz [20]
Hanging mercury drop electrode	CV	100-500 μ M	—	0.1 M HCl, pH 1-2, purged	Ralph <i>et al.</i> [21]
Lead disk electrode	RD CV	0.5-10 mM	—	0.1 M HCl, pH 1-2, 1800 rpm	Ralph <i>et al.</i> [22]

Key: BSB = borate saline buffer, CA = chronoamperometry, CV = cyclic voltammetry, LC = liquid chromatography, LSV = linear sweep voltammetry, FI = flow injection, GCE = glassy carbon electrode, P = potentiometry, RD = rotating disc, V = voltammetry

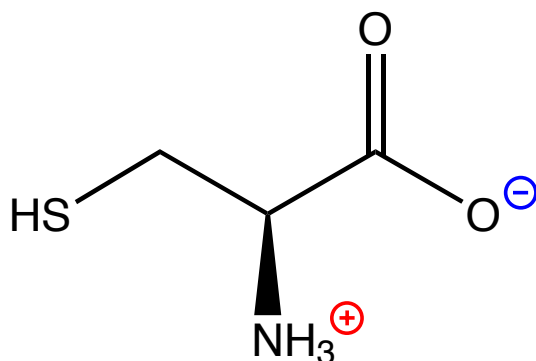
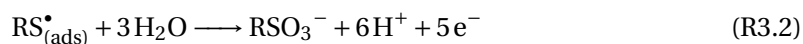
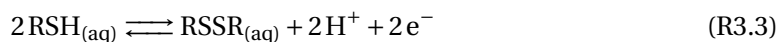


Figure 3.5: Molecular diagram showing zwitterionic form of L-cysteine.



At neutral pH, cysteine is present in its zwitterionic form (hydroxyl group deprotonated and amine group protonated, as shown in Figure 3.5) and with controlled potential the one electron oxidation to cystine can be expected to occur as per Reaction R3.3. In the reverse reaction cystine is reduced via the two electron pathway to form 2 cysteine molecules.



The one electron product, cystine, is also strongly chemisorbed, requiring strong negative applied potentials for reductive desorption back to cysteine [19]. The adsorption modes for cysteine and cystine at gold surfaces differ. Current literature suggests that the mechanism for cystine adsorption is through vertical buckling of a rotated and relaxed S–S bond, generating two inequivalent thiol groups, with spin quantum numbers (m_s) of $+\frac{1}{2}$ and $-\frac{1}{2}$, which bind at distances of 3.54 Å and 2.86 Å from the gold surface, respectively [46].

Moving attention to the cathodic reaction, the reduction of cystine at gold is reported to occur

via a complex kinetic system. Hager *et al.* performed extensive cyclic voltammetric studies in neutral media with monolayers of predominantly cysteine or cystine formed by careful potentiometric pretreatment [19]. The study showed a complex convoluted shoulder on the reductive sweep. This was attributed to first a reduction of adsorbed cystine/cysteine between about -0.65 V and -0.55 V *vs.* SCE followed by a second reduction peak occurring at more negative potentials, around -0.95 V *vs.* SCE for the reduction of cystine.

3.2.2 Experimental information

Reagents

L-cysteine (97%), L-cystine (99%), sodium hydroxide (98-100.5%), sodium phosphate monobasic (98-102%), and potassium chloride (99-100.5%) [Sigma-Aldrich] were used without further purification. Purified water (18.2 M Ω ·cm) sourced from a PURELAB Classic purifier [ELGA] was used to make all aqueous solutions. Cysteine was stored below 5 °C and both cysteine and cystine solutions were prepared immediately before use with 1 minute ultrasonic agitation to assist solubilisation. All experiments used 0.1 M phosphate-buffered saline (PBS) (pH 7.0) as a supporting electrolyte. The pH was measured using a 3505 pH meter [Jenway] which was calibrated with pH 4.0, pH 7.0 and pH 11.0 standards prior to use.

Apparatus

Electrochemical measurements were performed using an Autolab PGSTAT12 [Metrohm] bipotentiostat equipped with a differential electrometer amplifier. All experiments used a saturated KCl calomel reference electrode (SCE) [Radiometer Analytical] and Pt wire counter electrode [CH Instruments]. Macro electrode experiments used a three-electrode configuration utilising a conventional 1 mm diameter gold macrodisc electrode. Experiments performed with the microgap sensor used a four-electrode arrangement, utilising the two working electrodes of the gold–gold dual-plate microgap sensor.

A polytetrafluoroethylene (PTFE) jig was used to hold the electrodes in reproducible positions within a 50 mL glass beaker. Argon purging and blanketing was performed only for macrodisc experiments, for at least 5 minutes in ≈ 20 mL of solution. GPES software [Metrohm] was used to perform cyclic voltammetry and linear baseline correction was used to improve presentation of data where appropriate.

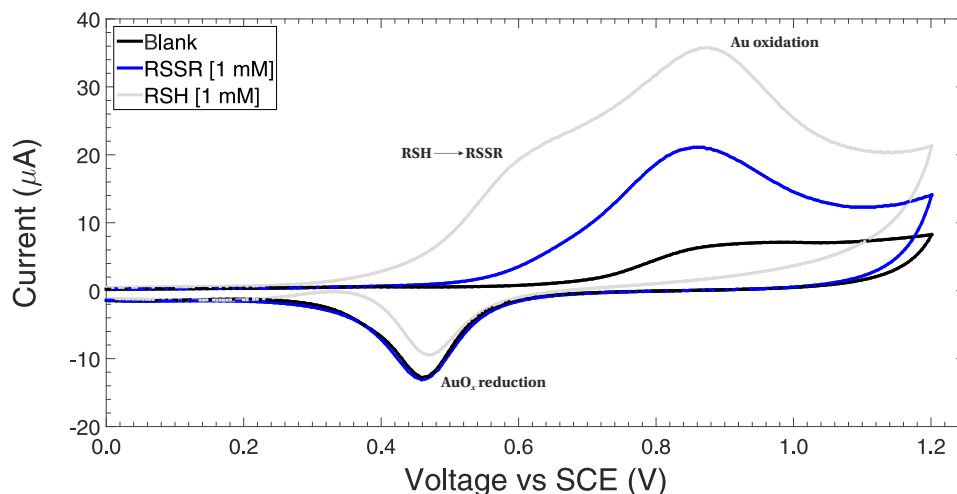


Figure 3.6: Cyclic voltammogram showing the oxidative sweeps of 1 mM cysteine (RSH) and 1 mM cystine (RSSR) at a 1 mm gold electrode in purged 0.1 M PBS, pH 7.0, at a scan rate of $100 \text{ mV} \cdot \text{s}^{-1}$.

3.2.3 Results

Electrochemical behaviour at a macro electrode

In order to validate the behaviour of both cysteine and cystine at a gold surface, a 1 mm diameter macrodisc electrode was used to perform cyclic voltammetry in monopotentiostatic mode. Before each test the electrode was polished for 5 minutes using using $1 \mu\text{m}$ de-agglomerated alumina slurry then a further 5 minutes with $0.3 \mu\text{m}$ de-agglomerated alumina slurry [both from Buehler], before finally cleaning in DI water with ultrasonic agitation. The electrochemical cell was purged using argon for 5 minutes prior to tests and then blanketed and sealed with Parafilm M[®] film. A potential sweep initiated from 0.0 V to 1.2 V, down to -1.2 V and returning to 0.0 V (all *vs.* SCE), was repeated 5 times at a scan rate of $100 \text{ mV} \cdot \text{s}^{-1}$. Figure 3.6 shows cysteine undergoing oxidation via a complex surface reaction that starts around 0.25 V *vs.* SCE then peaking around 0.6 V *vs.* SCE. The oxidation peak attributed to gold oxidation is at $\approx 0.85 \text{ V}$ *vs.* SCE.

Taking the peak anodic current (i_{pa}), the diffusion coefficient (D) can be estimated using the Randles–Sevcik equation [Equation 3.2]. The calculated value of $6.0 \times 10^{-9} \text{ m}^2 \cdot \text{s}^{-1}$ is much too high to be physically realistic (literature value for cysteine’s diffusion coefficient is $8.1 \times 10^{-10} \text{ m}^2 \cdot \text{s}^{-1}$ [47]), indicating either: multi electron transfer, or contributions from adsorbed cysteine, or both. This supports the premise of cysteine participating in surface reactions prior to oxidation. Also visible is a response for cystine, indicative of the formation

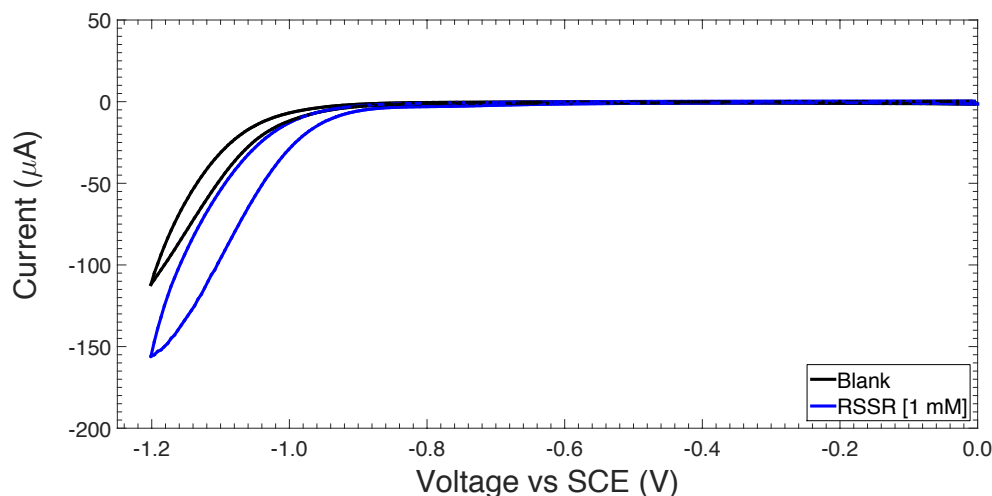


Figure 3.7: Cyclic voltammogram showing the reductive sweep of 1 mM cystine (RSSR) at a 1 mm gold electrode in purged 0.1 M PBS, pH 7.0, at a scan rate of $100 \text{ mV} \cdot \text{s}^{-1}$.

of surface-adsorbed intermediates and/or multi electron oxidation of cystine to cysteic acid.

$$i_p = 0.4463 n F A c_i \sqrt{\frac{n F v D_i}{RT}} \quad (3.2)$$

The diffusion coefficient for cystine was determined as $4.8 \times 10^{-10} \text{ m}^2 \cdot \text{s}^{-1}$. The cyclic voltammogram (CV) in Figure 3.7 shows the reduction of cystine commencing at -0.8 V vs. SCE , but without a clear cathodic peak and with relatively high current ($\approx 40 \mu\text{A}$ at -1.2 V vs. SCE) it suggests the response may be affected by the adsorption of cystine on the electrode surface.

Given the complexity of the observed responses for cysteine and cystine at a single macro gold electrode, it is appreciable that a method to discriminate the redox behaviour from background processes would be advantageous. Here the use of a gold–gold dual-plate generator–collector microgap sensor offers just that; the small interelectrode separation reduces the shuttling time for interdiffusion, providing an amplification of the current response through the feedback process. This should lead to an improved analytical performance when compared to a single electrode.

Sensor mode optimisation

The sensor can be operated in two distinct modes with the collector set at a potential to either reduce or oxidise. Unlike the generator, the collector is held at a static potential (ϕ_c) and consequently capacitive charging of the electric double layer is reduced. The first mode investigated was using the generator set to sweep into the cysteine oxidation potential and

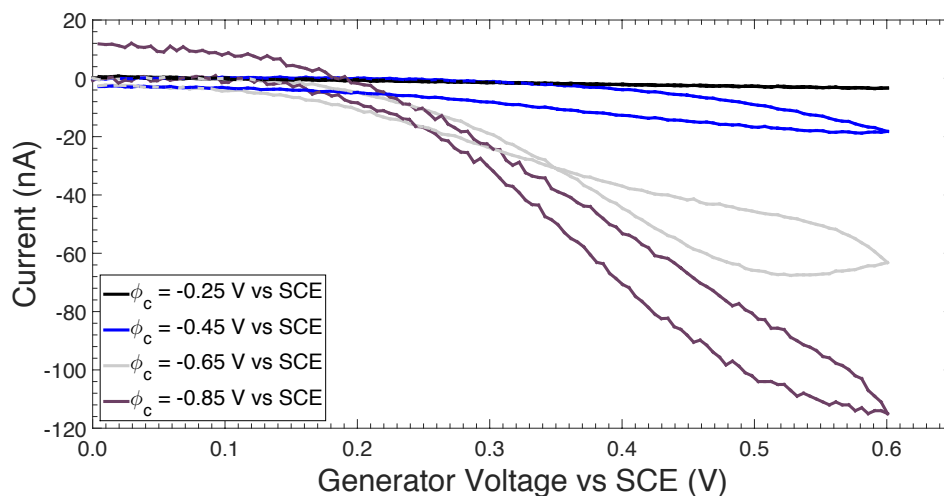


Figure 3.8: Cyclic voltammogram showing the effect of collector potential (ϕ_c) on the collector current response for 1 mM cysteine in 0.1 M PBS, pH 7.0 at a scan rate of $25 \text{ mV}\cdot\text{s}^{-1}$.

the collector held at different negative potentials to reduce any generated cystine. Figure 3.8 shows that a value of -0.85 V vs. SCE provided the highest signal. Holding the collector at more negative potentials than this decreased the stability of the sensor.

The effect of the collector potential on the generator current can be seen in Figure 3.9. When the collector is held at the more negative potential, the reduction of generated cystine becomes more efficient, regenerating more of the reduced species. As a consequence there is a greater flux of analyte at the generator and the current increases. This coupling of reactions demonstrates the feedback amplification.

The study was repeated for the second mode of operation, this time the generator sweeps into negative potentials to reduce cystine, forming cysteine. The collector is then held at an oxidising potential to oxidise and generated cystine. In the first mode, static potentials below -0.85 V vs. SCE caused destabilisation of the sensor. However, the transient nature of the generator allows a greater over-potential to be created, sweeping down to -1.05 V vs. SCE . The responses for a range of collector potentials are shown in Figure 3.10. As expected, the current response for (ϕ_c) = 0.65 V vs. SCE provided the best response. However, to reduce the gold oxidation masking the analytical signal the collector potential was reduced to 0.6 V vs. SCE .

Cysteine dose response

A dose response was performed with increasing concentrations of cysteine in 0.1 M PBS, pH 7.0. Figures 3.11 and 3.12 show the CVs for the generator and collector electrodes, respectively. The generator potential was swept from 0.0 V to 0.6 V vs. SCE at a scan rate of $25 \text{ mV}\cdot\text{s}^{-1}$. The

3.2. Electrochemical redox cycling with a microgap sensor

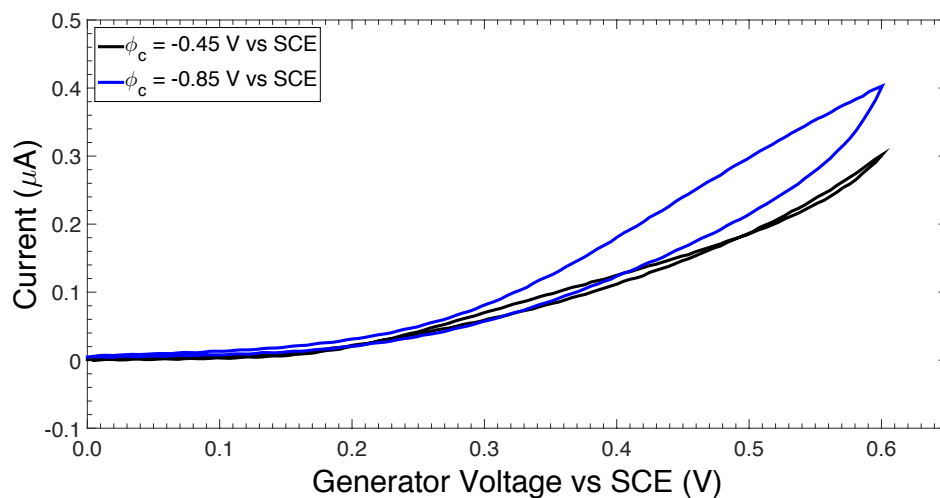


Figure 3.9: Cyclic voltammogram demonstrating how the collector potential affects the generator current response for 1 mM cysteine in 0.1 M PBS, pH 7.0, at a scan rate of 25 mV·s⁻¹.

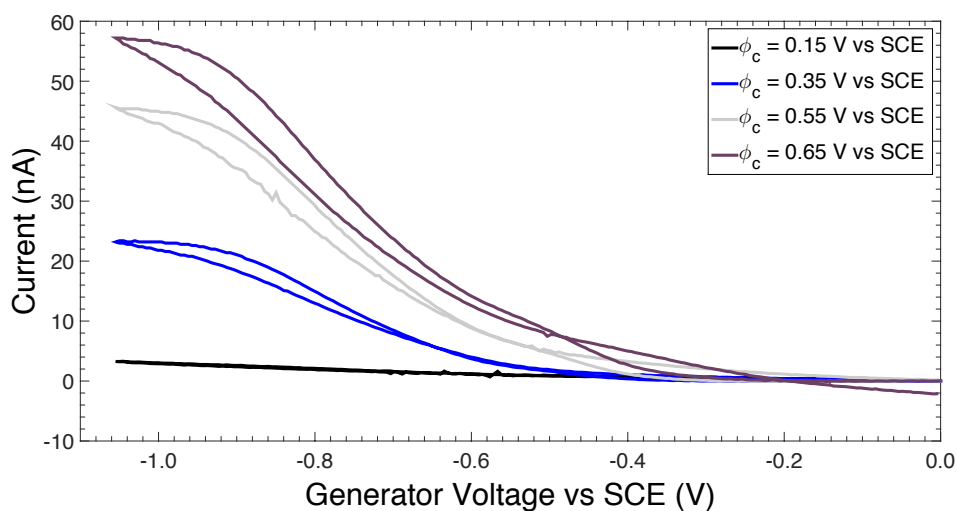


Figure 3.10: Cyclic voltammogram showing the effect of collector potential (ϕ_c) on the collector current response for 1 mM cysteine in 0.1 M PBS, pH 7.0, at a scan rate of 25 mV·s⁻¹.

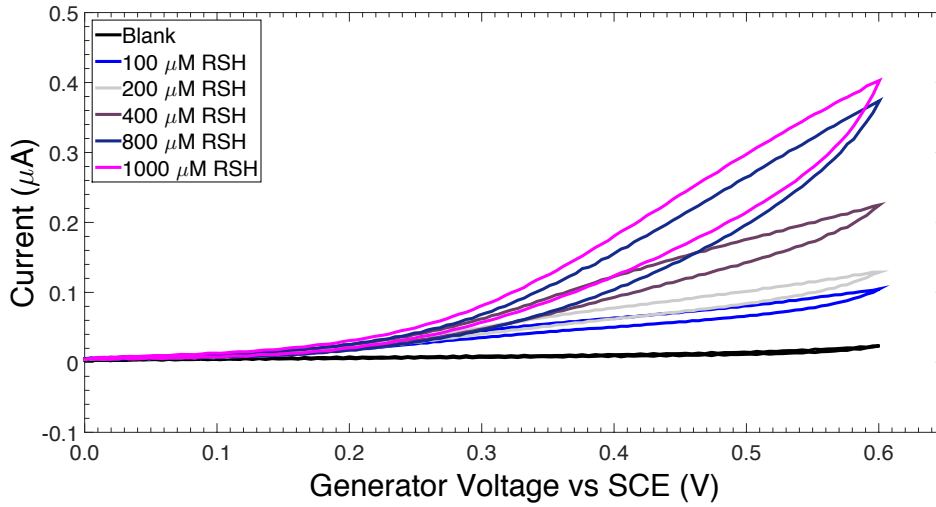


Figure 3.11: Cyclic voltammogram showing the effect of increasing concentration of cysteine (RSH) on the generator current in 0.1 M PBS, pH 7.0, at a scan rate of $25 \text{ mV}\cdot\text{s}^{-1}$ and the collector held at -0.85 V vs. SCE .

collector electrode was held at -0.85 V vs. SCE .

Figure 3.13 shows that plotting the limiting current against cysteine concentration provides a linear response with a gradient of $140.28 \text{ nA}\cdot\text{mM}^{-1}$. Despite the complexity of the overall redox process a feedback current can be tentatively identified and expressed in terms of the Nernst model for dual-plate diffusion processes as:

$$I_{\text{lim},D} = \frac{2FAc_0}{x} \frac{D_{\text{red}} \times D_{\text{ox}}}{D_{\text{red}} + D_{\text{ox}}} \quad (3.3)$$

Here $I_{\text{lim},D}$ is the feedback current under mass transport control, F is the Faraday constant, A is the electrode area, x is the interelectrode spacing, and the concentration is defined as $c_0 = c_{\text{red}} + 2c_{\text{ox}}$. On the basis of this expression the gradient of the line should be $2.9 \mu\text{A}\cdot\text{mM}^{-1}$, which is around 20 times higher than that observed experimentally. Therefore the feedback current is inconsistent with diffusion-limited control and is likely to be kinetically limited.

Cystine dose response

A dose response was also performed with increasing cystine concentrations with the sensor operating in the second mode (*i.e.*, with the generator reducing cystine and the collector oxidising cystine). The generator potential was swept from 0.0 V to -1.05 V vs. SCE at a

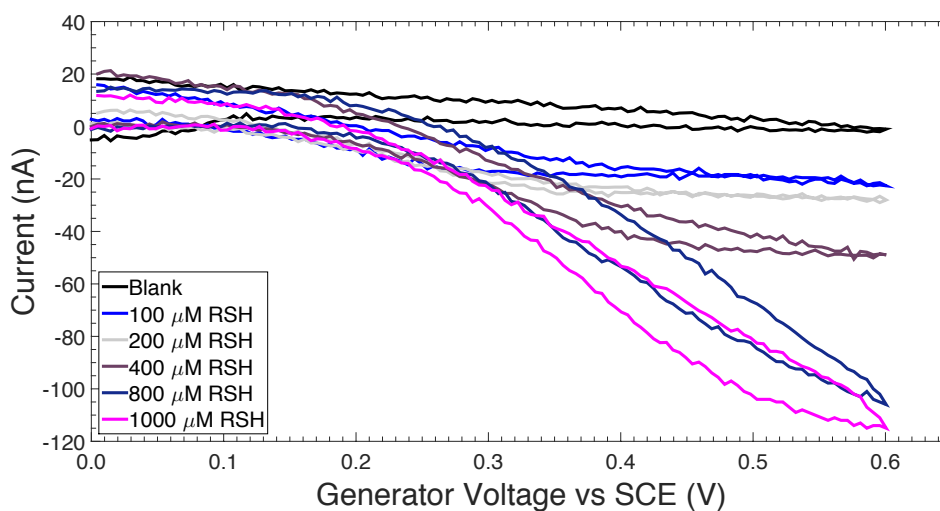


Figure 3.12: Cyclic voltammogram showing the effect of increasing concentration of cysteine (RSH) on the collector current in 0.1 M PBS, pH 7.0, at a scan rate of $25 \text{ mV} \cdot \text{s}^{-1}$ and collector held at -0.85 V vs. SCE .

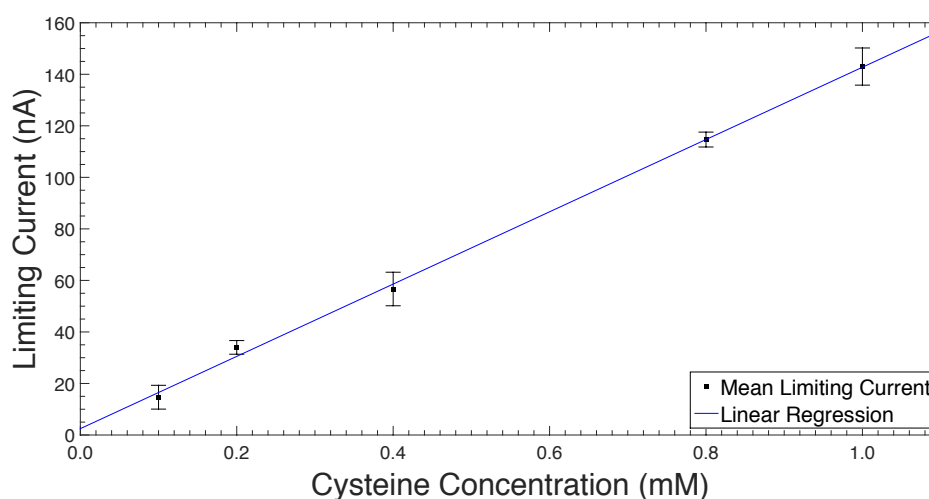


Figure 3.13: Plot showing dose response of cysteine (RSH) at the collector with the collector held at -0.85 V vs. SCE in 0.1 M PBS, pH 7.0, at a scan rate of $25 \text{ mV} \cdot \text{s}^{-1}$. Error bars indicate $\pm \sigma$, $n = 5$. Linear regression constants: 140.28 and $+2.464$.

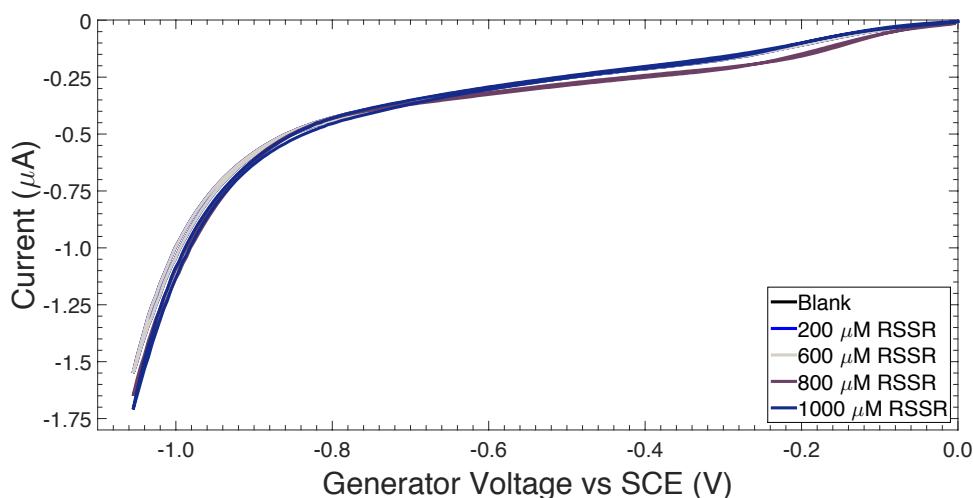


Figure 3.14: Cyclic voltammogram showing the effect increasing concentration of cystine (RSSR) on the generator current in 0.1 M PBS, pH 7.0, at a scan rate of $25 \text{ mV}\cdot\text{s}^{-1}$ and the collector held at 0.60 V vs. SCE .

scan rate of $25 \text{ mV}\cdot\text{s}^{-1}$ and the collector electrode was held at 0.6 V vs. SCE . The CVs for the generator [Figure 3.14] show very high background currents due to the onset of hydrogen evolution at the strong negative potentials. However, the collector response [Figure 3.15] demonstrates a well-defined steady-state limiting current for the redox process and therefore provides a much more useful analytical signal compared to the first mode. (*i.e.*, with the generator oxidising cystine and the collector reducing cystine).

Plotting the limiting current against cystine concentration shows approximately linear correlation [Figure 3.16]. Again the gradient of the line was an order of magnitude lower than the value of $1.45 \mu\text{A}\cdot\text{mM}^{-1}$ expected based on Equation 3.3. Therefore simple diffusion controlled reaction conditions are unlikely to govern this process.

3.2. Electrochemical redox cycling with a microgap sensor

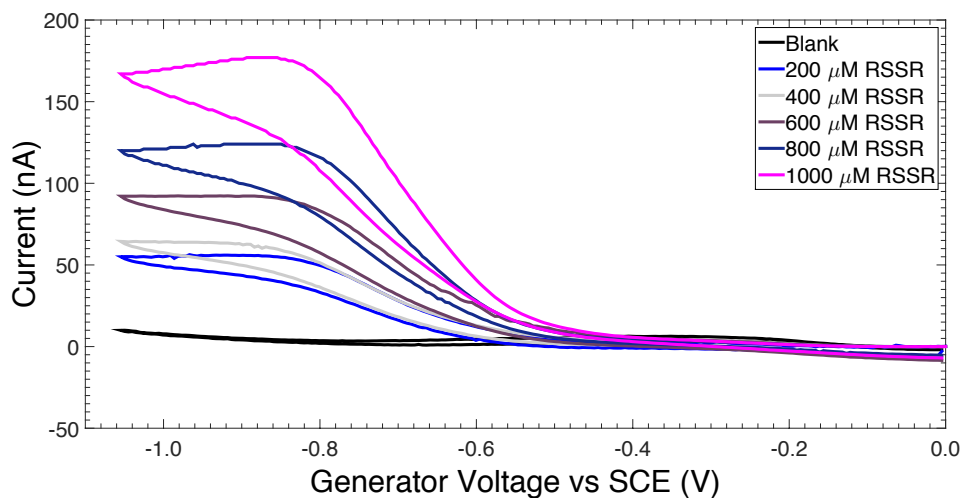


Figure 3.15: Cyclic voltammogram showing the effect of increasing concentration of cystine (RSSR) on the collector current in 0.1 M PBS, pH 7.0, at a scan rate of $25 \text{ mV}\cdot\text{s}^{-1}$ and the collector held at 0.60 V *vs.* SCE.

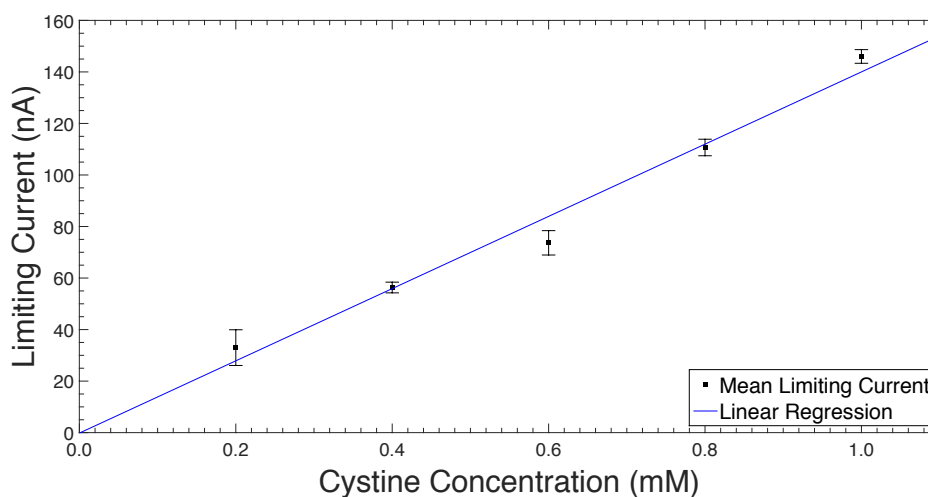


Figure 3.16: Plot showing dose response of cystine (RSSR) at the collector with the collector held at 0.60 V *vs.* SCE in 0.1 M PBS, pH 7.0, at a scan rate of $25 \text{ mV}\cdot\text{s}^{-1}$. Error bars indicate $\pm\sigma$, $n = 5$. Linear regression constants: 140.17 and -0.168 .

Combined dose response

It is possible to express a case of kinetically limited dual-plate process based on $i = nFAj$ and $j = k_0 c_i$:

$$i_{\text{ox}} = F A k_{\text{ox}} c_{\text{red}} \quad (3.4)$$

$$i_{\text{red}} = F A k_{\text{red}} c_{\text{ox}} \quad (3.5)$$

Irrespective of the nature of both k_{ox} and k_{red} , equating the two expressions shows that:

$$\frac{c_{\text{ox}}}{c_{\text{red}}} = \frac{k_{\text{ox}}}{2k_{\text{red}}} \quad (3.6)$$

This suggests that depending on the applied potential, either cysteine or cystine will be present within the sensor. By substituting $c_i = c_0 = c_{\text{red}} + 2c_{\text{ox}}$ the kinetically controlled dual-plate limiting current as:

$$I_{\text{lim},k} = F A c_0 \frac{k_{\text{ox}} \times k_{\text{red}}}{k_{\text{ox}} + k_{\text{red}}} \quad (3.7)$$

Based on this equation a kinetically controlled limiting current should be obtained with a linear response to the combined concentration, c_0 . In order to validate this hypothesis an experiment involving sequences of cystine/cysteine/cystine additions was performed. Here the combined concentration was incremented by 50 μM at a time. Cystine proved to be insoluble at higher concentrations so modest stock concentrations were used (2 mM and 1 mM for cystine and cysteine, respectively). To prevent dilution of the test solution through additions, the entire sample volume was exchanged with the next concentration. The sensor was operated in the preferred mode (mode 2), with the generator reducing cystine and the collector oxidising cysteine.

The experiment comprised of three stages, the first and third involved 50 μM cystine additions whilst the second stage involved 50 μM cysteine additions:

$$50 \mu\text{M } c_0 \text{ addition} \begin{cases} \text{cystine, for } c_0 \leq 500 \mu\text{M} \\ \text{cysteine, for } 500 \mu\text{M} < c_0 \leq 750 \mu\text{M} \\ \text{cystine, for } 750 \mu\text{M} < c_0 \leq 1.25 \text{ mM} \end{cases} \quad (3.8)$$

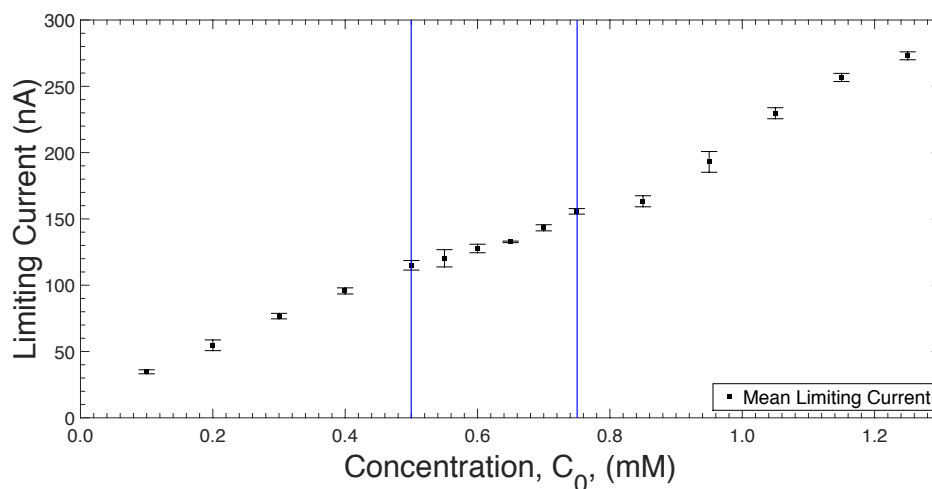


Figure 3.17: Plot showing combined dose response of both cysteine and cystine at the collector, collector held at 0.60 V *vs.* SCE in 0.1 M PBS, pH 7.0, at a scan rate of 25 mV·s⁻¹. Error bars indicate $\pm\sigma$, $n = 5$.

The kinetically controlled limiting current for increasing combined concentrations (c_0) is demonstrated in Figure 3.17. Agreement with Equation 3.7 is acceptable and any remaining nonlinearity may be attributed to the adsorption/desorption kinetics, some degree of multi electron oxidation and the transient nature of the cyclic voltammetry method. In particular, the very high surface-to-volume ratio (in this case $\approx 2 \times 10^5 \text{ m}^{-1}$) leads to pronounced effects of the adsorption/desorption kinetics as previously reported [48–50].

It is interesting to note that all experiments were performed in the presence of ambient levels of oxygen. The reduction of oxygen was observed at the generator at -0.4 V vs. SCE , but does not appear to interfere with the cysteine–cystine redox signal. For the overall cysteine–cystine process there are two possible scenarios to explain the lower than expected diffusion controlled limiting current responses: if the cysteine oxidation occurs as a multi electron process with products other than cystine, this will induce a concentration depletion effect within the sensor; and/or if a slow surface process is associated with a kinetically limiting factor (most likely adsorption/desorption hampering electron transfer), lower conversion and therefore lower currents would be anticipated during feedback between the two electrodes. The second hypothesis appears most likely, but the first hypothesis may still be contributing.

3.2.4 Discussion

This work demonstrated that a microgap sensor operated in a generator–collector configuration could be utilised to produce well-defined (but kinetically limited) steady-state current responses for a complex analytical system such as the cysteine–cystine redox couple. The

results were achieved in non-purged PBS buffer at pH 7.0, down to physiologically relevant concentrations. Given the importance of the redox couple's involvement in signalling pathways for the regulation of protein function, interaction and localisation, such a platform presents a promising tool for monitoring and/or detection of a wide range of diseases.

Interfering signals from the gold surface oxidation and thiol adsorption were suppressed and the analytical signal is feedback-enhanced. Attenuation of the current response for both the reduction and oxidation processes was evident. Formation of tertiary products from the multi electron oxidation of cysteine and adsorption/desorption affecting electron transfer could be playing a role. The use of a nanogap sensor may alleviate this issue, reducing any concentration depletion effects and should allow the adsorption/desorption processes to be studied.

The use of other electrode materials or modification of the electrode surface to further increase the surface area such as the formation of mesoporous gold [51] may help overcome the slow surface processes. The use of electrocatalysts could also be investigated to provide greater specificity, allowing different types of thiols and disulfides to be selectively determined.

3.3 Dielectric spectroscopy measurements with a microgap sensor

Dielectric spectroscopy provides a method of detecting changes in the dielectric constant of a medium as a function of the perturbing signal's frequency. For the case of a biosensor, the affinity reaction between the probe layer and analyte will lead to restructuring of the bilayer properties which should lead to a change in the capacitance. Both the size and the total charge of the analyte can contribute to the signal change. For instance, biomolecules are generally characterised by having a relative permittivity, ϵ_r , of 2-5, whereas aqueous solutions usually exhibit a value of ϵ_r between 78 and 80 [52]. Displacement of the solvent ions due to binding events will therefore result in a change of the charge density at the electrode-electrolyte interface.

3.3.1 Detection of *Escherichia coli*

In this work a dual-plate microgap sensor was used to demonstrate dielectric spectroscopy sensing of bacteria using mannose-specific type 1 *Escherichia coli* PKL1162 as a case study. The acceptable limits of *Escherichia coli* (*E. coli*) in samples vary between countries. Typically a zero-tolerance in drinking water is enforced, however a cut-off concentration of 500 colony-forming units per mL (CFU·mL⁻¹) is deemed acceptable in some countries. It is important to highlight that the current protocol for the detection of pathogenic bacteria involves a compulsory growth step in order to provide sufficient mass for analysis. Post-growth analysis allows isolation and characterisation of a single species in a sample, usually achieved with elaborate and expensive techniques such as immunology, matrix-assisted laser desorption/ionisation time-of-flight mass spectrometry (MALDI-TOF MS), PCR, and staining [53]. In this context an affordable and rapid biosensor for pre-screening at this stage could significantly reduce time and costs associated with these more complex analysis methods.

Uropathogenic *E. coli* (UPEC) is responsible for urinary tract infections. UPEC exploit hair-like protein structures called fimbriae present on their surface in order to adhere to the cell, anchoring themselves during urinary flow. This attachment involves the fimbriae on the bacteria surface with glycosylated proteins on the cell surface. Lectin protein structures are expressed in at least 9 out of 10 UPEC strains [54]. Several fimbriae have been identified and among them mannose-specific type 1 fimbriae is one of the most commonly expressed [55]. The mannose-specific protein called FimH, situated at the tip of the fimbrial rod of the pathogenic bacteria, undergoes a reaction with the glycosylated cell of the urinary tract.

In this study the recognition event involves the uropathogenic mannose-specific type 1 fimbrial *E. coli* PKL1162 (PKL) with α -D-mannose (MANN) sugar (mimicking a glycosylated cell of the urinary tract). Figure 3.18 illustrates the desired biorecognition stack. An alternative sugar, 2-Acetamido-2-deoxy- α -D-glucopyranose (GAL), and bacterium strain, *E. coli* K-12 (K12), are used as controls. Different concentrations of PBS are used to study the effect of ionic strength

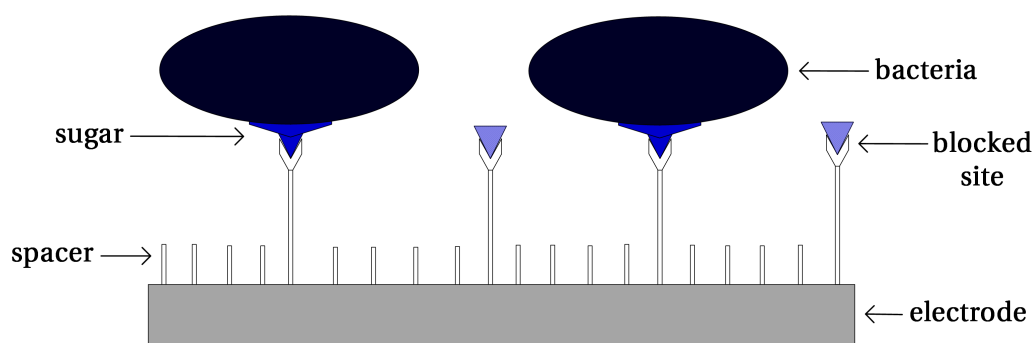


Figure 3.18: Diagram illustrating the expected biorecognition stack after the addition of the specific bacteria.

Table 3.2: Combinations of sugars and bacteria immobilised on the different electrodes for the dielectric spectroscopy study.

Electrode	Sugar	Bacteria	Buffers
A	MANN	PKL	10 mM, 1mM & 100 μ M PBS
B	MANN	K12	10 mM, 1mM & 100 μ M PBS
C	GAL	PKL	10 mM, 1mM & 100 μ M PBS

on the capacitive response. Table 3.2 provides an overview of the experimental design.

3.3.2 Experimental information

Reagents

Dimethyl sulfoxide (DMSO), *N*-(3-Dimethylaminopropyl)-*N'*-ethylcarbodiimide hydrochloride (EDC) [CAS 25952-52-8], ethanolamine (ETA) [CAS 141-43-5], *N*-Hydroxysuccinimide (NHS) [CAS 6066-82-6] and PBS tablets were all purchased from Sigma-Aldrich. All aqueous solutions were prepared using 18.2 M Ω ·cm ultra-pure class 1 DI water treated with a Biopak[®] polishing pack from a Direct-Q[®] 5 UV system [Millipore]. A stock 10 mM PBS solution (pH 7.4) [with 2.7 mM KCl and 137 mM NaCl] was prepared and diluted to two further working concentrations of 1 μ M and 100 μ M. The pH of solutions were measured using a SevenCompact[™] pH meter [Mettler-Toledo] which was calibrated with pH 4.0, pH 7.0 and pH 11.0 standards prior to use. *E. coli* PKL1162, engineered using the SAR18 strain with pPKL174 plasmid [56] and *E. coli* K12 was grown overnight in an incubated shaker at 37 °C in lysogeny broth growing

3.3. Dielectric spectroscopy measurements with a microgap sensor

media. The test concentrations for the bacteria affinity capture was 4.2×10^9 CFU·mL⁻¹. The aminoethyl glycosides were prepared at concentrations of 50 mM in 10 mM PBS.

Apparatus

A total of 3 gold–gold dual-plate microgap sensors were used, all with approximate dimensions of around 5 mm × 80 μm and gap sizes of 10 μm. The electrodes were electrochemically cycled in 0.1 M PBS (pH 7.0) to stabilise the gold surface prior to experiments. Due to the slight differences in geometry a relative percentage shift is reported when comparing data from different electrodes.

The measurement setup consisted of a B1500A semiconductor device parameter analyser [Agilent Technologies] fitted with a 1 kHz to 5 MHz multi-frequency capacitance measurement unit (MFCMU). Connections to the device were made with coaxial cables terminated with miniature crocodile clips with a shielded 2-terminal configuration inside a large Faraday cage. Open, short and phase correction was performed to account for the changes in residual admittance, impedance and phase caused by the extended cabling. The dielectric spectra were recorded for a frequency range of 1 kHz to 500 kHz with a 0.0 V DC bias and 10 mV AC perturbing signal using a ‘medium’ integration time (8 power line cycles). A total of 150 frequency points (logarithmic) were recorded. Five scans were taken and averaged for each device at each step. The capacitance reported is the ‘parallel’ capacitance, calculated from the measured susceptance (B) of the auto-balancing bridge of the measurement instrument as $\frac{B}{\omega}$.

Experimental procedure

The key steps for the experimental process are summarised in Table 3.3. First baseline capacitance spectra were recorded in all three of the experimental buffers (100 μM, 1 mM and 10 mM PBS). Measurement drift was checked by performing measurements at the start and end of the day with negligible (<0.1%) difference. Next solutions of the linker (HS-(CH₂)₁₇-PEG₆-COOH, 0.476 mM, 0.2 mg·mL⁻¹ in DMSO) and the spacer (HS-(CH₂)₁₇-PEG₃-OH, 0.328 mM, 0.2 mg·mL⁻¹ in DMSO) were prepared. The mixed SAM solution was then prepared using a 1:4 ratio (53 μL:147 μL, linker:spacer) with 20 minutes ultrasonic agitation (100%). Each electrode was incubated overnight in a humidity chamber with 2 μL of solution. The electrodes were then rinsed in ethanol, dried with N₂ and placed in desiccator for 15 minutes to promote evacuation of the microgap. The capacitance spectra was then recorded in the 3 experimental buffers, allowing 5 minutes stabilisation period before measurements.

The SAM was then activated with 5 μL of EDC/NHS solution (5:1, 100 mg·mL⁻¹ : 20 mg·mL⁻¹) for 1 hour before immobilising the MANN and GAL sugars overnight in a humidity chamber at <5 °C with 5 μL solution at a concentration of 50 mM in 100 μM PBS. The electrodes were then

Chapter 3. Pilot Tests with a Dual-Plate Microgap Sensor

rinsed in ethanol (10 min), dried with N₂ and placed in desiccator for 15 minutes. A blocking step of the non-reacted sites was performed using a 10 mM ETA, 100 μ M PBS solution (pH 8.5) for 50 minutes. The electrodes were then rinsed in 100 μ M PBS (pH 7.4) and capacitance spectra recorded in the three experimental buffers, again allowing 5 minutes stabilisation period before measurements.

Table 3.3: Sequence of key experimental steps for the capacitive sensing of sugar–bacteria interactions.

Step	Description	Duration
1a	Electrochemical cleaning of the electrode surfaces	20 min
1b	Perform capacitance measurements	2.5 h
2a	Formation of self-assembled monolayer (linker & spacer)	20 h
2b	Perform capacitance measurements	2.5 h
3	Glycosylation with EDC/NHS	1 h
4	Immobilisation of MANN & GAL sugars	15 h
5a	Blocking of unreacted sites with ETA	50 min
5b	Perform capacitance measurements	2.5 h
6a	Incubation of PKL & K12 bacteria	2.5 h
6b	Perform capacitance measurements	2.5 h
7a	Recovery of sensor by ethanol wash	15 h
7b	Perform capacitance measurements	2.5 h

The bacteria were removed from -80°C storage and cultivated in lysogeny broth overnight in an incubated shaker at 37°C . To harvest the bacteria the solutions were dispensed into a centrifuge tube and centrifuged for 15 minutes at 4000 rpm at 4°C . The pelleted bacterial cells were resuspended in 2.5 mL of 10 mM PBS (pH 7.4) and diluted further in 10 mM PBS (pH 7.4) for a total volume of 10 mL. This solution was then centrifuged for a further 10 minutes at 4°C . This ‘washing’ step was again repeated before a final re-suspension into 1 mL 10 mM PBS. The optical density was confirmed between $3.0\text{ CFU}\cdot\text{mL}^{-1}$ and $6.0\text{ CFU}\cdot\text{mL}^{-1}$. The electrodes were incubated with 2.5 μ L of the PKL and K12 solutions in a humidity chamber at 37°C for 2 hours. Finally the electrodes were washed with 10 mM PBS (pH 7.4) and stored in 100 μ M PBS (pH 7.4) prior to further measurements.

The capacitance spectra after bacteria incubation were then recorded with the three experimental PBS buffers with great care taken to reduce cross-contamination through the exchange, washing and storage steps. Finally the electrodes were stored in ethanol overnight in an attempt to remove the bacteria and recover the sensor. The electrodes were then rinsed in ethanol, dried with N₂ before taking the final capacitance spectra in the three experimental PBS buffers.

3.3.3 Results

Self-assembled monolayer formation

A high-density insulating SAM to reduce charge leakage is paramount to reliable and sensitive capacitive sensing [57]. The SAM in this work consists of a 1:4 ratio of linker to spacer as per the optimised protocol demonstrated by Zhi *et al.* [58] and Šaržík *et al.* [59]. Figure 3.19 shows the change in capacitance after SAM immobilisation. The relative percentage change from the initial characterisation of the bare gold electrodes is reported due to the differences in geometry between the three electrodes. All the electrodes experienced a significant decrease in capacitance after SAM immobilisation, demonstrating a compact and insulating layer formation.

The capacitance spectra for Electrode A before and after SAM formation in 100 μM [Figure 3.20a], 1 mM [Figure 3.20b] and 10 mM [Figure 3.20c] show the reduction in capacitance across the frequency range.

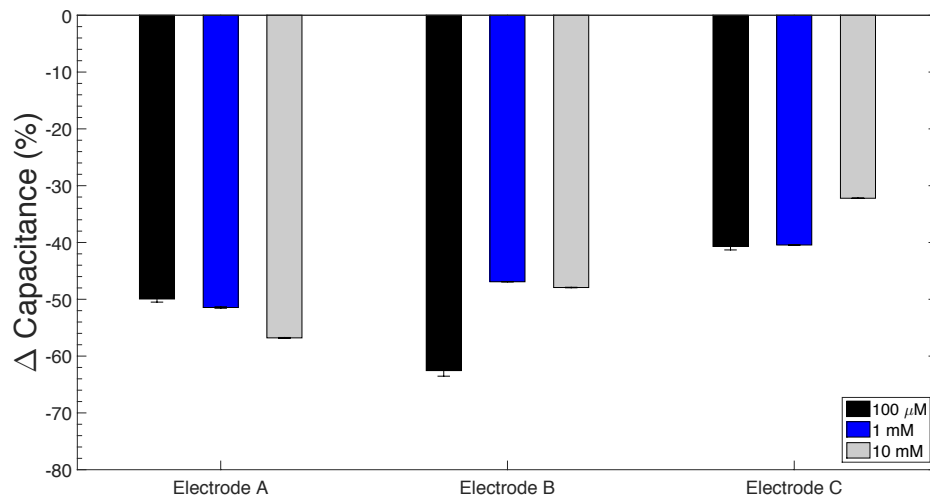


Figure 3.19: Barchart showing the relative capacitance change (%) after SAM immobilisation. Error bars indicate $\pm\sigma$, $n = 5$.

The capacitance is seen to increase with increasing ionic strength, corresponding to a more compact electric double layer at the electrode–electrolyte interface. At 1 kHz the capacitance drops from 12.62 nF to 6.32 nF, 16.32 nF to 7.92 nF and 22.97 nF to 9.93 nF for PBS concentrations of 100 μM , 1 mM and 10 mM, respectively.

The capacitance of the SAM measured at 1 kHz can then be calculated using Equation 3.9. This falsely assumes that the electric double layer contribution does not change after SAM

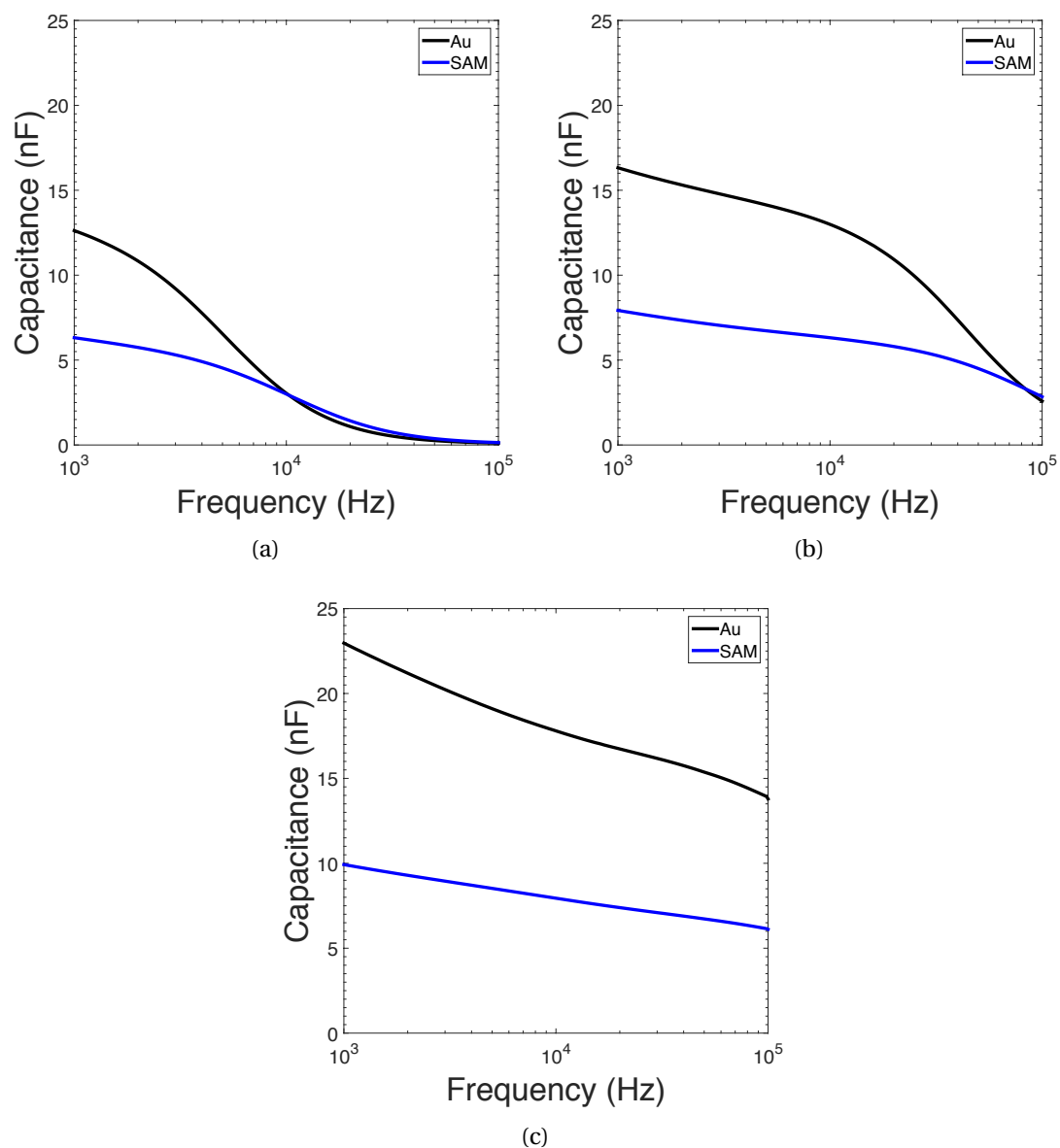


Figure 3.20: Capacitance spectra of Electrode A after SAM formation in (a) 100 μ M PBS, (b) 1 mM PBS and (c) 10 mM PBS.

3.3. Dielectric spectroscopy measurements with a microgap sensor

Table 3.4: Calculated capacitance per unit area for the self-assembled monolayer at a frequency of 1 kHz in different PBS concentrations.

Capacitance per unit area	PBS concentration	Frequency
$\approx 3.1 \mu\text{F}\cdot\text{cm}^{-2}$	100 μM	1 kHz
$\approx 3.8 \mu\text{F}\cdot\text{cm}^{-2}$	1 mM	1 kHz
$\approx 4.4 \mu\text{F}\cdot\text{cm}^{-2}$	10 mM	1 kHz

formation, but does significantly simplify the calculation whilst providing a reasonable estimate for comparison. Table 3.4 presents the values of capacitance per unit area (C'') of the SAM at 1 kHz in the three PBS concentrations. These are calculated using an estimated area of $4.0 \times 10^{-7} \text{ m}^2$.

$$C_{\text{ins}} = \frac{C_{\text{EDL}} \times C_{\text{tot}}}{C_{\text{EDL}} - C_{\text{tot}}} \quad (3.9)$$

The obtained values of capacitance per unit area are in agreement with values obtained by other authors. For instance Riepl *et al.* [60] reported $3\text{-}9 \mu\text{F}\cdot\text{cm}^{-2}$ for 11-mercaptoundecanoic acid (5 mM PB & 100 mM KCl) and Carrara *et al.* reported $4 \mu\text{F}\cdot\text{cm}^{-2}$ for the same 11-mercaptoundecanoic acid monolayers (100 mM PBS) [61]. Table 3.4 shows the calculated capacitance per unit areas in the different PBS concentrations at 1 kHz.

Capacitance spectra

Capacitance profiles for Electrode A (MANN–PKL interaction) in 100 μM , 1 mM and 10 mM are shown in Figures 3.21, 3.22 and 3.23, respectively. It is interesting to note the effect of increasing concentration of the PBS buffer on the capacitance response. The stock 10 mM PBS buffer (2.7 mM KCl and 137 mM NaCl) was diluted to provide two further working concentrations of 1 mM and 100 μM . The ionic strengths of these solutions was 162 mM, 16.2 mM and 1.62 mM, respectively.

The Debye length of the electrolyte varies from 7.5 nm at the lowest ionic strength to 7.5 Å at the highest, therefore occupying a relatively small fraction of the 10 μm interelectrode distance. The Debye length could be drastically increased by reducing the ionic strength of the solution, but further dilution was avoided as it has been reported that this can lead to cell damage due to the osmotic pressure induced by the high concentration gradient between the inner and outer bacterial membranes [62, 63].

As the concentration of ions increases the electric double layer becomes more compact and provides a higher capacitance. The shoulder observed in the 100 μM spectra, caused by the dielectric relaxation, slowly shifts to higher frequencies until at 10 mM it is barely visible. This effect has been explicitly reported by both Yi *et al.* [64] and Mannoor *et al.* [65] whom studied the permittivity of ionic strengths ranging from 100 μM to 10 mM as a function of frequency. This behaviour is also consistent with the results reported by other authors [66, 67].

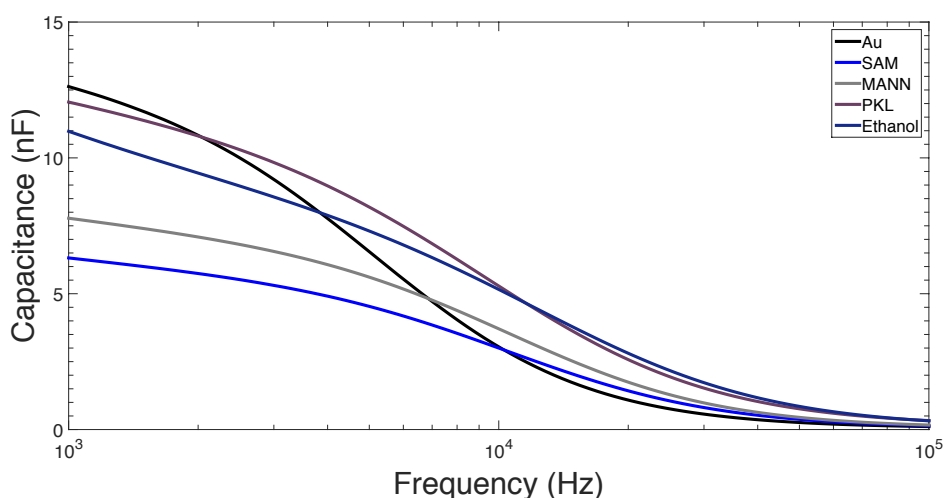


Figure 3.21: Frequency profile for Electrode A in 100 μM PBS.

Glycosylation with the MANN sugar leads to only a minor, but measurable relative increase in capacitance. On binding the $4.2 \times 10^9 \text{ CFU} \cdot \text{mL}^{-1}$ concentration of *E. coli* PKL1162 a significantly larger signal is recorded. The large negatively charged bacterium leads to a

3.3. Dielectric spectroscopy measurements with a microgap sensor

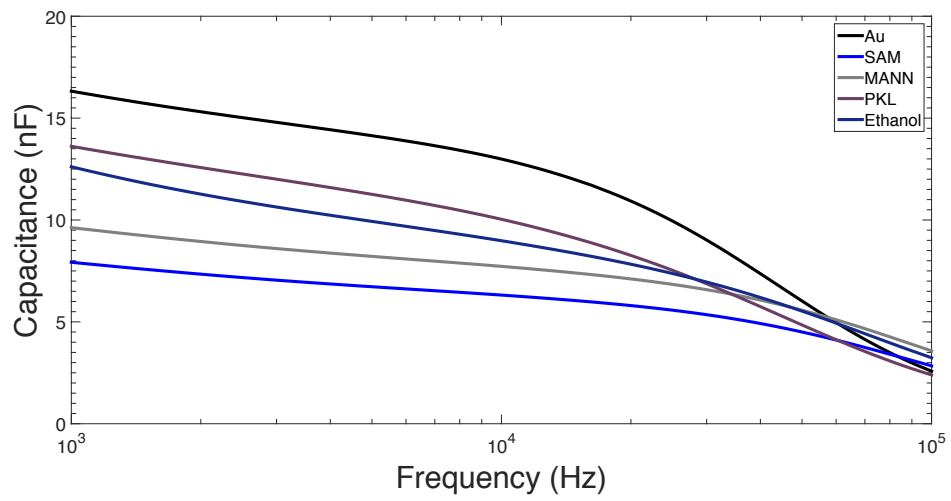


Figure 3.22: Frequency profile for Electrode A in 1 mM PBS.

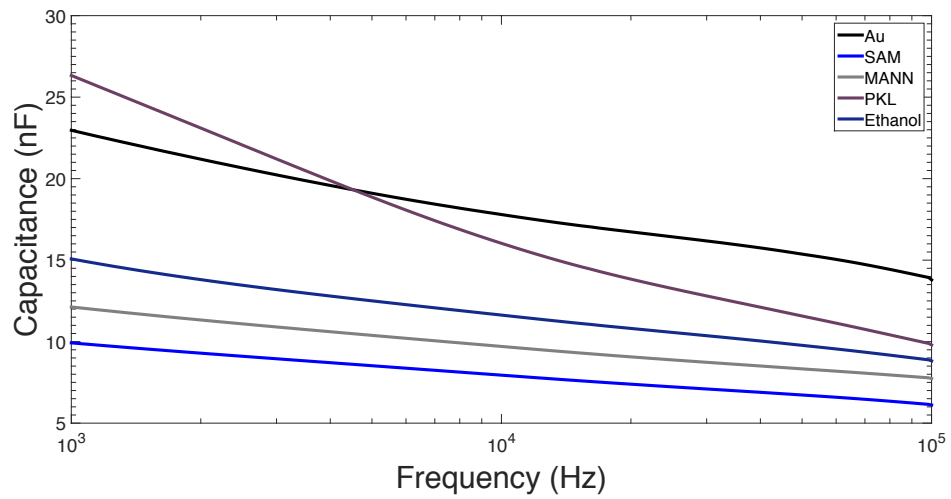


Figure 3.23: Frequency profile for Electrode A in 10 mM PBS.

significant disruption of the electric double layer and charge redistribution, resulting in an increase in the measured capacitance. A washing step with ethanol was used in an attempt to regenerate the probe layer through disruption of the bacterial membrane. Whilst some recovery is observed, full regeneration of the biosensor could not be achieved. This could be explained by some partial retention of bacterial membrane fragments on the probe surface.

Comparison to controls

Figure 3.24 charts the change in capacitance (%) for the MANN–PKL interaction as well as the two negative controls (MANN–K12 and GAL–PKL) in the form. The measurement errors for the shifts were calculated using Equation 3.10. Interestingly glycosylation with the GAL sugar appears to result in a decrease in the capacitance, an opposite behaviour to that of the MANN sugar. Addition of the bacteria leads to an increase in capacitance for all the cases, with clear contributions from the non-specific interactions. A maximum shift is given in 10 mM PBS, with a percentage increase of 117%.

$$\sigma = \left| \left(\frac{\bar{y} - \bar{x}}{\bar{x}} \right) \times 100 \right| \sqrt{\frac{\sigma_y^2 + \sigma_x^2}{(\bar{y} - \bar{x})^2} + \left(\frac{\sigma_x}{\bar{x}} \right)^2} \quad (3.10)$$

The ratio of the specific to non-specific interaction signals are presented in Table 3.5. Considering just these values, there does not seem to be any clear advantage of using a higher ionic strength buffer other than the creation of a larger capacitive signal. However, considering the total frequency spectrum a higher ionic strength does seem to offer the ability to detect changes in the system at higher frequencies.

Table 3.5: Ratios of specific to non-specific signals at a frequency of 1 kHz in different PBS concentrations.

Concentration	specific:nonspecific (bacteria)	specific:nonspecific (sugar)
100 μ M	2.6	2.1
1 mM	1.5	1.7
10 mM	2.5	5.2

3.3. Dielectric spectroscopy measurements with a microgap sensor

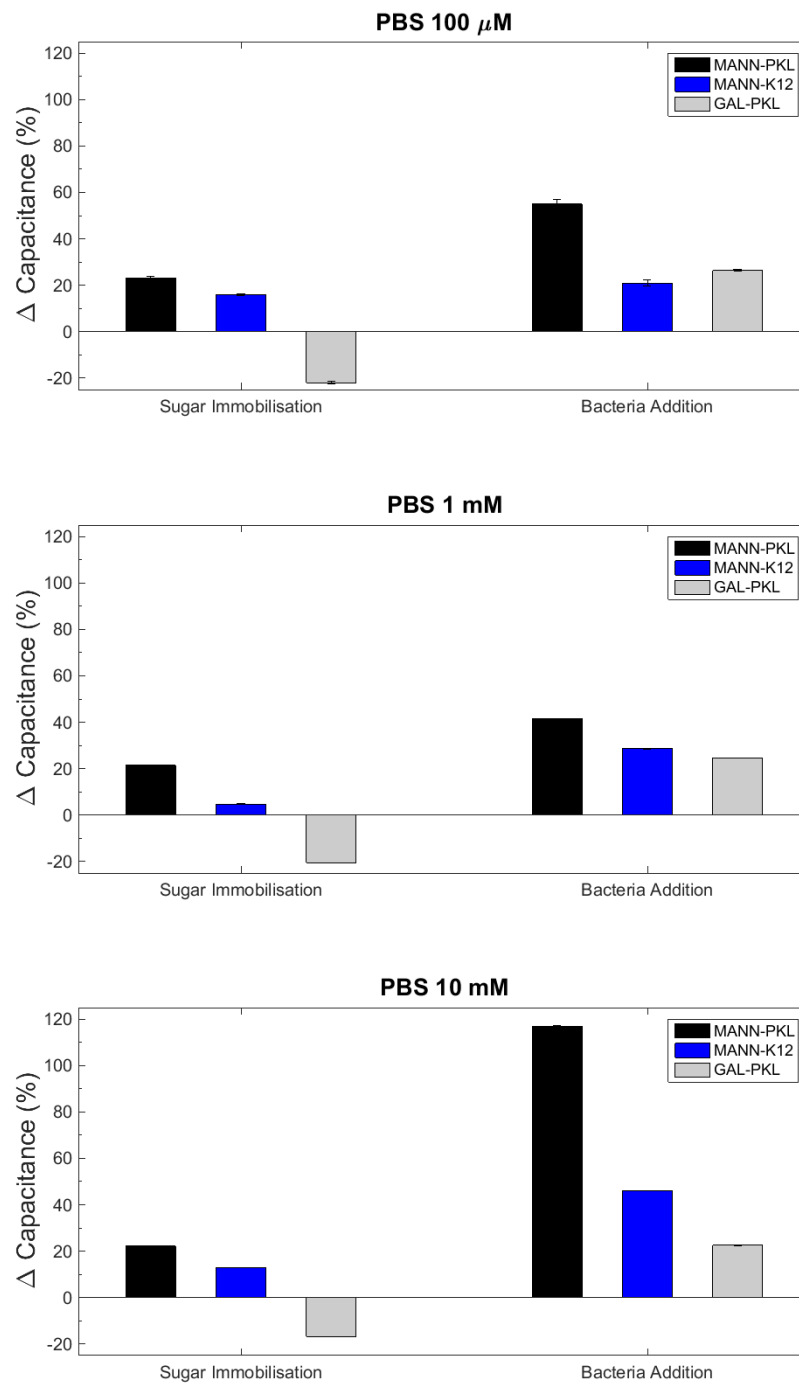


Figure 3.24: Set of barcharts showing the capacitance change (%) for different electrodes after immobilisation of sugar and bacteria in 100 μM , 1 mM and 10 mM PBS. Error bars indicate $\pm\sigma$, $n = 5$.

Verification of sugar–bacteria binding using SEM

For completeness of the study, the bacterial binding and anti-fouling properties of the surface towards non-specific interactions were checked using SEM. Figure 3.25a shows the the surface after MANN immobilisation and Figures 3.25b to 3.25d show the different surfaces after the addition of bacteria at a concentration 4.2×10^9 CFU·mL⁻¹. The SEM reveals that even with carefully controlled surface chemistry there is still evidence of non-specific interactions for both the sugar and bacteria controls.

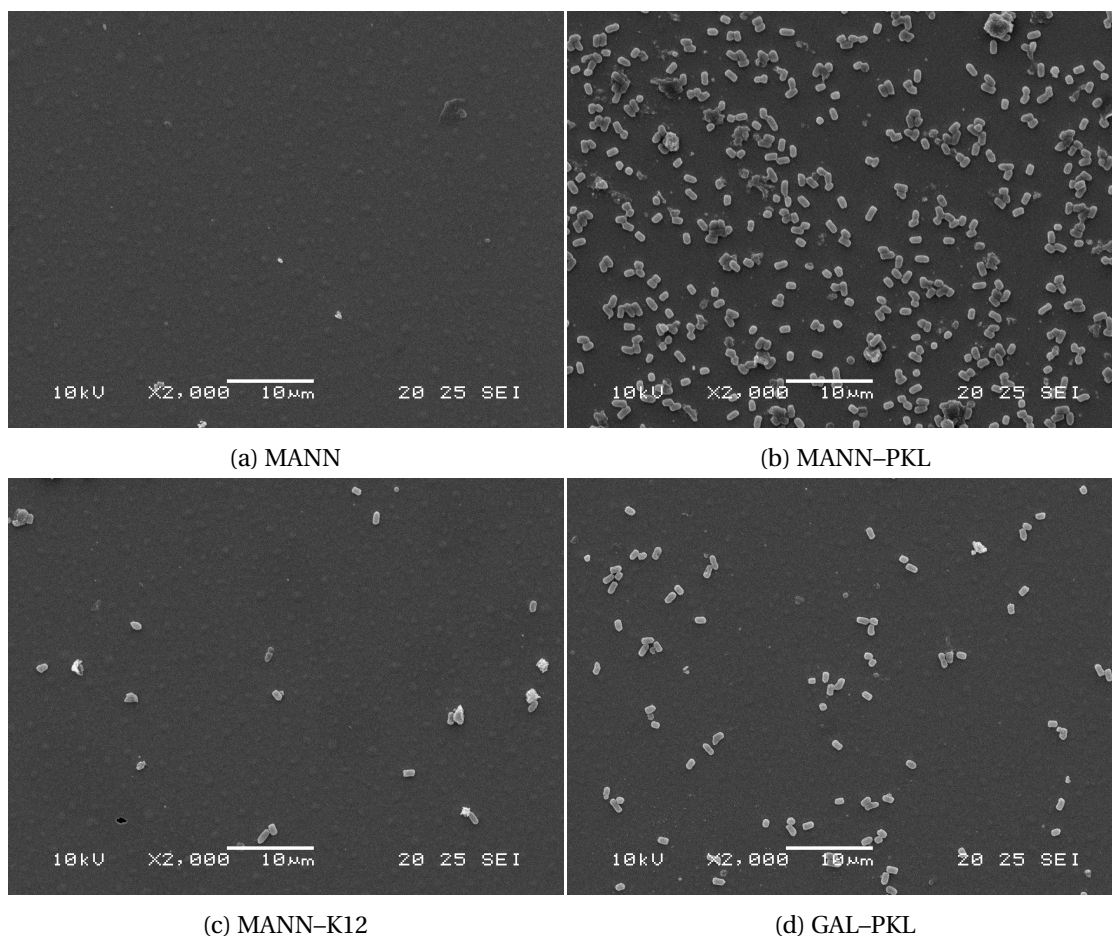


Figure 3.25: SEM images showing gold surfaces after immobilisation of different molecules used for the sugar–bacteria affinity capture assay.

3.3.4 Discussion

The principle of dielectric spectroscopy has been demonstrated using a dual-plate microgap sensor for the detection of *E. coli*. The use of a long PEG-terminated SAM proved to be highly effective in providing a good insulating layer prior to further functionalisation. In this system, increasing the ionic strength of the buffer was shown to increase the overall capacitance,

3.3. Dielectric spectroscopy measurements with a microgap sensor

caused by greater charge accumulation at the electrode–electrolyte interface. No clear benefit in terms of selectivity is provided by the use of a higher ionic strength buffer, but maybe more interesting is that it may allow capacitance changes to be more easily detected at higher frequencies due to the increased high-frequency permittivity of the buffer.

Further decreasing the interelectrode distance should improve sensitivity of the system as the EDLs would occupy a greater fraction of the sensor volume. However, it is important to highlight that for gap sizes smaller than the EDL, the potential at the electrode–electrolyte interface surface would decrease with decreasing ionic strength, while the potential at the centre of the gap increases. This has the benefit of reducing the potential difference and therefore the capacitance would increase with decreasing ionic strength (in contrast to gap sizes larger than the EDL). On the contrary, the accumulated charge at the electrode–electrolyte interface decreases, reducing the overall capacitance. One advantage of these two competing effects would be that the system capacitance would be less susceptible to ionic fluctuations.

Although the selectivity of the system was affected by non-specific interactions, the system does show clear sensitivity to changes in the dielectric properties of the biolayer. Considering the application of pre-screening samples, Formisano *et al.* recently demonstrated the use of MALDI-ToF MS for the same sugar–bacteria study and determined the limit of quantification as 2.7×10^9 CFU·mL⁻¹ [68]. Obviously the fingerprint given by techniques such as MALDI-ToF or PCR is essential for obtaining detailed information such as antimicrobial susceptibility, virulence and intra-species typing [69]. However, such evidence is only needed once the pathogenicity of a sample has been confirmed. An initial screening step utilising a low-cost direct electrochemical technique could prove an appealing option to optimise time and expense of the fingerprint assays.

The dual-plate microgap sensor offers advantages of being relatively simple to fabricate and can be easily used as part of a conventional four-electrode electrochemical cell. However, the device does present issues relating to the yield and control of the geometry. Some of these issues were addressed in related work by defining the electrode area by thermal evaporation [70] or by controlling the interelectrode spacing by spincoating an epoxy-based photoresist [71]. For biological studies involving the formation of functionalised probe layers and to allow a dose response to be undertaken it would be desirable to have the capacity to produce a batch of devices with repeatable and well-controlled geometry. Furthermore, reducing the interelectrode separation to the point of creating nanogap devices should increase sensitivity for both redox cycling and dielectric spectroscopy techniques.

References

- [1] S. E. C. Dale, A. Vuorema, M. Sillanpää, J. Weber, A. J. Wain, E. O. Barnes, R. G. Compton, and F. Marken. Nano-Litre Proton/Hydrogen Titration in a Dual-Plate Platinum-Platinum Generator-Collector Electrode Micro-Trench. *Electrochimica Acta*, 125:94–100, 2014.
- [2] S. M. Marino and V. N. Gladyshev. Analysis and functional prediction of reactive cysteine residues. *Journal of Biological Chemistry*, 287(7):4419–4425, 2012.
- [3] H. S. Chung, S. B. Wang, V. Venkatraman, C. I. Murray, and J. E. Van Eyk. Cysteine oxidative posttranslational modifications: Emerging regulation in the cardiovascular system. *Circulation Research*, 112(2):382–392, 2013.
- [4] D. P. Jones. Cysteine/cystine couple is a newly recognized node in the circuitry for biologic redox signaling and control. *The FASEB Journal*, 18:1246–1248, 2004.
- [5] C. E. Paulsen and K. S. Carroll. Cysteine-mediated redox signaling: chemistry, biology, and tools for discovery. *Chemical Reviews*, 113(7):4633–4679, 2013.
- [6] C. S. Sevier and C. A. Kaiser. Formation and transfer of disulphide bonds in living cells. *Nature Reviews Molecular Cell Biology*, 3(11):836–847, 2002.
- [7] A. Pastore, R. Massoud, C. Motti, A. Lo Russo, G. Fucci, C. Cortese, and G. Federici. Fully automated assay for total homocysteine, cysteine, cysteinylglycine, glutathione, cysteamine, and 2-mercaptopropionylglycine in plasma and urine. *Clinical Chemistry*, 44(4):825–832, 1998.
- [8] G. Salemi, M. C. Gueli, M. D’Amelio, V. Saia, P. Mangiapane, P. Aridon, P. Ragonese, and I. Lupo. Blood levels of homocysteine, cysteine, glutathione, folic acid, and vitamin B12 in the acute phase of atherothrombotic stroke. *Neurological Sciences*, 30(4):361–364, 2009.
- [9] Y. Özkan, S. Yardim-Akaydin, H. Firat, E. Çalışkan-Can, S. Ardiç, and B. Şimşek. Usefulness of homocysteine as a cancer marker: Total thiol compounds and folate levels in untreated lung cancer patients. *Anticancer Research*, 27(2):1185–1189, 2007.
- [10] H. Birwe and A. Hesse. High-performance liquid chromatographic determination of urinary cysteine and cystine. *Clinica Chimica Acta*, 199:33–42, 1991.

References

- [11] M. Guillén, D. Corella, M. L. Cabello, A. M. García, and J. Hernández-Yago. Reference values of urinary excretion of cystine and dibasic aminoacids: Classification of patients with cystinuria in the Valencian Community, Spain. *Clinical Biochemistry*, 32(1):25–30, 1999.
- [12] E. Bald, R. Glowacki, and J. Drzewoski. Determination by liquid chromatography of free and total cysteine in human urine in the form of its S-quinolinium derivative. *Journal of Chromatography A*, 913(1-2):319–329, 2001.
- [13] P. G. Winyard, C. J. Moody, and C. Jacob. Oxidative activation of antioxidant defence. *Trends in Biochemical Sciences*, 30(8):453–461, 2005.
- [14] N. Sumorok and D. S. Goldfarb. Update on cystinuria. *Current Opinion in Nephrology and Hypertension*, 22(4):427–431, 2013.
- [15] W. Hao, A. McBride, S. McBride, J. P. Gao, and Z. Y. Wang. Colorimetric and near-infrared fluorescence turn-on molecular probe for direct and highly selective detection of cysteine in human plasma. *Journal of Materials Chemistry*, 21(4):1040–1048, 2011.
- [16] X. Guan, B. Hoffman, C. Dwivedi, and D. P. Matthees. A simultaneous liquid chromatography/mass spectrometric assay of glutathione, cysteine, homocysteine and their disulfides in biological samples. *Journal of Pharmaceutical and Biomedical Analysis*, 31(2):251–261, 2003.
- [17] X. Chen, Y. Yang, and M. Ding. Electrocatalytic oxidation and sensitive detection of cysteine at layer-by-layer assembled carbon nanotube-modified electrode. *Analytica Chimica Acta*, 557(1-2):52–56, 2006.
- [18] T. R. Ralph, M. L. Hitchman, J. P. Millington, and F. C. Walsh. The electrochemistry of l-cystine and l-cysteine. *Journal of Electroanalytical Chemistry*, 375(1-2):1–15, 1994.
- [19] G. Hager and A. G. Brolo. Adsorption/desorption behaviour of cysteine and cystine in neutral and basic media: Electrochemical evidence for differing thiol and disulfide adsorption to a Au(1 1 1) single crystal electrode. *Journal of Electroanalytical Chemistry*, 550-551:291–301, 2003.
- [20] B. Monterroso-Marco. pH effect on cysteine and cystine behaviour at hanging mercury drop electrode. *Talanta*, 61(5):733–741, 2003.
- [21] T. R. Ralph, M. L. Hitchman, J. P. Millington, and F. C. Walsh. The reduction of l-cystine in hydrochloric acid at mercury drop electrodes. *Journal of Electroanalytical Chemistry*, 587(1):31–41, 2006.
- [22] T. R. Ralph, M. L. Hitchman, J. P. Millington, and F. C. Walsh. The reduction of l-cystine hydrochloride at stationary and rotating disc mercury electrodes. *Electrochimica Acta*, 51(1):133–145, 2005.

- [23] J. H. Zagal, M. J. Aguirre, C. G. Parodi, and J. Sturm. Electrocatalytic activity of vitamin B12 adsorbed on graphite electrode for the oxidation of cysteine and glutathione and the reduction of cystine. *Journal of Electroanalytical Chemistry*, 374(1):215–222, 1994.
- [24] D. Mimica, F. Bedioui, and J. H. Zagal. Reversibility of the l-cysteine/l-cystine redox process at physiological pH on graphite electrodes modified with coenzyme B12 and vitamin B12. *Electrochimica Acta*, 48(4):323–329, 2002.
- [25] L. G. Shaidarova, S. A. Ziganshina, A. V. Gedmina, I. A. Chelnokova, and G. K. Budnikov. Electrochemical behavior and voltammetric determination of cysteine and cystine at carbon-paste electrodes modified with metal phthalocyanines. *Journal of Analytical Chemistry*, 66(7):633–641, 2011.
- [26] C. Xiao, J. Chen, B. Liu, X. Chu, L. Wu, and S. Yao. Sensitive and selective electrochemical sensing of l-cysteine based on a caterpillar-like manganese dioxide–carbon nanocomposite. *Physical Chemistry Chemical Physics*, 13(4):1568–1574, 2011.
- [27] S. M. Chen, J. Y. Chen, and R. Thangamuthu. Electrochemical preparation of brilliant-blue-modified poly(diallyldimethylammonium chloride) and nafion-coated glassy carbon electrodes and their electrocatalytic behavior towards oxygen and L-cysteine. *Electroanalysis*, 20(14):1565–1573, 2008.
- [28] P. K. Sonkar, V. Ganesan, and V. Rao. Electrocatalytic Oxidation and Determination of Cysteine at Oxovanadium (IV) Salen Coated Electrodes. *International Journal of Electrochemistry*, 2014:1–6, 2014.
- [29] Z. Chen, H. Zheng, C. Lu, and Y. Zu. Oxidation of L-cysteine at a fluorosurfactant-modified gold electrode: Lower overpotential and higher selectivity. *Langmuir*, 23(21):10816–10822, 2007.
- [30] S. Fei, J. Chen, S. Yao, G. Deng, D. He, and Y. Kuang. Electrochemical behavior of L-cysteine and its detection at carbon nanotube electrode modified with platinum. *Analytical Biochemistry*, 339(1):29–35, 2005.
- [31] M. F. S. Teixeira, E. R. Dockal, and É. T. G. Cavalheiro. Sensor for cysteine based on oxovanadium(IV) complex of Salen modified carbon paste electrode. *Sensors and Actuators, B: Chemical*, 106(2):619–625, 2005.
- [32] J. C. Obirai and T. Nyokong. Thiol oxidation at 2-mercaptopyrimidine-appended cobalt phthalocyanine modified glassy carbon electrodes. *Journal of Electroanalytical Chemistry*, 600(2):251–256, 2007.
- [33] A. Salimi and S. Pourbeyram. Renewable sol–gel carbon ceramic electrodes modified with a Ru-complex for the amperometric detection of L-cysteine and glutathione. *Talanta*, 60(1):205–214, 2003.

References

- [34] N. Spătaru, B. V. Sarada, E. Popa, D. A. Tryk, and A. Fujishima. Voltammetric Determination of L-Cysteine at Conductive Diamond Electrodes. *Analytical Chemistry*, 73(3):514–519, 2001.
- [35] R. Drożdż, J. Naskalski, and A. Ząbek-Adamska. Potentiometric determination of cysteine with thiol sensitive silver-mercury electrode. *Acta Biochimica Polonica*, 54(1):205–211, 2007.
- [36] S. Shahrokhian. Lead phthalocyanine as a selective carrier for preparation of a cysteine-selective electrode. *Analytical Chemistry*, 73(24):5972–5978, 2001.
- [37] P. Dharmapandian, S. Rajesh, S. Rajasingh, A. Rajendran, and C. Karunakaran. Electrochemical cysteine biosensor based on the selective oxidase-peroxidase activities of copper, zinc superoxide dismutase. *Sensors and Actuators, B: Chemical*, 148(1):17–22, 2010.
- [38] M. Zhou, J. Ding, L. P. Guo, and Q. K. Shang. Electrochemical behavior of L-cysteine and its detection at ordered mesoporous carbon-modified glassy carbon electrode. *Analytical Chemistry*, 79(14):5328–5335, 2007.
- [39] Z. N. Gao, H. Q. Yao, and W. Y. Liu. Study on electrocatalytic oxidation of L-cysteine at glassy carbon electrode by (FcM)TMA and its electrochemical kinetics. *Electroanalysis*, 17(7):619–624, 2005.
- [40] C. A. Martínez-Huitle, C. Carlesi Jara, M. Cerro-Lopez, and M. A. Quiroz. Cu-doped polymeric-modified electrode for determination of cysteine. *Latin American Applied Research*, 40(1):47–51, 2010.
- [41] W. R. Fawcett, M. Fedurco, Z. Kováčová, and Z. Borkowska. Oxidation of cysteine, cysteinesulfinic acid and cysteic acid on a polycrystalline gold electrode. *Journal of Electroanalytical Chemistry*, 368(1):265–274, 1994.
- [42] A. J. Tudos, P. J. Vandeberg, and D. C. Johnson. Evaluation of Eqcm Data From a Study of Cysteine Adsorption on Cold Electrodes in Acidic Media. *Analytical Chemistry*, 67(3):552–556, 1995.
- [43] D. W. M. Arrigan and L. L. Bihan. A study of L-cysteine adsorption on gold via electrochemical desorption and copper(II) ion complexation. *The Analyst*, 124(11):1645–1649, 1999.
- [44] K. F. Babu, R. Sivasubramanian, M. Noel, and M. A. Kulandainathan. A homogeneous redox catalytic process for the paired synthesis of l-cysteine and l-cysteic acid from l-cystine. *Electrochimica Acta*, 56(27):9797–9801, 2011.
- [45] E. V. Milsom, J. Novak, M. Oyama, and F. Marken. Electrocatalytic oxidation of nitric oxide at TiO₂-Au nanocomposite film electrodes. *Electrochemistry Communications*, 9(3):436–442, 2007.

- [46] R. Di Felice and A. Selloni. Adsorption modes of cysteine on Au(111): Thiolate, amino-thiolate, disulfide. *Journal of Chemical Physics*, 120(10):4906–4914, 2004.
- [47] A. Abbaspour and A. Ghaffarinejad. Electrocatalytic oxidation of L-cysteine with a stable copper-cobalt hexacyanoferrate electrochemically modified carbon paste electrode. *Electrochimica Acta*, 53(22):6643–6650, 2008.
- [48] S. Kang, K. Mathwig, and S. G. Lemay. Response time of nanofluidic electrochemical sensors. *Lab on a Chip*, 12(7):1262, 2012.
- [49] K. Mathwig and S. G. Lemay. Mass transport in electrochemical nanogap sensors. *Electrochimica Acta*, 112:943–949, 2013.
- [50] E. Kätelhön, D. Mayer, M. Banzet, A. Offenhäusser, and B. Wolfrum. Nanocavity crossbar arrays for parallel electrochemical sensing on a chip. *Beilstein Journal of Nanotechnology*, 5(1):1137–1143, 2014.
- [51] H. du Toit and M. Di Lorenzo. Electrodeposited highly porous gold microelectrodes for the direct electrocatalytic oxidation of aqueous glucose. *Sensors and Actuators, B: Chemical*, 192:725–729, 2014.
- [52] J. S. Daniels and N. Pourmand. Label-Free Impedance Biosensors: Opportunities and Challenges. *Electroanalysis*, 19(12):1239–1257, 2007.
- [53] WHO and OECD. Assessing Microbial Safety of Drinking Water Improving Approaches and Methods. Technical report, 2004.
- [54] T.A. Oelschlaeger, U. Dobrindt, and J. Hacker. Pathogenicity islands of uropathogenic *E. coli* and the evolution of virulence. *International Journal of Antimicrobial Agents*, 19(6):517–521, 2002.
- [55] M. Hartmann and T. K. Lindhorst. The Bacterial Lectin FimH, a Target for Drug Discovery - Carbohydrate Inhibitors of Type 1 Fimbriae-Mediated Bacterial Adhesion. *European Journal of Organic Chemistry*, 2011(20-21):3583–3609, 2011.
- [56] A. Reisner, J. A. J. Haagensen, M. A. Schembri, E. L. Zechner, and S. Molin. Development and maturation of *Escherichia coli* K-12 biofilms. *Molecular Microbiology*, 48(4):933–46, 2003.
- [57] C. Berggren, B. Bjarnason, and G. Johansson. Capacitive Biosensors. *Electroanalysis*, 13(3):173–180, 2001.
- [58] Z. L. Zhi, N. Laurent, A. K. Powell, R. Karamanska, M. Fais, J. Voglmeir, A. Wright, J. M. Blackburn, P. R. Crocker, D. A. Russell, S. Flitsch, R. A. Field, and J. E. Turnbull. A versatile gold surface approach for fabrication and interrogation of glycoarrays. *ChemBioChem*, 9(10):1568–1575, 2008.

References

- [59] R. Šardžik, R. Sharma, S. Kaloo, J. Voglmeir, P. R. Crocker, and S. L. Flitsch. Chemoenzymatic synthesis of sialooligosaccharides on arrays for studies of cell surface adhesion. *Chemical Communications*, 47(19):5425, 2011.
- [60] M. Riepl, V. M. Mirsky, I. Novotny, V. Tvarozek, V. Rehacek, and O. S. Wolfbeis. Optimization of capacitive affinity sensors: Drift suppression and signal amplification. *Analytica Chimica Acta*, 392(1):77–84, 1999.
- [61] S. Carrara, V. Bhalla, C. Stagni, L. Benini, A. Ferretti, F. Valle, A. Gallotta, B. Riccò, and B. Samorì. Label-free cancer markers detection by capacitance biochip. *Sensors and Actuators B: Chemical*, 136(1):163–172, 2009.
- [62] B. W. Peterson, P. K. Sharma, H. C. van der Mei, and H. J. Busscher. Bacterial cell surface damage due to centrifugal compaction. *Applied and Environmental Microbiology*, 78(1):120–125, 2012.
- [63] N. Couniot, T. Vanzieleghem, J. Rasson, N. Van Overstraeten-Schlögel, O. Poncelet, J. Mahillon, L. A. Francis, and D. Flandre. Lytic enzymes as selectivity means for label-free, microfluidic and impedimetric detection of whole-cell bacteria using ALD-Al₂O₃ passivated microelectrodes. *Biosensors and Bioelectronics*, 67:154–161, 2015.
- [64] M. Yi, K. H. Jeong, and L. P. Lee. Theoretical and experimental study towards a nanogap dielectric biosensor. *Biosensors and Bioelectronics*, 20(7):1320–1326, 2005.
- [65] M. S. Mannoor, T. James, D. V. Ivanov, L. Beadling, and W. Braunlin. Nanogap dielectric spectroscopy for aptamer-based protein detection. *Biophysical Journal*, 98(4):724–732, 2010.
- [66] J. Hong, D. S. Yoon, M. I. Park, J. Choi, T. S. Kim, G. Im, S. Kim, Y. E. Pak, and K. No. A dielectric biosensor using the capacitance change with AC frequency integrated on glass substrates. *Japanese Journal of Applied Physics, Part 1: Regular Papers and Short Notes and Review Papers*, 43(8A):5639–5645, 2004.
- [67] Y. Yusof, K. Sugimoto, H. Ozawa, S. Uno, and K. Nakazato. On-chip Microelectrode Capacitance Measurement for Biosensing Applications. *Japanese Journal of Applied Physics*, 49(1):01AG05–1–01AG05–5, 2010.
- [68] N. Formisano, N. Bhalla, M. Heeran, J. Reyes Martinez, A. Sarkar, M. Laabei, P. Jolly, C. R. Bowen, J. T. Taylor, S. Flitsch, and P. Estrela. Inexpensive and fast pathogenic bacteria screening using field-effect transistors. *Biosensors and Bioelectronics*, 85:103–109, 2016.
- [69] X. Didelot, R. Bowden, D. J. Wilson, T. E. A. Peto, and D. W. Crook. Transforming clinical microbiology with bacterial genome sequencing. *Nature Reviews Genetics*, 13(9):601–612, 2012.

- [70] M. Li, S. Y. Xu, A. J. Gross, J. L. Hammond, P. Estrela, J. Weber, K. Lacina, T. D. James, and F. Marken. Ferrocene-Boronic Acid-Fructose Binding Based on Dual-Plate Generator-Collector Voltammetry and Square-Wave Voltammetry. *ChemElectroChem*, 2(6):867–871, 2015.
- [71] H. M. Harvey, A. J. Gross, P. Brooksby, A. J. Downard, S. J. Green, C. P. Winlove, N. Benjamin, P. G. Winyard, M. Whiteman, J. L. Hammond, P. Estrela, and F. Marken. Boron-Doped Diamond Dual-Plate Deep-Microtrench Device for Generator-Collector Sulfide Sensing. *Electroanalysis*, 27(11):2645–2653, 2015.

4 Fabrication of a Large Area Vertical Coplanar Nanogap Device

This chapter covers the design and fabrication of a large area vertical coplanar nanogap device. Existing fabrication techniques used to create vertical nanogaps are reviewed before discussing some alternative approaches. The adopted methodology is then explained before presenting the fabrication process.

The large area vertical coplanar nanogap device is based on etching a channel in a silicon substrate using inductively-coupled plasma reactive ion etching to achieve precisely controlled depths. This channel is then used to bury a passivation layer and lower metallic electrode. The upper metallic electrode is then patterned on a glass substrate before the two sensor halves are anodically bonded together. Laser micromachined apertures in both the silicon and glass provide access to electrical contact pads whilst the glass substrate also has circular holes for microfluidic connections.

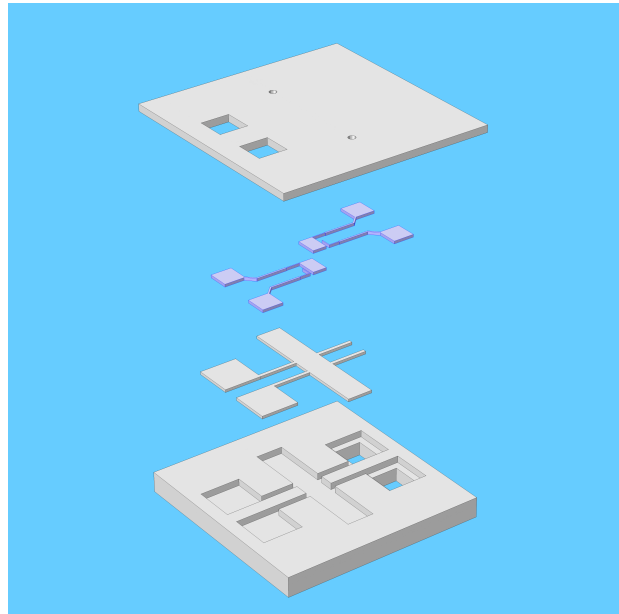


Figure 4.1: 3D exploded diagram of the vertical coplanar nanogap device showing silicon substrate, silicon nitride and electrode layers (highlighted) and glass substrate.

The fabrication method for the dual-plate microgap sensors employed in Chapter 3 provided a relatively simple and affordable way to build microgap sensors. However, it suffered from complications such as scalability of production (limited to around 1 device every 24 hours),

limited control of geometry (aspect ratios varied from 2 to 36) and limited control and range of interelectrode separation (2 μm to 62 μm). The following attributes were desired for the next device generation:

- precise control of submicron interelectrode separation;
- large electrode surface area;
- high reproducibility;
- integrated microfluidics;
- and dual-plate geometry.

For amperometric detection the current response is related to the electrode area and interelectrode spacing as $I_{\text{lim}} \propto \frac{A}{x}$ where A is the electrode area and x is the separation between the electrodes. Clearly the sensor response can be increased with larger electrode areas and/or by decreasing the interelectrode spacing. Importantly, increasing the surface area creates a greater sensor volume and this leads to improved molar sensitivity. For many sensing applications this is often more important than simply providing maximum amplification of a very small number of molecules. A dual-plate geometry is also desirable as it minimises fringing effects and provides a predominantly planar diffusive flux and electric field, simplifying analysis and maximising sensitivity.

The main issue associated with dielectric spectroscopy sensing is overcoming the screening effect caused by the electric double layer (EDL). This can be achieved by reducing the interelectrode spacing in order to minimise potential drop across the EDL or by reducing the ionic concentration of the sample medium. This results in the electric double layers occupying a greater fraction of the sensing volume. However, for many biological samples the ionic concentration cannot be reduced without causing adverse effects to the analyte or biorecognition layer. Increasing the electrode area not only reduces the proportional contribution of fringing effects, but also provides a capacity to increase probe loading, ensuring that probe spacing can be optimised to minimise steric hindrance and maximising the number of detection sites.

In order to achieve nanometre separation and the other desired features a different approach is needed. Micro- and nanofabrication techniques offer several broad benefits including, in principle: well-developed protocols that provide highly reproducible results; wide selection of characterisation techniques available at each fabrication step, allowing protocols to be optimised for high yield; reduced requirement to characterise every device due to the high reproducibility of the optimised protocol; and the capacity to scale the process for mass-production including integration of CMOS circuitry and/or sample handling. Nevertheless, it is important to emphasise that there are drawbacks with adopting micro- and/or nanofabrication practices. The processes often require highly specialised and sophisticated equipment and the need for a clean room environment. Then there is the time-consuming nature of developing and/or optimising non-standard protocols along with characterising the processes so that adjustments in the procedure can be understood.

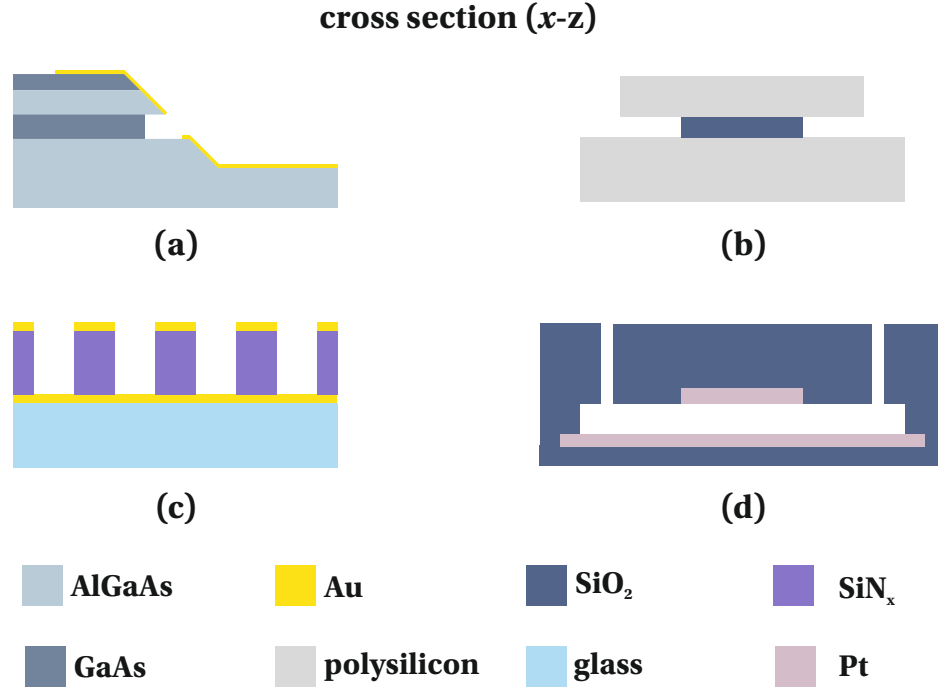


Figure 4.2: Diagram demonstrating some of the geometries used to obtain vertical nanogaps: (a) use of a sacrificial layer within a mesa structure then angled deposition; (b) etching a sacrificial layer to create a deep undercut; (c) formation of nanopores with plane-recessed disc electrodes using nanosphere templates; and (d) etching a sacrificial layer to form an encapsulated cavity.

4.1 Present fabrication techniques for vertical nanogap devices

Whilst vertical nanogap devices existed as early as 1986, they were in the guise of the scanning electrochemical microscope (SECM) [1,2]. However, such a platform does not lend itself to miniaturisation. Nevertheless, with improvements in access to microfabrication facilities, many researchers have developed new methods to fabricate vertical coplanar nanogaps. Some examples of the techniques are illustrated in Figure 4.2. Many of these methods take advantage of thin film deposition/growth on account of the controlled precision of layer thickness that can be achieved during the fabrication process, and the wide range of available wet and dry etch processes that have been well characterised over the years.

Sacrificial etch in a mesa structure followed by angled deposition

One technique is the use of a sacrificial etch to create a cavity within the sidewall of a ‘mesa’ structure followed by angled deposition of the metallic layers. For example, Krahne *et al.* [3]

used molecular beam epitaxy to grow GaAs between two AlGaAs layers. Using a citric acid/hydrogen peroxide wet etch the GaAs layer could be etched with a selectivity of around 100:1 (GaAs:AlGaAs). Metallic electrodes are then deposited using an angled deposition step. In similar fashion, Strobel *et al.* [4] used reactive ion etching (RIE) of a silicon-on-insulator (SOI) substrate with buried silicon dioxide layer to create the mesa structure. The intermediate silicon dioxide layer was then partially etched to create a recess. Next, the surfaces are thermally oxidised before an angled deposition step to create a metallic vertically orientated nanogap in the exposed sidewall. Schukfeh *et al.* [5] also used this approach but replaced the RIE step with an anisotropic wet etch to form the mesa structure. Another alternative was demonstrated by Van Megen *et al.*, whereby the low stress properties of silicon rich nitride was utilised to create an overhanging ridge on a mesa structure followed by evaporation to create ≈ 100 nm vertically separated Au electrodes [6].

Etching of a vertical stack to create ring–ring structures

Pairs of ring–ring electrodes separated by an insulating layer can be fabricated by etching down through a vertical stack. As an example Lee *et al.* [7] used a 550 nm parylene layer to vertically separate two Au electrodes. The vertical nanogap was then created by wet etching down through both gold layers with a low-frequency plasma step for 1 hour to remove the parylene film. Han *et al.* developed a similar geometry, but used a focussed ion beam (FIB) milling step to etch through the gold and insulating silicon nitride (SiN_x) layers [8].

Etching of a vertical stack to form nanoporous plane-recessed disc structures

As a slight deviation to the ring–ring geometry, nanoporous structures with a plane-recessed disc geometry can be fabricated by maintaining the lower electrode layer. Neugebauer [9, 10] and Lohmüller [11] from the Stelzle group used nanosphere lithography to create 200–800 nm pores (typically 500 nm) in a $\text{Au/Si}_3\text{N}_4/\text{Au}$ stack with 100–200 nm interelectrode separation. The group of Bohn also adopted this technique using polystyrene nanospheres to reduce the typical pore diameter down to 250 nm [12–15].

Very high density nanoporous structures with this geometry, created with electron-beam lithography (EBL), has since been demonstrated by Hüske *et al.* [16]. With the capabilities of EBL processing electrode separation of ≈ 100 nm and pore radii of ≈ 50 nm has typically been achieved. Hüske *et al.* [17] also demonstrated how a nanoporous alumina template could be anodised to form a TiO_2 capped structure before depositing the upper metallic layer and electrodepositing an insulating polymer at the base of the pore to complete fabrication. This further reduced the obtainable pore radii down to ≈ 20 nm and removed the serial EBL processing step.

Sacrificial etch to create deep sidewall cavities

Groups from the University of California, Berkeley created 1 electrode, and later, an array of 5 electrodes with deep sidewall cavities by selectively etching a thermally grown silicon dioxide sacrificial layer, undercutting the upper electrode by $1.5\ \mu\text{m}$ to form $<300\ \text{nm}$ nanocavities between doped polysilicon electrodes [18, 19]. Using the same methodology, Jang *et al.* [20] exploited atomic layer deposition (ALD) of Al_2O_3 to form thinner, but precisely controlled sacrificial layers between two Au electrodes. A buffered HF etch was then used to laterally etch the Al_2O_3 , however the selectivity of the etch process creates significantly limits the depth of the sidewall cavity. Okay *et al.* later progressed the design by creating an array of these electrodes for biotin–streptavidin binding studies and significantly improved the undercut to $\approx 500\ \text{nm}$ [21].

Naturally the deep sidewall cavities progressed into ring–ring nanocavities, whereby a Cr sacrificial layer is etched between either ring–ring or ring–disc metallic electrodes. This technique allows microwells to be incorporated into the design and has been used by the Matsue group to evaluate electrochemical activity of embryoid bodies [22] and by Chen *et al.* to study the effects of electrostatics on ion transport within the electrochemical cell [23].

Sacrificial etch to form encapsulated cavities

The Lemay group pioneered the technique of creating an encapsulated nanocavity by etching a Cr sacrificial layer between two metallic electrodes [24]. This technique can not only provide the optimal parallel-plate geometry, but can also provide an integrated nanofluidic channel. This technique has been extensively used by the groups of Lemay, Wolfrum (originally Lemay) and Rassaei (originally Lemay) [25–45].

One drawback of the technique of these encapsulated devices is that complete removal of the sacrificial layer and any residues becomes extremely difficult for larger areas without causing collapse. Furthermore, without judicious choice of material or geometry any residual stress in the top electrode can lead to buckling, altering the interelectrode spacing along the nanochannel. This severely restricts the surface area that can be achieved, thus, demonstrated devices have typical electrode areas of $25\ \mu\text{m}^2$ to $300\ \mu\text{m}^2$ [42]. One way to increase the total sensing area is to create arrays of these electrodes, as demonstrated by Kätelhön *et al.* with the crossbar array consisting of two orthogonal sets of 16 parallel bars to create a total overlapping area of $1.68 \times 10^{-16}\ \text{m}^2$ [40].

Another non-ideal feature is that these devices feature an asymmetric geometry, with the lower electrode spanning a greater distance than the upper electrode to retain device integrity. For instance, Zevenbergen reports dimensions of $40\ \mu\text{m} \times 1.5\ \mu\text{m}$ ($60\ \mu\text{m}^2$) and $10.0\ \mu\text{m} \times 2.5\ \mu\text{m}$ ($25\ \mu\text{m}^2$) for the lower and upper electrodes, respectively [26]. This asymmetry typically leads

to a 'dead' volume of up to 40% [35]. Whilst these devices provide enough amplification to detect a few hundred molecules, the small volume (<100 fL) of the active region of the device limits their molar sensitivity, which is often more important than the amplification factor in many sensing applications.

4.2 Alternative fabrication techniques for vertical nanogap devices

4.2.1 SU-8 as a sacrificial layer/adhesive

Initial attempts in this work involved the use of an epoxy-based SU-8 photoresist. SU-8 is a popular photoresist for high aspect ratio and three dimensional photolithography providing favourable material properties such as high chemical and mechanical stability [46], high dielectric strength [47] and optical transparency.

Researchers have successfully demonstrated that SU-8 that is not fully cross-linked can be used as a sacrificial layer to create cavities between floor and ceiling structures. Specifically, Chung and Allen demonstrated $5\text{ }\mu\text{m}$ to $250\text{ }\mu\text{m}$ separation between a silicon substrate and suspended $3\text{ mm} \times 250\text{ }\mu\text{m}$ NiFe electrodes [48]. Given this success, the first attempt in the current work involved the use of SU-8 that is not cross-linked as a sacrificial layer.

The first prototype device consisted of a lower Au electrode patterned on a glass substrate using standard photolithography followed by spincoating a 500 nm SU-8 insulating layer (SU-8 2002 [MicroChem] diluted with cyclopentanone to produce SU-8 2000.5). Regions of the SU-8 layer were then exposed to form partially cross-linked support blocks but not fully developed, leaving a central $50\text{ }\mu\text{m} \times 100\text{ }\mu\text{m}$ unexposed region that is not cross-linked, therefore acting as the sacrificial layer. Next the Au layer of the upper electrode was thermally evaporated and a thicker SU-8 2010 layer was spincoated and patterned to simultaneously act as an etch mask for the upper electrode as well as to provide structural rigidity. The Au was wet etched to pattern the upper electrode and any remaining SU-8 structures that are not cross-linked are fully developed. Unfortunately the devices were highly prone to collapse, even after increasing the thickness of the final SU-8 layer to $30\text{ }\mu\text{m}$ in an attempt to improve structural integrity.

The second failed attempt involved the use of SU-8 as an adhesive layer. SU-8 derives its name from the presence of 8 epoxy groups and is sometimes referred to generally as a 'photodefinable epoxy'. It has been used to bond different substrates together for a range of applications and provides bond strengths typically between approximately 5 MPa and 20 MPa [49]. However, the film thickness used for these applications is typically around $10\text{--}100\text{ }\mu\text{m}$ [49, 50]. Svasek *et al.* did investigate thinner films ($1\text{--}15\text{ }\mu\text{m}$) for $44.1\text{ mm} \times 4.4\text{ mm}$ microfluidic mixers with integrated capillary electrophoresis devices but reported significant decrease in the yield ($\approx 30\%$, 20 of 62 devices) for an SU-8 thickness of $4.0\text{ }\mu\text{m}$ [51]. It was expected that the bond strength of even thinner films ($<1\text{ }\mu\text{m}$) could present an issue so a high contact force during

bonding would be needed as per the recommendation by Svasek *et al.*.

For the second prototype device, large (1.0 mm × 1.5 mm) Au electrodes were optically patterned on ultra-flat quartz glass substrates. A diluted 1.0 μm SU-8 film (SU-8 2001) was then spincoated onto one of the substrates, softbaked, exposed and developed whilst maintaining the SU-8 below the glass transition temperature of 65 °C. Then the second substrate was aligned and a force (≈ 2 kN) applied whilst performing the hardbake. The device was then placed in a Perspex[®] jig to minimise stresses during electrical testing. The bond quality of the device was very poor with many of the devices becoming misaligned as the substrates slipped. Tests conducted to determine whether the bond strength could be improved by bonding the two substrates at a different point in the SU-8 crosslinking process (*i.e.*, softbake, exposure, hardbake) offered no significant improvement.

4.2.2 Wafer bonding

Wafer bonding to form MEMS devices is not a new concept. Often a wafer bonding process is used to form hermetically sealed devices to trap various gases at specified operating pressures with integrated CMOS circuitry [52]. There exist many different wafer bonding techniques such as: adhesive [53], anodic [54], eutectic [55], fusion [56], thermocompression [57], transient liquid phase [58] and ultrasonic [59]. These bonding techniques provide different suitability to the end application depending on alignment precision, particle sensitivity, process temperature and surface roughness [60]. The anodic bonding technique was selected as it does not require a special intermediate bonding layer and provides a simple, relatively low temperature uniform bonding between glass and silicon.

Anodic bonding

Anodic bonding accounts for the majority of all packaging applications for MEMS, with silicon–glass anodic bonding being the most prominent. Anodic bonding provides a significant advantage over other bonding techniques in that it can tolerate rougher surfaces and is less sensitive to particles. However, no examples of wafer bonding to achieve vertical coplanar electrodes were found in literature. Even though anodic bonding was first developed in 1968 and published in scientific literature in 1969 [61], the bonding mechanism is mainly only quantitatively understood.

The mechanism for silicon–glass bonding is illustrated in Figure 4.3. A DC voltage is applied between heated silicon and glass (with glass held at a negative potential) so that positive alkali ions in the glass (Na^+ and K^+) are displaced to form a depletion layer at the interface. Oxygen anions drifting towards the silicon lead to the formation of an oxide layer. At the start of the process the surface roughness of the two surfaces results in intimate contact at only a few

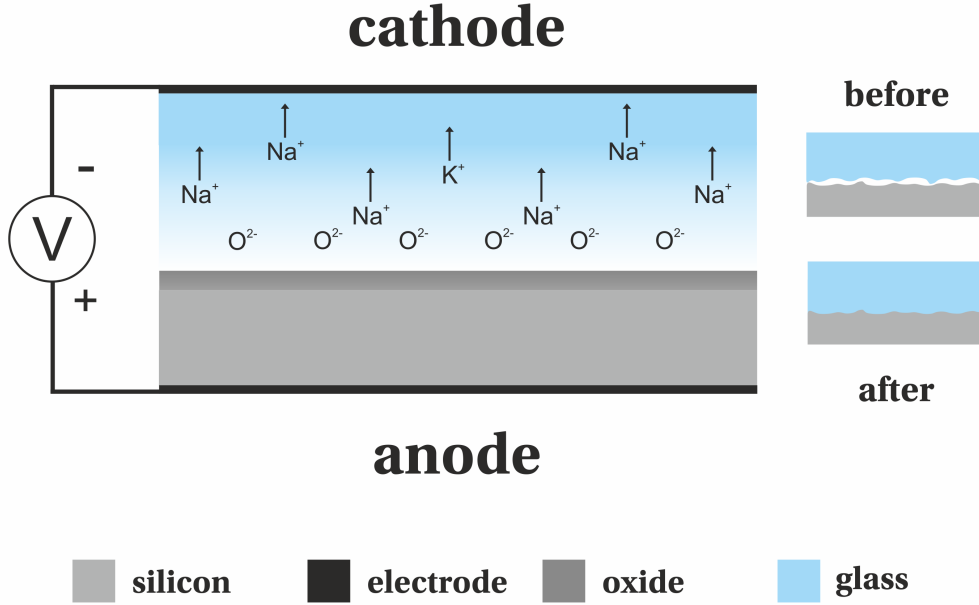


Figure 4.3: Diagram demonstrating the mechanism of silicon–glass anodic bonding.

locations, with the rest of the surface separated by a small gap. This can be visualised by the abundance of interference fringes across the surfaces. The electric field at the interface is very high ($\text{MV}\cdot\text{cm}^{-1}$) and largest at the periphery of points in intimate contact. The electrostatic forces act to pull adjacent surfaces together, slowly leading to migration of the bonding front and the disappearance of interference fringes [62].

The attractive force per unit area of interface can be considered as an electrostatic pressure (P_e), given by Equation 4.1 [63]. Where ϵ_0 is the permittivity of free space, ϕ is the potential difference across the air gap of adjacent surfaces, separated by a distance x and \mathbf{E} is the local electrostatic field in the gap:

$$P_e = \frac{1}{2}\epsilon_0 \frac{\phi^2}{x^2} = \frac{1}{2}\epsilon_0 \mathbf{E}^2 \quad (4.1)$$

The chemical reactions that take place at the interface result in the oxidation of the silicon and hence permanent bonds between the two substrates. There is no general agreement on the chemistry of the interface reactions but the formation of thin oxide layer has been experimentally proven [62]. The resultant bond is often much stronger than the glass or silicon itself, with measured values varying between 5 MPa and 25 MPa [64].

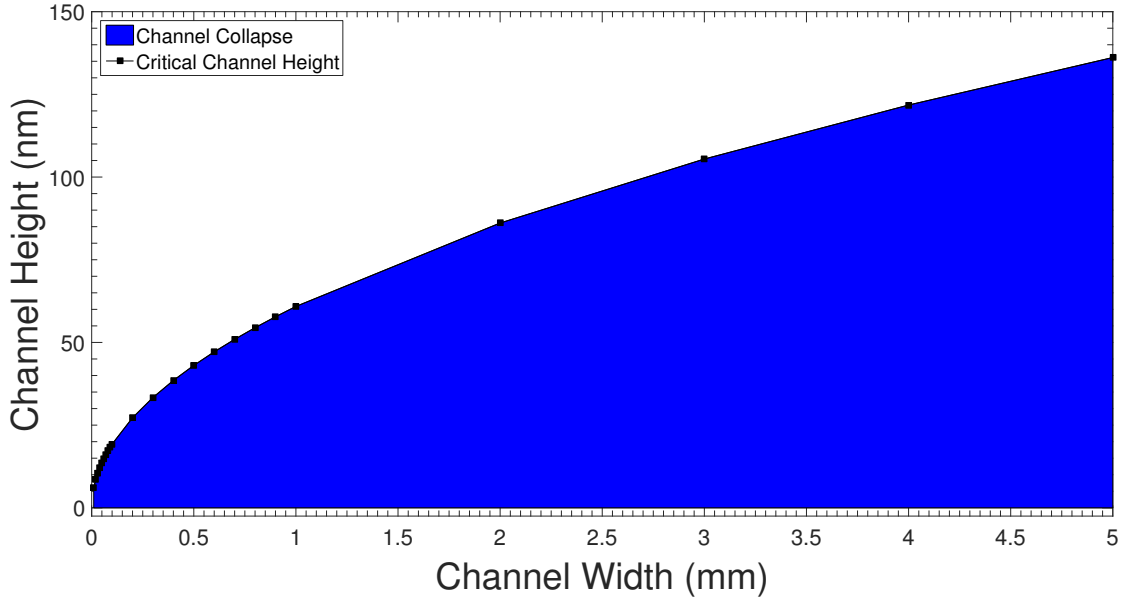


Figure 4.4: Calculated critical channel heights (h_c) for a range of channel widths (w).

From Equation 4.1, and assuming the temperature is great enough to provide sufficient ion mobility, it is clear that applying greater voltages or reducing the separation between the silicon and glass surfaces (*i.e.*, increasing the area of intimate contact) will result in increased electrostatic pressure and therefore faster and more successful bonding. However, sealing of nanochannels with anodic bonding means that careful control of the voltage is required to prevent channel collapse [65–67].

The criteria to predict whether a channel will collapse during bonding of wafers of different thickness and/or material is given by the equation developed by Tong & Gösele [68]:

$$h_c = 2.6 \sqrt{\frac{w\gamma}{4}} \times \sqrt{\left(\frac{1}{E_1} + \frac{1}{E_2}\right)} \quad (4.2)$$

Where h_c is the critical channel height [m] and channel collapse occurs when $h < h_c$, w is the channel width [m], γ is the surface energy density [$\text{J}\cdot\text{m}^{-2}$] and E is the Young's modulus [Pa]. Using a value* of $100 \text{ mJ}\cdot\text{m}^{-2}$ for γ , $E_1 = 165 \text{ GPa}$ for silicon and $E_2 = 64 \text{ GPa}$ for borosilicate glass it is calculated that for a 2 mm wide channel, collapse will occur for channel heights less than $\approx 85 \text{ nm}$. Figure 4.4 shows the critical heights for channel widths ranging from $10 \mu\text{m}$ to 5 mm calculated using MATLAB.

Choice of wafer materials can also affect the bonding process. Bowing of the bonded device can

*Typical values of γ are $100 \text{ mJ}\cdot\text{m}^{-2}$ and $20 \text{ mJ}\cdot\text{m}^{-2}$ for hydrophilic and hydrophobic surfaces, respectively [67].

be minimised by closely matching the thermal expansion coefficient of the chosen glass with that of the silicon substrate [69, 70]. Corning's Pyrex® 7740 and SCHOTT's BOROFLOAT® 33 glasses have been widely adopted for use with anodic bonding [62, 71] due to their high alkali content ($\approx 4\%$) and lower thermal expansion coefficients ($\approx 3.2 \times 10^{-6} \text{ K}^{-1}$), similar to that of silicon ($\approx 2.6 \times 10^{-6} \text{ K}^{-1}$). The efficacy of the silicon–glass anodic bonding process is then maximised with $\langle 100 \rangle$ orientated p-type silicon as the silicon substrate as shown by the extensive study by Lee *et al.* [72].

4.2.3 Prototype device and pilot tests for anodic bonding

A prototype device was designed to allow some basic pilot tests of the anodic bonding process to be carried out. The prototype device uses KOH wet etching to define two raised blocks ($3.0 \text{ mm} \times 5.5 \text{ mm}$) in a silicon substrate to form an 800 nm deep central channel ($2.0 \text{ mm} \times 5.5 \text{ mm}$). In this channel a large sensing electrode ($1.0 \text{ mm} \times 1.5 \text{ mm}$) and auxiliary electrode ($100 \mu\text{m} \times 1.5 \text{ mm}$), passivated by a SiO_2 layer, are patterned using lift-off photolithography. On a separate glass substrate an identical stack of $\text{SiO}_2/\text{Ti}/\text{Au}$ (45 nm/5 nm/100 nm) are again patterned using lift-off photolithography. The two substrates are then brought into intimate contact before anodic bonding to create a 500 nm interelectrode spacing. The key steps of the fabrication process are outlined in Figure 4.5 and the processing parameters in Table 4.1.

Silicon etching

First an AZ® nLOF 2070 ($2.0 \mu\text{m}$) photoresist lift-off mask is patterned using photolithography as per steps 1a-1h of Table 4.1. Samples were then mounted onto glass microscope slides using MICROPOSIT™ S183 photoresist. A 115 nm Cr layer was then deposited using thermal evaporation ($0.5 \text{ nm}\cdot\text{s}^{-1}$ at 90 A) and lift-off performed in MICROPOSIT™ Remover PR1165. Next, the silicon was etched using an optimised anisotropic KOH process (18.5 g : 50.0 g, KOH:H₂O) at 60 °C on a hotplate with thermocouple control and agitated with a magnetic stirrer at 500 rpm for 170 seconds.

The channel depth was measured as $799.6 \text{ nm} \pm 2.9 \text{ nm}$ using a mechanical profilometer [Dektak 8, Veeco], equating to an etch rate of $4.70 \text{ nm}\cdot\text{s}^{-1}$. The etch rate was non-linear (varying from $3.17 \text{ nm}\cdot\text{s}^{-1}$ to $4.70 \text{ nm}\cdot\text{s}^{-1}$ for durations of 100 s to 170 s), however this may be improved by slowing the etch rate either by increasing the KOH content or lowering the temperature [73]. Due to the anisotropic nature of the KOH etch, an angled sidewall with a 54.74° angle between the $\langle 111 \rangle$ and $\langle 100 \rangle$ planes is developed. Using the trigonometric identity $\tan(\phi) = \frac{\text{opp}}{\text{adj}}$, and taking an etch depth of 800 nm the lateral distance is calculated as 677 nm. This means that the channel width is reduced by $<1.5 \mu\text{m}$ which can be considered negligible. The selectivity of the KOH was measured as 32:1 (Si:Cr), confirming the suitability of Cr as an etch mask. The Cr was then removed in Cr etchant [MicroChemicals] at room

4.2. Alternative fabrication techniques for vertical nanogap devices

temperature (RT). Several samples required an elevated temperature of $\approx 50^\circ\text{C}$ to completely remove the Cr layer.

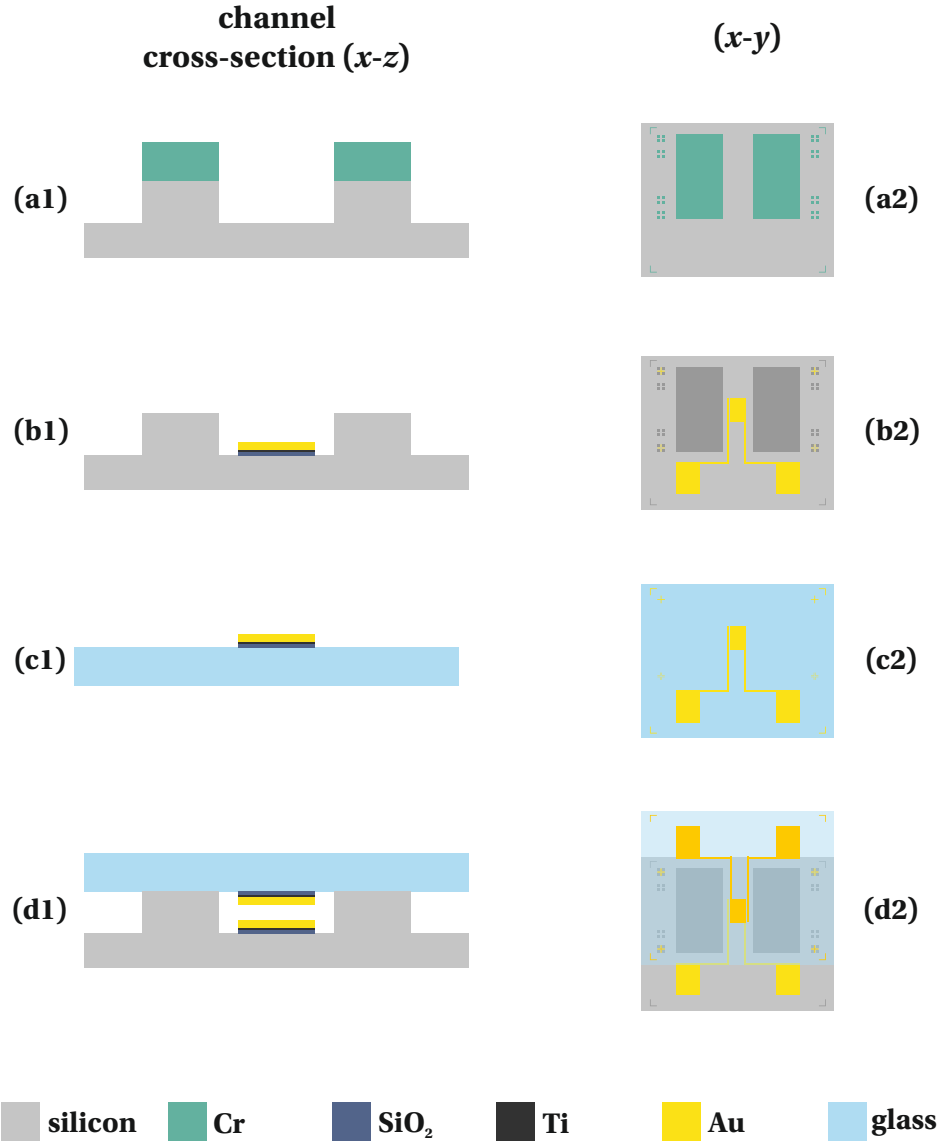


Figure 4.5: Fabrication process of the prototype vertical nanogap sensor. (a): A Cr layer is patterned by lift-off photolithography on the silicon substrate to act as an etch mask for KOH etching a submicron channel. (b): The Cr mask is removed in Cr etchant then a stack of SiO₂/Ti/Au, forming the passivation and electrode layers, is deposited using electron-beam evaporation and patterned using lift-off photolithography. (c): On a separate borosilicate glass substrate an identical stack of SiO₂/Ti/Au is also patterned using lift-off lithography. (d): Finally the two halves of the device are anodically bonded.

Table 4.1: Process parameters for the prototype device fabrication.

Step	Description
1a	Clean substrates: acetone & IPA rinse, N ₂ dry
1b	Dehydration bake in oven, 30 min at 90 °C
1c	Spincoat AZ [®] nLOF 2070 (2.0 μm), 5 s at 500 rpm, 100 rpm·s ⁻¹ , 30 s at 3000 rpm, 10,000 rpm·s ⁻¹
1d	Softbake on hotplate, 2 min at 110 °C
1e	Exposure, 10 s at ≈6.5 mW·cm ² (365 nm) [Karl Süss MJB3]
1f	Post-exposure bake on hotplate, 1 min at 110 °C
1g	Manual agitation in AZ [®] 826 MIF developer, 60 s at RT
1h	DI water rinse, N ₂ dry
2a	Thermal evaporation of Cr hard mask (115 nm, 0.5 nm·s ⁻¹ at 90 A, $P = < 1.0 \times 10^{-6}$ mbar)
2b	Lift-off in MICROPOSIT [™] PR1165 Remover, 5 min at 65 °C
3a	Etch silicon in KOH:H ₂ O (18.5:50, wt.) 170 s on a hotplate at 60 °C, stirring at 500 rpm, quench in DI water
3b	DI water rinse, N ₂ dry
4a	Remove Cr in Cr etchant on a hotplate at 50 °C, quench in DI water
4b	DI water rinse, N ₂ dry
5a	Clean substrates: acetone & IPA rinse, N ₂ dry
5b	Dehydration bake in oven, 30 min at 90 °C
5c	Spincoat AZ [®] nLOF 2070 (2.0 μm), 5 s at 500 rpm, 100 rpm·s ⁻¹ , 30 s at 3000 rpm, 10,000 rpm·s ⁻¹
5d	Softbake on hotplate, 2 min at 110 °C
5e	Exposure, 10 s at ≈6.5 mW·cm ² (365 nm) [Karl Süss MJB3]
5f	Post-exposure bake on hotplate, 1 min at 110 °C
5g	Manual agitation in AZ [®] 826 MIF developer, 60 s at RT
5h	DI water rinse, N ₂ dry
6a	Electron-beam evaporation of SiO ₂ passivation layer (45 nm, 0.15 nm·s ⁻¹ at 5.0 kV, 15 mA)
6b	Electron-beam evaporation of electrode layer Ti (5 nm, 0.1 nm·s ⁻¹ at 5.0 kV, 85 mA) and Au (100 nm, 0.2 nm·s ⁻¹ at 5.0 kV, 100 mA)
6c	Lift-off in MICROPOSIT [™] PR1165 Remover, 5 min at 65 °C
6d	Ultrasonic agitation (50%) in MICROPOSIT [™] PR1165 Remover, 5 min at 65 °C
6e	Ultrasonic agitation (50%) in acetone, 5 min at RT
6f	Rinse in acetone then in IPA, N ₂ dry
7a	Surface activation in H ₂ SO ₄ , H ₂ O ₂ (5:1, vol.), 10 min at RT
7b	Align and apply pressure to create prebond
8	Anodically bond at 250 V, in a tube furnace at 300 °C, <1 h

Electrode layers

Electrodes were patterned on the etched silicon and glass samples using lift-off masks prepared as per steps 5a-5h of Table 4.1. A stack of SiO₂ (45 nm), Ti (5 nm) and Au (100 nm) were deposited using electron-beam evaporation to form the passivation and electrode layers

4.2. Alternative fabrication techniques for vertical nanogap devices

without breaking vacuum and lift-off performed in MICROPOSIT™ PR1165 Remover with ultrasonic agitation [steps 6a-6f of Table 4.1].

Anodic bonding

First surface activation was carried out using Piranha solution ($\text{H}_2\text{SO}_4:\text{H}_2\text{O}_2$, 5:1, vol.) for 10 minutes to provide increased hydroxyl groups ($-\text{OH}$). This improves the van der Waals forces and provides a 'prebond' between the two surfaces. The prebonded device is then mounted between two steel plates clamped together with alumina bolts. The steel clamp is transferred to a tube furnace [Carbolite] preheated to 300°C and connected to a N5751 high voltage DC power supply [Agilent Technologies] by wires insulated with alumina feedthroughs. The device is then left for 5 minutes to allow the temperature to settle and for the power supply to autozero. A voltage of 250 V is applied between the prebonded device with the glass connected to the negative terminal and the current measured using a data-logging U1282A digital multimeter [Keysight]. Typical peak currents of $2.65\ \mu\text{A}$ were recorded with a bonding time of 40 minutes. The peak current density was calculated to be $\approx 0.08\ \mu\text{A}\cdot\text{mm}^{-2}$.

Figure 4.6 shows an anodically bonded device with the channel partially collapsed along the centreline. The fringing fields show the areas in intimate contact and can be seen to emanate from areas that have been bonded. It can also be seen that unsupported regions of glass on the perimeter are very prone to undergo bonding and could be leading to channel collapse.

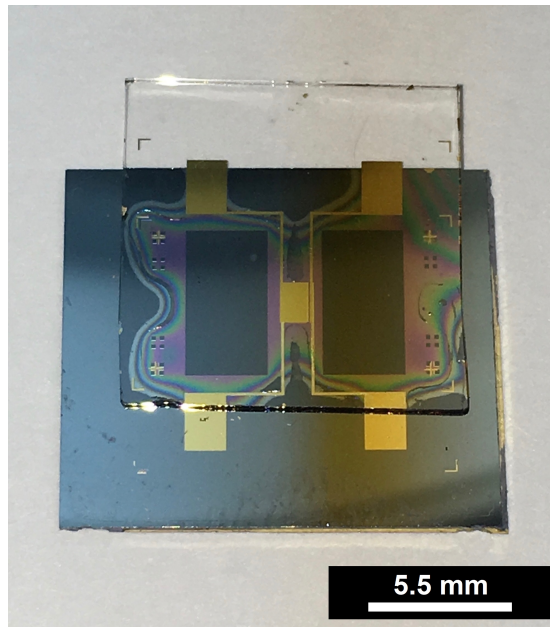


Figure 4.6: Optical image showing one of the prototype devices after unsuccessful anodic bonding.

To reduce the likelihood of channel collapse a revised design should minimise the area of unsupported glass. This should stop the bond front propagating towards the channel during anodic bonding. The prototype device used an overhang of the silicon and glass substrates to provide access to electrical contact pads, however this overhang appears to also contribute to the undesirable bonding. One way to resolve both of these issues is to encapsulate the electrodes and contact pads within the channel. This would provide increased support of the glass substrate and also reduce stress on the device when making external electrical connections. An enclosed channel also provides a way to incorporate a fluidic channel for sample delivery. One drawback of this approach is that access to the electrical contact pads and fluidic connections becomes non-trivial.

The electrodes of the prototype device were isolated from the silicon substrate by using an electron-beam deposited SiO_2 layer. This layer was patterned simultaneously with the Ti and Au layers using the same lift-off mask to reduce the number of processing steps. However, if a separate step is added the passivation layer can be extended to cover the floor of the channel. This would act to reduce the electric field across the channel, reducing the electrostatic pressure and therefore should reduce the likelihood of channel collapse.

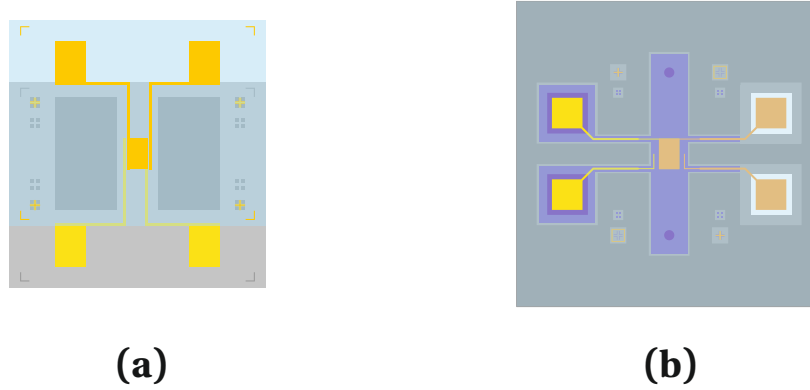


Figure 4.7: Comparison of the geometry for (a) the prototype and (b) the revised design.

4.3 Revised fabrication process

The anodic bonding trials performed with the prototype device highlighted several aspects that needed to be addressed. In this section a revised design is adopted and a detailed fabrication process is provided. Key changes include: altering the etch mask to provide a greater elevated area surrounding the etched channel; replacing the KOH wet etch with a more precise inductively-coupled plasma reactive ion etching (ICP-RIE) process; and increasing the extent of the passivation layer. The result is a more robust device, less susceptible to channel collapse during bonding and with an integrated fluidic channel.

Figure 4.7 shows the prototype and revised devices. The size of the sensing electrodes is maintained at $1.0 \text{ mm} \times 1.5 \text{ mm}$, however the area of all the connecting wires exposed to the fluidic flow is now significantly reduced by connecting them perpendicular to the channel. A greater border area is created around the channel and contact pads, providing a much greater area void of features that can be used for sample handling during the fabrication process. The total size of the silicon substrate is increased from a size of $12.5 \text{ mm} \times 11.0 \text{ mm}$ to $15 \text{ mm} \times 15 \text{ mm}$, with the elevated area surrounding the channel increased from 33 mm^2 to 161 mm^2 . The elevated area now accounts for 71.5% of the die area compared to around 24.0% of the prototype design. Completely encapsulating the electrodes between the silicon and glass substrates now creates a definitive rectangular ($2 \text{ mm} \times 10 \text{ mm}$) fluidic channel.

The key steps of the fabrication sequence are outlined in Figure 4.8. In brief, the fabrication process consists of laser micromachining (LMM), inductively-coupled plasma reactive ion etching (ICP-RIE), plasma-enhanced chemical vapour deposition (PECVD), lift-off photolithography and anodic bonding. These steps are discussed further in the following subsections.

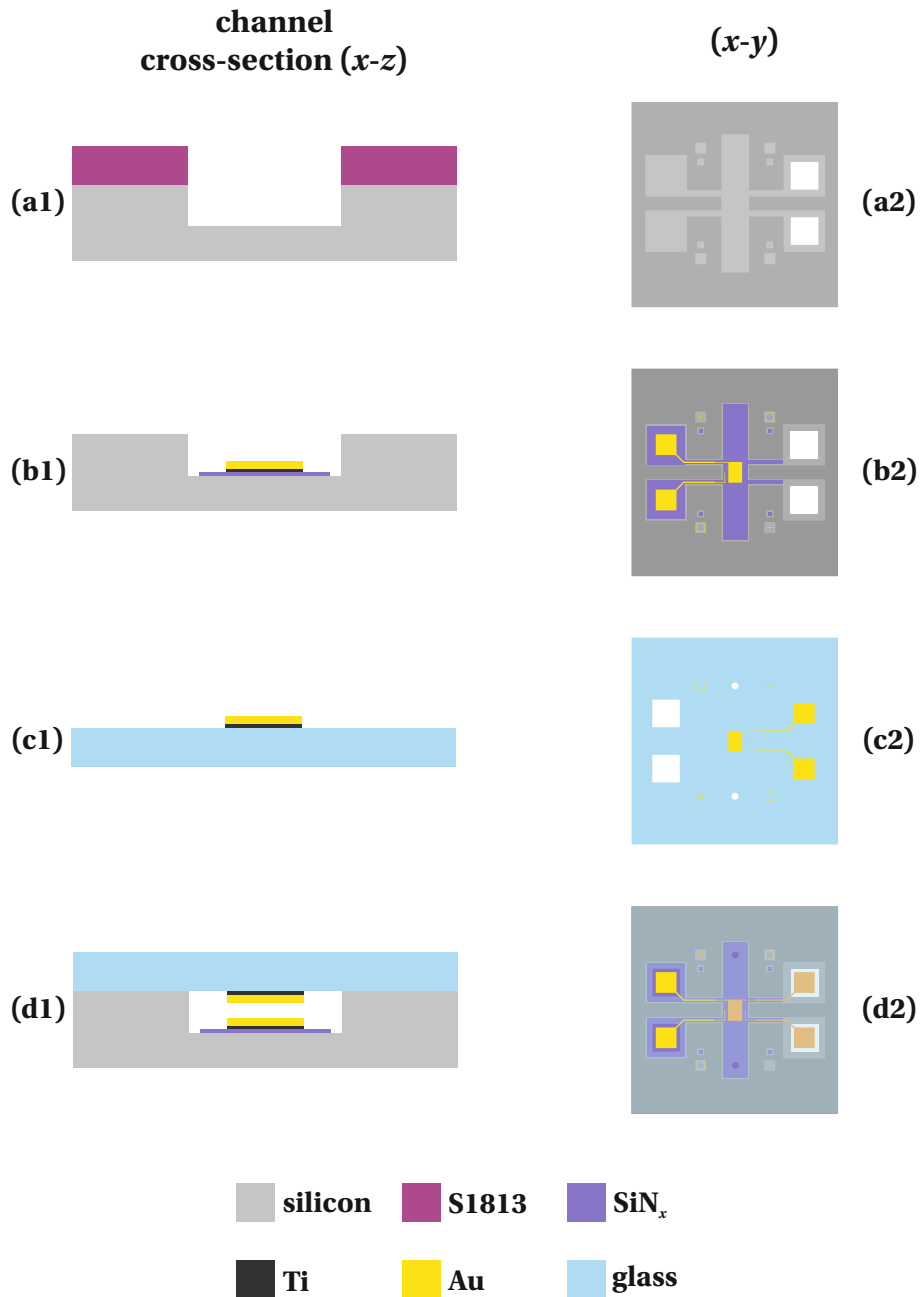


Figure 4.8: Fabrication process of the vertical nanogap sensor. (a): A photoresist layer is patterned on a silicon substrate to provide an etch mask before inductively-coupled plasma reactive ion etching a submicron channel. (b): A silicon nitride passivation layer is grown using plasma-enhanced chemical vapour deposition (PECVD) before patterning the lower metallic electrodes using lift-off photolithography. (c): On a separate borosilicate glass substrate the upper electrodes are patterned using lift-off photolithography. (d): Finally the two halves of the device are pretreated and anodically bonded.

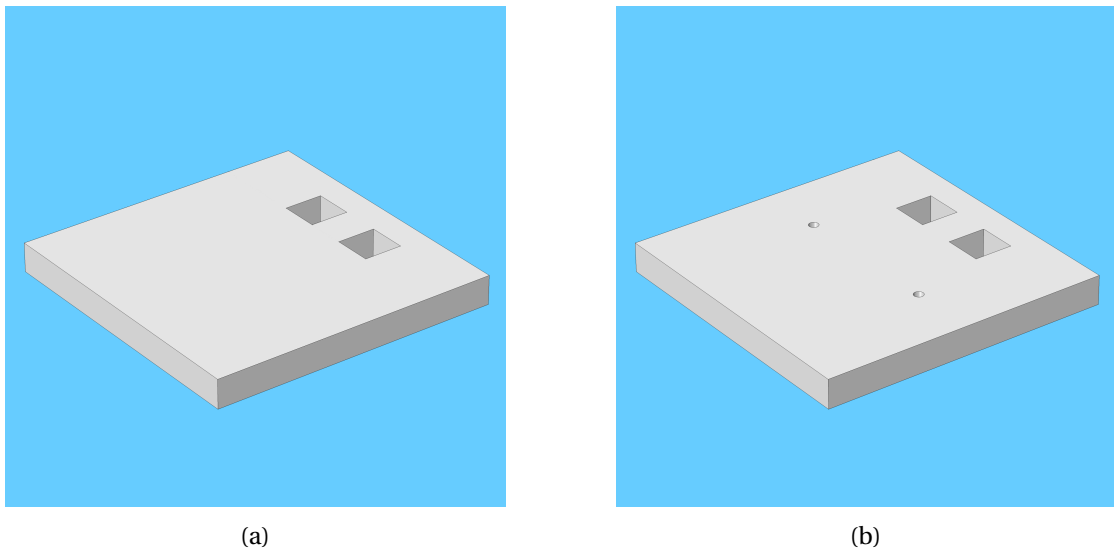


Figure 4.9: 3D diagram showing the prepared (a) silicon and (b) glass substrates.

4.3.1 Substrate preparation

Wafer dicing

3" silicon wafers (p-type (boron), (100), $380\ \mu\text{m} \pm 50\ \mu\text{m}$, $1\text{-}10\ \Omega\cdot\text{cm}$, single-side polished) [PI-KEM] were diced into $15\ \text{mm} \times 15\ \text{mm}$ dies by manual scribing with a Karl Süss HR-100 manual scriber and cleaving. 3" BOROFLOAT® 33 glass wafers ($500\ \mu\text{m} \pm 25\ \mu\text{m}$, double-side polished) [PI-KEM] were mounted on dicing tape and diced into $15\ \text{mm} \times 15\ \text{mm}$ dies using a MicroAce 66 semi-automatic wafer saw [LoadPoint]. All the dies were then rinsed in acetone then IPA to remove debris and placed in acetone then IPA with ultrasonic agitation (100 %) for 10 minutes. They were then rinsed with acetone then IPA, dried with N_2 and stored in membrane boxes.

Laser micromachining

Laser micromachining (LMM) offers high geometrical accuracy, alignment between features and surface integrity of machined features. For small to medium scale production, LMM offers a flexible and efficient process chain capable of rapid, single-process fabrication when compared to alternatives [74]. LMM was used to provide access to the four electrical contact pads and the fluidic channel of the final device and was conducted by Dr. Pavel Penchev at the University of Birmingham with a Lasea LS5 multi-axis laser equipped with a Satsuma femtosecond laser (5 W) and a MOPA-based Yb fibre laser (50 W). Two large square apertures ($2\ \text{mm} \times 2\ \text{mm}$) were created in both the silicon and glass substrate to provide access to the electrical contact pad of the electrodes on the opposing substrate. Then two circular

apertures with a radius of $500\ \mu\text{m}$, separated by a distance of 8 mm were also created in the glass substrate to provide access to the $2\ \text{mm} \times 10\ \text{mm}$ fluidic channel.

Cleaning

After LMM the dies were rinsed in acetone then IPA to remove immediate debris and placed in acetone then IPA with ultrasonic agitation (100 %) for 5 minutes. The dies were then rinsed with acetone then IPA and dried with N_2 . To ensure any remaining residues were removed the substrates were then cleaned in Piranha solution ($\text{H}_2\text{SO}_4:\text{H}_2\text{O}_2$, 5:1, vol.) for 10 minutes followed by a DI water rinse and N_2 dry and stored until further use.

4.3.2 Silicon etching

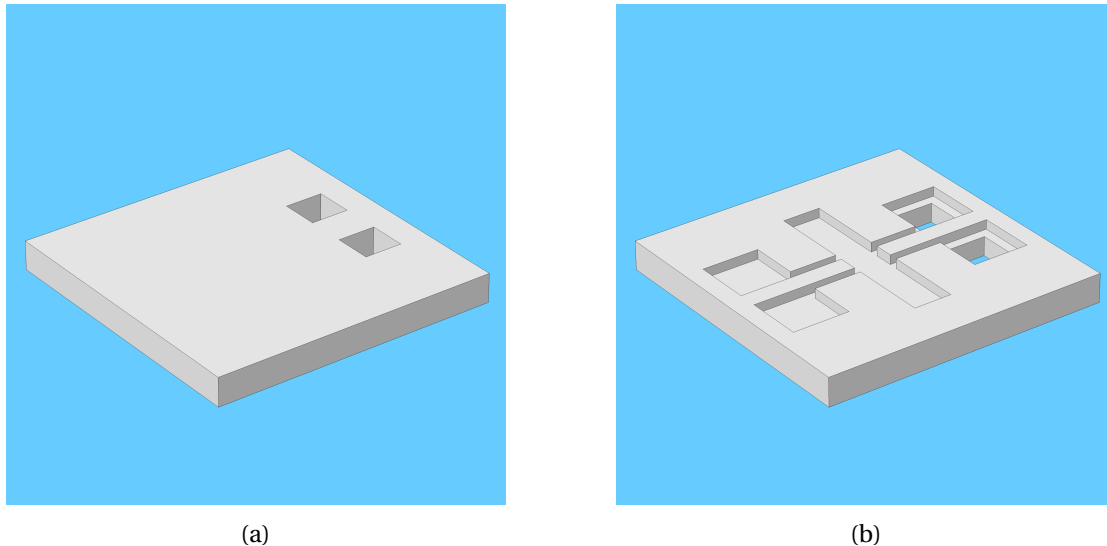


Figure 4.10: 3D diagram showing the substrate (a) before and (b) after channel formation.

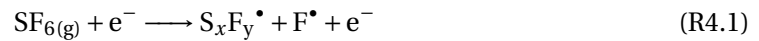
ICP-RIE

For the prototype device a liquid-phase ‘wet’ KOH etch process was used to create the channel in the silicon substrate. Because the reaction is stopped by quenching in DI water, slight deviations in the etch duration between batches may arise. The etch rate was found to be nonlinear making it difficult to accurately predict the etch depth of different etch durations. To provide improved control, a ‘dry’ etch process was investigated. In dry etching, plasmas or etchant gasses are used to remove substrate material by physical bombardment with high kinetic energy particles, chemical reactions or both. One of the most diverse and widely used processes in industry and research is reactive ion etching (RIE) whereby a chemically reactive plasma is used in both physical and chemical mechanisms.

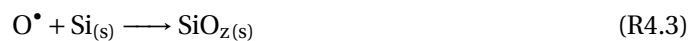
Most RIE systems generate a plasma by applying a strong RF electromagnetic field between an upper and lower electrode in the chamber. The oscillating field ionises gas molecules by stripping them of electrons, creating the plasma. A negative self-bias develops on the lower electrode due to an accumulation of electrons and creates an electric field that drives positive ions in the plasma towards the substrate. The ions react with the surface of the substrate as well as sputter material due to their kinetic energy. The mostly vertical motion of the reactive ions often leads to highly anisotropic etch profiles.

An evolution of the RIE system is the inductively-coupled plasma (ICP) RIE (ICP-RIE) system, where the plasma is generated inductively via a coil wrapped around the RIE chamber. This arrangement provides independent control of the ion density and other plasma properties without significantly affecting the incident energy of the ions which is controlled by RIE configuration.

In this work a SF_6/O_2 chemistry was used to etch the silicon channel. Fluorine-based chemistries are widely adopted for silicon etching [75, 76]. The addition of oxygen allows deep channels to be formed by protecting the sidewalls to provide highly anisotropic etch profiles with rapid etch rates [77, 78]. The formation of ion and radical species by electron impact disassociation are outlined in Reactions R4.1 and R4.2:



The role of oxygen is to passivate the silicon surface (specifically to protect the sidewalls) by reacting with the silicon to form an oxide layer:



The surface passivation layer is then removed by the plasma, where the ion bombardment plays a critical role by enhancing the adsorption, reaction and desorption:

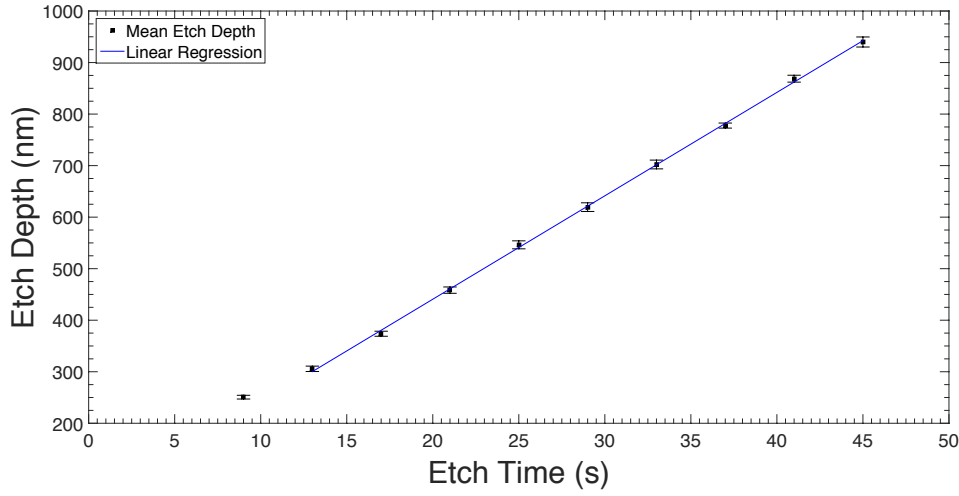
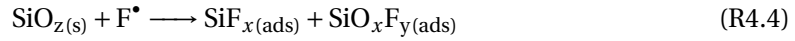
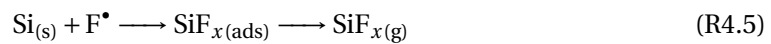


Figure 4.11: Channel depth as a function of time for SF_6/O_2 ICP-RIE. Error bars indicate $\pm\sigma$, $n = 5$.



The fluorine radical then proceeds to etch the silicon by adsorption, product formation then desorption:



Trials were conducted to characterise the etch rates for a range of etch durations. 15 mm × 15 mm silicon dies without laser micromachined features were patterned with a MICROPOSIT™ 351 photoresist etch mask as per the parameters outlined in Table 4.2. A total of 11 different durations were tested with 5 samples spread across the carrier wafer. The depth of the channel was found to be a linear function of the etch duration as shown by Figure 4.11.

The etch rate is calculated to be $20.9 \text{ nm}\cdot\text{s}^{-1}$ for $t_s + t = 45 \text{ s}$, where t_s is the duration of the plasma stabilisation step and t is the duration of the second step. The stabilisation step consists of an elevated power for a duration of 8 seconds and leads to slightly increased rates for shorter durations. Nevertheless, altering the duration provides a relatively simple way of tuning the electrode separation and it is envisaged that more precise control could be obtained

Table 4.2: Process parameters for etching the channel in silicon.

Step	Description
1a	Clean substrates: acetone & IPA rinse, N ₂ dry
1b	Dehydration bake on hotplate, 5 min at 200 °C
1c	Spincoat MICROPOSIT™ S1813, 5 s at 500 rpm, 100 rpm·s ⁻¹ , 30 s at 4000 rpm, 10,000 rpm·s ⁻¹
1d	Softbake on hotplate, 3 min at 100 °C
1e	Exposure, 15 s at 8.8-10.5 mW·cm ² (365 nm) [Karl Süss MJB3]
1f	Manual agitation in AZ® 826 MIF developer, 50 s at RT, quench in DI water
1g	DI water rinse, N ₂ dry
1h	Hardbake in oven 30 min at 90 °C
2a	Clean ICP-RIE chamber and carrier wafer using O ₂ chemistry, 30 min
2b	ICP-RIE using SF ₆ /O ₂ chemistry, 8 s at 1300 W, 33 s at 1200 W
2c	Remove MICROPOSIT™ S1813 in acetone bath, ≈60 s
2d	Rinse in acetone then IPA, N ₂ dry

Table 4.3: ICP-RIE parameters used to characterise the effect of etch duration.

Parameter	Value
SF ₆ flow rate	50 SCCM
O ₂ flow rate	8 SCCM
He backing flow rate	5 SCCM
Operating pressure	10 mTorr
Substrate temperature	0.0 °C
RF power	90 W
ICP power (stabilisation)	1300 W, $t_s = 8$ s
ICP power	1200 W

by reducing the power.

Substrates were then processed using the same parameters as those in Table 4.3 but with a total etch duration of 43 seconds ($t_s = 8$ s, $t = 35$ s). The processing steps are outlined in Table 4.2. Profilometry data of 15 samples provided a mean value of 900.8 nm \pm 4.3 nm, $n = 35$, with four of the dies measured at six positions. The etch rate is calculated as 20.95 nm·s⁻¹. Figure 4.12 shows a typical surface profile across the channel wall, demonstrating the flatness achieved from the ICP-RIE process.

One advantage of this process is that even though the etch depth could be reliably controlled, it can be quickly confirmed using mechanical profilometry. The thickness of passivation and electrode layers can then be adjusted to account for the over/under etch to provide the target interelectrode distance. Deviations between batches was generally acceptable (<10 nm total), particularly larger gap sizes, and very small for samples etched during the same process. Adjustments can therefore be made to batches and in some instances, for groups of similar batches.

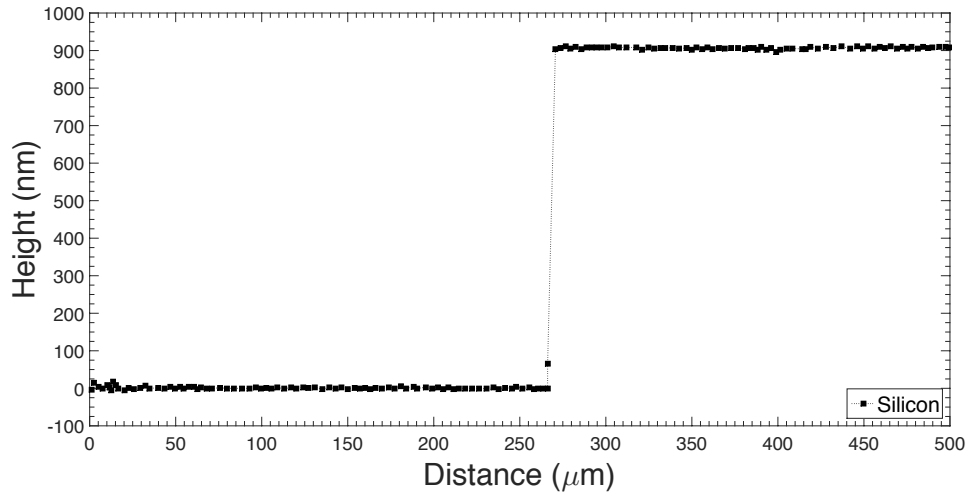


Figure 4.12: Profilometer data showing the 900 nm deep silicon channel.

4.3.3 Passivation layer

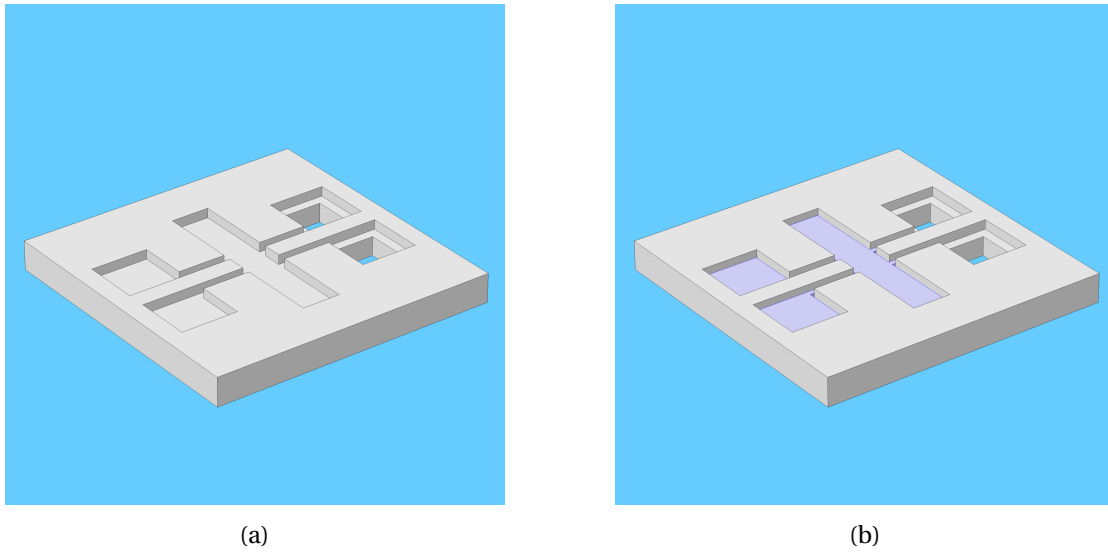


Figure 4.13: 3D diagram showing the substrate (a) before and (b) after patterning the silicon nitride passivation layer.

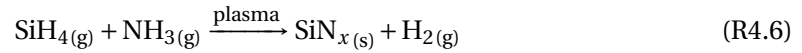
PECVD of SiN_x

Silicon nitride (SiN_x) is used as the passivation material as it provides an excellent high density insulating surface with excellent chemical resistance [79–81]. Using plasma-enhanced chemical vapour deposition (PECVD), SiN_x can be deposited at low temperatures (*e.g.*, below the melting point of Au), allowing passivation of pre-patterned metallic layers and with fast

Table 4.4: PECVD parameters for SiN_x deposition.

Parameter	Value
Substrate temperature	300 °C
Operating pressure	1750 mTorr
SiH ₄ flow rate	250 SCCM
NH ₃ flow rate	5 SCCM
RF power	50 W
Deposition time	4 × 60 s
Deposition rate	0.42-0.50 nm·s ⁻¹

deposition rates whilst maintaining film quality. The silicon nitride deposition was achieved using a silane (SiH₄) and ammonia (NH₃) chemistry as per the reaction:



A multi-layer deposition process was used to provide superior passivation properties. Yota [82] has previously demonstrated that multi-layer deposited SiN_x films deposited by PECVD at 300 °C exhibited significantly higher dielectric breakdown voltage and lower leakage current characteristics compared to single layer films. A major advantage is that pinhole defects present in a specific layer are usually covered by overlying and subsequent layers, reducing charge leakage. A 50 nm multi-layer SiN_x film should provide a leakage density less than $1 \times 10^{-15} \text{ A} \cdot \mu\text{m}^{-2}$ for voltages below 20 V, with breakdown occurring at $\approx 55 \text{ V}$ [82].

PECVD was performed using a 790 series system [Plasma-Therm]. Prior to loading the samples the PECVD system is first cleaned using a SF₆/N₂O chemistry before performing a SiN_x ‘dedication run’. The native silicon oxide is then removed from the silicon substrates using a 5:1 (NH₄F:HF) buffered oxide etch (BOE) and immediately loaded onto the chuck of the PECVD system. Multi-step PECVD of SiN_x is then performed using the parameters outlined in Table 4.4. After forming the SiN_x layer a MICROPOSITTM S1813 photoresist etch mask is defined using standard contact photolithography. The SiN_x layer is then patterned using a 5:1 BOE before removing the etch mask in acetone. The full process is described in Table 4.5.

One issue attributed to the use of a wet etchant is that undercutting of photoresist can lead to line edge roughness (LER) as the etchant etches beyond the intended limits. The main cause of this is usually poor adhesion between the substrate and photoresist or poor contact during exposure. Figure 4.14a shows an optical microscope image of the SiN_x surface achieved for the majority of samples after BOE etching and photoresist removal.

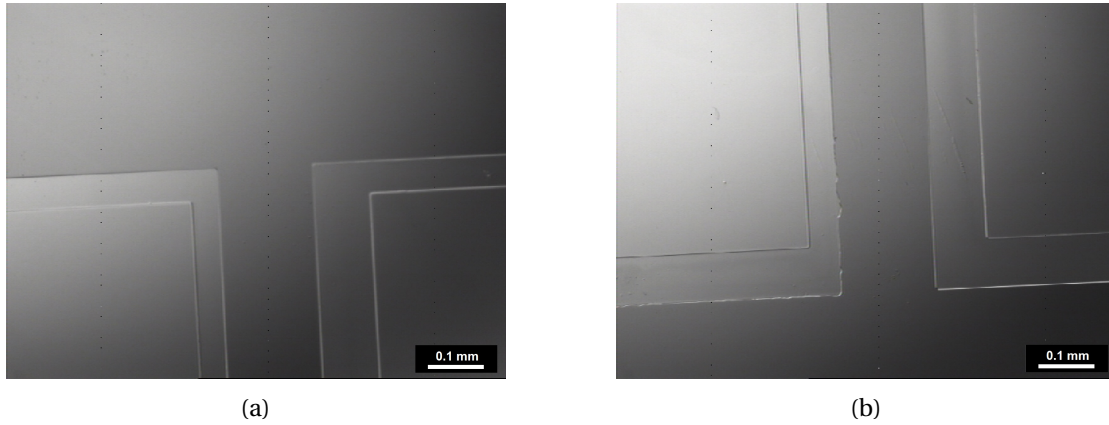


Figure 4.14: Optical images showing the buffered oxide etched SiN_x passivation layer after photoresist removal: (a) without defects; (b) and with minor edge defects caused by undercutting of the photoresist mask.

Table 4.5: Process parameters for patterning the SiN_x passivation layer.

Step	Description
1a	Clean PECVD chamber with $\text{SF}_6/\text{N}_2\text{O}$ chemistry
1b	Perform SiN_x dedication run
2a	Clean substrates: $\text{H}_2\text{SO}_4:\text{H}_2\text{O}_2$ (5:1, vol.), 5 min at RT
2b	Rinse in DI water, N_2 dry
2c	Remove native oxide in BOE (5:1, vol.), 3 min at RT, quench in DI water
2d	Rinse in DI water, N_2 dry
3a	Load samples into PECVD chamber
3b	Multi-step deposition of SiN_x by PECVD, 4×60 s, 100 nm target
3c	Unload samples from PECVD chamber
4a	Spincoat MICROPOSIT TM S1813, 5 s at 500 rpm, 100 rpm·s ⁻¹ , 30 s at 4000 rpm, 10,000 rpm·s ⁻¹
4b	Softbake on hotplate, 3 min at 100 °C
4c	Exposure, 15 s at 8.5 mW·cm ² (365 nm) [Karl Süss MJB3]
4d	Manual agitation in MICROPOSIT TM 351 developer, 50 s at RT
4e	Hardbake in oven, 30 min at 90 °C
5a	BOE (5:1, vol.) etch, 5 min at RT, quench in DI water
5b	Rinse in DI water, N_2 dry
6a	Remove MICROPOSIT TM S1813 in acetone bath, ≈ 60 s
6b	Rinse in acetone then IPA, N_2 dry

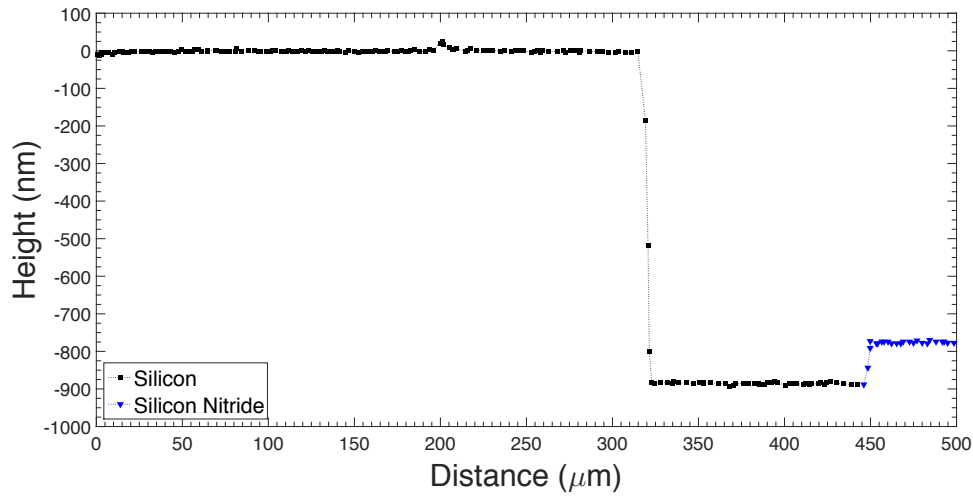


Figure 4.15: Profilometer data showing a 900 nm silicon channel with a 110 nm silicon nitride passivation layer.

A few samples exhibited rather extensive undercutting and therefore LER, as shown by Figure 4.14b. Fortunately, the design of this device mitigates the majority of issues related to this type of defect as well as alignment issues. It is expected that a more stringent cleaning protocol and/or a dehydration bake between the SiN_x deposition and spincoating the MICROPOSITTM S1813 photoresist mask may alleviate this issue.

After patterning the SiN_x passivation layer the film thickness was measured as $110.4 \text{ nm} \pm 2.2 \text{ nm}$ ($n = 10$), which was $\approx 10 \text{ nm}$ above the target thickness of 100 nm. As previously mentioned, this discrepancy can be easily measured using mechanical profilometry and accounted for by adjusting the thickness of the electrode layer. A typical surface profile is shown in Figure 4.15, demonstrating the flatness of both the Si and SiN_x surfaces.

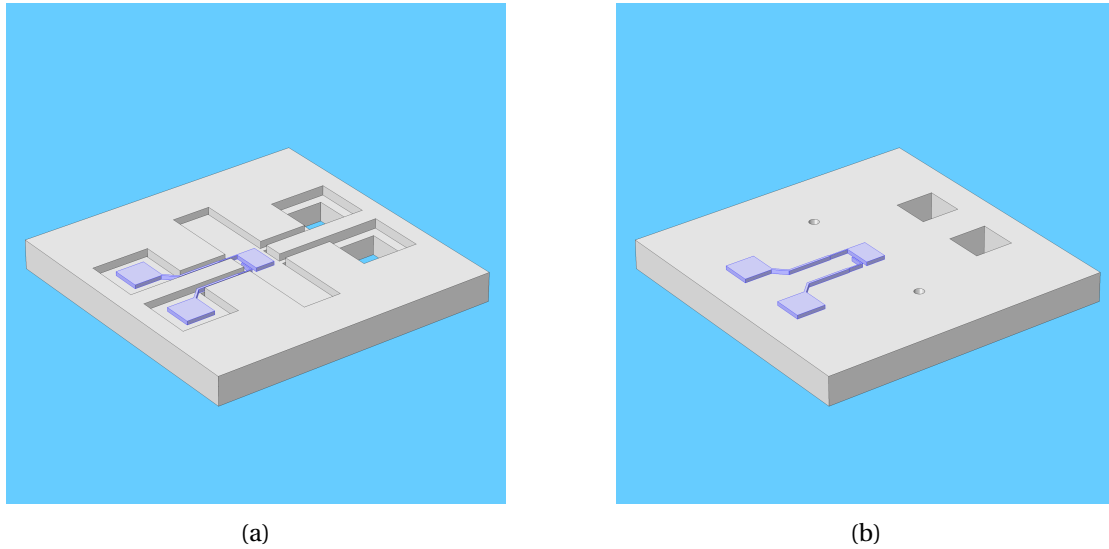


Figure 4.16: 3D diagrams showing (a) the silicon substrate after patterning the lower electrode and (b) the glass substrate after patterning the upper electrode.

4.3.4 Electrode layers

Figure 4.16 shows both the silicon and glass substrates after patterning the electrodes. The same AZ[®] nLOF 2070 (2.0 μm dilution) lift-off mask was used for both the lower (on Si/SiN_x) and upper (on glass) electrodes, with the process parameters outlined in Table 4.6. The patterned lift-off mask on the silicon substrates is shown in Figure 4.17. The samples were checked under an optical microscope for any defects and patterned again where necessary. Electron-beam evaporation was used to deposit a 5 nm Ti adhesion layer and a 140 nm Au layer. The layer thickness was monitored using a quartz crystal microbalance (QCM), with the tooling factor calibrated on previous run, and the beam current reduced as the target thickness was approached. The accuracy of the QCM and the ability to somewhat control the deposition rate makes this step the most suitable for resolving any deviations in the channel depth or passivation thickness.

With the channel measuring ≈ 900 nm deep and the SiN_x passivation layer measuring ≈ 110 nm thick the 145 nm electrode layers should provide an interelectrode distance of around 500 nm when the silicon and glass substrates are bonded together. Some issues were encountered during electrode patterning resulting in a few samples with gold areas around the edges of the die. Fortunately these seem to occur at a distance far enough from the channel not to interfere with the localised bonding.

Table 4.6: Process parameters for patterning the lower and upper electrodes.

Step	Description
1a	Clean substrates: $\text{H}_2\text{SO}_4:\text{H}_2\text{O}_2$ (5:1, vol.), 5 min at RT
1b	Rinse in DI water, N_2 dry
1c	Rinse in acetone then IPA, N_2 dry
1d	Spincoat AZ [®] nLOF 2070 (2.0 μm), 5 s at 500 rpm, 100 $\text{rpm}\cdot\text{s}^{-1}$, 30 s at 3000 rpm, 10,000 $\text{rpm}\cdot\text{s}^{-1}$
1e	Softbake on hotplate, 2 min at 110 °C
1f	Exposure, 8 s at $\approx 8.0 \text{ mW}\cdot\text{cm}^{-2}$ (365 nm) [Karl Süss MJB3]
1g	Post-exposure bake on hotplate, 1 min at 110 °C
1h	Manual agitation in AZ [®] 826 MIF developer, 60 s at RT
1i	DI water rinse, N_2 dry
2	Electron-beam evaporation of electrode layer Ti (5 nm, $0.1 \text{ nm}\cdot\text{s}^{-1}$ at 5.0 kV, 85 mA) and Au (140 nm, $0.1 \text{ nm}\cdot\text{s}^{-1}$ at 5.0 kV, 80 mA)
3a	Lift-off in MICROPOSIT [™] PR1165 Remover, 5 min at 65 °C
3b	Ultrasonic agitation (50%) in MICROPOSIT [™] PR1165 Remover, 15 min at 65 °C
3c	Ultrasonic agitation (50%) in acetone, 15 min at RT
3d	Rinse in acetone then IPA, N_2 dry

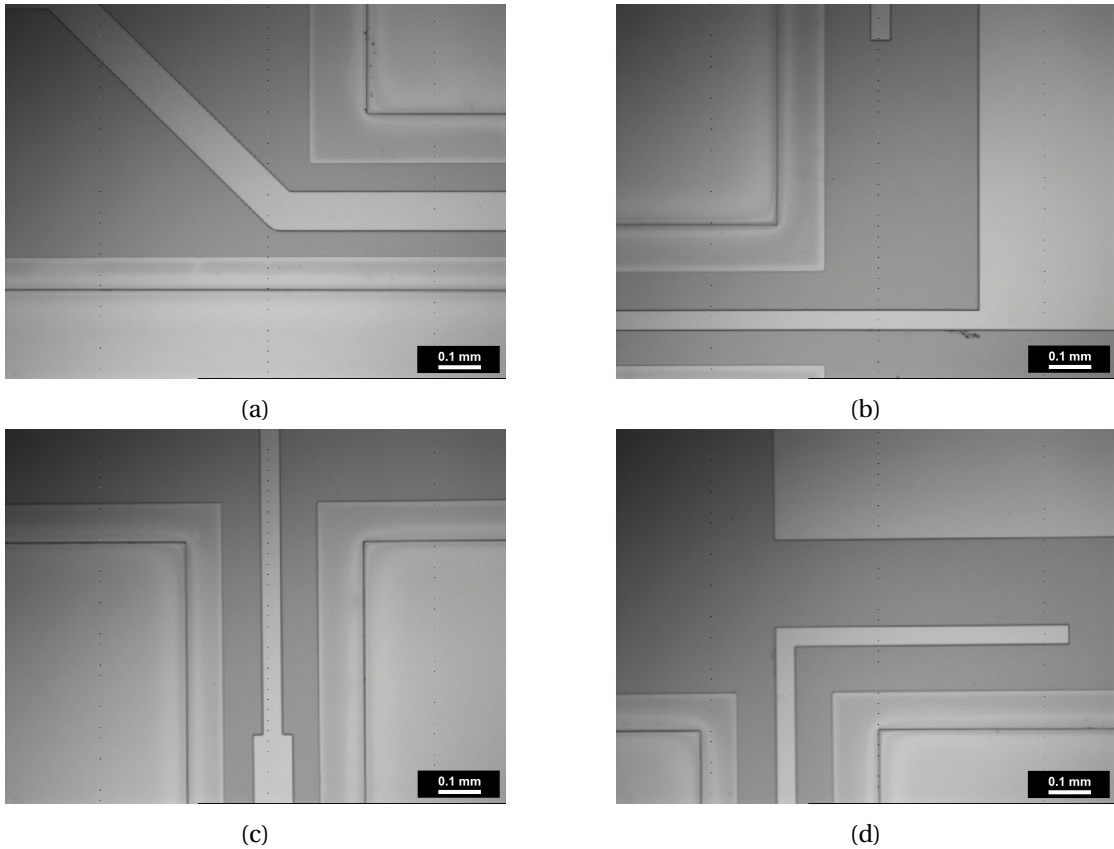


Figure 4.17: Optical images of the lift-off mask showing: (a) the transition to contact pad; (b) connection to the sensing electrode; (c) transition of the connect; and (d) the auxiliary electrode.

4.3.5 Anodic bonding

To finalise the sensor fabrication, the glass and silicon substrates were anodically bonded. This process required careful optimisation to prevent channel collapse so a large number of devices without laser micromachined apertures were used to tune the voltage and temperature (*vide infra*). The full process parameters are provided in Table 4.7. First the surfaces of the silicon and glass dies were activated using Piranha solution ($\text{H}_2\text{SO}_4:\text{H}_2\text{O}_2$, 10:1, vol.) for 10 minutes to provide increased hydroxyl groups ($-\text{OH}$). The ratio was adjusted from earlier trials (5:1) to prevent damage to the Au surfaces (presumably caused from reactions with a titanium oxide layer through pinhole defects in the gold). The electrodes were then rinsed in DI water and dried with N_2 taking care to ensure that there was no remaining water on the surfaces. The two dies were then brought into intimate contact, at which point fringing fields appear, and aligned under a stereoscope. Using a Perspex[®] jig a small pressure is applied to form distinctive dark regions indicative of successful prebonding. Figure 4.18 shows microscope images of a prebonded device, highlighting the problem of misalignment.

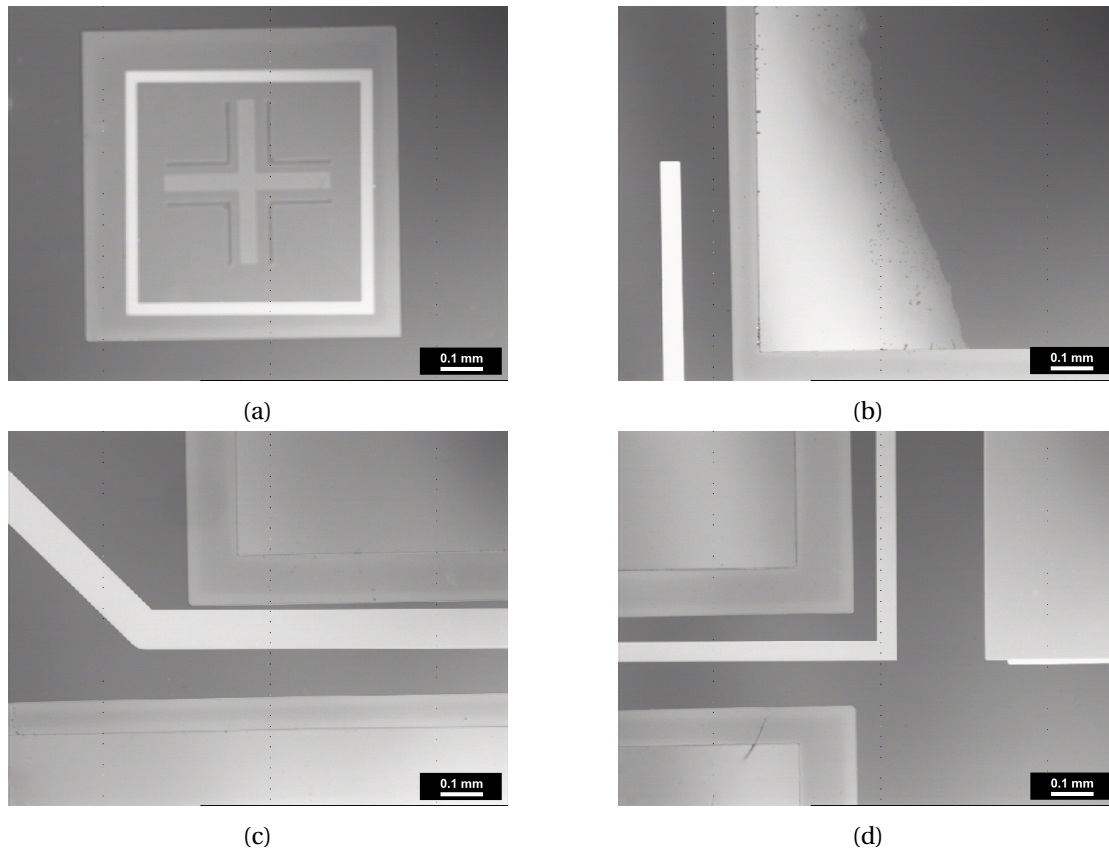


Figure 4.18: Optical images of the vertical nanogap device after prebonding: (a) alignment marks; (b) visible darker prebonded area on raised silicon section; (c) connect wire between contact pad and electrode; and (d) misalignment of the main sensing electrodes.

The prebonded device is then transferred to the anodic bonding setup described earlier.

Table 4.7: Process parameters for silicon–glass anodic bonding.

Step	Description
1a	Surface activation: $\text{H}_2\text{SO}_4\text{:H}_2\text{O}_2$ (10:1, vol.), 10 min at RT
1b	Rinse in DI water, N_2 dry
2a	Bring silicon and glass dies into intimate contact and align under stereoscope ensuring that there is no fouling
2b	Apply small amount of pressure using Perspex [®] jig to form prebond
3a	Transfer prebonded device to steel jig and fasten with alumina bolts
3b	Preheat tube furnace to 225 °C
3c	Slide mounted device into tube furnace, make electrical connections and allow 5 min to acclimatise
4a	Ramp voltage to 225 V ($\approx 10 \text{ V}\cdot\text{s}^{-1}$)
4b	Either monitor current and turn off voltage supply at $\approx 10\%$ of peak current or turn off voltage supply after 2.5 h
5a	Disconnect electrical connections and remove mounted device from tube furnace
5b	Allow mounted device to naturally cool down to room temperature
5c	Unfasten alumina bolts and remove device from steel jig

Voltages of 225–300 V and temperatures of 225–300 °C were used to bond the devices. It is interesting to highlight that literature shows that Cr atoms can readily diffuse into the Au layer at relatively low temperatures, significantly affecting the resistivity [83] [84] and have the potential to affect the electrochemical response. For example Huang *et al.* demonstrated that annealing at a temperature of just 200 °C for 30 minutes leads to a significant fraction of Cr atoms diffusing into the Au layer and that at 250 °C this occurs at an even shorter time of around 5 minutes [84]. At least for lower temperatures (<300 °C) the effect seems less prominent for Ti [85], possibly due the larger ionic radii reducing diffusivity.

Figure 4.19 shows a typical current profile for the anodic bonding process. Initially the current rises rapidly as the area of intimately contacted area grows due to the increasing electrostatic pressure. A maxima is reached but bonding continues until a plateau is reached (around 10% of peak current). It was found that the bonding process could be stopped and restarted without any obvious consequence, allowing the device to be inspected. The total bonding time was approximately 2.5 hours. Peak current was $10.61 \mu\text{A}$ and with a total bonded area[†] of $\approx 150 \text{ mm}^2$, the peak current density is $\approx 0.07 \mu\text{A}\cdot\text{mm}^{-2}$. Experiments showed that devices with greater intimately contacted areas formed during the prebonding stage led to higher initial currents, in agreement with the model developed by He *et al.* [86].

For the revised design both the voltage and the temperature needed to be reduced to improve the yield. Due to the increased surface area in intimate contact, at higher voltages and temperatures the increased electric field and ion mobility was found to cause channel collapse. Table 4.8 shows the yield of a number of devices at different voltage and and temperature settings. For the final devices a voltage of 225 V and temperature of 225 °C ensured channel

[†]This value is based on a visual estimation of unbonded regions.

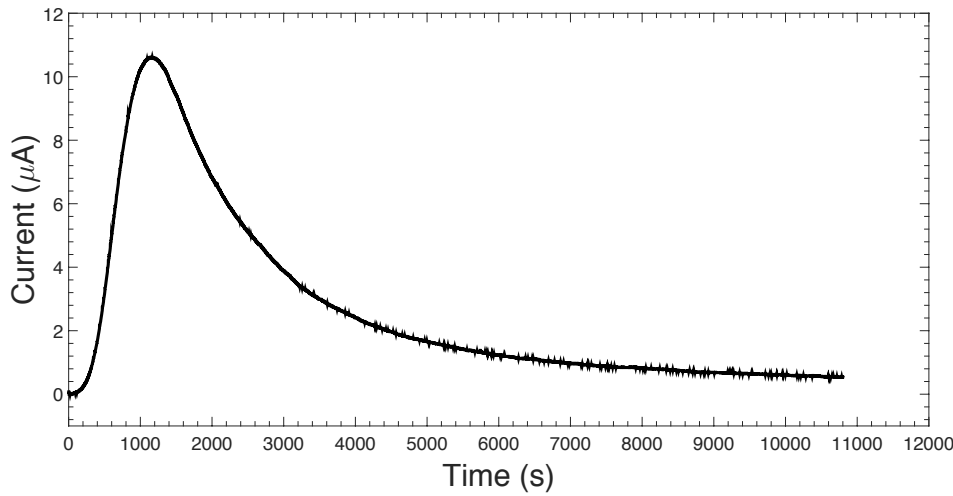


Figure 4.19: Current profile for glass-silicon anodic bonding at 225 V, 250 °C.

collapse did not occur, however these settings did sometimes result in unbonded regions at the corners of the device. Elevating the temperature to 250 °C appeared to resolve this issue.

Although the entire parameter space was not explored, Table 4.8 does demonstrate a clear trend towards collapsed devices when moving towards both increased voltage and temperature. For the majority of devices that exhibited partial channel collapse, the failure occurred during the initial bonding period as the current density approached its maximum value. An ideal anodic bonding setup may actively control the applied voltage based on the current density and its rate of change in order to prevent this failure mode.

A completed device is shown in Figure B.3, with the microscope images highlighting the issue with misalignment during the prebonding stage. This misalignment would lead to a reduced amplification factor as well as fringing fields. However, the overlapping region of the sensing electrodes still accounts for the majority of the total area. The misalignment is estimated to reduce the overlapping area by 0.052 mm² to 1.448 mm², a reduction of around 3.5%. It is envisaged that performing alignment at the wafer-scale or using a commercial anodic bonding system this could be minimised if not eliminated.

Table 4.8: Anodic bonding parameters and respective device yield.

	Voltage (V)			
	225	250	275	300
Temperature (°C)	225	250	275	300
225	7 × S	1 × S	—	—
250	2 × S	2 × S, 2 × PC	1 × PC	1 × PC, 1 × F
275	1 × S, 1 × PC	1 × S, 2 × PC	1 × PC, 1 × F	2 × F
300	1 × PC	2 × PC	2 × F	8 × F

Key: **S** = success, **PC** = partial collapse, **F** = fail

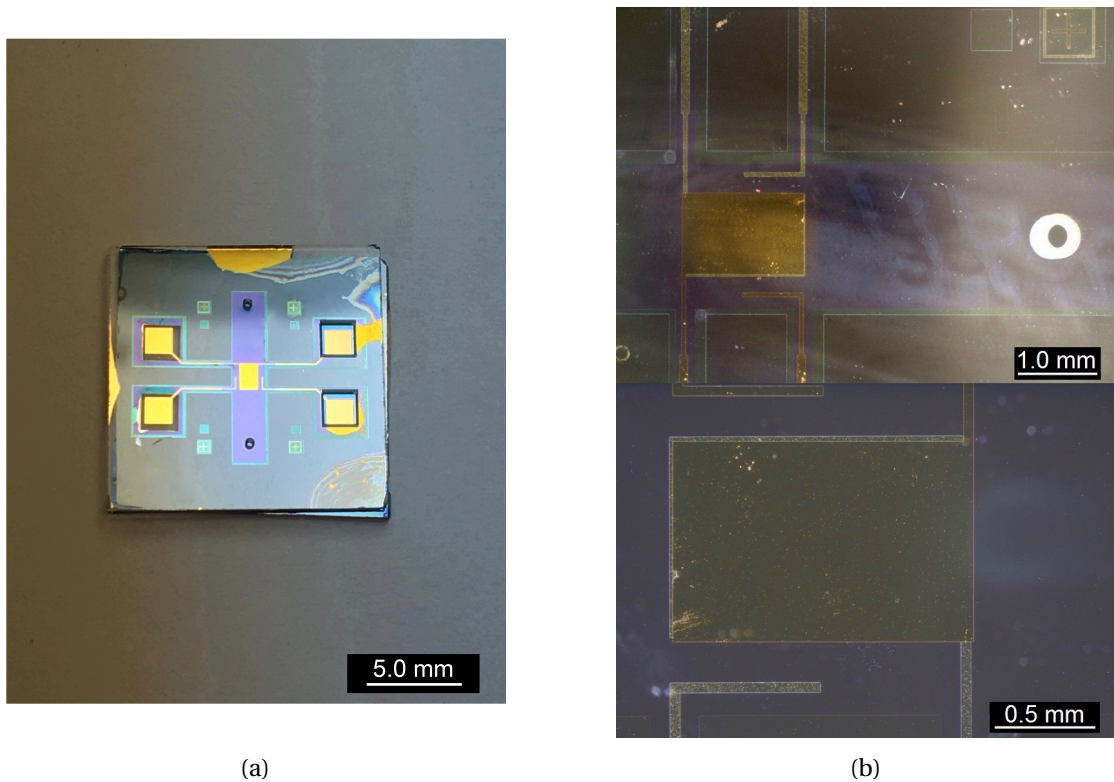


Figure 4.20: Images showing a completed vertical coplanar nanogap device. Left: Photograph showing an entire device. Top-right: microscope image with a microfluidic inlet/outlet and alignment marks visible. Bottom-right: Microscope image with increased magnification showing the misalignment at the sensing electrodes.

4.4 Simulation

4.4.1 Microfluidics

Flow conditions within the sensor's fluidic channel were simulated using COMSOL Multiphysics® to provide an understanding of the flow's velocity at the electrodes. When simulating microfluidic devices it is important to first consider the Reynolds number (Re) and the Mach number (Ma) of the system. This allows suitable selection of the governing equations that need to be solved.

Reynolds number

The Reynolds number is an important indicator of the ratio of the relative magnitude of the flow's inertial to viscous forces and is defined as $Re = \frac{\rho \mathbf{u} L}{\mu}$ where ρ is the density of the fluid [$\text{kg}\cdot\text{m}^{-3}$], \mathbf{u} is the velocity vector of the fluid [$\text{m}\cdot\text{s}^{-1}$], L is the characteristic length [m] and μ is the dynamic viscosity of the fluid [$\text{Pa}\cdot\text{s}$]. For Reynolds numbers <1 the flow can be considered laminar and if it is $\ll 1$ the flow can be considered as a Stokes flow and the inertial term in the Navier-Stokes equations can be neglected [87].

Considering that for this device the majority of the fluidic channel has a characteristic length of 800 nm, assuming a maximum velocity of $1 \times 10^{-2} \text{ m}\cdot\text{s}^{-1}$ and using values for the density and viscosity of water at 20 °C of $1000 \text{ kg}\cdot\text{m}^{-3}$ and $1.0 \text{ mPa}\cdot\text{s}$, respectively the Re number can be calculated as 0.008. This value is $\ll 1$ and therefore the fluidic flow can be considered to be a Stokes flow.

Mach number

The Mach number provides a ratio of the convective speed to the speed of sound in the medium. It is defined as $Ma = \frac{\mathbf{u}}{c}$ where \mathbf{u} is the flow velocity [$\text{m}\cdot\text{s}^{-1}$] and c is the speed of sound in the medium [$\text{m}\cdot\text{s}^{-1}$]. Importantly, when $Ma < 0.3$ the density and temperature of the fluid is not affected by the velocity and the flow can be considered as quasi-steady meaning that simplified incompressible flow equations can be used. For this device, assuming a maximum velocity of $1 \times 10^{-2} \text{ m}\cdot\text{s}^{-1}$ and using a value of $1482 \text{ m}\cdot\text{s}^{-1}$ for the speed of sound in water at 20 °C, the Ma number is calculated as 6.75×10^{-6} . This value is $\ll 0.3$ and therefore the incompressible flow equations can be considered valid.

Navier–Stokes equation

The simulation solves the Navier–Stokes momentum equation, [Equation 4.3] along with the continuation equation for mass conservation [Equation 4.4] where ρ is the density [$\text{kg}\cdot\text{m}^{-3}$], \mathbf{u} is the velocity vector [$\text{m}\cdot\text{s}^{-1}$], P is the pressure [Pa], \mathbf{I} is the identity matrix, \mathbf{F} is the volume force vector [$\text{N}\cdot\text{m}^{-3}$]. The indicated terms correspond to the inertial forces (1), pressure forces (2), viscous forces (3) and any external forces applied to the fluid (4).

$$\underbrace{\rho \frac{\partial \mathbf{u}}{\partial t}}_1 + \underbrace{\rho \mathbf{u} \cdot \nabla \mathbf{u}}_2 = -\nabla P + \underbrace{\nabla \cdot \left[\mu \left(\nabla \mathbf{u} + (\nabla \mathbf{u})^T \right) - \frac{2}{3} \mu (\nabla \cdot \mathbf{u}) \mathbf{I} \right]}_3 + \underbrace{\mathbf{F}}_4 \quad (4.3)$$

$$\frac{\partial \rho}{\partial t} + \nabla \cdot (\rho \mathbf{u}) = 0 \quad (4.4)$$

For incompressible flow a single-phase fluid can often be assumed incompressible (*i.e.*, ρ is either constant or nearly constant). Equation 4.3 then becomes:

$$\rho \frac{\partial \mathbf{u}}{\partial t} + \rho (\mathbf{u} \cdot \nabla) \mathbf{u} = \nabla \cdot \left[-P \mathbf{I} + \mu \left(\nabla \mathbf{u} + (\nabla \mathbf{u})^T \right) \right] + \mathbf{F} \quad (4.5)$$

And the continuity equation, Equation 4.4, simplifies to:

$$\rho \nabla \cdot \mathbf{u} = 0 \quad (4.6)$$

Hagen–Poiseuille flow

The Hagen–Poiseuille flow can be shown to be an exact solution to the Navier–Stokes equations for an incompressible and Newtonian fluid in laminar flow through a channel of constant cross section. Whilst it is only strictly valid for a steady Stokes flow, it is also a good approximation for $\text{Re} \lesssim 1$ in long channels. For a cylindrical cross section the volumetric flow rate (Q) is given by:

$$Q = \frac{\pi r^4}{8\mu l} \Delta P \quad (4.7)$$

Or more generally as:

$$Q = \frac{\Delta P}{R_h} \quad (4.8)$$

It describes the relationship between the volumetric flow rate (Q), pressure drop (ΔP) and hydraulic resistance (R_h) which represents the channel geometry and fluid viscosity (μ). For pressure- or vacuum-driven flow systems a pump (analogous to a DC voltage supply) is used to apply a pressure drop either directly across the ports of a device or to pressurise an externally connected reservoir. The Hagen–Poiseuille law ($\Delta P = Q \times R_h$) can be considered analogous to Ohm's law ($\Delta V = I \times R$), and provides a simple way of determining the volumetric flow through a microfluidic network. This is particularly true for systems where inertial effects (analogous to inductance) and hydraulic compliance (analogous to capacitance) are negligible and the operating frequency is below the resonance frequency of the flow [88].

Hydraulic resistance

The hydraulic resistance (R_h) is a central concept in characterising microfluidic system, describing how a channel impedes a fluidic flow. For a cylinder with radius r [m] the flow resistance is given by:

$$R_h = \frac{8\mu l}{\pi r^4} \quad (4.9)$$

Where μ is the dynamic viscosity [$\text{m}^2 \cdot \text{s}^{-1}$] and l is the length of the cylinder [m]. For rectangular channels with width w [m] and height h [m] (where $l \gg w$, and $w \gg h$) it is given by:

$$R_h = \frac{12\mu l}{h^3 w} \quad (4.10)$$

The hydraulic circuit in Figure 4.21 represents a vacuum pump generating a flow through a fluidic network comprising of a device between two sections of tubing. In this system one section of tubing (R_{h1}) is selected to provide a significantly larger hydraulic resistance. In the case where $R_{h1} \gg (R_{h2} + R_{h3})$, the flow rate will be dominated by R_{h1} and pressure drop across R_{h2} and R_{h3} will be minimised.

Table 4.9 shows the calculated hydraulic resistances of various fluidic circuit components. Clearly using tubing with a smaller internal diameter will provide greater hydraulic resistance but importantly it also minimises the 'dead volume' of the connections. This is particularly

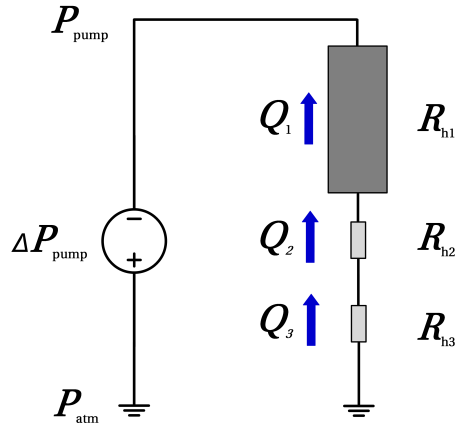


Figure 4.21: Diagram representing a typical hydraulic circuit.

Table 4.9: Hydraulic resistances of fluidic circuit components.

Component	R_h (Pa·s·m ⁻³)	Volume (nL)
25 μ m ID, 0.25 m long tubing	2.61×10^{16}	122.7
50 μ m ID, 0.25 m long tubing	1.63×10^{15}	490.8
65 μ m ID, 0.25 m long tubing	5.70×10^{14}	829.6
100 μ m ID, 0.25 m long tubing	1.02×10^{14}	1963.5
500 μ m ID, 0.25 m long tubing	1.63×10^{11}	49087.5
800 nm \times 2 mm \times 10 mm channel	2.50×10^{10}	15.5

evident when considering the volume of the nanogap device is just 15.5 nL[‡]. Reducing the length of the tubing will help reduce the dead volume, however the practical limitations of shorter lengths must be taken into account.

Flow rates

The expected flow rates achievable with a Mitos Fluika low vacuum pump [Dolomite] capable of generating 5-350 mbar below atmospheric pressure are presented in Table 4.10. Here the length of the flow-limiting tubing is set as 0.25 m and the internal diameter and the vacuum pressure varied.

[‡]This value accounts for the reduced volume caused by the displacement of the electrodes.

Table 4.10: Expected flow rates of 0.25 m tubing using a 5-350 mbar vacuum pump.

Vacuum (mbar)	ID (μm)		
	25	50	65
5	1.2 nL·min ⁻¹	18.4 nL·min ⁻¹	52.6 nL·min ⁻¹
25	5.8 nL·min ⁻¹	92.0 nL·min ⁻¹	262.9 nL·min ⁻¹
100	23.0 nL·min ⁻¹	368.1 nL·min ⁻¹	1051.4 nL·min ⁻¹
150	34.5 nL·min ⁻¹	552.2 nL·min ⁻¹	1577.1 nL·min ⁻¹
250	57.5 nL·min ⁻¹	920.4 nL·min ⁻¹	2628.6 nL·min ⁻¹
350	80.5 nL·min ⁻¹	1288.5 nL·min ⁻¹	3680.0 nL·min ⁻¹
Resolution (nL·min ⁻¹ ·mbar ⁻¹)	0.23	3.68	10.51

Flow velocity

With the connection tubing set to dominate the hydraulic resistance of the microfluidic network, the volumetric flow determined by the Hagen–Poiseuille law [Equation 4.8] can be used as a boundary condition (BC) for simulating the flow velocity inside the sensor with the laminar flow interface of the computational fluid dynamics module in COMSOL Multiphysics®. With the hydraulic resistance dominated by the tubing and the device itself being structurally rigid, the device is unlikely to exhibit any change in volume. The hydraulic capacitance (C_h) can be considered to be negligible and thus volumetric flow entering the device should equal that exiting the device.

The simulation solves the Navier–Stokes equation with the inertial term neglected due to the low Re number (Stokes flow) and the term $-\frac{2}{3}\mu(\nabla \cdot \mathbf{u})\mathbf{I}$ removed from the viscous term[§] as the low Ma number allows the flow to be considered as incompressible. A shallow channel approximation is made to allow the system to be modelled in 2D by adding a drag force of $-12\frac{\mu\mathbf{u}}{h^2}$ where h is the channel thickness. The final equation to solve is:

$$0 = \nabla \cdot \left[-P\mathbf{I} + \mu(\nabla\mathbf{u} + (\nabla\mathbf{u})^T) \right] - 12\frac{\mu\mathbf{u}}{h^2} \quad (4.11)$$

Along with the continuity equation:

$$\rho\nabla \cdot (\mathbf{u}) = 0 \quad (4.12)$$

The outlet velocity (vacuum driven flow) determined by the Hagen–Poiseuille law is used as the outlet port BC. With the inlet port taking an ‘open boundary’ condition (describing the unrestricted flow from sample reservoir) and the square apertures set as inlet BCs with zero inlet velocity initial values. A surface plot showing the steady-state surface velocity through the sensor channel for a flow rate of 80.5 nL·min⁻¹ is shown in Figure 4.22a. The area of the

[§]This is because the divergence of the velocity is equal to zero, *i.e.*, $(\nabla \cdot \mathbf{u} = 0)$.

sensing electrode is indicated with a black rectangle. Some minor disturbance of the flow can be seen where the electrode connection wires are fed towards the contact pads however this does not seem to interfere with the flow across the sensor surface. The flow velocity across the sensor surface is approximately 30% lower than the outlet velocity, regardless of flow rate. Table 4.11 provides the simulated flow velocities across the sensor surface for a range of flow rates.

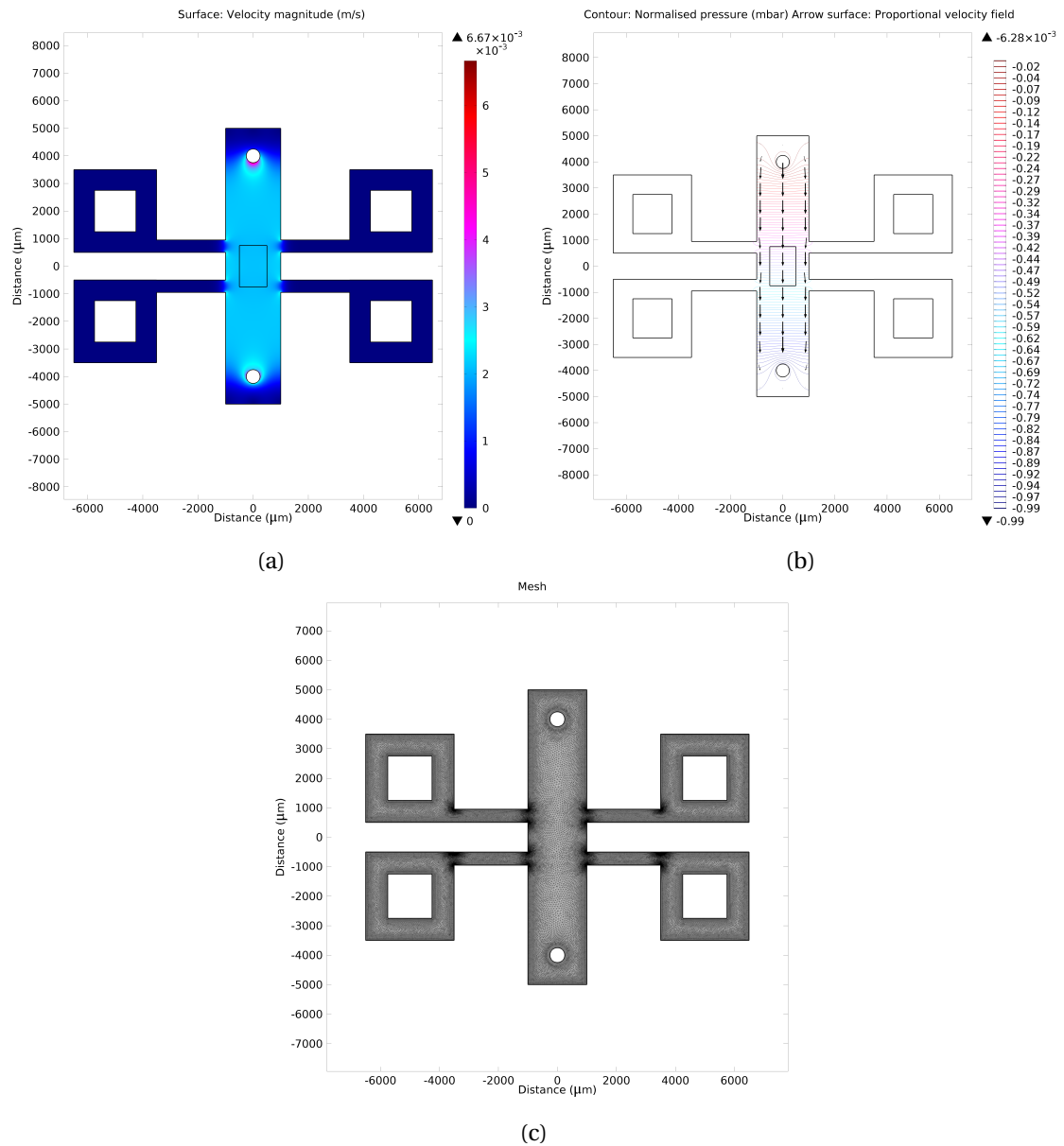


Figure 4.22: Simulated results for microfluidic flow: (a) surface velocity; (b) normalised pressure contours with proportional velocity arrows; and (c) the utilised mesh for the simulations.

Based on these results, the sensor volume could be considerably reduced by reducing the

Table 4.11: Simulated flow velocities at the sensor surface.

Vacuum (mbar)	Flow rate (nL·min ⁻¹)	Outlet velocity (mm·s ⁻¹)	Sensor surface velocity (mm·s ⁻¹)
5	1.15	0.039	0.030
25	5.75	0.195	0.150
100	23.0	0.781	0.602
150	34.5	1.171	0.090
250	57.5	1.952	1.500
350	80.5	2.733	2.080

length of the channel. Unlike reducing the channel width, this is unlikely to cause any major disruption to the flow over the sensing electrodes. This would also help to minimise the likelihood of channel collapse by reducing the suspended area of glass. These results also show that in the current configuration it may be possible to place large electrodes both upstream and downstream of the central electrodes. This could be particularly interesting for performing hydrodynamic electrochemical measurements.

4.4.2 Electroanalysis

The effect of interelectrode spacing on the limiting current density was studied using the electroanalysis interface of the electrochemistry module in COMSOL Multiphysics[®]. This is a chemical species transport interface solving the diffusion-convection equation for mass transport, which incorporates electrode kinetic boundary conditions to drive a flux of chemical species at a electrode–electrolyte interfaces as a function of the overpotential. The model assumes that there is a supporting electrolyte in considerable excess to the quantity of electroactive species such that the solution resistance does not contribute noticeably to the behaviour of the electrochemical cell.

The flux in an electrolyte can be described by the Nernst–Planck equations and accounts for the diffusion, migration and convection of the charged solute species, given respectively as the first, second and third terms in the following equation:

$$j_i = -D_i \nabla c_i - z_i \mu_i F c_i \nabla \phi + c_i \mathbf{u} \quad (4.13)$$

Where j_i is the flux of species ‘ i ’ [mol·m⁻²·s⁻¹]. In the absence of convection ($\mathbf{u} = 0$) and ignoring migration (considered appropriate for a ratio of supporting electrolyte in excess of 100 [89]) the flux reduces to:

$$j_i = -D_i \nabla c_i \quad (4.14)$$

Table 4.12: Parameters used to simulate the effect of interelectrode distance on limiting current density.

α_c	0.49	E_{eq}	0.251 V <i>vs.</i> Ag/AgCl
α_a	0.51	F	96485 C·mol ⁻¹
$c_{\text{red},b}$	0.05 mol·m ⁻³	k_0	0.06 m·s ⁻¹
$c_{\text{ox},b}$	0.0 mol·m ⁻³	R	8.31 J·K ⁻¹
D_{red}	6.7×10^{-10} m ² ·s ⁻¹	T	293.15 K
D_{ox}	6.7×10^{-10} m ² ·s ⁻¹	ν	10 mV·s ⁻¹

The model then solves the electroanalytical Butler–Volmer equation[‡]:

$$i = nFk_0 \left[\exp\left(\frac{\alpha_a F \eta}{RT}\right) c_{\text{red}} - \exp\left(\frac{-\alpha_c F \eta}{RT}\right) c_{\text{ox}} \right] \quad (4.15)$$

The Butler–Volmer model has been shown to be applicable for >100 nm interelectrode spacing for k_0 of $\approx 1 \times 10^{-2}$ m·s⁻¹ and >20 nm for k_0 of $\approx 1 \times 10^{-1}$ m·s⁻¹ (demonstrated using a 0.5 M monovalent supporting electrolyte and 1 mM redox species) [90]. However, for gap sizes <50 nm the Butler–Volmer model does not accurately predict the response as the effects of the electric double layer start to dominate. A further consideration is for systems with slow electron transfer kinetics, for instance a value for k_0 of 1×10^{-3} m·s⁻¹ is only correctly predicted for interelectrode spacings greater than ≈ 400 nm. For accurate simulations outside of these limitations the Marcus–Hush–Chidsey model is required [91].

To demonstrate the effect of reducing the interelectrode distance (x) on the limiting current density, an archetypical redox reaction involving $\text{Fc}(\text{MeOH})_2^+ + \text{e}^- \rightleftharpoons \text{Fc}(\text{MeOH})_2$ was studied with the parameters outlined in Table 4.12. To maintain the validity of the Butler–Volmer model, the value of x was kept above 100 nm and the concentration of the redox marker kept considerably low (0.05 mol·m⁻³ or 50 μM) so that the concentration of a typical supporting electrolyte can be considered to be in excess.

Figure 4.23a shows the cyclic voltammogram for $x = 500$ nm. The limiting current density [$\text{A}\cdot\text{m}^2$] is then plotted against the interelectrode distance (x) [μm] in Figure 4.23b. This demonstrates that as the distance between the electrodes is reduced the time taken for the reduced and oxidised species to diffuse between the electrodes is also reduced, leading to significantly increased amplification factor and therefore current density. This current response is termed an approach curve and is the foundation of the scanning electrochemical microscope.

[‡]When the current is zero the electroanalytical equation can be rearranged to the thermodynamic Nernst equation: $c_{\text{red}} = c_{\text{ox}} \exp\left(\frac{-FE_{\text{eq}}}{RT}\right)$, and with $c_{\text{red}} \approx c_{\text{ox}} \approx c$, the exchange current density i_0 is related by $i_0 = nFk_0c$.

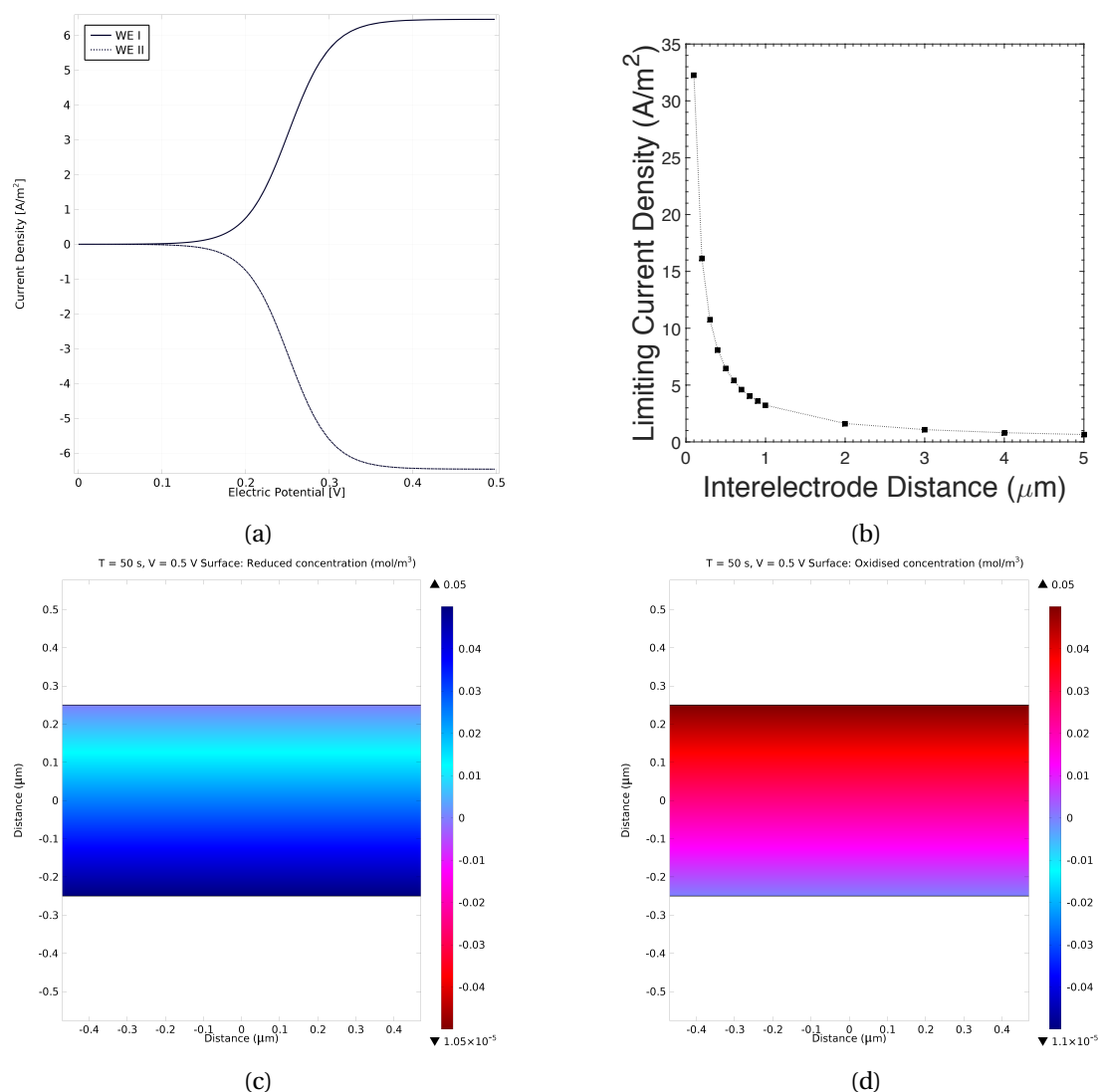


Figure 4.23: Simulated electrochemical response for $\text{Fc}(\text{MeOH})_2$: (a) cyclic voltammogram ($10 \text{ mV}\cdot\text{s}^{-1}$) for a 500 nm nanogap; (b) effect of the interelectrode distance (x) on the limiting current density; (c) concentration profile of c_{red} at I_{lim} ; and (d) concentration profile of c_{ox} at I_{lim} .

4.5 Electrical characterisation

I-V sweeps of the device were performed within a Faraday cage using a B1500A semiconductor device analyser [Agilent Technologies] and a probe station [Wentworth Laboratories]. A two-terminal configuration was created using a micropositioner for the topside (through glass) lower electrode contact and three different connection methods for the backside (through silicon) upper electrode contact. These included using solder paste, wire with solder paste and simply wire to connect to an underlying pad on a printed circuit board. The current response was at the level of the measurement noise, indicating an isolation of $>1 \text{ T}\Omega$.

One of the key benefits of this geometry and the use of anodic bonding is that the bond interface isolates both substrates, therefore the leakage current path is through the air gap. Failed devices can be quickly identified as the device would be expected to fail in such a way that it creates an electrical short. Some caution should be taken as applying larger potentials directly between the electrodes may lead to electrostatic collapse.

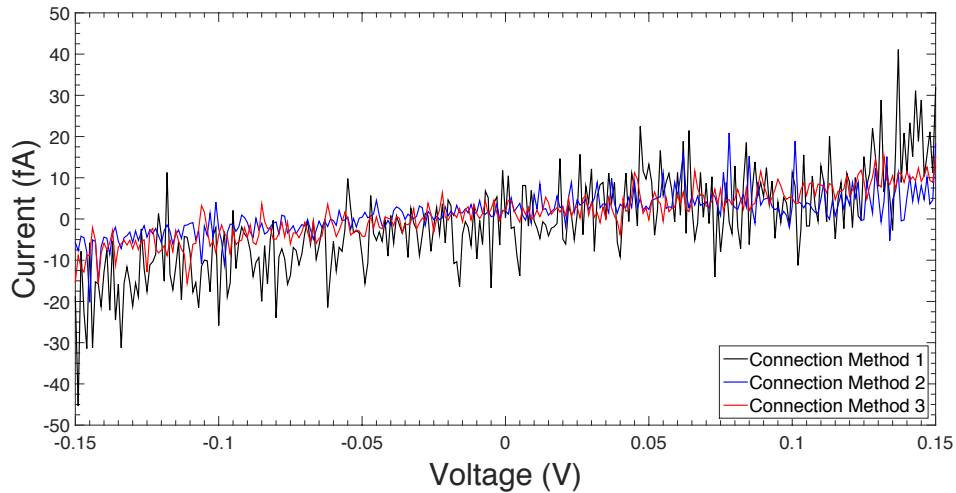


Figure 4.24: I-V traces for vertical nanogap device filled with air for backside connection modes: (1) solder paste; (2) coiled wire with solder paste; and (3) coiled wire.

The capacitance response of the device in air was recorded using a B1500A semiconductor device analyser fitted with a 1 kHz to 5 MHz multi-frequency capacitance measurement unit (MFCMU) [Agilent Technologies]. A shielded two-terminal configuration was created, shorting the L_p & L_c and H_p & H_c terminals inside the Faraday cage. Here the electrical connection to the backside contact (upper electrode) was made with a coiled piece of wire. The response was recorded for a frequency range of 1 kHz to 500 kHz with a 0.0 V DC bias and a 10 mV AC signal using a ‘long’ integration time (16 power line cycles). Figure 4.25 shows that the capacitance at 1 kHz is $\approx 21.8 \text{ pF} \pm 0.2 \text{ pF}$. This value is close to the expected theoretical value for a parallel-plate capacitor with the same geometry.

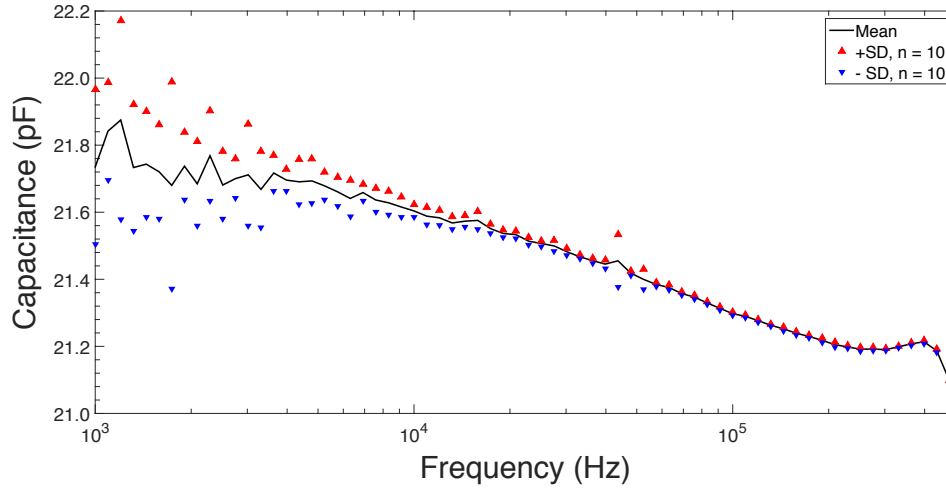


Figure 4.25: Capacitance profile for a 500 nm vertical nanogap device filled with air for the frequency range 1 kHz to 500 kHz.

4.6 Discussion

In summary, a novel process for the fabrication of large area vertical coplanar nanogap device has been presented. The fabrication process is primarily based on the use of ICP-RIE of a silicon substrate to form a channel and then silicon–glass anodic bonding to a nanogap between electrodes patterned on these opposing substrates. The linear response of the SF_6/O_2 ICP-RIE process provides predictable control of the channel depth. Furthermore, this dry etch process allows the use of a photoresist mask instead of a hard mask, reducing the necessary processing steps.

Anodic bonding of silicon and glass substrates to form nanochannels without causing collapse still remains a challenge. Undeniably there must be a practical limit to the channel depth that can be achieved without drastically affecting the device yield. However, this work has shown that large area electrodes can be contained in the channel by reducing the electrostatic pressure across the channel through geometric design, electrical passivation as well as lowering the applied voltage and temperature.

Prior to anodic bonding one of the critical steps in the fabrication is accurate alignment of the two substrates during the prebonding step. This was considered in the design by providing significant lateral and rotational tolerance between features. Commercial anodic bonding systems often provide built-in alignment with submicron accuracy that would resolve this issue. One of the main difficulties associated with this type of device is forming electrical connection to the upper electrode contact pad through the backside of the silicon. This could be addressed by developing a spring-loaded ‘pogo pin’ interface. Ideally the device would

incorporate an internal via to connect the upper electrode to a contact pad on the silicon substrate to simplify usability.

References

- [1] R. C. Engstrom, M. Weber, D. J. Wunder, R. Burgess, and S. Winquist. Measurements within the diffusion layer using a microelectrode probe. *Analytical Chemistry*, 58(4):844–848, 1986.
- [2] A. J. Bard, F.-R. F. Fan, J. Kwak, and O. Lev. Scanning Electrochemical Microscopy. Introduction and Principles. *Analytical Chemistry*, 61(2):132–138, 1989.
- [3] R. Krahne, A. Yacoby, H. Shtrikman, I. Bar-Joseph, T. Dadosh, and J. Sperling. Fabrication of nanoscale gaps in integrated circuits. *Applied Physics Letters*, 81(4):730–732, 2002.
- [4] S. Strobel, K. Arinaga, A. Hansen, and M. Tornow. A silicon-on-insulator vertical nanogap device for electrical transport measurements in aqueous electrolyte solution. *Nanotechnology*, 18(29):295201, 2007.
- [5] M. I. Schukfeh, L. Sepunaru, P. Behr, W. Li, I. Pecht, M. Sheves, D. Cahen, and M. Tornow. Towards nanometer-spaced silicon contacts to proteins. *Nanotechnology*, 27(11):115302, 2016.
- [6] M. J. J. van Megen, J. G. Bomer, W. Olthuis, and A. van den Berg. Solid state nanogaps for electrochemical detection fabricated using edge lithography. *Microelectronic Engineering*, 115:21–25, 2014.
- [7] G. Y. Lee, Y. H. Choi, H. W. Chung, H. Ko, S. Cho, and J. C. Pyun. Capacitive immunoaffinity biosensor based on vertically paired ring-electrodes. *Biosensors and Bioelectronics*, 40(1):227–232, 2013.
- [8] D. Han, L. P. Zaino, K. Fu, and P. W. Bohn. Redox Cycling in Nanopore-Confined Recessed Dual-Ring Electrode Arrays. *Journal of Physical Chemistry C*, 120(37):20634–20641, 2016.
- [9] S. Neugebauer, U. Müller, T. Lohmüller, J. P. Spatz, M. Stelzle, and W. Schuhmann. Characterization of nanopore electrode structures as basis for amplified electrochemical assays. *Electroanalysis*, 18(19-20):1929–1936, 2006.
- [10] S. Neugebauer, L. Stoica, D. Guschin, and W. Schuhmann. Redox-amplified biosensors based on selective modification of nanopore electrode structures with enzymes entrapped within electrodeposition paints. *Microchimica Acta*, 163(1-2):33–40, 2008.

References

- [11] T. Lohmüller, U. Müller, S. Breisch, W. Nisch, R. Rudolf, W. Schuhmann, S. Neugebauer, M. Kaczor, S. Linke, S. Lechner, J. Spatz, and M. Stelzle. Nano-porous electrode systems by colloidal lithography for sensitive electrochemical detection: fabrication technology and properties. *Journal of Micromechanics and Microengineering*, 18(11):115011, 2008.
- [12] C. Ma, N. M. Contento, L. R. Gibson, and P. W. Bohn. Redox cycling in nanoscale-recessed ring-disk electrode arrays for enhanced electrochemical sensitivity. *ACS Nano*, 7(6):5483–5490, 2013.
- [13] C. Ma, N. M. Contento, and P. W. Bohn. Redox cycling on recessed ring-disk nanoelectrode arrays in the absence of supporting electrolyte. *Journal of the American Chemical Society*, 136(20):7225–7228, 2014.
- [14] C. Ma, W. Xu, W. R. A. Wichert, and P. W. Bohn. Ion Accumulation and Migration Effects on Redox Cycling in Nanopore Electrode Arrays at Low Ionic Strength. *ACS Nano*, 10(3):3658–3664, 2016.
- [15] K. Fu, D. Han, C. Ma, and P. W. Bohn. Electrochemistry at single molecule occupancy in nanopore-confined recessed ring-disk electrode arrays. *Faraday Discussions*, 193:51–64, 2016.
- [16] M. Hüske, R. Stockmann, A. Offenhäusser, and B. Wolfrum. Redox cycling in nanoporous electrochemical devices. *Nanoscale*, 6(1):589–98, 2014.
- [17] M. Hüske, A. Offenhäusser, and B. Wolfrum. Nanoporous dual-electrodes with millimetre extensions: parallelized fabrication and area effects on redox cycling. *Physical chemistry chemical physics : PCCP*, 16(23):11609–11616, 2014.
- [18] M. Yi, K. H. Jeong, and L. P. Lee. Theoretical and experimental study towards a nanogap dielectric biosensor. *Biosensors and Bioelectronics*, 20(7):1320–1326, 2005.
- [19] C. Ionescu-Zanetti, J. T. Nevill, D. Di Carlo, K. H. Jeong, and L. P. Lee. Nanogap capacitors: Sensitivity to sample permittivity changes. *Journal of Applied Physics*, 99(2):024305, 2006.
- [20] D.-Y. Jang, Y.-P. Kim, H.-S. Kim, S.-H. Ko Park, S.-Y. Choi, and Y.-K. Choi. Sublithographic vertical gold nanogap for label-free electrical detection of protein-ligand binding. *Journal of Vacuum Science & Technology B: Microelectronics and Nanometer Structures*, 25(2):443–447, 2007.
- [21] A. K. Okyay, O. Hanoglu, M. Yuksel, H. Acar, S. Sülek, B. Tekcan, S. Agan, N. Biyikli, and M. O. Guler. Using nanogap in label-free impedance based electrical biosensors to overcome electrical double layer effect. *Microsystem Technologies*, 23(4):889–897, 2017.
- [22] Y. Kanno, K. Ino, H. Shiku, and T. Matsue. A local redox cycling-based electrochemical chip device with nanocavities for multi-electrochemical evaluation of embryoid bodies. *Lab on a Chip*, 15(23):4404–4414, 2015.

-
- [23] Q. Chen, K. McKelvey, M. A. Edwards, and H. S. White. Redox Cycling in Nanogap Electrochemical Cells. the Role of Electrostatics in Determining the Cell Response. *Journal of Physical Chemistry C*, 120(31):17251–17260, 2016.
- [24] M. A. G. Zevenbergen, D. Krapf, M. R. Zuiddam, and S. G. Lemay. Mesoscopic Concentration Fluctuations in a Fluidic Nanocavity Detected by Redox Cycling. *Nano Letters*, 7(2):384–388, 2007.
- [25] B. Wolfrum, M. Zevenbergen, and S. Lemay. Nanofluidic redox cycling amplification for the selective detection of catechol. *Analytical Chemistry*, 80(4):972–977, 2008.
- [26] M. A. G. Zevenbergen, B. L. Wolfrum, E. D. Goluch, P. S. Singh, and S. G. Lemay. Fast electron-transfer kinetics probed in nanofluidic channels. *Journal of the American Chemical Society*, 131(32):11471–11477, 2009.
- [27] M. A. G. Zevenbergen, P. S. Singh, E. D. Goluch, B. L. Wolfrum, and S. G. Lemay. Electrochemical correlation spectroscopy in nanofluidic cavities. *Analytical Chemistry*, 81(19):8203–8212, 2009.
- [28] E. Kätelhön, B. Hofmann, S. G. Lemay, M. A. G. Zevenbergen, A. Offenhäusser, and B. Wolfrum. Nanocavity redox cycling sensors for the detection of dopamine fluctuations in microfluidic gradients. *Analytical Chemistry*, 82(20):8502–8509, 2010.
- [29] P. S. Singh, H. S. M. Chan, S. Kang, and S. G. Lemay. Stochastic amperometric fluctuations as a probe for dynamic adsorption in nanofluidic electrochemical systems. *Journal of the American Chemical Society*, 133(45):18289–18295, 2011.
- [30] M. A. G. Zevenbergen, P. S. Singh, E. D. Goluch, B. L. Wolfrum, and S. G. Lemay. Stochastic sensing of single molecules in a nanofluidic electrochemical device. *Nano Letters*, 11(7):2881–2886, 2011.
- [31] S. Kang, K. Mathwig, and S. G. Lemay. Response time of nanofluidic electrochemical sensors. *Lab on a Chip*, 12(7):1262, 2012.
- [32] K. Mathwig, D. Mampallil, S. Kang, and S. G. Lemay. Electrical cross-correlation spectroscopy: Measuring picoliter-per-minute flows in nanochannels. *Physical Review Letters*, 109(11):1–5, 2012.
- [33] L. Rassaei, K. Mathwig, E. D. Goluch, and S. G. Lemay. Hydrodynamic voltammetry with nanogap electrodes. *Journal of Physical Chemistry C*, 116(20):10913–10916, 2012.
- [34] P. S. Singh, E. Kätelhön, K. Mathwig, B. Wolfrum, and S. G. Lemay. Stochasticity in Single-Molecule Nanoelectrochemistry: Origins, Consequences, and Solutions. *ACS Nano*, 6(11):9662–9671, 2012.
- [35] S. Kang, A. F. Nieuwenhuis, K. Mathwig, D. Mampallil, and S. G. Lemay. Electrochemical single-molecule detection in aqueous solution using self-aligned nanogap transducers. *ACS Nano*, 7(12):10931–10937, 2013.

References

- [36] E. Kätelhön, K. J. Krause, P. S. Singh, S. G. Lemay, and B. Wolfrum. Noise characteristics of nanoscaled redox-cycling sensors: Investigations based on random walks. *Journal of the American Chemical Society*, 135(24):8874–8881, 2013.
- [37] D. Mampallil, K. Mathwig, S. Kang, and S. G. Lemay. Redox couples with unequal diffusion coefficients: Effect on redox cycling. *Analytical Chemistry*, 85(12):6053–6058, 2013.
- [38] K. Mathwig and S. G. Lemay. Mass transport in electrochemical nanogap sensors. *Electrochimica Acta*, 112:943–949, 2013.
- [39] K. Mathwig and S. G. Lemay. Pushing the limits of electrical detection of ultralow flows in nanofluidic channels. *Micromachines*, 4(2):138–148, 2013.
- [40] E. Kätelhön, D. Mayer, M. Banzet, A. Offenhäusser, and B. Wolfrum. Nanocavity crossbar arrays for parallel electrochemical sensing on a chip. *Beilstein Journal of Nanotechnology*, 5(1):1137–1143, 2014.
- [41] E. Kätelhön, K. J. Krause, K. Mathwig, S. G. Lemay, and B. Wolfrum. Noise phenomena caused by reversible adsorption in nanoscale electrochemical devices. *ACS Nano*, 8(5):4924–4930, 2014.
- [42] D. Mampallil, K. Mathwig, S. Kang, and S. G. Lemay. Reversible adsorption of outer-sphere redox molecules at Pt electrodes. *Journal of Physical Chemistry Letters*, 5(3):636–640, 2014.
- [43] L. Rassaei, K. Mathwig, S. Kang, H. A. Heering, and S. G. Lemay. Integrated biodetection in a nanofluidic device. *ACS Nano*, 8(8):8278–8284, 2014.
- [44] S. Sarkar, K. Mathwig, S. Kang, Ab. F. Nieuwenhuis, and S. G. Lemay. Redox cycling without reference electrodes. *The Analyst*, 139(22):6052–7, 2014.
- [45] H. R. Zafarani, K. Mathwig, S. G. Lemay, E. J. R. Sudhölter, and L. Rassaei. Modulating Selectivity in Nanogap Sensors. *ACS Sensors*, 1(12):1439–1444, 2016.
- [46] A. del Campo and C. Greiner. SU-8: a photoresist for high-aspect-ratio and 3D submicron lithography. *Journal of Micromechanics and Microengineering*, 17(6):R81–R95, 2007.
- [47] J. Melai, C. Salm, S. Smits, J. Visschers, and J. Schmitz. The electrical conduction and dielectric strength of SU-8. *Journal of Micromechanics and Microengineering*, 19(6):065012, 2009.
- [48] C. Chung and M. Allen. Uncrosslinked SU-8 as a sacrificial material. *Journal of Micromechanics and Microengineering*, 15(1):N1–N5, 2005.
- [49] C. Pang, Z. Zhao, L. Du, and Z. Fang. Adhesive bonding with SU-8 in a vacuum for capacitive pressure sensors. *Sensors and Actuators A: Physical*, 147(2):672–676, 2008.

-
- [50] R. J. Jackman, T. M. Floyd, R. Ghodssi, M. A. Schmidt, and K. F. Jensen. Microfluidic systems with on-line UV detection fabricated in photodefinable epoxy. *Journal of Micromechanics and Microengineering*, 11(3):263–269, 2001.
- [51] P. Svasek, E. Svasek, B. Lendl, and M. Vellekoop. Fabrication of miniaturized fluidic devices using SU-8 based lithography and low temperature wafer bonding. *Sensors and Actuators A: Physical*, 115(2-3):591–599, 2004.
- [52] V. Dragoi and E. Pabo. Wafer Bonding for MEMS Vacuum Packaging. *ECS Transactions*, 64(1):221–229, 2014.
- [53] F. Niklaus, G. Stemme, J. Q. Lu, and R. J. Gutmann. Adhesive wafer bonding. *Journal of Applied Physics*, 99(3):031101, 2006.
- [54] M. M. Torunbalci, S. E. Alper, and T. Akin. Wafer level hermetic sealing of MEMS devices with vertical feedthroughs using anodic bonding. *Sensors and Actuators A: Physical*, 224:169–176, 2015.
- [55] D. Sparks, G. Queen, R. Weston, G. Woodward, M. Putty, L. Jordan, S. Zarabadi, and K. Jayakar. Wafer-to-wafer bonding of nonplanarized MEMS surfaces using solder. *Journal of Micromechanics and Microengineering*, 11(6):630–634, 2001.
- [56] Y. T. Cheng, L. Lin, and K. Najafi. Localized silicon fusion and eutectic bonding for MEMS fabrication and packaging. *Journal of Microelectromechanical Systems*, 9(1):3–8, 2000.
- [57] C. S. Tan, J. Fan, D. F. Lim, G. Y. Chong, and K. H. Li. Low temperature wafer-level bonding for hermetic packaging of 3D microsystems. *Journal of Micromechanics and Microengineering*, 21(7):075006, 2011.
- [58] H. Ishida, T. Ogashiwa, T. Yazaki, T. Ikoma, T. Nishimori, H. Kusamori, and J. Mizuno. Low-Temperature Wafer Bonding for MEMS Hermetic Packaging Using Sub-micron Au Particles. *Transactions of The Japan Institute of Electronics Packaging*, 3(1):62–67, 2010.
- [59] J. Kim, B. Jeong, M. Chiao, and L. Lin. Ultrasonic Bonding for MEMS Sealing and Packaging. *IEEE Transactions on Advanced Packaging*, 32(2):461–467, 2009.
- [60] R. Pelzer, H. Kirchberger, and P. Kettner. Wafer-to-Wafer Bonding Techniques: From MEMS Packaging to IC Integration Applications. In *6th International Conference on Electronic Packaging Technology*, volume 2005, pages 1–6. IEEE, 2005.
- [61] G. Wallis and D. I. Pomerantz. Field Assisted Glass-Metal Sealing. *Journal of Applied Physics*, 40(10):3946–3949, 1969.
- [62] A. C. Lapadatu and H. Jakobsen. Anodic Bonding. In *Handbook of Silicon Based MEMS Materials and Technologies*, pages 513–520. Elsevier, 2010.
- [63] T. R. Anthony. Anodic bonding of imperfect surfaces. *Journal of Applied Physics*, 54(5):2419–2428, 1983.

References

- [64] M. X. Chen, X. J. Yi, Z. Y. Gan, and S. Liu. Reliability of anodically bonded silicon-glass packages. *Sensors and Actuators, A: Physical*, 120(1):291–295, 2005.
- [65] W.-S. Kim, J. Lee, and R. S. Ruoff. Nanofluidic Channel Fabrication and Characterization by Micromachining. In *Electronic and Photonic Packaging, Electrical Systems and Photonic Design, and Nanotechnology*, volume 2003, pages 841–846, 2003.
- [66] W.-P. Shih, C.-Y. Hui, and N. C. Tien. Collapse of microchannels during anodic bonding: Theory and experiments. *Journal of Applied Physics*, 95(5):2800–2808, 2004.
- [67] J. L. Perry and S. G. Kandlikar. Review of fabrication of nanochannels for single phase liquid flow. *Microfluidics and Nanofluidics*, 2(3):185–193, 2006.
- [68] Q.-Y. Tong and U. Gösele. Thickness Considerations in Direct Silicon Wafer Bonding. *Journal of The Electrochemical Society*, 142(11):3975, 1995.
- [69] T. Rogers. Considerations of anodic bonding for capacitive type silicon/glass sensor fabrication. *Journal of Micromechanics and Microengineering*, 2(3):164–166, 1992.
- [70] T. Rogers and J. Kowal. Selection of glass, anodic bonding conditions and material compatibility for silicon–glass capacitive sensors. *Sensors and Actuators, A: Physical*, 46-47:113–120, 1995.
- [71] K. M. Knowles and A. T. J. van Helvoort. Anodic bonding. *International Materials Reviews*, 51(5):273–311, 2006.
- [72] T. M. H. Lee, D. H. Y. Lee, C. Y. N. Liaw, A. I. K. Lao, and I. Mi. Hsing. Detailed characterization of anodic bonding process between glass and thin-film coated silicon substrates. *Sensors and Actuators, A: Physical*, 86(1-2):103–107, 2000.
- [73] H. Seidel and L. Csepregi. Anisotropic Etching of Crystalline Silicon in Alkaline Solutions. *Journal of The Electrochemical Society*, 137(11):3612–26, 1990.
- [74] P. Penchev, X. Shang, S. Dimov, and M. Lancaster. Novel Manufacturing Route for Scale Up Production of Terahertz Technology Devices. *Journal of Micro and Nano-Manufacturing*, 4(2):021002, 2016.
- [75] C. G. Van de Walle, F. R. McFeely, and S. T. Pantelides. Fluorine-silicon reactions and the etching of crystalline silicon. *Physical Review Letters*, 61(16):1867–1870, 1988.
- [76] H. Jansen, H. Gardeniers, M. de Boer, M. Elwenspoek, and J. Fluitman. A survey on the reactive ion etching of silicon in microtechnology. *Journal of Micromechanics and Microengineering*, 6:14–28, 1996.
- [77] R. D’Agostino and D. L. Flamm. Plasma etching of Si and SiO₂ in SF₆-O₂ mixtures. *Journal of Applied Physics*, 52(1):162–167, 1981.

-
- [78] T. Syau, B. J. Baliga, and R. W. Hamaker. Reactive Ion Etching of Silicon Trenches Using SF₆/O₂ Gas Mixtures. *Journal of The Electrochemical Society*, 138(10):3076–3081, 1991.
- [79] B. C. Joshi, G. Eranna, D. P. Runthala, B. B. Dixit, O. P. Wadhawan, and P. D. Vyas. LPCVD and PECVD silicon nitride for microelectronics technology. *Indian Journal of Engineering and Materials Sciences*, 7(5-6):303–309, 2000.
- [80] H. Huang, K. J. Winchester, A. Suvorova, B. R. Lawn, Y. Liu, X. Z. Hu, J. M. Dell, and L. Faraone. Effect of deposition conditions on mechanical properties of low-temperature PECVD silicon nitride films. *Materials Science and Engineering A*, 435-436:453–459, 2006.
- [81] L. Liu, W.-G. Liu, N. Cao, and C.-L. Cai. Study on The Performance of PECVD Silicon Nitride Thin Films. *Defence Technology*, 9(2):121–126, 2013.
- [82] J. Yota. Effects of Deposition Method of PECVD Silicon Nitride as MIM Capacitor Dielectric for GaAs HBT Technology. *ECS Transactions*, 35(4):229–240, 2011.
- [83] J. R. Rairden, C. A. Neugebauer, and R. A. Sigsbee. Interdiffusion in thin conductor films — chromium/gold, nickel/gold and chromium silicide/gold. *Metallurgical Transactions*, 2(3):719–722, 1971.
- [84] Y. Huang, H. Qiu, F. Wang, L. Pan, Y. Tian, and P. Wu. Effect of annealing on the characteristics of Au/Cr bilayer films grown on glass. *Vacuum*, 71(4):523–528, 2003.
- [85] W. E. Martinez, G. Gregori, and T. Mates. Titanium diffusion in gold thin films. *Thin Solid Films*, 518(10):2585–2591, 2010.
- [86] J. He, F. Yang, W. Wang, L. Zhang, X. Huang, and D. Zhang. Electric current characteristic of anodic bonding. *Journal of Micromechanics and Microengineering*, 25(6):065002, 2015.
- [87] T. M. Squires and S. R. Quake. Microfluidics: Fluid physics at the nanoliter scale. *Reviews Of Modern Physics*, 77(3):977–1026, 2005.
- [88] K. W. Oh, K. Lee, B. Ahn, and E. P. Furlani. Design of pressure-driven microfluidic networks using electric circuit analogy. *Lab on a Chip*, 12(3):515–45, 2012.
- [89] C. Batchelor-McAuley, E. Kätelhön, E. O. Barnes, R. G. Compton, E. Laborda, and A. Molina. Recent Advances in Voltammetry. *ChemistryOpen*, 4(3):224–260, 2015.
- [90] L. Fan, Y. Liu, J. Xiong, H. S. White, and S. Chen. Electron-transfer kinetics and electric double layer effects in nanometer-wide thin-layer cells. *ACS Nano*, 8(10):10426–10436, 2014.
- [91] C. E. D. Chidsey. Free Energy and Temperature Dependence of Electron Transfer at the Metal-Electrolyte Interface. *Science*, 251(4996):919–922, 1991.

5 Fabrication of a Large Area Horizontal Coplanar Nanogap Device

Here the design and fabrication of a large area horizontal nanogap device is presented. The fabrication process is largely based on electron beam lithography and uses a serpentine geometry so to maximise the length of the electrodes in the writeable area. The electrodes are covered by a passivation layer to maximise the planar interdiffusion between the nanogap. As an example application the device is used for dielectric spectroscopy sensing of PNA–DNA binding.

The device is comprised of two electrodes separated by a central nanogap in the shape of a serpentine. This serpentine consists of twenty $400\text{ }\mu\text{m}$ straight sections connected with twenty arcs of $50\text{ }\mu\text{m}$ radius to provide a total length of $\approx 11\text{ mm}$. The electrodes are covered by a thin SU-8 passivation layer in order to maximise the planar diffusion between the nanogap. The electrodes are easily addressed by large $4\text{ mm} \times 12\text{ mm}$ rectangular contact pads on either side of the nanogap. The top layer consists of a SU-8 microfluidic layer with a $35\text{ }\mu\text{m}$ wide serpentine directly above the nanogap along with funnelled inlet and outlet reservoirs.

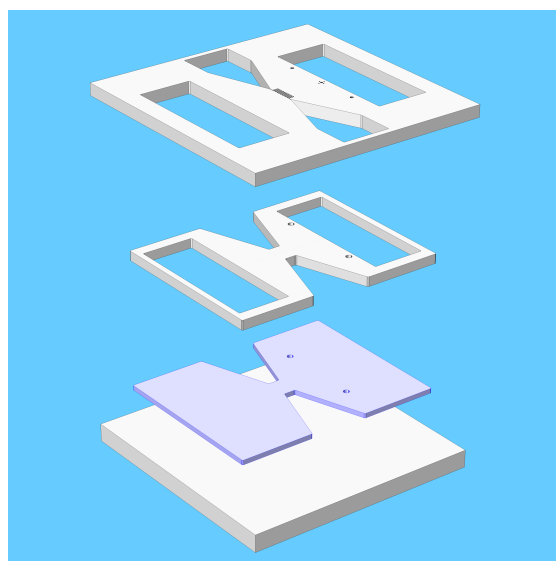


Figure 5.1: 3D exploded diagram of the horizontal nanogap device showing glass substrate, electrode layer (highlighted) and the SU-8 passivation & microfluidic layers.

Nanogap devices have been used in research for several decades and have predominantly exhibited horizontal coplanar geometry. As a consequence, there are several comprehensive

reviews on the subject of fabricating horizontal coplanar nanogaps [1–4]. However, the majority are used for molecular junctions where the objective is to trap a molecule between two point-like electrodes. Here it is desirable for the interelectrode distance to be similar to that of the target molecule and for the contact area to be kept at a minimum in order to improve selectivity.

For electrochemical sensing applications the criteria is rather different. Reducing the inter-electrode distance will lead to improved redox cycling and dielectric spectroscopy sensing, however the surface area must also be considered. Increasing the surface area not only leads to higher measurable currents and higher molar sensitivity but it can also allow greater probe loading for affinity-based biosensing.

Fabricating nanogap electrodes with larger surface areas presents several complications. After all, nanogap fabrication itself often goes beyond the capability of traditional microfabrication technologies. In the previous chapter the primary issue faced with many vertical nanogap devices is preventing the collapse or deformation of the upper electrode. For horizontal nanogap devices the main issue is normally associated with the electrodes shorting from discontinuities, often arising from misalignment.

5.1 Present fabrication techniques for horizontal nanogap devices

Despite the obstacles, several effective and creative methods of fabricating nanogap electrodes with controlled spacing have emerged, these include: adhesion lithography [5–7], chemical-mechanical polishing [8], deep-ultraviolet lithography with silylation [9], dip-pen nanolithography [10], direct chemical synthesis [11], electrochemical synthesis [12], electromigration [13–15], electron-beam lithography, [16, 17], electroplating [18], focused ion beam (FIB) milling [19–22], mechanical break junctions [23, 24], molecular lithography [25], molecular rulers [26, 27], oblique-angle [28] and double oblique-angle evaporation [29], on-wire lithography [30], oxidative plasma ablation [31] and transfer printing [32]. All of these methods have provided promising results and offer their own characteristics. Some examples of these fabrication methods are illustrated in Figure 5.2. It is not uncommon for devices to be fabricated by an amalgamation of methods in order to achieve the desired geometry.

The tool of choice for the creation of nanogap electrodes is, without any doubt, electron-beam lithography (EBL). EBL is a serial process and therefore is more time consuming and costly compared to optical lithography. However, it does provide exceptional resolution, with modern systems capable of achieving features <10 nm. Nevertheless, several non-standard steps can be incorporated with optical lithography to overcome the inherent resolution limitations of the light source wavelength. In the next few pages some of the alternative fabrication techniques to EBL are discussed before moving on to nanogap devices that rely on EBL for at least one step of the fabrication process.

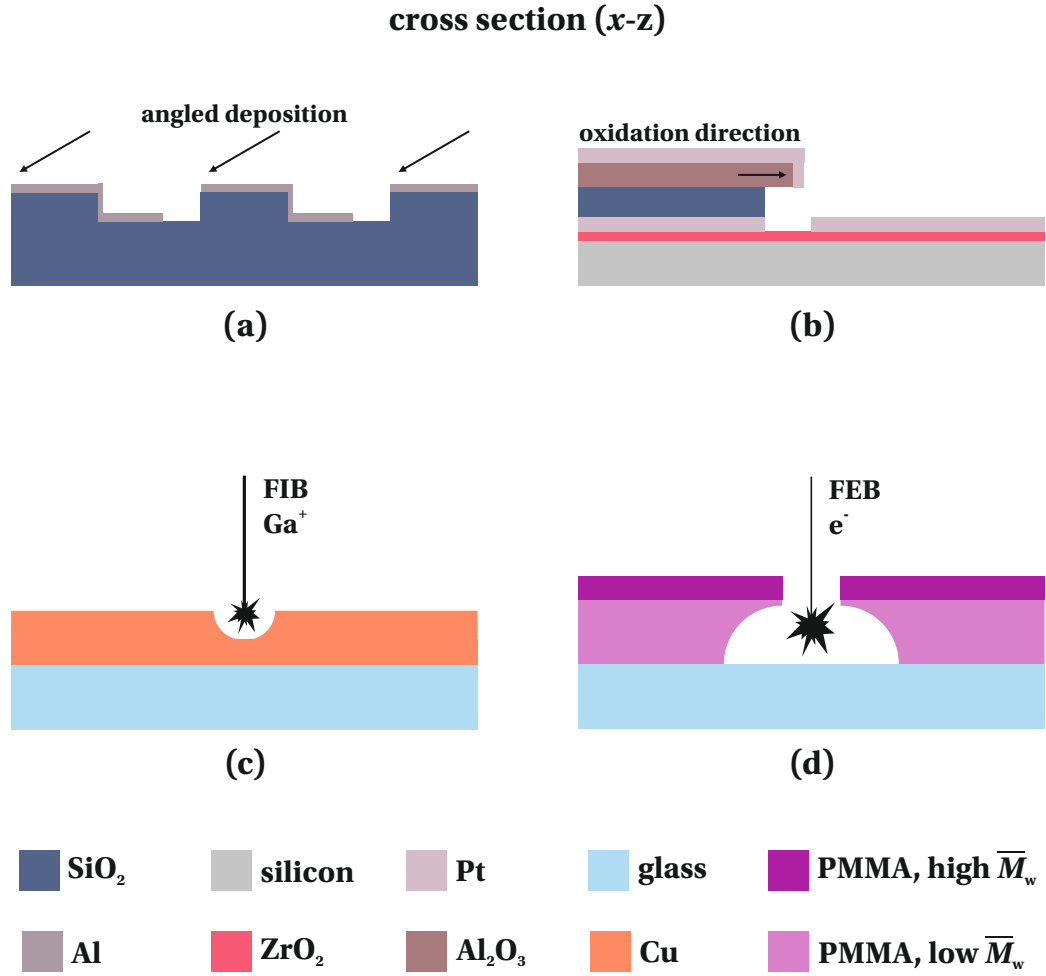


Figure 5.2: Diagram demonstrating some of the fabrication techniques used to obtain horizontal nanogaps: (a) use of oblique-angle deposition with microchannels acting as a shadow-mask [33]; (b) oxidation of a metallic layer to create an overhanging self-aligned mask [34]; (c) milling through a metallic layer with a Ga^+ focused ion beam [35]; and (d) use of a focused electron beam to pattern a bilayer of positive tone electron-beam resists to create the desired lift-off profile.

Oblique-angle deposition/shadow masks

One of the early reports to improve the feature size using optical lithography techniques was oblique-angle deposition. This involves depositing thin films with the substrate set at an angle so that it creates a shadowing effect. Dean and Matarese [36] as well as Dolan [37] demonstrated in the mid 1970s that submicron structures could be created using a single mask and oblique-angle thin-film deposition. Many applications were found in transistor fabrication, for instance Tracy Turner Jones *et al.* used angled deposition to create 50-70 nm source-drain separation [38].

An inventive technique was shown by Ishii *et al.* [39], where an electrospun fibre is stretched to control its diameter and then used as a shadow mask. In this work average gaps of $865 \text{ nm} \pm 109 \text{ nm}$ over an electrode length of 2 mm were achieved. Although the gap deviated by around 13% of the gap size, it does represent a simple, low-cost technique with the merit of achieving long electrode lengths.

The use of micrometre channels acting as shadowmasks has been used by several groups. Adjusting the height of the channels as well as the angle of deposition provides some control over the shadowing effect and thus the final geometry of the nanogaps. Van Gerwen developed this technique and demonstrated fabrication of 500 nm spaced Pd electrodes [40]. Later Jeon *et al.* fabricated 400 nm spaced Al electrodes using this technique for use in impedimetric studies [33]. More recently, Yun *et al.* [41] demonstrated the use of PMMA as a shadow mask to create electrodes separated by 500 nm. The significance of this work is that the technique is solvent-free and therefore sensitive organic materials can be utilised.

As a final note, by performing deposition in opposite directions the shadowing effect can be exploited twice. This 'double oblique-angle deposition' technique has been used to achieve even smaller (5-60 nm) nanogaps [29, 42]. Here the conditions of the second deposition are critical in ensuring that the granularity of the electrode materials do not lead to defects. Liang and Chou successfully used this technique to form electrodes with a width of 45 nm and interelectrode distance of <13 nm perpendicular to a 45 nm wide fluidic channel. This nanofluidic channel allowed electrical signals from double-stranded DNA sequence to be observed as it passed through the gap [43].

Oxidation layer as a self-aligned mask

Another technique avoiding the use of EBL is oxidising a layer in an optically patterned stack to act as self-aligned mask. Hashioka *et al.* [44] first showed how a Ti layer could be used to grow a self-aligned oxide mask, strictly acting as a sacrificial layer. In the initial step a Ti electrode is patterned and covered with a photoresist to allow the Ti to be oxidised laterally by anodic oxidation. An Au layer is then deposited over the entire surface before performing

5.1. Present fabrication techniques for horizontal nanogap devices

lift-off and etching the TiO_x . One issue with this process is that the final device consists of electrodes of dissimilar materials.

A similar approach was taken by Tang *et al.* [34], but with a two-step evaporation to achieve identical electrode materials. First Pt/ SiO_2 /Al layers are patterned on a Si/ ZrO_2 substrate. The Al layer is then oxidised to create an overhanging structure before aligning a second Pt layer. The Al_2O_3 layer acts as a mask creating a nanogap between adjacent Pt layers and the initial SiO_2 /Al layers then act as sacrificial layers allowing lift-off patterning of the second electrode.

Fursina *et al.* [45] adopted this technique but eliminated the difficulties associated with the chemical etching of Al_2O_3 mask by using Cr_xO_y as a substitute. The revised process involved evaporating a Ti/Au/Cr stack before oxidising the Cr layer to create the overhang. This is then used as the mask to deposit a second Ti/Au layer perpendicular to the first, separated by a nanogap. This technique is particularly appealing as it not only provides a self-aligned process but in theory could provide a wide range of interelectrode distances, with gap sizes of ≈ 2 -50 nm and electrode lengths of 1-20 μm having already been demonstrated.

Focused ion beam milling/deposition

A focused ion beam (FIB) can be used to both ablate or deposit material in order to create nanogaps. FIB milling is a process where ions such as Ga^+ or Ar^+ are accelerated towards the substrate to cause sputtering. At higher primary currents relatively large amounts of material can be removed at the expense of surface roughness caused by redeposition. Alternatively, material can be deposited by allowing a precursor gas to chemisorb on the surface before irradiating the area with the beam to invoke deposition.

Santschi *et al.* used FIB milling to create a 1 μm^2 Ti IDA with 50 nm interelectrode distance. The introduction of XeF_2 was shown to reduce redeposition effects [46]. Nanogaps with a range of 56-815 nm, between 100 nm \times 5 μm electrodes, have been fabricated by Hatsuki *et al.* [47]. The group later used a similar device with 250 nm \times 5 μm electrodes separated by a 510 nm gap for impedimetric virus detection [22].

Purohit and coworkers created 40 nm \times ≈ 10 μm Au electrodes separated by 200-300 nm gaps [48]. In this work they report large leakage currents that they attribute to damage of the SiO_2 substrate during FIB milling, highlighting one of the drawbacks of the techniques. Electrodes of different materials (including Au and Cu) with widths of 200 μm and nanogaps ranging from 100 nm to 500 nm were fabricated by Singh *et al.*. These were patterned on different insulating substrates to study the effect of the substrate on leakage current. In this work they also created smaller 20-200 nm nanogaps with ≈ 2 μm wide W electrodes using FIB induced deposition [35].

Although highly complex 3D structures have been fabricated with FIB induced deposition [49], it is often considered a much more time-consuming approach than its counterpart. One major complication is that the induced deposition generated by secondary electrons is bigger than the diameter of the incident beam, leading to a halo effect [50]. This is usually resolved by adopting a suspended substrate, but is less problematic for larger geometries.

A technique using ion irradiation to induce deformation with a FIB system was demonstrated by Cheang-Wong and coworkers. Here FIB milling is first used to create ≈ 800 nm gaps between PdSi electrodes. Then O^{2+} ion irradiation is used to deform the supporting structure, in turn reducing the gap size to around 200 nm [51].

Electron-beam lithography

The use of electron-beam lithography (EBL) is by far the most popular approach to fabricate nanogap devices. EBL uses a focused electron beam to pattern electron-sensitive resists and provides significantly greater resolution capabilities than optical lithography. Early EBL systems were adapted from scanning electron microscopes (SEMs) with dedicated EBL systems developed in the 1970s [52]. Although the proximity effect (interaction of primary electrons with resist and substrate) presents a challenge to EBL processing, at present nanogaps < 10 nm can be routinely created between nanowires using EBL [53, 54]. One of the most important works on metal nanogaps was by the group of Dekker, who developed an EBL fabrication technique [55] that was later used [56] for direct measurement of electrical transport through DNA molecules. Given that the majority of modern techniques to fabricate nanogap electrodes utilise EBL for at least one of the steps, nanogap devices that specifically use EBL to achieve nanogap structures for electrochemical sensing are next discussed.

For electrochemical sensing applications fabricating an interdigitated array (IDA) of electrodes is an effective way of increasing the surface area. An early showcase of the use of EBL to fabricate nanospaced IDAs with a variety electrode materials for electrochemical sensing was the work by Niwa and coworkers [57–59]. Since this there has been a plethora of examples: Au and AuGe IDAs with interelectrode spacings of 150–1300 nm created using EBL were used by Montelius *et al.* for admittance spectroscopy [60]; Au IDAs with interelectrode distances of 250–2000 nm, 200 nm and 30–50 nm have been demonstrated by Hayashi *et al.* [61], Finot *et al.* [62] and Ueno *et al.* [63], respectively.

Although IDAs fabricated by EBL provide a simple way provide nanogap electrode separation with large surface areas, the majority of this area is often exposed to the bulk solution. For highly efficient and selective redox cycling the residence time of electroactive molecules in the nanogap sensing volume should be maximised. For exposed IDAs these molecules can easily diffuse into the bulk solution and therefore the efficiency and selective enhancement is reduced. Solutions have been developed to mitigate this effect, an early example being

the work by Dam to create out-of-plane IDAs with 2 μm interelectrode distances by dry etching microchannels in Si followed by oblique-angle deposition. This work demonstrated that improved confinement of the redox species leads to higher efficiencies and therefore amplification factors [64].

Confinement of nanospaced IDAs was achieved by Goluch *et al.* [65] by creating what they termed a 'nanofluidic IDE' (nF-IDE). First Pt IDAs with 250 nm wide spacing were fabricated using EBL. Nanochannels with widths of 3 μm and heights of 75 nm were then defined by patterning a Cr sacrificial layer before encasing the entire structure in SiO_2 . RIE is then used to define access holes before removing the sacrificial layer with Cr etchant. The authors used the device to show that nF-IDEs provide significantly greater amplification factors through improved confinement of the sample within the nanogap.

Electrochemical and chemical deposition methods

One way to reduce the interelectrode distances without necessarily using laborious non-standard techniques with direct-write technologies is to make use of electrochemical or chemical deposition. These techniques provide a relatively simple and controllable way of tuning the gap size to the nanometre or even atomic scale. However, to date these approaches have only been used for small electrode areas for molecular junction applications

In 1999 the Tao group demonstrated how electrochemical etching or deposition could be used to create structures similar to break junctions between nanowires [66]. Morpurgo *et al.* used the same approach to reduce 50-400 nm nanogaps down to ≈ 1 nm nanogaps [18]. One interesting feature of this process is that it can be easily reversed into the 'dissolution' mode to widen the gap again. This technique has since been demonstrated with a range of electrolytes and metal materials [12, 67–71]. One of the difficulties in this approach is depositing Au electrodes without the use of toxic compounds or strong acids, therefore Pt electrodeposition is favoured [68].

More recently several techniques using chemical deposition have been demonstrated. This technique has the benefit of avoiding the need of external circuitry to conduct the electrochemical deposition. Hatzor & Weiss [26] showed how submicron gaps could be reduced further by the use of layer-by-layer deposition of 'molecular rulers'. Similar demonstrations of electroless plating to reduce nanogap dimensions have since been reported by several others [27, 72–74]. Importantly the work by Ah *et al.* [72] demonstrated that an array of a large number of nanowires separated by 50 nm nanogaps could be processed simultaneously, potentially providing a future high-throughput method of fabrication.

5.2 Fabrication process

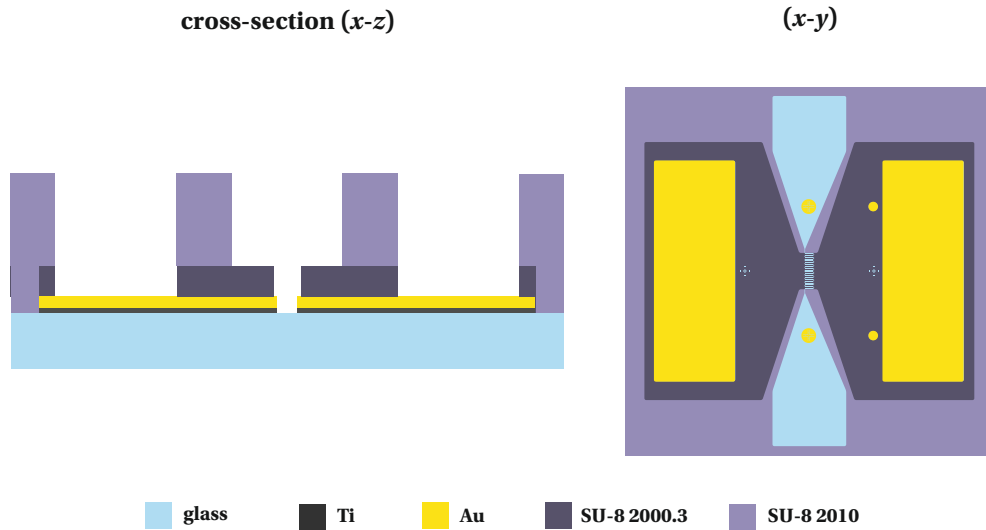


Figure 5.3: Diagram showing the horizontal nanogap device (cross section not to scale).

5.2.1 Overview

This section describes the fabrication of a ≈ 11 mm long nanogap with demonstrated inter-electrode distances between 80 nm and 300 nm. Most importantly, the electrodes are covered by a passivation layer to maximise the planar interdiffusion between the nanogap. A serpentine consisting of twenty $400\ \mu\text{m}$ straight sections connected by twenty arcs of $50\ \mu\text{m}$ radius ensures that the length of the nanogap can be maximised in the writeable area of the EBL instrument. The device takes the shape of a bow-tie with the nanogap situated at the centre and large $4\ \text{mm} \times 12\ \text{mm}$ contact pads on either side. An SU-8 microfluidic layer with a $35\ \mu\text{m}$ wide serpentine sits directly above the nanogap connected to funnelled inlet/outlet reservoirs.

Passivating the top surface of the electrodes was a major challenge in the fabrication. Originally the aim was to use a single EBL step to pattern a Ti hard mask on top of a Ti/Au/SU-8 stack. This hard mask was then used to create the nanogap in both the SU-8 insulating layer and Ti/Au electrode layer using a dry etch and FIB milling process, respectively. ICP-RIE was found to provide satisfactory results for etching through the SU-8 layer, however FIB milling caused significant erosion of both the Ti mask & SU-8 insulating layers and redeposition of milled material limited the aspect ratio. With no current compatible chemistry for dry etching gold (Cl_2/Ar needs to be above $200\ ^\circ\text{C}$ which is too aggressive for this process), a lift-off process was adopted. Some of the early trials are discussed in more detail in Appendix B.1.

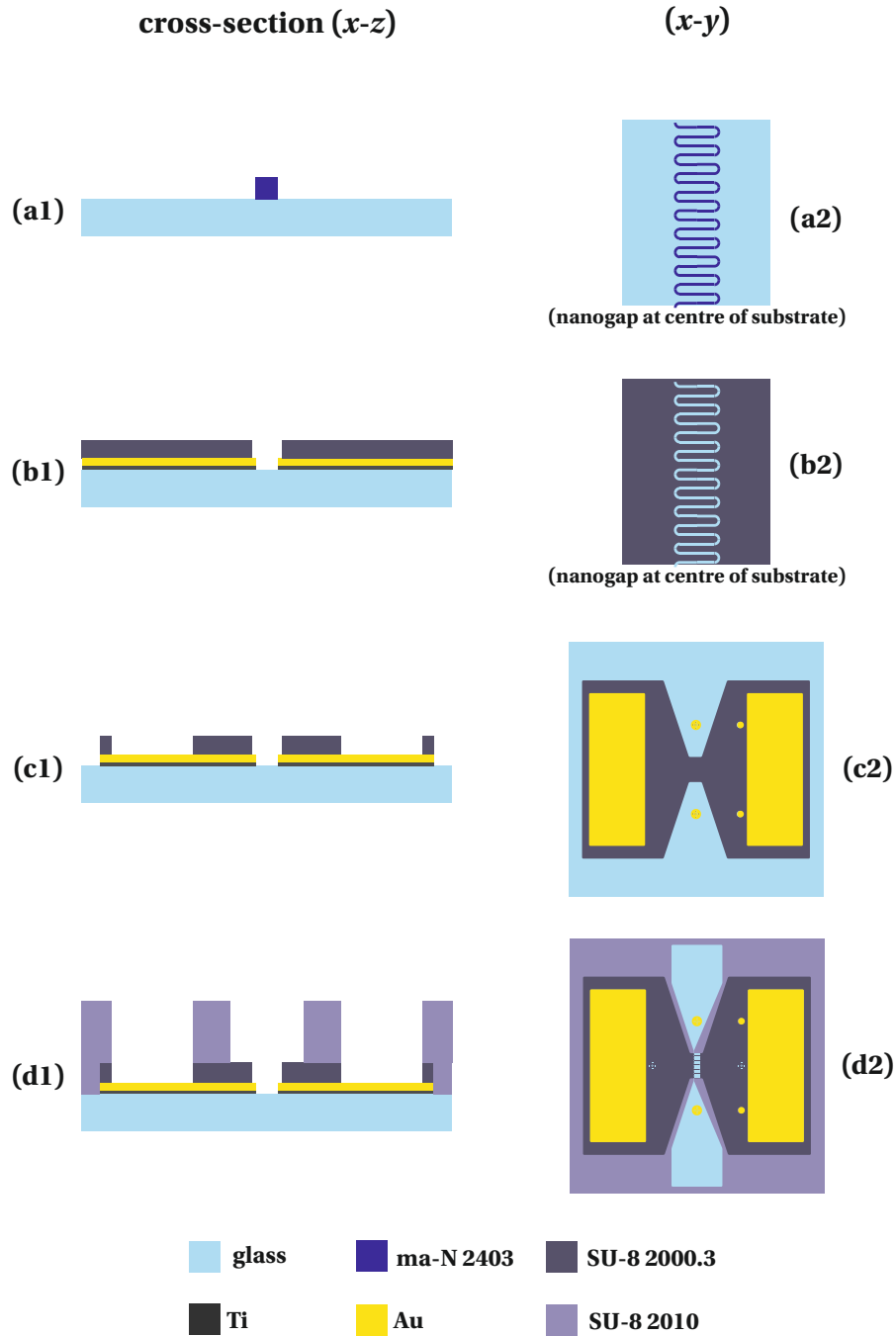


Figure 5.4: Fabrication process of the horizontal nanogap sensor. (a): Electron-beam lithography (EBL) is used to pattern the electrode layers by lift-off method. (b) A thin SU-8 layer is deposited and blanket exposed to form a passivation layer. An aluminium hard mask, patterned with a second EBL lift-off mask, is used to pattern the thin SU-8 layer by reactive ion etching (RIE). (c) A series of wet and dry etching steps are used to define the device geometry and provide access to electrical contact pads. (d) Finally a thick SU-8 layer is optically patterned to provide a microfluidic layer.

The successful fabrication process is based primarily on electron-beam lithography (EBL) using a two-stage process to pattern the electrode layer followed by the passivation layer. In brief, first a Ti/Au electrode layer is patterned using lift-off using a ma-N 2403 negative tone electron-beam resist [MicroChem]. The entire device is then coated with a 300 nm thick SU-8 layer. This SU-8 layer is removed in the vicinity of the nanogap, using a reactive ion etch (RIE) process through an Al hard mask, patterned by lift-off using a second ma-N 2403 resist layer defined with EBL. After patterning the SU-8 passivation layer the Al hard mask is removed using a wet etch process. Two MICROPOSITTM S1813 masks are optically patterned and used to define the device geometry through a sequence of wet and dry etch processes before finally patterning a 10.0 μm thick SU-8 microfluidic layer. The key steps of the fabrication process are summarised in Figure 5.4 and described in more detail throughout this section.

5.2.2 Electrode layer

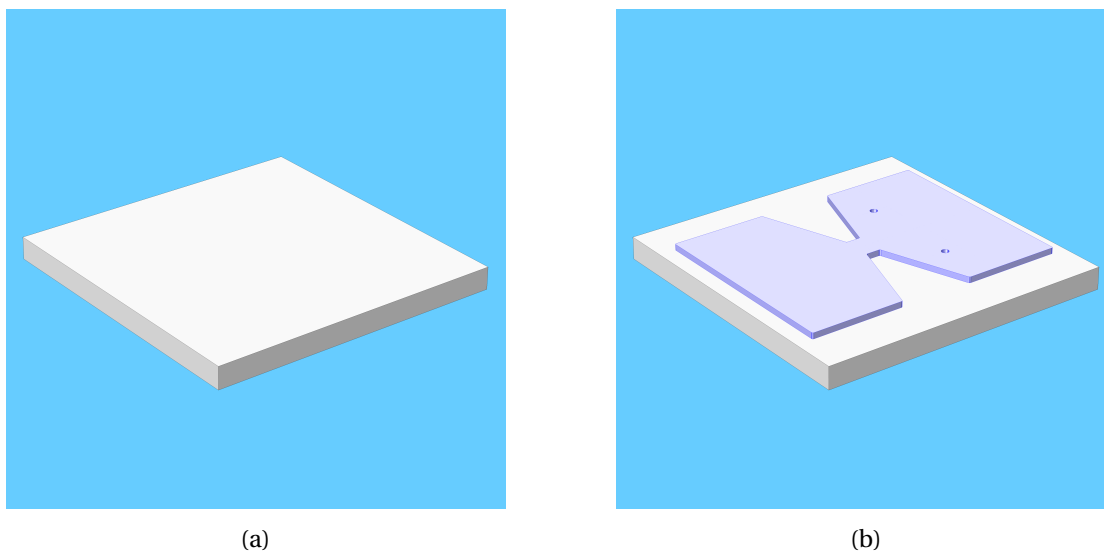


Figure 5.5: 3D diagram showing the (a) glass substrate and (b) patterned electrode layers.

The electrode layer is patterned by a lift-off process using a ma-N 2403 electron-beam resist [MicroChem] patterned with a state-of-the-art JBX-6300FS EBL instrument [JEOL] in a ISO 3 cleanroom. First a 3" BOROFLOAT[®] 33 glass wafer was diced into 20 mm \times 20 mm dies using a MicroAce 66 semi-automatic wafer saw [Loadpoint], then cleaned in acetone then IPA with ultrasonic agitation. The cleaned glass dies were then dehydrated on a hotplate at 200 $^{\circ}\text{C}$ for 10 minutes and allowed to cool.

Next a 300 nm ma-N 2403 negative tone resist was spincoated at 4000 rpm for 40 seconds. A 5 nm Al was then thermally evaporated [Edwards Auto 306] to serve as an anti-charging layer. Originally Au was used as an anti-charging layer but was prone to leaving residues after etching. The ma-N 2403 resist was then patterned to form a 11 mm long, 200 nm wide

serpentine using EBL (exposure conditions: 100 kV, 3.0 nA beam current, 4 nm shot pitch, $1600 \mu\text{C}\cdot\text{cm}^{-2}$ dose).

BEAMER software [GenISys] was used to perform proximity effect correction (PEC), modulating the relative dose and the exposure pattern to address scattering effects within the resist and substrate that spatially and energetically redistribute the electrons of the incident beam. PEC therefore improves the productivity and process reproducibility of EBL and high contrast 3D PEC has been successfully demonstrated for complex applications such as the fabrication of suspended masks [75].

The Al layer was then removed by wet etching in PAN etchant ($\text{H}_3\text{PO}_4:\text{HNO}_3:\text{HAc}:\text{H}_2\text{O}$, 80:5:5:10, vol.) with manual agitation for 90 seconds before developing the resist in MICROPOSITTM MF-322. The electrode layer was formed by an electron-beam evaporation [Leybold Vacuum Univex 350] of a 5 nm Ti adhesion layer followed by 150 nm Au (multi-step deposition). Lift-off was performed in *N*-Methyl-2-pyrrolidone (NMP) (MICROPOSITTM Remover 1165) at 80 °C for 10 minutes followed by 5 minutes with 50% ultrasonic agitation at room temperature (RT).

Table 5.1: Process parameters for patterning the electrode layer.

Step	Description
1a	Dice wafer into 20 mm × 20 mm dies using semi-automated wafer saw
1b	Clean substrates: ultrasonic agitation in acetone then IPA, rinse in IPA, N ₂ dry
1c	Dehydration bake on hot plate, 10 min at 200 °C
1d	Allow samples to cool to RT and use immediately
2a	Spincoat ma-N 2403 (300 nm), 5 s at 500 rpm, 100 rpm·s ⁻¹ , 40 s at 4000 rpm, 10,000 rpm·s ⁻¹
2b	Softbake on hotplate, 2 min at 90 °C
2c	Thermal evaporation of Al anti-charging layer (5 nm, 0.3 nm·s ⁻¹ at 34 A, $P = 4.0 \times 10^{-7}$ mbar)
3a	Electron-beam exposure, 100 kV, 3.0 nA beam current, 4 nm shot pitch, $1600 \mu\text{C}\cdot\text{cm}^{-2}$ dose [JEOL JBX-6300FS]
3b	Remove Al anti-charging layer in PAN etchant (80:5:5:10, $\text{H}_3\text{PO}_4:\text{HNO}_3:\text{HAc}:\text{H}_2\text{O}$, vol.), 90 s with manual agitation, quench in DI water
3c	DI water rinse, N ₂ dry
3d	Manual agitation in MICROPOSIT TM MF-322 developer, 90 s at RT
4a	Electron-beam evaporation of electrode layer Ti (5 nm, 0.1 nm·s ⁻¹ at 7.33 kV, 20 mA) and Au (40/60/30/20 nm, 1.0 nm·s ⁻¹ at 7.51 kV, 278 mA, $P = 1.2 \times 10^{-6}$ mbar)
4b	Lift-off in MICROPOSIT TM PR1165 Remover, 10 min at 80 °C
4c	Ultrasonic agitation (50%) in MICROPOSIT TM PR1165 Remover, 5 min at RT
4d	DI water rinse, N ₂ dry

Adhesion of the ma-N 2403 to the substrate was found to be a limiting factor for reducing the nanogap size. Trials showed that pattern collapse occurs for ma-N 2403 for features <70 nm. The use of PMMA as an adhesion layer was trialled but the PMMA was cross-linked under the ma-N 2403 leading to a ‘halo’ effect. Attempts to etch the PMMA by ICP-RIE with O₂ chemistry were unsuccessful. These trials are discussed further in Appendix B.2.

An alternative would be to add a thin Cr adhesion layer under the ma-N 2403, this could be easily removed with a wet etch during the sequence of etch processes after patterning the passivation layer. Preliminary trials showed that the Cr significantly improved the adhesion, allowing smaller nanogaps to be patterned. Providing the layer is kept very thin and assuming some level of undercutting during the wet etch process, its affect on the sensor performance should be minimal. Furthermore, dedicated adhesion promoters such as SurPass 3000/4000 [DisChem] could also be used.

5.2.3 Passivation layer

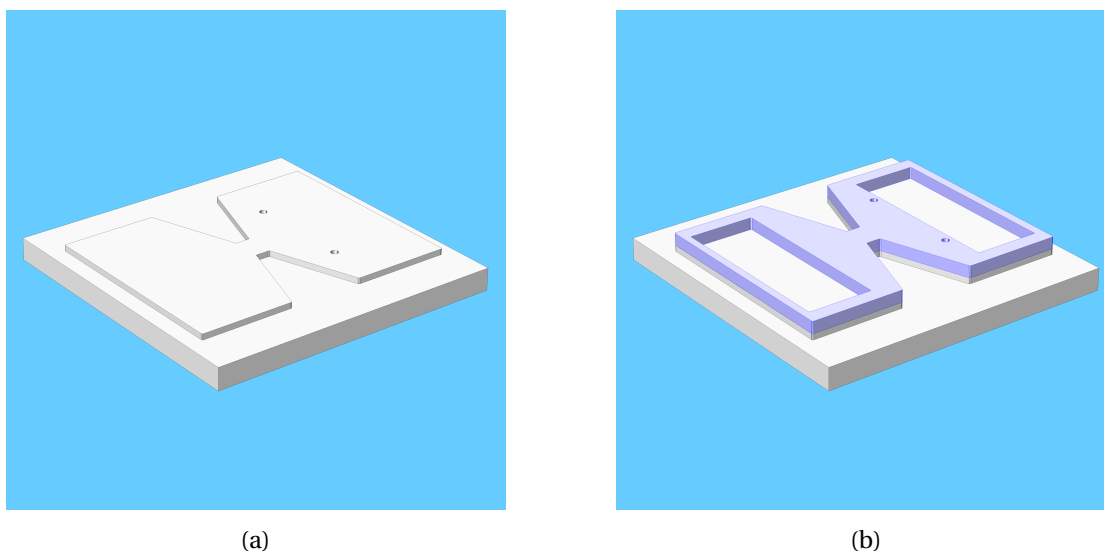


Figure 5.6: 3D diagram showing the sample with (a) just the electrode layer and (b) both the electrode and passivation layers.

At this point a serpentine nanogap has been created between two Ti/Au electrodes. However, the top surface of the electrodes must be passivated so that it does not provide any contribution to the sensor response. This ensures that the electric field and interdiffusion is primarily planar across the nanogap. The high dielectric strength ($0.44 \text{ GV}\cdot\text{m}^{-1}$ for SU-8 2000 [76]) and long-term stability of SU-8 makes it well suited to sensor applications with high electric fields.

In order to achieve a 300 nm thickness, SU-8 2002 [MicroChem] was diluted with cyclopentanone (8:15, SU-8 2002 : cyclopentanone, wt.). Samples were first cleaned with UV-ozone [Jelight Company 42-220] the the diluted SU-8 was applied and spincoated at 4000 rpm for 40 seconds, softbaked and flood-exposed for 10 seconds at $14.6 \text{ mW}\cdot\text{cm}^{-2}$ (365 nm) to initiate cross-linking using a EVG 610 lithography system. Further cross-linking is achieved through an acid-catalysed thermally driven post-exposure bake on two separate hotplates, first at 95°C , then at 130°C . This passivation layer is then patterned, providing access to the nanogap, using ICP-RIE with a O_2 chemistry using a Al hard mask patterned with a ma-N 2403 lift-off mask defined by EBL.

The second ma-N 2403 lift-off layer was carefully aligned to the initial layer (accurate alignment critical in preventing defects) and an identical nanogap serpentine patterned by EBL (exposure conditions: 100 kV, 3.0 nA beam current, 4 nm shot pitch, $1600 \mu\text{C}\cdot\text{cm}^{-2}$ dose). Again, BEAMER software was used to perform PEC. After exposure the resist was developed in MICROPOSITTM MF-322. Figure 5.7 shows the developed lift-off mask; on inspection, some subsidence of the SU-8 film is visible, but this does not seem to dramatically affect the lift-off process (and provides a marked improvement over the 80 nm film used in the FIB trials). A 25 nm Al was then deposited by electron-beam evaporation before lift-off in NMP.

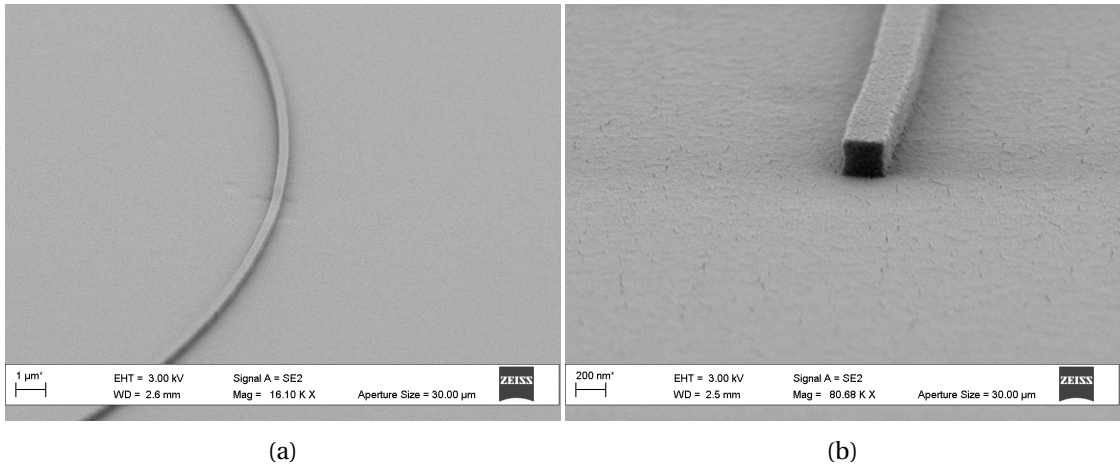


Figure 5.7: SEM images showing the second ma-N 2403 layer after development.

Using the Al as a hard mask, the SU-8 in the nanogap was removed by low-pressure ICP-RIE with an O₂ chemistry [Advanced Vacuum Vision ICP] using the parameters in Table 5.2. The Al layer is then removed using PAN etchant before rinsing in DI water. Figure 5.8 shows a straight $\approx 12.5 \mu\text{m}$ section of the passivated nanogap, the gap is measured to be $\approx 215 \text{ nm}$, with the SU-8 passivation layer receded 60 nm perpendicular from each electrode face [Figure 5.8b].

Table 5.2: ICP-RIE parameters used for low-pressure SU-8 etching.

Parameter	Value
O ₂ flow rate	20 SCCM
Operating pressure (stabilisation)	10 mTorr
Operating pressure	1 mTorr
Substrate temperature	25.0 °C
RF power	40 W
ICP power	150 W, $t_s = 10 \text{ s}$, $t = 4 \text{ min}$

The receding of the SU-8 layer is undesirable as it partially exposes the top surface of the electrodes, which will result in some fringing fields and hemispherical diffusion. The low pressure improves directionality by increasing the mean free path in the plasma and hence increased ion energy, however etch anisotropy could be further improved with the addition

of SF_6 , as demonstrated by Rasmussen *et al.* [77]. SF_6 adds more heavy, charged and non-charged particles that can be exploited to increase directionality providing a high RF power (>25 W) is maintained. The presence of fluorine should also help reduce the antimony present in SU-8 accumulating during the etch process through the formation of antimony tri- and pentafluoride which can evaporate from the surface, also reducing surface roughness.

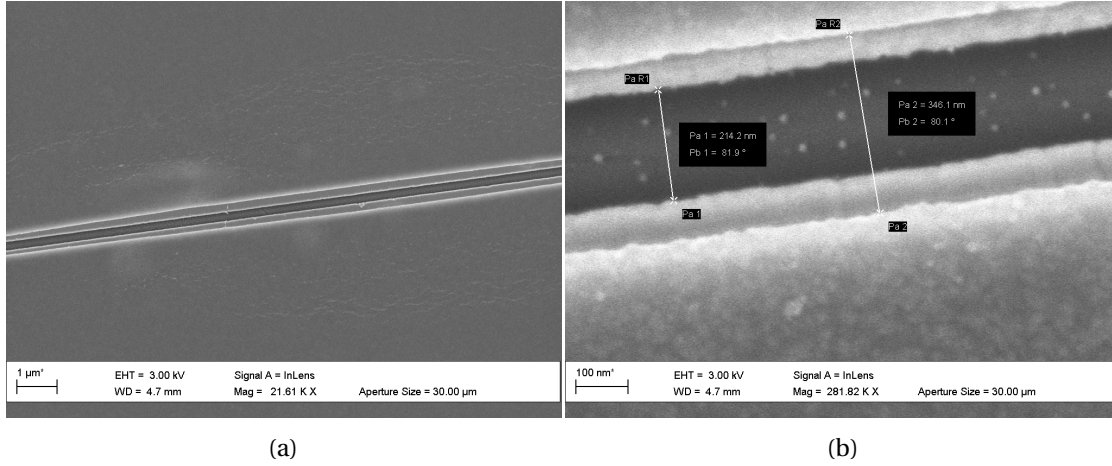


Figure 5.8: SEM images showing the electrode and passivation layers after lift-off (Figure 5.4, view (b).): (a) A ≈ 12 μm straight section of the serpentine. (b) Measurements of the separation of both the electrode and passivation layers.

Table 5.3: Process parameters for patterning the passivation layer.

Step	Description
1a	Clean samples with UV-ozone, 10 min
1b	Spincoat diluted SU-8 (8:15, SU-8 2002 : cyclopentanone, wt.) 5 s at 500 rpm, 100 rpm·s ⁻¹ , 40 s at 4000 rpm, 10,000 rpm·s ⁻¹
1c	Softbake on hotplate, 5 min at 95 °C
1d	Flood exposure, 10 s at 14.6 mW·cm ⁻² (365 nm) [EVG 610]
1e	Post-exposure bake on hotplate, 2 min at 95 °C, then 3 min at 130 °C
2a	Spincoat ma-N 2403 (300 nm), 5 s at 500 rpm, 100 rpm·s ⁻¹ , 40 s at 4000 rpm, 10,000 rpm·s ⁻¹
2b	Softbake on hotplate, 2 min at 90 °C
2c	Electron-beam exposure, 100 kV, 3.0 nA beam current, 4 nm shot pitch, 1600 $\mu\text{C}\cdot\text{cm}^{-2}$ dose [JEOL JBX-6300FS]
2d	Manual agitation in MICROPOSIT TM MF-322 developer, 120 s at RT
2e	DI water rinse, N ₂ dry
3a	Electron-beam evaporation of Al hard mask (25 nm, 1.3 nm·s ⁻¹ at 7.57 kV, 174 mA, $P = 2.7 \times 10^{-7}$ mbar
3b	Lift-off in MICROPOSIT TM PR1165 Remover, 10 min at RT
3c	Ultrasonic agitation (50%) in MICROPOSIT TM PR1165 Remover, 5 min at RT
4a	Etch SU-8 using low-pressure ICP RIE with O ₂ chemistry, 4 min at 150 W
4b	Etch Al hard mask in PAN etchant (80:5:5:10, H ₃ PO ₄ :HNO ₃ :HAC:H ₂ O, vol.), 90 s with manual agitation, quench in DI water
4c	DI water rinse, N ₂ dry

5.2.4 Etch processes for defining device geometry and electrical access

With the nanogap electrodes now passivated, the device is patterned with a series of wet and dry etch processes to define the bow-tie geometry and provide access to electrical contact pads. All optical lithography was performed by optical lithography using 4" chrome masks (CBL4009Du-AZ1500) patterned using a μPG 101 direct laser writer (DLW) [both from Heidelberg Instruments Mikrotechnik]. Photomask designs were created using CleWin4 layout editor [WieWeb].

The first MICROPOSITTM S1813 mask is used to define the boundary of the electrodes followed by low-pressure ICP-RIE to clear the SU-8 followed by KI:I₂:H₂O and HF:H₂O wet etches to etch the Au and Ti layers, respectively. The dilute HF etch caused significant undercutting ($\approx 1 \mu\text{m}$) of the Au layer at the boundary. Reducing this undercut is difficult without leaving Ti residues so the undercut was accepted.

A second MICROPOSITTM S1813 mask is used with the same low-pressure ICP-RIE process to etch through the SU-8 and provide access to the electrical contact pads. This is then removed in acetone and the device cleaned with an IPA rinse and N₂ dry before proceeding to pattern the microfluidic layer. The process parameters for the optical lithography and etch processes are detailed in Table 5.4.

Chapter 5. Fabrication of a Large Area Horizontal Coplanar Nanogap Device

Table 5.4: Process parameters for the sequence of etch processes to define device geometry and provide electrical access.

Step	Description
1a	Spincoat MICROPOSIT TM S1813, 5 s at 500 rpm, 100 rpm·s ⁻¹ , 40 s at 3000 rpm, 10,000 rpm·s ⁻¹
1b	Softbake on hotplate, 3 min at 110 °C
1c	Exposure, 3.2 s at 14.6 mW·cm ⁻² (365 nm), soft contact [EVG 610]
1d	Manual agitation in MICROPOSIT TM MF-319 developer, 60 s at RT
1e	DI water rinse, N ₂ dry
2a	Etch SU-8 using low-pressure ICP-RIE with O ₂ chemistry, 105 s at 150 W
2b	Etch Au in KI:I ₂ :H ₂ O (8:2:80, vol.), 90 s with manual agitation, quench in DI water
2c	Etch Ti in HF:H ₂ O (1:10, vol.), 25 s with manual agitation, quench in DI water
2d	Remove MICROPOSIT TM S1813 in acetone, IPA rinse, N ₂ dry
3a	Spincoat MICROPOSIT TM S1813, 5 s at 500 rpm, 100 rpm·s ⁻¹ , 40 s at 3000 rpm, 10,000 rpm·s ⁻¹
3b	Softbake on hotplate, 3 min at 110 °C
3c	Exposure, 3.2 s at 14.6 mW·cm ⁻² (365 nm), soft contact [EVG 610]
3d	Manual agitation in MICROPOSIT TM MF-319 developer, 60 s at RT
3e	DI water rinse, N ₂ dry
4a	Etch SU-8 using low-pressure ICP RIE with O ₂ chemistry, 115 s at 150 W
4b	Remove S1813 in acetone, IPA rinse, N ₂ dry

5.2.5 Microfluidic layer

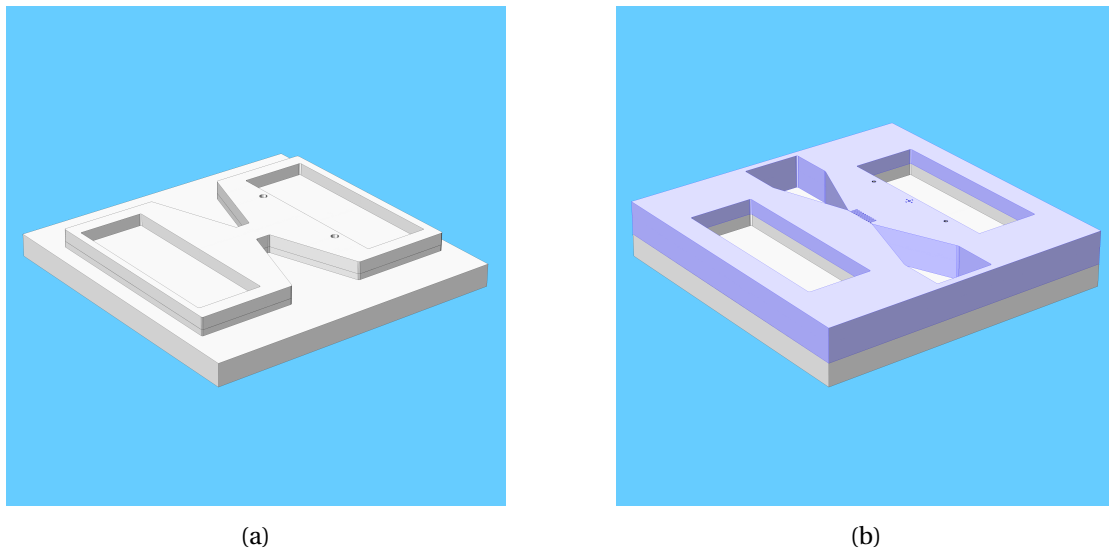


Figure 5.9: 3D diagram showing the sample (a) before and (b) after patterning the microfluidic layer.

With the passivated nanogap now formed, the final step is to optically pattern the microfluidic layer. A 10.0 μm SU-8 2010 [MicroChem] microfluidic layer is spincoated and optically patterned using an EVG 610 semi-automated mask aligner system. The pattern consists of a 35 μm wide serpentine directly above the nanogap serpentine connected to funnelled inlet and outlet reservoirs. To reduce ‘T-topping’ the exposure was performed with the addition of a ZJB360 long-pass ($\lambda_c = 365 \text{ nm}$) optical i-line filter [Omega Optical]. T-topping is a phenomenon observed in patterning thick SU-8 films, where the top surface is overexposed to the UV spectrum and results in an undesirable overhang. This is resolved by blocking the shorter wavelengths ($<350 \text{ nm}$) during exposure [78].

The SU-8 was then developed with MICROPOSITTM EC Solvent 11 in two separate baths and hardbaked at 150 °C for 20 minutes. Early devices were covered in surface cracks, presumably from the residual stress in the thick SU-8 layer. To resolve this the processing parameters were optimised using a batch of test devices mimicking the stack of layers. Slightly increased exposure doses and extending the second step of the post-exposure bake (95 °C) improved matters but ultimately the problem was best resolved with a lengthy hardbake. The prolonged elevated temperature of the hardbake anneals the surface cracks of even the worst samples.

Table 5.5: Process parameters for patterning the microfluidic layer.

Step	Description
1a	Spincoat SU-8 2010, 5 s at 500 rpm, 100 rpm·s ⁻¹ , 40 s at 4000 rpm, 10,000 rpm·s ⁻¹
1b	Softbake on hotplate, 1 min at 65 °C then 5 min at 95 °C, allow to cool to RT
1c	Exposure, 1050 mJ·cm ⁻² (365 nm), soft contact, ZJB360 filter [EVG 610]
1d	Post-exposure bake on hotplate, 1 min at 65 °C then 3 min at 95 °C, allow to cool to RT
1e	Manual agitation in MICROPOSIT TM EC Solvent 11, 2 min bath 1, 1 min bath 2, at RT
1f	IPA rinse, N ₂ dry
1g	Hardbake on hotplate, 20 min at 150 °C

Figure 5.10 shows a completed device with the microfluidic serpentine visible at the centre of the device, surrounding alignment marks and the electrical contact pads on either side of the device. A close-up shows the surface cracks due to the residual stress in the SU-8 layer [Figure 5.10b]. The majority of these surface cracks disappear after annealing with the hardbake. Samples can be introduced into the device by pipetting a small volume into the reservoirs and allowing capillary flow to transport the solution towards the centre of the device (typically 25 seconds). Alternatively a polydimethylsiloxane (PDMS) lid can be bonded to the SU-8 microfluidic layer with O₂ plasma activation and silanisation with (3-Aminopropyl)triethoxysilane (APTES) [79,80].

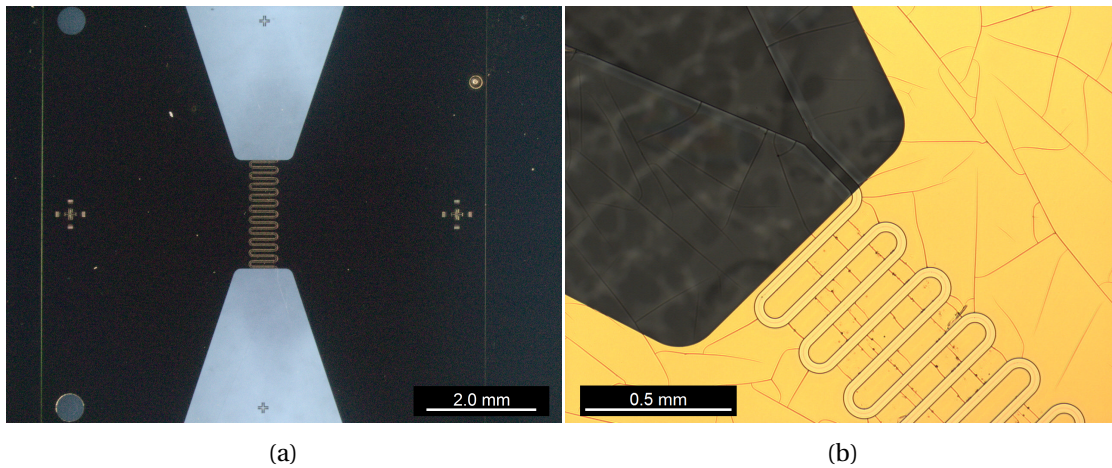


Figure 5.10: Microscope images showing a completed device: (a) The bow-tie-shaped sensor with contact pads and central microfluidic channel visible. (b) A close-up showing the serpentine microfluidic channel with funnelled inlet/outlet.

5.3 Simulation

To further understand the importance of the geometry at the micro- and nanoscale, the system was modelled using COMSOL Multiphysics[®] finite element analysis software. The electrostatics and microfluidic simulations are covered separately in Appendices C.1 & C.2, respectively. Figure 5.11 shows a cross section of the fabricated device.

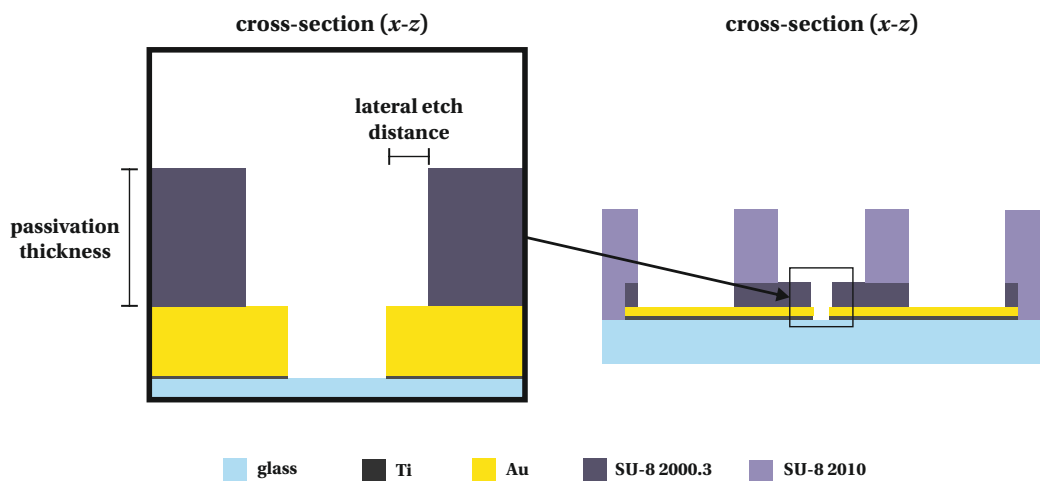


Figure 5.11: Annotated diagram depicting exposed top surface of the nanogap electrodes.

5.3.1 Effect of the passivation layer on device performance

The passivation layer is formed by coating the electrodes with SU-8, in the process filling the nanogap, before cross-linking. The SU-8 between the electrodes is then etched using ICP-RIE with a Al hard mask. Some undercutting of the Al hard mask occurs leading to undesirable lateral etching of the passivation layer. The result is that a portion of the top surface of the electrode is left exposed. For an ideal geometry the lateral etch distance would be zero, meaning that the top surface of the electrodes would be completely covered. However, due to the undercutting during ICP-RIE, the actual lateral etch distance of the fabricated device is ≈ 65 nm. The effect of this nonideality on the limiting current density was simulated using the electroanalysis interface of the electrochemistry module in COMSOL Multiphysics®. Figure 5.12 shows the cyclic voltammograms (CVs) and surface concentration plots for the fabricated device geometry and ideal geometry. The lateral etching of the passivation layer leads to a reduction the limiting current density from $19.88 \text{ A}\cdot\text{m}^{-2}$ to $17.19 \text{ A}\cdot\text{m}^{-2}$, a reduction of $\approx 13.5\%$.

The effect of this nonideality was studied by simulating the limiting current density as a function of the lateral etch distance whilst maintaining the passivation thickness at 300 nm [Figure 5.13a]. Increasing the lateral etch distance from 0 nm to 135 nm results in a decrease of the limiting current density from $19.88 \text{ A}\cdot\text{m}^{-2}$ to $14.37 \text{ A}\cdot\text{m}^{-2}$, a reduction of 27.7%.

In comparison, the effect of the passivation thickness is less pronounced. Figure 5.13b shows the limiting current density plotted against passivation thickness. In this case the interelectrode distance is set as 215 nm, the lateral etch distance is maintained at 65 nm (345 nm total distance) and the height of the electrodes is 150 nm. Reducing the passivation thickness to 100 nm led to a greater current density ($17.47 \text{ A}\cdot\text{m}^{-2}$), possibly due to improved diffusive access. When increasing the passivation thickness to 500 nm the current density was decreased by 1.7% ($17.18 \text{ A}\cdot\text{m}^{-2}$). Here the passivation thickness did not appear to affect the collection efficiency.

For an ideal geometry the decrease in current density when increasing the passivation thickness from 100 nm to 500 nm was just 0.2% (19.93 to $19.88 \text{ A}\cdot\text{m}^{-2}$, data not shown), yet there was a $\approx 1\%$ increase in collection efficiency. This may be explained by the fact that here the diffusive flux between the generator and collector is entirely planar, so increasing the passivation layer provides improved confinement of the redox species, reducing the probability of diffusion back into the microchannel.

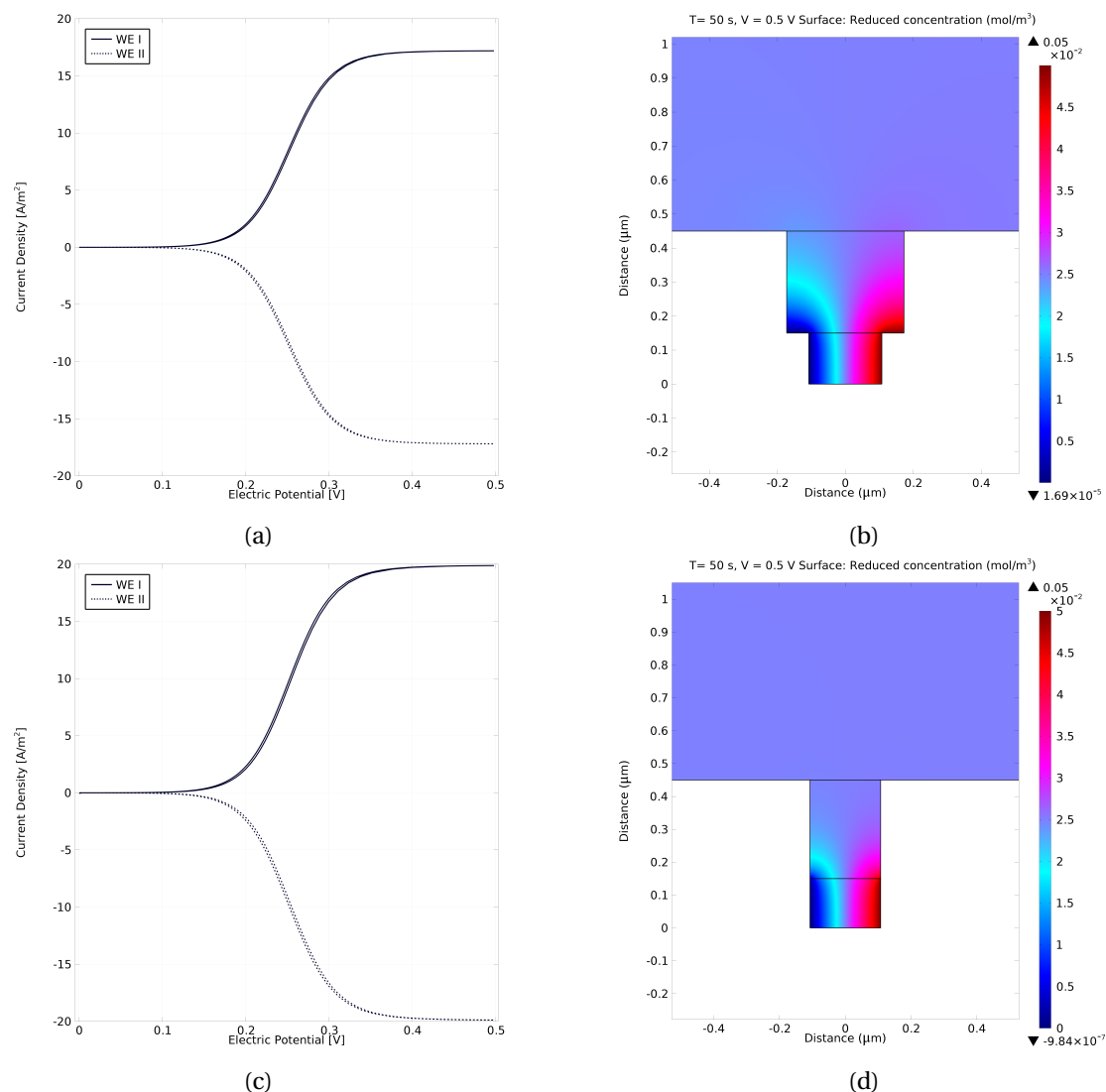


Figure 5.12: Simulated current response and surface concentration plots demonstrating the effect of undesirable lateral etching of the passivation layer.

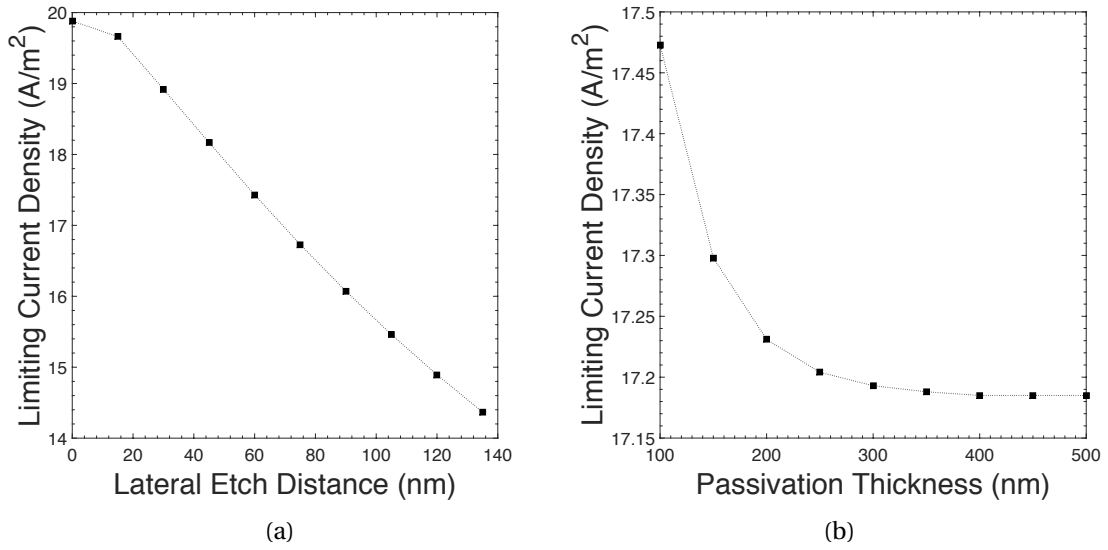


Figure 5.13: Simulated limiting current density for (a) increasing lateral etch distance and (b) increasing passivation height.

5.4 Electrical characterisation

I-V characteristics in air were measured using a B1500A semiconductor device analyser [Agilent Technologies] and a probe station [Wentworth Labs] placed on an isolation table [Newport] equipped with 4 micropositioners [JMicron Technology]. Connections to the device were made using a four-terminal (Kelvin) configuration. The entire setup was housed in a large Faraday cage. Figure 5.14 shows that the leakage current at -125 mV is ≈ 500 pA, equating to an isolation of ≈ 0.25 G Ω . Increasing the potential window further eventually led to breakdown, with the device exhibiting ohmic behaviour, indicating a short.

The device could be recovered by permitting higher currents to ‘blow’ the short (potentially creating more in the process), returning the device to open-circuit behaviour. However, the Joule heating leaves a small, approximately symmetric, crater along the nanogap. After recovering from breakdown the leakage current increased to ≈ 1.5 nA at 100 mV, equating to an isolation of ≈ 67 M Ω .

The capacitance response in air and in 10 mM PBS (with 2.7 mM KCl and 137 mM NaCl) were recorded using a B1500A semiconductor device analyser fitted with a 1 kHz to 5 MHz multi-frequency capacitance measurement unit (MFCMU) [Agilent Technologies]. Connections were made using a four-terminal pair configuration with the L_p & L_c and H_p & H_c terminals shorted on the contact pads of the device. The response was recorded for a frequency range of 1 kHz to 1 MHz with a 0.0 V DC bias and a 10 mV AC signal using a ‘long’ integration time (16 power line cycles).

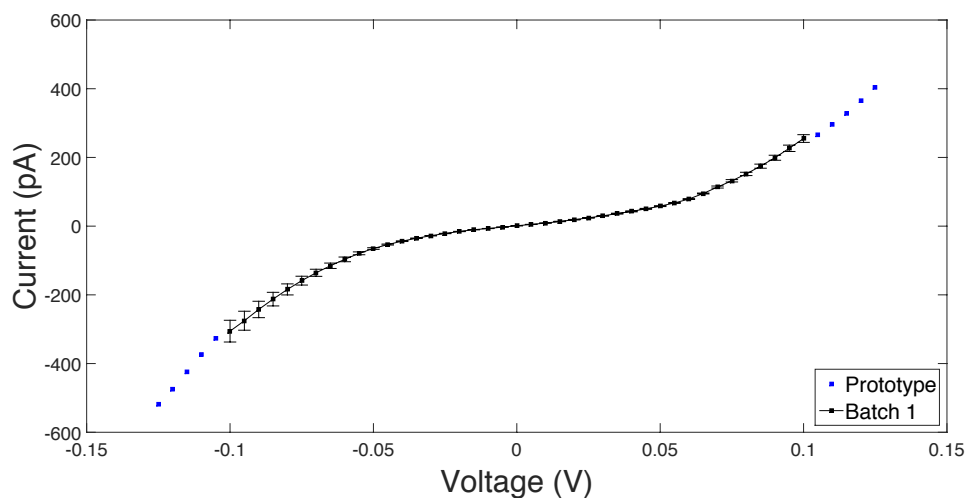


Figure 5.14: Measured I-V responses in air for a prototype and a batch of five horizontal nanogap devices.

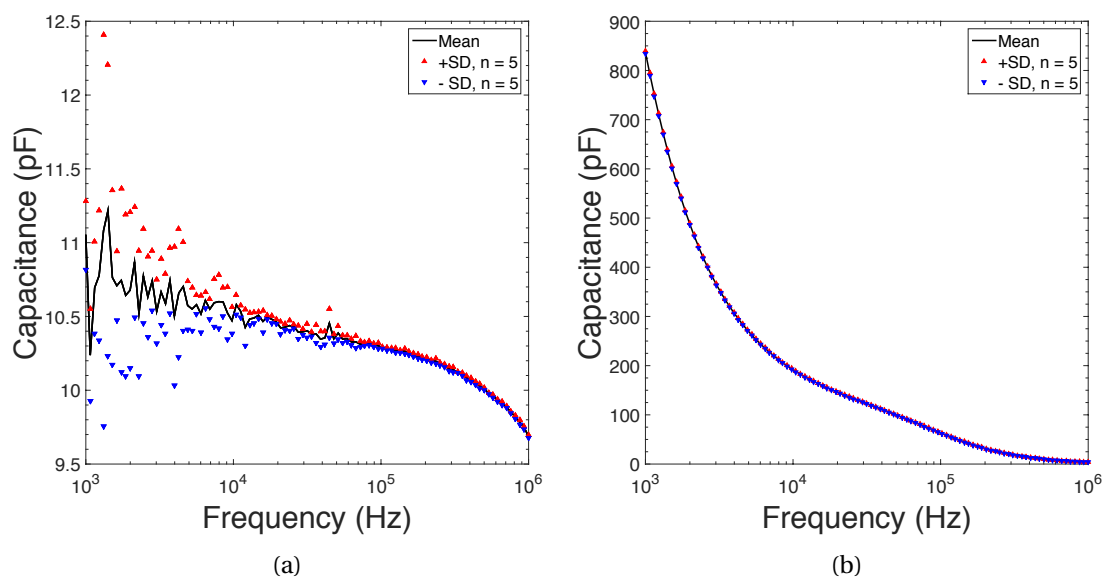


Figure 5.15: Capacitance profiles for the frequency range 1 kHz to 1 MHz in (a) air and in (b) 10 mM PBS.

The electrochemical response was confirmed by performing redox cycling with 50 μM 1,1'-ferrocenedimethanol ($\text{Fc}(\text{CH}_2\text{OH})_2$) in 10 mM phosphate buffer (with 2.7 mM KCl and 137 mM NaCl) [both from Sigma Aldrich]. A potential window of 0.0 V to 0.5 V *vs.* Ag/AgCl was used with a scan rate of 2.5 $\text{mV}\cdot\text{s}^{-1}$. The electrochemical measurements were taken using the B1500A semiconductor device [Agilent Technologies], with a potential step size of 1 mV and both the hold and delay time set to 200 ms. All connections were made to the device using micropositioners [JMicron Technology]. A pseudo reference electrode created using Ag wire and Ag/AgCl ink [BASi®] was connected to the dedicated ground unit (GNDU) and both the generator and collector electrodes connected to individual source measurement units (SMUs).

Figure 5.16 shows that steady-state response is reached, with the limiting currents for the generator and collector calculated as 25.11 nA and -24.84 nA, respectively, yielding a collection efficiency (η_c) of 98.9%. The simulated response [data not shown] provided limiting current densities of $17.198 \text{ A}\cdot\text{m}^{-2}$ and $-17.197 \text{ A}\cdot\text{m}^{-2}$ for the generator and collector, respectively, with a value for η_c of 99.9%. Using the calculated length of the nanogap serpentine (10.91 mm) and electrode height (150 nm), the overlapping region of the electrodes is calculated as $1.6365 \times 10^{-9} \text{ m}^2$. Multiplying by the current density provided an expected limiting current of 28.14 nA, which is much higher than that measured experimentally. It is possible that this could be caused by intrinsic defects in the passivation layer, defects caused by SEM inspection or defects caused by Joule heating during I-V sweeps.

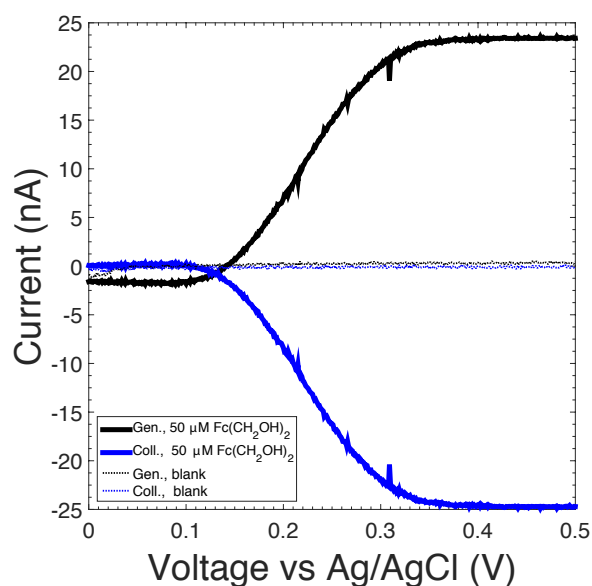


Figure 5.16: Current response in 10 mM phosphate buffer, 2.7 mM KCl, 137 mM NaCl, pH 7.4, with and without the addition of 50 μM $\text{Fc}(\text{CH}_2\text{OH})_2$ at a scan rate of 2.5 $\text{mV}\cdot\text{s}^{-1}$. In both cases the collector is held at 0.0 V *vs.* Ag/AgCl.

5.5 Oligonucleotide detection by dielectric spectroscopy sensing

The horizontal coplanar nanogap device was used to demonstrate how oligonucleotide hybridisation can be detected by dielectric spectroscopy sensing. The capacitance formed by the accumulation of counter-ions near the electrode surface is sensitive to the changes in dielectric and charge environment at the electrode–electrolyte interface. Hybridisation of probe and target oligonucleotides disrupts the electric double layer and charge transport between the polarised electrodes. Detection is based on changes in the measured sensor capacitance across a frequency range as a result of the formation of a oligonucleotide duplex.

Oligonucleotides are short nucleic acid oligomers consisting of a low number of parts. They readily bind in a sequence-specific manner to complementary oligonucleotides through a process termed hybridisation to form double-stranded (ds) oligonucleotides. The base pairing of adenine–thymine (A–T) or cytosine–guanine (C–G) of two complementary single-stranded (ss) oligonucleotides occurs with high efficiency and specificity in the presence of a mixture of many different non-complementary nucleic acids. They can therefore serve as effective probes for the detection of target analyte sequences.

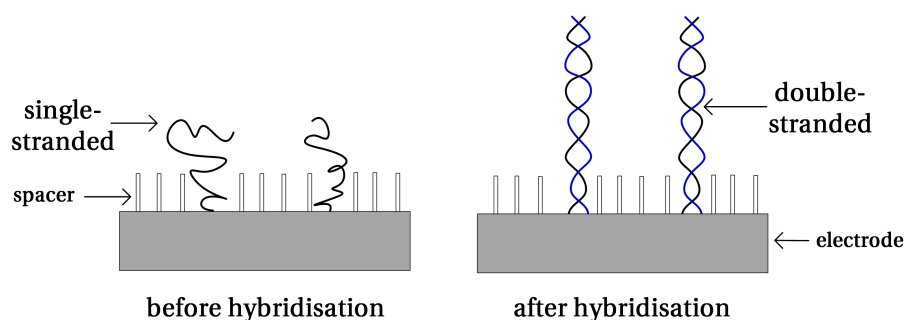


Figure 5.17: Diagram illustrating the physical displacement occurring after oligonucleotide hybridisation.

The hybridisation of two single-stranded oligonucleotides results in a physical change from a flexible to rigid state, as demonstrated in Figure 5.17. This physical displacement results in a redistribution of the surrounding ions that form the electric double layer, in turn leading to changes in the capacitance. Furthermore, target oligonucleotides with localised charge will lead to further changes in the capacitance.

5.5.1 Peptide nucleic acids as a probe layer

Peptide nucleic acid (PNA) was developed in 1991 as a chemical analogue of DNA, replacing the sugar–phosphate backbone with repeating *N*-(2-aminoethyl)-glycine units linked by peptide

5.5. Oligonucleotide detection by dielectric spectroscopy sensing

bonds. The resulting structure does not carry charge at physiological pH and this leads to stronger binding between ssPNA and ssDNA due to lack of electrostatic repulsion compared with conventional ssDNA to ssDNA binding. Figure 5.18 shows the structure of DNA and PNA.

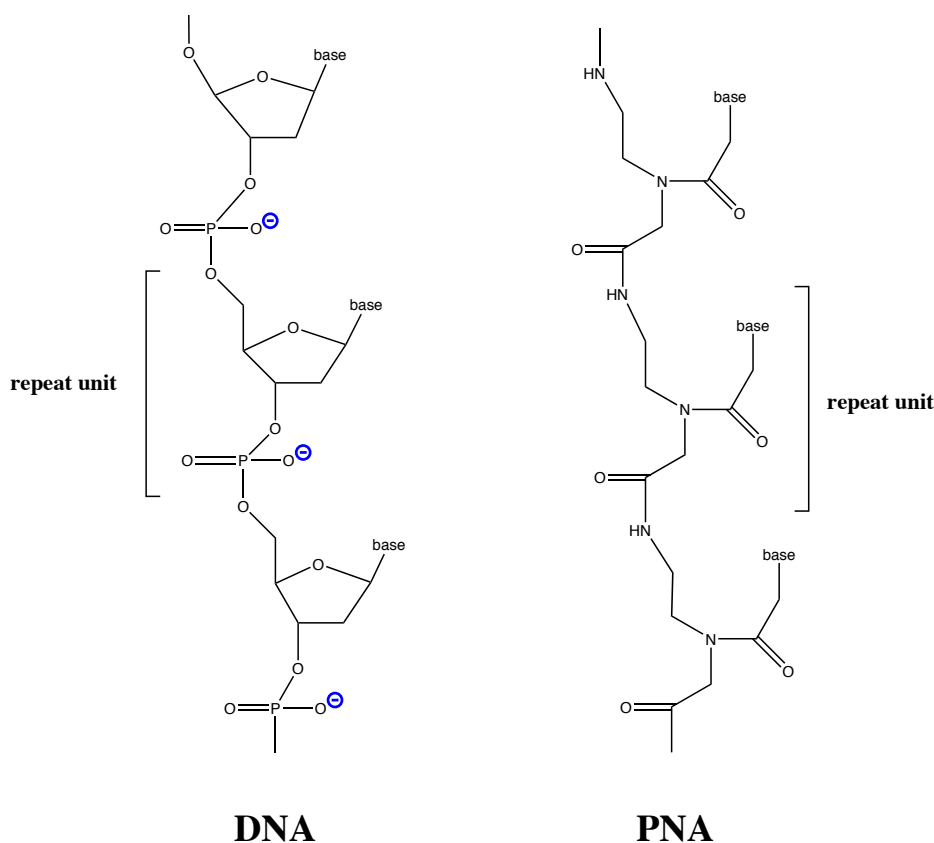


Figure 5.18: Molecular diagram comparing DNA and PNA structures.

The use of PNA as a probe can provide several advantages, as outlined by numerous reviews [81–88]. One of the most significant advantages is that the detection mechanism proceeds from an uncharged to charged state (compared to states of increasing charge for the DNA–DNA case). This also results in PNA–DNA and PNA–RNA duplexes exhibiting higher thermal stabilities ($\approx 1^\circ\text{C}$ per base [89]) compared with DNA–DNA or DNA–RNA duplexes. Furthermore, the duplex melting temperature (T_m) is relatively insensitive to ionic strength [81], providing a greater freedom in the choice of hybridisation and measurement conditions. The hybridisation kinetics of ssPNA hybridisation tend to be faster and with greater specificity [90], with single point mismatches being better discriminated by PNA than by DNA or RNA [91]. Finally, the peptide backbone bearing purine and pyrimidine bases are not easily recognisable by other nucleases or proteases, therefore extending the lifetime of these compounds both *in vivo* and *in vitro* [92].

5.5.2 Experimental information

Reagents

Dimethyl sulfoxide (DMSO), ethylenediaminetetraacetic acid (EDTA) [CAS 60-00-04], 6-mercapto-1-hexanol (MCH) [CAS 1633-78-9], and phosphate-buffered saline (PBS) tablets (10 mM phosphate buffer, 2.7 mM KCl & 137 mM NaCl, pH 7.4 at 25 °C) were all purchased from Sigma-Aldrich. All aqueous solutions were prepared using 18.2 M Ω ·cm ultra-pure class 1 DI water treated with a Biopak[®] polishing pack from a Direct-Q[®] 5 UV system [Millipore]. A stock 10 mM PBS solution (pH 7.4) was prepared and filtered with a 0.2 μ m pore nylon membrane bottle top filter [Corning] under vacuum prior to use.

Thiolated ssPNA [Cambridge Research Biochemicals] with sequence HS-C₆-AEEEE-ACA-ACA-ACA-ACA-ACA (N- to C-terminus, where AEEEE is a 1.8 nm long 9-amino-4,7- dioxanonoic acid linker used to distance the hybridisation portion of the molecule from the anchoring group) was suspended in a 1:1 volumetric ratio of DMSO:DI to create a 100 μ M stock. The use of a DMSO-based solvent is to improve the solubility of PNA. Complementary TGT-TGT-TGT-TGT-TGT and complete mismatch CAC-CAC-CAC-CAC-CAC ssDNA sequences (both from Sigma-Aldrich) were suspended in a 10 mM Tris-HCl pH 7.4, 1 mM buffer to form a 100 μ M stock. The use of an ionic solution is to provide a suitable electrostatic environment for the charged ssDNA.

Apparatus

The measurement setup consisted of a B1500A semiconductor device parameter analyser [Agilent Technologies] fitted with a 1 kHz to 5 MHz multi frequency capacitance measurement unit (MFCMU). Connections were made using micropositioners with a four-terminal pair configuration with the L_p & L_c and H_p & H_c terminals shorted on the contact pads of the device. The response was recorded for a frequency range of 1 kHz to 1 MHz with a 0.0 V DC bias and a 10 mV AC signal using a 'long' integration time (16 power line cycles).

Open, short, and phase corrections were performed prior to measurements to correct for residual admittance, impedance, and phase in the system, respectively. The capacitance was recorded between 1 kHz and 1 MHz with a 0.0 V DC bias and a 10 mV AC perturbing signal with a 'long' integration time (16 power line cycles). A total of 76 frequency points (logarithmic) were recorded. Five scans were taken and averaged for each device at each step. The capacitance reported is the 'parallel' capacitance, calculated from the measured susceptance (B) of the auto-balancing bridge of the measurement instrument as $\frac{B}{\omega}$. All measurements were taken on the same day with temperature varying from 20.4 °C to 22.5 °C and relative humidity from 58%–64%.

Experimental procedure

The sensors were first cleaned by rinsing with acetone, IPA then DI water and dried with a N₂ stream. The thiolated ssPNA (HS-C₆-AEEEA-ACA-ACA-ACA-ACA-ACA) 100 μ M stock heated to 55 °C for 10 minutes using a digital dry block heater followed by vortex mixing for 30 seconds and ultrasonic agitation for 1 minute. The stock was then diluted to 1 μ M aliquots in DMSO:DI (1:1, vol.) ready for co-immobilisation. A 1 mM stock solution of MCH was prepared in DMSO:DI (1:1, vol.) for backfilling of the probe layer and also diluted to 4 μ M aliquots for co-immobilisation with the PNA probe.

The importance of the spatial density of the PNA probe has previously been studied by Keighley *et al.* [93]. If the probe density is too high, the steric hindrance actually leads to a decrease in target hybridisation. Therefore co-immobilisation of PNA with MCH (acting as a spacer molecule) was performed with a molar ratio of 1:4 to provide optimised spatial density of the probe. The sensors were incubated with 10 μ L of solution in a humidity chamber (to reduce evaporation) at 5 °C for 16 hours. Next, the sensors were rinsed with DI water then, to ensure complete thiol coverage, backfilled with 10 μ L of 1 mM MCH in DMSO:DI (1:1, vol.) for 1 hour at room temperature. Finally the backfilled sensors were rinsed with 10 mM PBS solution and stabilised in 5 μ L of 10 mM PBS.

The stock solutions of complementary (TGT-TGT-TGT-TGT-TGT) and complete mismatch (CAC-CAC-CAC-CAC-CAC) 15-mer ssDNA sequences were then prepared for the hybridisation studies. First the stock solutions were vortex mixed for 30 seconds followed by ultrasonic agitation for 1 minute and a further 30 seconds vortex mixing before preparing 10 μ L aliquots of working concentrations (10 pM to 100 nM) in 10 mM PBS.

Capacitance measurements were taken of the ssPNA probe layer and then with increasing concentrations of the complementary and complete mismatch non-complementary ssDNA sequences. A total of four sensors were used: two for the complementary target sequence (TGT repeat) and two for the non-complementary control sequence (CAC repeat). Between measurement steps the sensors were washed with DI water, dried with N₂, and then incubated for 30 minutes at room temperature with 5 μ L of ssDNA sequences. After incubation the sensors were then rinsed in 10 mM PBS, dried with N₂, stabilised with 5 μ L 10 mM PBS for 5 minutes, before taking measurements.

5.5.3 Results

Figure 5.19 shows the capacitance spectra after hybridising with increasing complementary [Figures 5.19a & 5.19b] and non-complementary [Figures 5.19c & 5.19d] ssDNA sequences. One of the controls [Figure 5.19d] shows a very unusual response for the SAM measurement, with the capacitance much higher than the other sensors. Although the capacitance response

Chapter 5. Fabrication of a Large Area Horizontal Coplanar Nanogap Device

Table 5.6: Sequence of key experimental steps for the capacitive sensing of PNA–DNA interactions.

Step	Description	Duration
1	Clean sensors: rinse with acetone then IPA, dry with N ₂	—
2a	Co-immobilisation of 10 μ L PNA:MCH (1 μ M : 4 μ M) in DMSO:DI (1:1, vol.) at 5 °C	16 h
2b	Rinse sensors with DI water	—
3a	Backfilling with 10 μ L of 1 mM MCH (in DMSO:DI, 1:1, vol.) at RT	1 h
3b	Rinse sensors with DI water, N ₂ dry	—
3c	Stabilise with 5 μ L 10 mM PBS	1 h
4a	Perform capacitance measurements	<1 h
4b	Rinse with DI water, N ₂ dry	—
5a	Incubate with 5 μ L ssDNA at RT	30 min
5b	Rinse with 10 mM PBS, N ₂ dry	—
5c	Stabilise with 5 μ L 10 mM PBS	5 min
6a	Perform capacitance measurements	<1 h
6b	Rinse with DI water, N ₂ dry	—
7	Repeat steps 5a-6b for increasing ssDNA concentrations	—

is provided for a wide frequency range, it is important to highlight that below 10 kHz the capacitive behaviour is marred by the fact that the low-frequency dielectric response is dominated by ionic relaxation.

Even with the use of nanogaps, problems associated with low-frequency measurements have been well reported in literature [22, 47, 94–98]. Fluctuations of the buffer can not only mask the the dielectric changes due to binding of the target oligonucleotide, but the conductivity of biological buffers also results in a large frequency-dependent dielectric dispersion. On the other hand, the capacitance changes due to the redistribution of ions within the buffer will be most significant at these lower frequencies. Equation 5.1 shows how the dielectric constant (ϵ_r) is comprised of the real (ϵ'_r) and imaginary (ϵ''_r) parts, with the imaginary part governed by the conductivity (σ) [Equation 5.2].

$$\epsilon_r = \epsilon'_r - i\epsilon''_r \quad (5.1)$$

$$\epsilon''_r = \frac{\sigma}{\omega\epsilon_0} \quad (5.2)$$

The frequency-dependent nature of the conductivity, $\sigma(\omega)$, is described by Jonscher's 'universal

5.5. Oligonucleotide detection by dielectric spectroscopy sensing

dielectric response' [99, 100]:

$$\sigma(\omega) = \sigma_0 + A\omega^n \quad (5.3)$$

Here σ_0 is the direct current (DC) conductivity, A is a pre-exponential factor related to temperature and n is a frequency exponent, where $(0 < n < 1)$.

At medium frequencies (10-100 kHz) the overall response is less dependent on the ionic contribution from the buffer, therefore providing a more reliable measurement of biomolecular interactions. Using the measurement of the SAM capacitance as a baseline, the relative percentage change at 25 kHz is calculated and plotted in Figure 5.20. The response for the addition of complementary ssDNA plotted in blue and the response of the controls (for the addition of non-complementary ssDNA) are plotted in black. The error bars represent the uncertainty in the measurement and were calculated using Equation 3.10.

Increasing the concentration of complementary ssDNA from 10 pM to 100 nM saw an increase in the measured capacitance, with one device showing a 5.2% shift and the other device showing a 12.2% shift. Although one of the controls shows very negative values due to an initial unexpected shift from its baseline, both the controls show much flatter responses to the addition of the non-complementary ssDNA. The capacitance of the controls varied by no more than $\pm 1.1\%$. The dose response for all the devices was consistent across the medium frequency range (10-100 kHz).

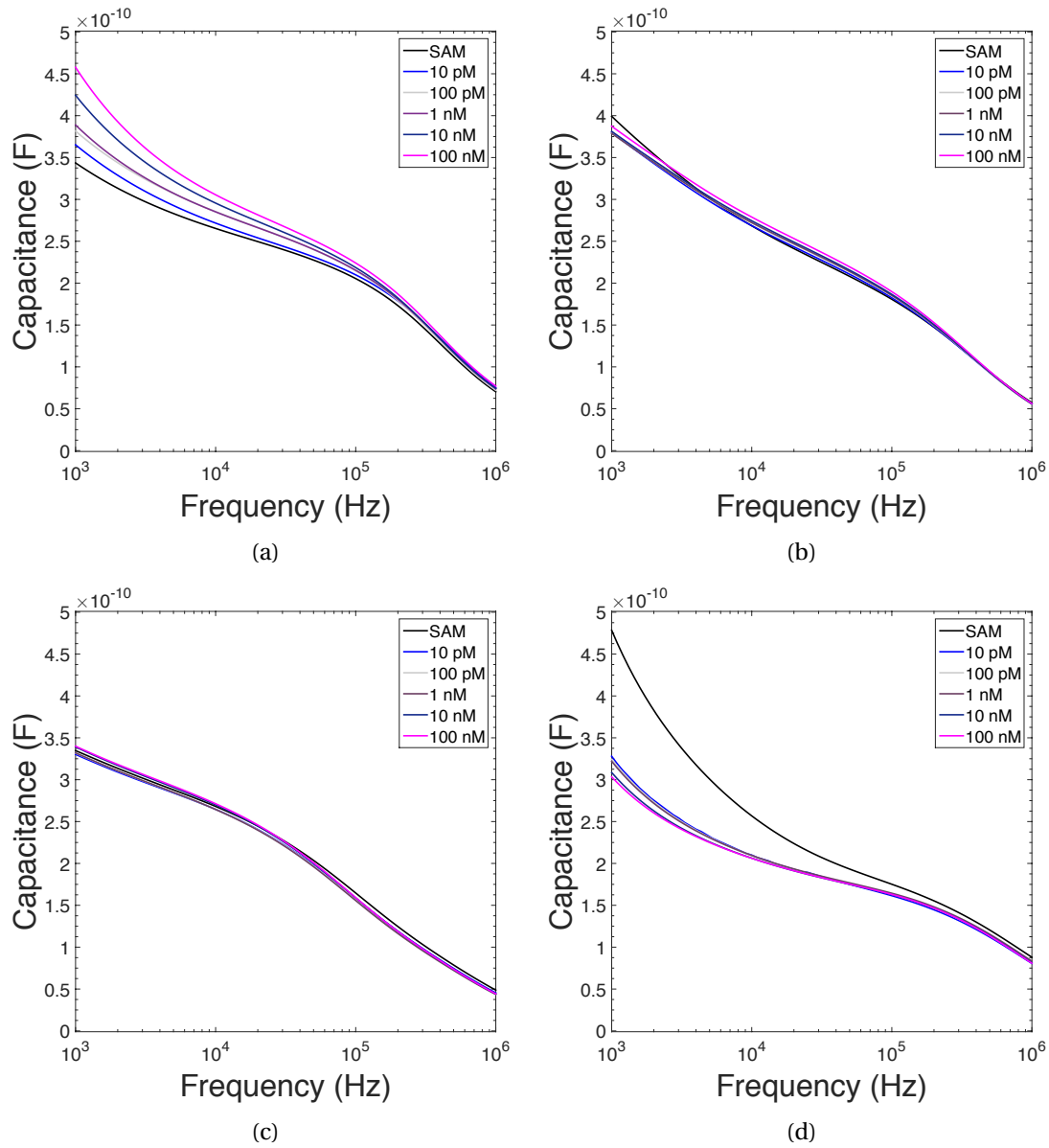


Figure 5.19: Capacitance spectra showing the dose response for: (a) & (b) complementary and (c) & (d) non-complementary single-stranded DNA.

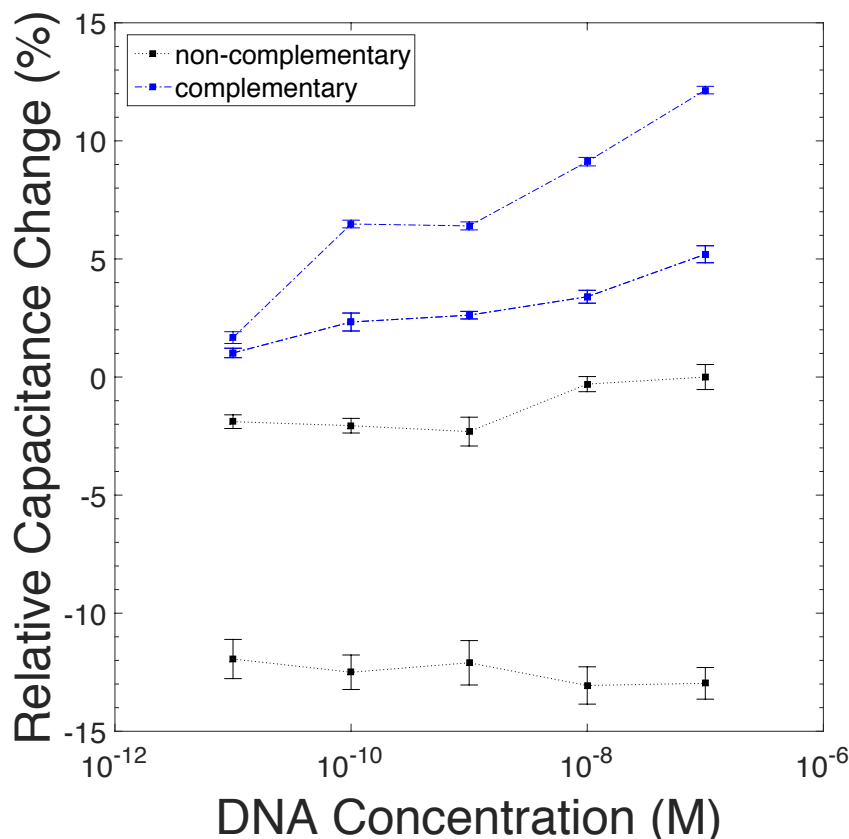


Figure 5.20: Relative percentage change in capacitance at 25 kHz for increasing concentrations of complementary and non-complementary single-stranded DNA. Error bars represent the measurement error calculated using Equation 3.10, for 5 measurements of each device at each stage in the experiment.

The increase in capacitance following the formation of the the PNA–DNA duplex can be attributed to redistribution of the electric double layer. After hybridisation the negative charge of target ssDNA causes an increased local cation concentration, resulting in an increase of the Gouy–Chapman diffuse layer capacitance, and an increase of the total measured capacitance.

Regeneration of the PNA probe layer

It is often highly desirable if the biorecognition layer of a biosensor can be regenerated. As the stability of the double-stranded oligonucleotide hydrogen bonds is highly dependent on temperature, one way to reverse the hybridisation of oligonucleotides is to elevate the thermal environment. The melting temperature (T_m) defines when 50% of the oligonucleotide and its complement are in duplex. As the PNA–DNA duplex has increased thermal stability compared with a DNA–DNA duplex, the T_m value for the PNA–DNA duplex was calculated as 74.8 °C (at

4 μM) [101]. An attempt to regenerate the PNA probe layer was made by submerging each of the devices in 20 mL DI water at 90 °C for 50 minutes with agitation on a 3D rocker. However, on inspection there was significant delamination of the SU-8 layer on two of the devices. This would lead to significantly increased electrostatic fringing fields and therefore no way to reproduce similar results. An alternative, less aggressive, approach could be to use a 10 mM NaOH solution to break the hydrogen bonds of the duplex as reported by Zaffino *et al.* [102]. However, due to the delamination observed this was not attempted.

5.6 Discussion

In this work a fabrication process to produce a large area horizontal nanogap with passivated electrodes was demonstrated using electron-beam lithography (EBL). The use of a serpentine shape allows the length of the electrodes to be maximised within the addressable area of the electron-beam tool. By increasing the surface area the sensing volume and therefore the number of molecules available for detection is also increased, this leads to improved ‘molar sensitivity’ when compared to other fabricated geometries. The use of a silicon mould patterned by EBL and dry etching [Appendix B.3] would allow the time-consuming EBL steps to be replaced with nanoimprint lithography (NIL). This would provide a low-cost, high-throughput approach to producing devices.

The importance of the passivation layer was demonstrated using finite element analysis. In particular, the limiting current density during redox cycling is drastically effected when partially exposing the top surface of the electrodes. This nonideality is a result of undercutting the Al hard mask during ICP-RIE removal of SU-8 in the nanogap. Addition of SF_6 to the plasma should improve the directionality of the etch process as well as reducing surface roughness [77].

With the current methodology the SU-8 passivation layer could be swapped with a thick SiN_x layer deposited by PECVD followed by a highly directional dry etch with a CHF_3/O_2 chemistry [103] or other fluorine-based recipes [104] to provide a more robust passivation layer. Ideally, a self-aligned process would be developed so that the second electron-beam lithography (EBL) step becomes redundant. A SiO_2 passivation layer could be deposited by electron-beam evaporation immediately after the Ti/Au electrode layer (after a thin Ti or Cr adhesion layer) before performing lift-off. Depositing an alternative material, such as SiN_x , by PECVD or sputtering would not be an option due to the required deposition temperature being above the working range of the electron-beam resist.

The positive sidewall of the ma-N 2403 negative-tone resist created during EBL exposure and the 300 nm resist thickness already complicates a single lift-off process. Even if a bilayer resist was adopted to create a negative sidewall for more efficient lift-off, the quality of an SiO_2 passivation layer would likely be inferior to that of SU-8. The other consideration is

that the electrode surface area is dependent on the thickness of the deposited Ti/Au layer thickness. Successful lift-off requires the resist to be thicker than the layers to be lifted off, with ratios greater than 2:1 typically used. Another major drawback with any single lift-off process would be the high risk of accidentally passivating the sidewalls of the electrodes, this being exacerbated with the greater degree of undercutting achieved from using a bilayer.

An interesting option worth exploring would be to grow an oxide layer. As an example, a relatively thick Ta layer could be deposited by evaporation after the Ti/Au electrode layers. This Ta layer could then be anodised to form $\text{Ta}_2\text{O}_3/\text{Ta}_2\text{O}_5$. This way a high-quality passivation layer covering the entire top surface of the electrodes could be achieved with reduced risk of accidentally covering the electrode sidewalls. Furthermore tantalum oxides have been shown to exhibit substantially lower leakage currents when compared to conventional SiO_2 or SiN_x films, with values of ϵ_r typically greater than 20, depending on the conditions of oxide formation [105].

Finally the device was used to demonstrate the detection of oligonucleotide hybridisation using dielectric spectroscopy sensing. With just a few devices used for the experiments it is difficult to draw any firm conclusions. At low frequencies (<10 kHz) the overall dielectric response is dominated by the ionic contribution of the buffer. By using a frequency range of 10-100 kHz these adverse effects are mitigated whilst still providing reasonable sensitivity. The neutral charge of the ssPNA probe results in an increase of local cation concentration, and therefore electric double layer capacitance after hybridisation with the negatively charged ss-DNA target. Nevertheless, the work is an important proof of concept and shows that large-area nanogap devices can be very useful for direct electrochemical detection of oligonucleotides.

References

- [1] R. L. McCreery and A. J. Bergren. Progress with Molecular Electronic Junctions: Meeting Experimental Challenges in Design and Fabrication. *Advanced Materials*, 21(43):4303–4322, 2009.
- [2] T. Li, W. Hu, and D. Zhu. Nanogap Electrodes. *Advanced Materials*, 22(2):286–300, 2010.
- [3] X. Chen, Z. Guo, G. M. Yang, J. Li, M. Q. Li, J. H. Liu, and X. J. Huang. Electrical nanogap devices for biosensing. *Materials Today*, 13(11):28–41, 2010.
- [4] A. Cui, H. Dong, and W. Hu. Nanogap Electrodes towards Solid State Single-Molecule Transistors. *Small*, 11(46):6115–6141, 2015.
- [5] X. Chen, H.-R. Park, M. Pelton, X. Piao, N. C. Lindquist, H. Im, Y. J. Kim, J. S. Ahn, K. J. Ahn, N. Park, D.-S. Kim, and S.-H. Oh. Atomic layer lithography of wafer-scale nanogap arrays for extreme confinement of electromagnetic waves. *Nature Communications*, 4:2361, 2013.
- [6] D. J. Beesley, J. Semple, J. L. Krishnan, A. Amassian, M. A. McLachlan, T. D. Anthopoulos, and J. C. deMello. Sub-15-nm patterning of asymmetric metal electrodes and devices by adhesion lithography. *Nature Communications*, 5:3933, 2014.
- [7] A. Cui, Z. Liu, H. Dong, F. Yang, Y. Zhen, W. Li, J. Li, C. Gu, X. Zhang, R. Li, and W. Hu. Mass Production of Nanogap Electrodes toward Robust Resistive Random Access Memory. *Advanced Materials*, 28(37):8227–8233, 2016.
- [8] C. Lee, E.-H. Yang, N. V. Myung, and T. George. A Nanochannel Fabrication Technique without Nanolithography. *Nano Letters*, 3(10):1339–1340, 2003.
- [9] A. E. Cohen and R. R. Kunz. Large-area interdigitated array microelectrodes for electrochemical sensing. *Sensors and Actuators, B: Chemical*, 62(1):23–29, 2000.
- [10] R. D. Piner, J. Zhu, F. Xu, S. Hong, and C. Mirkin. "Dip-Pen" Nanolithography. *Science*, 283:661–663, 1999.
- [11] T. Jain, Q. Tang, T. Bjørnholm, and K. Nørgaard. Wet chemical synthesis of soluble gold nanogaps. *Accounts of Chemical Research*, 47(1):2–11, 2014.

References

- [12] J. H. Kim, H. Moon, S. Yoo, and Y. K. Choi. Nanogap electrode fabrication for a nanoscale device by volume-expanding electrochemical synthesis. *Small*, 7(15):2210–2216, 2011.
- [13] J. Park, A. N. Pasupathy, J. I. Goldsmith, C. Chang, Y. Yaish, J. R. Petta, M. Rinkoski, J. P. Sethna, H. D. Abruna, P. L. McEuen, D. C. Ralph, H. D. Abruña, P. L. McEuen, and D. C. Ralph. Coulomb blockade and the Kondo effect in single-atom transistors. *Nature*, 417(6890):722–725, jun 2002.
- [14] A. K. Mahapatro, S. Ghosh, and D. B. Janes. Nanometer scale electrode separation (nanogap) using electromigration at room temperature. *IEEE Transactions on Nanotechnology*, 5(3):232–236, 2006.
- [15] M. Ito, K. Morihara, T. Toyonaka, K. Takikawa, and J.-I Shirakashi. High-throughput nanogap formation by field-emission-induced electromigration. *Journal of Vacuum Science & Technology B, Nanotechnology and Microelectronics: Materials, Processing, Measurement, and Phenomena*, 33(5):051801, 2015.
- [16] Th. Weimann, P. Hinze, H. Scherer, and J. Niemeyer. Fabrication of a metallic single electron tunneling transistor by multilayer technique using lithography with a scanning transmission electron microscope. *Microelectronic Engineering*, 46(1):165–168, 1999.
- [17] M. A. Guillorn, D. W. Carr, R. C. Tiberio, E. Greenbaum, and M. L. Simpson. Fabrication of dissimilar metal electrodes with nanometer interelectrode distance for molecular electronic device characterization. *Journal of Vacuum Science & Technology B: Microelectronics and Nanometer Structures*, 18(3):1177, 2000.
- [18] A. F. Morpurgo, C. M. Marcus, and D. B. Robinson. Controlled fabrication of metallic electrodes with atomic separation. *Applied Physics Letters*, 74(14):2084–2086, 1999.
- [19] T. Nagase, T. Kubota, and S. Mashiko. Fabrication of nano-gap electrodes for measuring electrical properties of organic molecules using a focused ion beam. *Thin Solid Films*, 438-439(3):374–377, 2003.
- [20] T. Blom, K. Welch, M. Strømme, E. Coronel, and K. Leifer. Fabrication and characterization of highly reproducible, high resistance nanogaps made by focused ion beam milling. *Nanotechnology*, 18(28):285301, 2007.
- [21] A. Cui, Z. Liu, H. Dong, Y. Wang, Y. Zhen, W. Li, J. Li, C. Gu, and W. Hu. Single grain boundary break junction for suspended nanogap electrodes with gapwidth down to 1-2 nm by focused ion beam milling. *Advanced Materials*, 27(19):3002–3006, 2015.
- [22] R. Hatsuki, A. Honda, M. Kajitani, and T. Yamamoto. Nonlinear electrical impedance spectroscopy of viruses using very high electric fields created by nanogap electrodes. *Frontiers in Microbiology*, 6:940, 2015.
- [23] J. Moreland and J. W. Ekin. Electron tunneling into superconducting filaments using mechanically adjustable barriers. *Applied Physics Letters*, 47(2):175–177, 1985.

-
- [24] M. A. Reed. Conductance of a Molecular Junction. *Science*, 278(5336):252–254, 1997.
- [25] G. S. McCarty, B. Moody, and M. K. Zachek. Enhancing electrochemical detection by scaling solid state nanogaps. *Journal of Electroanalytical Chemistry*, 643(1-2):9–14, 2010.
- [26] A. Hatzor and P. Weiss. Molecular rulers for scaling down nanostructures. *Science*, 291(5506):1019–1020, 2001.
- [27] V. M. Serdio V., T. Muraki, S. Takeshita, D. E. Hurtado S, S. Kano, T. Teranishi, and Y. Majima. Gap separation-controlled nanogap electrodes by molecular ruler electroless gold plating. *RSC Advances*, 5(28):22160–22167, 2015.
- [28] S. Kubatkin, A. Danilov, M. Hjort, J. Cornil, J.-L. Brédas, N. Stuhr-Hansen, P. Hedegård, and T. Bjørnholm. Single-electron transistor of a single organic molecule with access to several redox states. *Nature*, 425(6959):698–701, 2003.
- [29] Y. Naitoh, K. Tsukagoshi, K. Murata, and W. Mizutani. A Reliable Method for Fabricating sub-10 nm Gap Junctions Without Using Electron Beam Lithography. *e-Journal of Surface Science and Nanotechnology*, 1:41–44, 2003.
- [30] L. Qin. On-Wire Lithography. *Science*, 309(5731):113–115, 2005.
- [31] X. Guo, M. Myers, S. Xiao, M. Lefenfeld, R. Steiner, G. S. Tulevski, J. Tang, J. Baumert, F. Leibfarth, J. T. Yardley, M. L. Steigerwald, P. Kim, and C. Nuckolls. Chemosensitive monolayer transistors. *Proceedings of the National Academy of Sciences of the United States of America*, 103(31):11452–11456, 2006.
- [32] O. Fakhr, P. Altpeter, K. Karrai, and P. Lugli. Easy Fabrication of Electrically Insulating Nanogaps by Transfer Printing. *Small*, 7(17):2533–2538, 2011.
- [33] D.-Y. Jeon, S. So Jeong Park, Y. Kim, M.-J. Shin, P. Soo Kang, and G.-T. Kim. Impedance characterization of nanogap interdigitated electrode arrays fabricated by tilted angle evaporation for electrochemical biosensor applications. *Journal of Vacuum Science & Technology B, Nanotechnology and Microelectronics: Materials, Processing, Measurement, and Phenomena*, 32(2):021803, 2014.
- [34] J. Tang, Y. Wang, C. Nuckolls, and S. J. Wind. Chemically responsive molecular transistors fabricated by self-aligned lithography and chemical self-assembly. *Journal of Vacuum Science & Technology B: Microelectronics and Nanometer Structures*, 24(6):3227, 2006.
- [35] A. K. Singh, N. S. Rajput, N. Shukla, S. K. Tripathi, J. Kumar, and V. N. Kulkarni. The influence of insulating substrate on the electrical measurements of focused ion beam fabricated electrodes with nano-gap spacing. *Nuclear Instruments and Methods in Physics Research Section B: Beam Interactions with Materials and Atoms*, 268(19):3282–3286, 2010.
- [36] R. H. Dean and R. J. Matarese. Submicrometer self-aligned dual-gate GaAs FET. *IEEE Transactions on Electron Devices*, 22(6):358–360, 1975.

References

- [37] G. J. Dolan. Offset masks for lift-off photoprocessing. *Applied Physics Letters*, 31(5):337–339, 1977.
- [38] E. T. T. Jones, O. M. Chyan, and M. S. Wrighton. Preparation and characterization of molecule-based transistors with a 50-nanometer source-drain separation with use of shadow deposition techniques. Toward faster, more sensitive molecule-based devices. *Journal of the American Chemical Society*, 109(18):5526–5528, 1987.
- [39] Y. Ishii, H. Sakai, and H. Murata. Fabrication of a submicron patterned electrode using an electrospun single fiber as a shadow-mask. *Thin Solid Films*, 518(2):647–650, 2009.
- [40] P. Van Gerwen, W. Laureyn, A. Campitelli, P. Jacobs, P. Detemple, K. Baert, W. Sansen, and R. Mertens. Cost effective realization of nanoscaled interdigitated electrodes. *Journal of Micromechanics and Microengineering*, 10(3):N1–N6, 2000.
- [41] H. Yun, S. Kim, H. Kim, J. Lee, K. McAllister, J. Kim, S. Pyo, J. Sung Kim, E. E. B. Campbell, W. Hyung Lee, and S. Wook Lee. Stencil Nano Lithography Based on a Nanoscale Polymer Shadow Mask: Towards Organic Nanoelectronics. *Scientific Reports*, 5:10220, 2015.
- [42] A. Kanda, M. Wada, Y. Hamamoto, and Y. Ootuka. Simple and controlled fabrication of nanoscale gaps using double-angle evaporation. *Physica E: Low-Dimensional Systems and Nanostructures*, 29(3-4):707–711, 2005.
- [43] X. Liang and S. Y. Chou. Nanogap detector inside nanofluidic channel for fast real-time label-free DNA analysis. *Nano Letters*, 8(5):1472–1476, 2008.
- [44] S. Hashioka, M. Saito, E. Tamiya, and H. Matsumura. Deoxyribonucleic acid sensing device with 40-nm-gap-electrodes fabricated by low-cost conventional techniques. *Applied Physics Letters*, 85(4):687–688, 2004.
- [45] A. Fursina, S. Lee, R. G. S. Sofin, I. V. Shvets, and D. Natelson. Nanogaps with very large aspect ratios for electrical measurements. *Applied Physics Letters*, 92(11):113102, 2008.
- [46] Ch. Santschi, M. Jenke, P. Hoffmann, and J. Brugger. Interdigitated 50 nm Ti electrode arrays fabricated using XeF₂ enhanced focused ion beam etching. *Nanotechnology*, 17(11):2722–2729, 2006.
- [47] R. Hatsuki, F. Yujiro, and T. Yamamoto. Direct measurement of electric double layer in a nanochannel by electrical impedance spectroscopy. *Microfluidics and Nanofluidics*, 14(6):983–988, 2013.
- [48] G. Purohit, M. Shankar, D. Gupta, S. Damodaran, and M. Katiyar. Fabrication of nanogap electrodes using a focused ion beam for measuring electrical properties of molecular scale transistors. In *Proc. SPIE 8549, 16th International Workshop on Physics Of Semiconductor Devices*, pages 85492J1–85492J4, 2012.

-
- [49] S. Reyntjens and R. Puers. Focused ion beam induced deposition: fabrication of three-dimensional microstructures and Young's modulus of the deposited material. *Journal of Micromechanics and Microengineering*, 10(2):181–188, 2000.
- [50] Y.-W. Lan, W.-H. Chang, Y.-C. Chang, C.-S. Chang, and C.-D. Chen. Effect of focused ion beam deposition induced contamination on the transport properties of nano devices. *Nanotechnology*, 26(5):055705, 2015.
- [51] J. C. Cheang-Wong, K. Narumi, G. M. Schürmann, M. J. Aziz, and J. A. Golovchenko. Tunable nanometer electrode gaps by MeV ion irradiation. *Applied Physics Letters*, 100(15):153108, 2012.
- [52] G. L. Varnell, D. F. Spicer, and A. C. Rodger. E-Beam Writing Techniques for Semiconductor Device Fabrication. *Journal of Vacuum Science and Technology*, 10(6):1048–1051, 1973.
- [53] K. Liu, Ph. Avouris, J. Bucchignano, R. Martel, S. Sun, and J. Michl. Simple fabrication scheme for sub-10 nm electrode gaps using electron-beam lithography. *Applied Physics Letters*, 80(5):865–867, 2002.
- [54] M. Manheller, S. Trellenkamp, R. Waser, and S. Karthäuser. Reliable fabrication of 3 nm gaps between nanoelectrodes by electron-beam lithography. *Nanotechnology*, 23(12):125302, 2012.
- [55] A. Bezryadin and C. Dekker. Nanofabrication of electrodes with sub-5 nm spacing for transport experiments on single molecules and metal clusters. *Journal of Vacuum Science & Technology B: Microelectronics and Nanometer Structures*, 15(4):793, 1997.
- [56] D. Porath, A. Bezryadin, S. de Vries, and C. Dekker. Direct measurement of electrical transport through DNA molecules. *Nature*, 403(6770):635–638, 2000.
- [57] O. Niwa, M. Morita, and H. Tabei. Electrochemical behavior of reversible redox species at interdigitated array electrodes with different geometries: consideration of redox cycling and collection efficiency. *Analytical Chemistry*, 62(5):447–452, 1990.
- [58] O. Niwa, M. Morita, and H. Tabei. Highly sensitive and selective voltammetric detection of dopamine with vertically separated interdigitated array electrodes. *Electroanalysis*, 3(3):163–168, 1991.
- [59] O. Niwa, Y. Xu, H. B. Halsall, and W. R. Heineman. Small-volume voltammetric detection of 4-aminophenol with interdigitated array electrodes and its application to electrochemical enzyme immunoassay. *Analytical Chemistry*, 65(11):1559–63, 1993.
- [60] L. Montelius, J. O. Tegenfeldt, and T. G. I. Ling. Fabrication and characterization of a nanosensor for admittance spectroscopy of biomolecules. *Journal of Vacuum Science & Technology A: Vacuum, Surfaces, and Films*, 13(3):1755–1760, 1995.

References

- [61] K. Hayashi, J.-I. Takahashi, T. Horiuchi, Y. Iwasaki, and T. Haga. Development of Nanoscale Interdigitated Array Electrode as Electrochemical Sensor Platform for Highly Sensitive Detection of Biomolecules. *Journal of The Electrochemical Society*, 155(9):J240–J243, 2008.
- [62] E. Finot, E. Bourillot, R. Meunier-Prest, Y. Lacroute, G. Legay, M. Cherkaoui-Malki, N. Latruffe, O. Siri, P. Braunstein, and A. Dereux. Performance of interdigitated nanoelectrodes for electrochemical DNA biosensor. *Ultramicroscopy*, 97(1-4):441–449, 2003.
- [63] K. Ueno, M. Hayashida, J.-Y. Ye, and H. Misawa. Fabrication and electrochemical characterization of interdigitated nanoelectrode arrays. *Electrochemistry Communications*, 7(2):161–165, 2005.
- [64] V. A. T. Dam, W. Olthuis, and A. van den Berg. Redox cycling with facing interdigitated array electrodes as a method for selective detection of redox species. *The Analyst*, 132(4):365–370, 2007.
- [65] E. D. Goluch, B. Wolfrum, P. S. Singh, M. A. G. Zevenbergen, and S. G. Lemay. Redox cycling in nanofluidic channels using interdigitated electrodes. *Analytical and Bioanalytical Chemistry*, 394(2):447–456, 2009.
- [66] C. Z. Li, A. Bogozzi, W. Huang, and N. J. Tao. Fabrication of stable metallic nanowires with quantized conductance. *Nanotechnology*, 10(2):221–223, 1999.
- [67] S. Boussaad and N. J. Tao. Atom-size gaps and contacts between electrodes fabricated with a self-terminated electrochemical method. *Applied Physics Letters*, 80(13):2398–2400, 2002.
- [68] Y. V. Kervennic, H. S. J. Van der Zant, A. F. Morpurgo, L. Gurevich, and L. P. Kouwenhoven. Nanometer-spaced electrodes with calibrated separation. *Applied Physics Letters*, 80(2):321–323, jan 2002.
- [69] Y. Kashimura, H. Nakashima, K. Furukawa, and K. Torimitsu. Fabrication of nano-gap electrodes using electroplating technique. *Thin Solid Films*, 438-439(03):317–321, 2003.
- [70] F. Chen, Q. Qing, L. Ren, L. Tong, Z. Wu, and Z. Liu. Formation of nanogaps by nanoscale Cu electrodeposition and dissolution. *Electrochimica Acta*, 52(12):4210–4214, 2007.
- [71] L. de los Santos Valladares, L. L. Felix, A. B. Dominguez, T. Mitrelias, F. Sfigakis, S. I. Khondaker, C. H. W. Barnes, and Y. Majima. Controlled electroplating and electromigration in nickel electrodes for nanogap formation. *Nanotechnology*, 21(44):445304, 2010.
- [72] C. S. Ah, Y. J. Yun, J. S. Lee, H. J. Park, D. H. Ha, and W. S. Yun. Fabrication of integrated nanogap electrodes by surface-catalyzed chemical deposition. *Applied Physics Letters*, 88(13):133116, 2006.

-
- [73] Y. Yasutake, K. Kono, M. Kanehara, T. Teranishi, M. R. Buitelaar, C. G. Smith, and Y. Majima. Simultaneous fabrication of nanogap gold electrodes by electroless gold plating using a common medical liquid. *Applied Physics Letters*, 91(20):203107, 2007.
- [74] V. M. Serdio V., Y. Azuma, S. Takeshita, T. Muraki, T. Teranishi, and Y. Majima. Robust nanogap electrodes by self-terminating electroless gold plating. *Nanoscale*, 4(22):7161, 2012.
- [75] M. C. Rosamond, J. T. Batley, G. Burnell, B. J. Hickey, and E. H. Linfield. High contrast 3D proximity correction for electron-beam lithography: An enabling technique for the fabrication of suspended masks for complete device fabrication within an UHV environment. *Microelectronic Engineering*, 143:5–10, 2015.
- [76] J. Melai, C. Salm, S. Smits, J. Visschers, and J. Schmitz. The electrical conduction and dielectric strength of SU-8. *Journal of Micromechanics and Microengineering*, 19(6):065012, 2009.
- [77] K. H. Rasmussen, S. S. Keller, F. Jensen, A. M. Jorgensen, and O. Hansen. SU-8 etching in inductively coupled oxygen plasma. *Microelectronic Engineering*, 112:35–40, 2013.
- [78] S. J. Lee, W. Shi, P. Maciel, and S. W. Cha. Top-edge profile control for SU-8 structural photoresist. In *Proceedings of the 15th Biennial University/Government/ Industry Microelectronics Symposium*, pages 389–390. IEEE, 2003.
- [79] S. Talaei, O. Frey, P. D. van der Wal, N. F. de Rooij, and M. Koudelka-Hep. Hybrid microfluidic cartridge formed by irreversible bonding of SU-8 and PDMS for multi-layer flow applications. *Procedia Chemistry*, 1(1):381–384, 2009.
- [80] Yu. Ren, S. H. Huang, S. Mosser, M. O. Heuschkel, A. Bertsch, P. C. Fraering, J.-J. J. Chen, and P. Renaud. A Simple and Reliable PDMS and SU-8 Irreversible Bonding Method and Its Application on a Microfluidic-MEA Device for Neuroscience Research. *Micromachines*, 6(12):1923–1934, 2015.
- [81] H. Ørum, P. E. Nielsen, M. Jørgensen, C. Larsson, C. Stanley, and T. Koch. Sequence-specific purification of nucleic acids by PNA-controlled hybrid selection. *BioTechniques*, 19(3):472–80, 1995.
- [82] B. Hyrup and P. E. Nielsen. Peptide Nucleic Acids (PNA): Synthesis, Properties and Potential Applications. *Bioorganic and Medicinal Chemistry*, 4(1):5–23, 1996.
- [83] J. Wang. DNA biosensors based on peptide nucleic acid (PNA) recognition layers. A review. *Biosensors and Bioelectronics*, 13(7-8):757–762, 1998.
- [84] P. E. Nielsen. Peptide Nucleic Acid. A Molecule with Two Identities. *Accounts of Chemical Research*, 32(7):624–630, 1999.
- [85] A. Ray and B. Nordén. Peptide nucleic acid (PNA): its medical and biotechnical applications and promise for the future. *The FASEB Journal*, 14(9):1041–60, 2000.

References

- [86] A. Porcheddu and G. Giacomelli. Peptide Nucleic Acids (PNAs), A Chemical Overview. *Current Medicinal Chemistry*, 12(22):2561–2599, 2005.
- [87] Z. V. Zhilina, A. J. Ziemba, and S. W. Ebbinghaus. Peptide Nucleic Acid Conjugates: Synthesis, Properties and Applications. *Current Topics in Medicinal Chemistry*, 5(12):1119–1131, 2005.
- [88] S. Shakeel, S. Karim, and A. Ali. Peptide nucleic acid (PNA) - a review. *Journal of Chemical Technology & Biotechnology*, 81(6):892–899, 2006.
- [89] M. Egholm, O. Buchardt, L. Christensen, C. Behrens, S. M. Freier, D. A. Driver, R. H. Berg, S. K. Kim, B. Norden, and P. E. Nielsen. PNA hybridizes to complementary oligonucleotides obeying the Watson-Crick hydrogen-bonding rules. *Nature*, 365(6446):566–568, 1993.
- [90] K. K. Jensen, H. Ørum, P. E. Nielsen, and B. Nordén. Kinetics for Hybridization of Peptide Nucleic Acids (PNA) with DNA and RNA Studied with the BIAcore Technique. *Biochemistry*, 36(16):5072–5077, 1997.
- [91] J. Wang, G. Rivas, X. Cai, M. Chicharro, C. Parrado, N. Dontha, A. Begleiter, M. Mowat, E. Palecek, and P. E. Nielsen. Detection of point mutation in the p53 gene using a peptide nucleic acid biosensor. *Analytica Chimica Acta*, 344(1–2):111–118, 1997.
- [92] V. V. Demidov, V. N. Potaman, M. D. Frank-Kamenetskii, M. Egholm, O. Buchard, S. H. Sönnichsen, and P. E. Nielsen. Stability of peptide nucleic acids in human serum and cellular extracts. *Biochemical Pharmacology*, 48(6):1310–1313, 1994.
- [93] S. D. Keighley, P. Estrela, P. Li, and P. Migliorato. Optimization of label-free DNA detection with electrochemical impedance spectroscopy using PNA probes. *Biosensors and Bioelectronics*, 24(4):906–911, 2008.
- [94] J. T. Nevill, D. Di Carlo, P. Liu, K. R. Jeong, and L. P. Lee. Detection of protein conformational changes with a nanogap biosensor. In *The 13th International Conference on Solid-State Sensors, Actuators and Microsystems, 2005. Digest of Technical Papers. TRANSDUCERS '05*, volume 2, pages 1668–1671. IEEE, 2005.
- [95] M. Yi, K. H. Jeong, and L. P. Lee. Theoretical and experimental study towards a nanogap dielectric biosensor. *Biosensors and Bioelectronics*, 20(7):1320–1326, 2005.
- [96] M. S. Mannoor, T. James, D. V. Ivanov, L. Beadling, and W. Braunlin. Nanogap dielectric spectroscopy for aptamer-based protein detection. *Biophysical Journal*, 98(4):724–732, 2010.
- [97] Th. S. Dhahi, M. E. Ali, and U. Hashim. Electrical Properties of Silicon-Based Nanogap Electrodes for Label-Free Biomolecular Detection. *Journal of Nanoelectronics and Optoelectronics*, 8(2):156–159, 2013.

-
- [98] A. K. Okyay, O. Hanoglu, M. Yuksel, H. Acar, S. Sülek, B. Tekcan, S. Agan, N. Biyikli, and M. O. Guler. Using nanogap in label-free impedance based electrical biosensors to overcome electrical double layer effect. *Microsystem Technologies*, 23(4):889–897, 2017.
- [99] A. K. Jonscher. The ‘universal’ dielectric response. *Nature*, 267(5613):673–679, 1977.
- [100] A. K. Jonscher. Analysis of the alternating current properties of ionic conductors. *Journal of Materials Science*, 13(3):553–562, 1978.
- [101] U. Giesen, W. Kleider, C. Berding, A. Geiger, H. Ørum, and P. E. Nielsen. A formula for thermal stability (T_m) prediction of PNA/DNA duplexes. *Nucleic Acids Research*, 26(21):5004–5006, 1998.
- [102] R. L. Zaffino, M. Mir, and J. Samitier. Label-free detection of DNA hybridization and single point mutations in a nano-gap biosensor. *Nanotechnology*, 25(10):105501, 2014.
- [103] T. C. Mele. Selective and anisotropic reactive ion etch of LPCVD silicon nitride with CHF₃ based gases. *Journal of Vacuum Science & Technology B: Microelectronics and Nanometer Structures*, 2(4):684, 1984.
- [104] B. D. Pant and U. S. Tandon. Etching of Silicon Nitride in CCl₂F₂, CHF₃, SiF₄, and SF₆ Reactive Plasma: A Comparative Study. *Plasma Chemistry and Plasma Processing*, 19(4):545–563, 1999.
- [105] C. Chaneliere, J. L. Autran, R. A. B. Devine, and B. Balland. Tantalum pentoxide (Ta₂O₅) thin films for advanced dielectric applications. *Materials Science and Engineering: R: Reports*, 22(6):269–322, may 1998.

6 Summary and Outlook

6.1 Summary

Electrochemical sensors naturally lend themselves to monolithic chip integration for low-cost miniaturised devices by virtue of being inherently electrical in nature. Furthermore, techniques such as redox cycling and dielectric spectroscopy sensing can be used to provide improved sensitivity, without necessarily including a labelling step, when combined with micro- or nanogap devices. For both of these techniques the signal is maximised by reducing the inter-electrode distance as well as increasing the planar electroactive surface area. However, fabricating large-area coplanar nanogap devices is a challenging and complex endeavour.

This thesis first demonstrated how a microgap device can be used for biosensing for the detection of the cysteine–cystine couple, an important biomolecule in protein signalling pathways, by redox cycling. The use of a generator–collector system with micrometre electrode separation allowed interfering signals from the gold surface oxidation and thiol adsorption to be overcome. The sensor provided well-defined (but kinetically limited) steady-state current responses down to physiologically relevant concentrations in the presence of ambient oxygen. The microgap device was also used to show how binding of an α -mannose specific *E. coli* strain could be detected using dielectric spectroscopy. Although the developed self-assembled monolayer still suffered from non-specific interactions, consistently greater capacitance shifts were recorded for the target bacterium. Here the effect of ionic concentration on the capacitance response was also explored.

Although there are many existing methods to fabricate nanogap electrodes, the majority are limited to producing minute surface areas or do not provide passivation of the non-planar surfaces. Furthermore, the small surface area of many devices result in minuscule volumes that make efficient detection of low concentrations difficult. The main focus of this work was to explore methods to fabricate large-area coplanar nanogap devices. However, fabricating such

devices proved in practice to be incredibly challenging and resulted in many failed attempts. These included using an epoxy-based photoresist, SU-8, both as a sacrificial layer [Appendix A.1] and as an adhesive layer [Appendix A.2], as well as combining inductively-coupled plasma reactive ion etching (ICP-RIE) through a passivation layer and focused ion beam (FIB) milling through an electrode layer [Appendix B.1].

However, two fabrication techniques were successfully and demonstrated both vertical and horizontal coplanar geometries. The fabrication of the vertical coplanar device relies on simple optical lithography, a dry etch and the use of anodic bonding to permanently bond to opposing electrodes patterned on silicon and glass. Here the unique process is the use of silicon–glass anodic bonding which required careful optimisation of the device geometry, temperature and applied voltage during bonding to prevent collapse. One downside to using a vertical coplanar geometry is the difficulty in creating interconnections, particularly the electrical connection to the upper electrodes through the laser micromachined apertures.

A method to fabricate a horizontal coplanar device was also reported whereby two aligned electron-beam lithography (EBL) steps are used to define lift-off masks for electrode and passivation layers, respectively. Here a serpentine is used to maximise the length, and therefore area, of the nanogap in the writeable area of the EBL instrument. One issue with this technique was that during removal of the passivation material between the electrodes, lateral etching of the passivation layer occurs, partially exposing a non-planar region. Finite element analysis was used to predict how this affects the limiting current density, showing that completely passivating the top surface of the electrodes appears to be more important than the height of the passivation layer, at least for the length scales investigated.

Finally the horizontal coplanar device was used to demonstrate oligonucleotide detection with dielectric spectroscopy sensing. By using a single-stranded (ss) peptide nucleic acid (PNA) probe layer, hybridisation with a complementary single-stranded deoxyribonucleic acid (DNA) target results in a distinctive change from an uncharged to charged state. The presence of the negatively charged backbone of DNA after hybridisation causes a redistribution of the ions within the electric double layer (EDL), detected by an increase in measured capacitance. As reported by several others using nanogap devices [1–4] the capacitive response at frequencies below 10 kHz can be marred by the dependence on the ionic strength of the buffer. This is particularly true for biosensing where the high ionic concentration and conductivity of the necessary buffers results in a large frequency-dependent dielectric dispersion. Although the limited number of devices used for the experiments made it difficult to draw any firm conclusions, the behaviour of complementary and non-complementary targets was consistent between frequencies of 10 kHz and 100 kHz. If the gap size was made smaller than the EDL, either by reducing the physical interelectrode distance or by decreasing the ionic concentration, the measured capacitance would be less susceptible to ionic fluctuations and should therefore provide more stable measurements at low frequencies (<10 kHz).

6.2 Outlook

Practical limitations surrounding sample introduction and making electrical connections make testing of nanogap devices for biosensing applications extremely difficult. There remains a general requirement for reliable, low-cost and convenient interfaces between lab-on-a-chip/micro total analysis systems (μ TAS) devices and the outside world. This ‘interconnect bottleneck’ has been known for some time [5, 6], yet the problem remains largely unaddressed, with remarkably little progress made to date [7–9]. Often these critical issues are overlooked, or not fully considered at the design phase. Clearly some level of standardisation is required to alleviate these issues and help push research-based systems towards viable products.

Wider adoption of nanogap devices for sensing applications will ultimately depend on whether devices can be fabricated in large quantity and appropriate cost. A major advantage of the vertical coplanar nanogap device fabrication method is that all the key steps (*i.e.*, optical lithography, dry etching and anodic bonding) could be easily parallelised. Whilst the fabrication method for the horizontal coplanar nanogap device currently relies on a slow and expensive electron-beam lithography process, it is envisaged that this could be replaced by nanoimprint lithography to provide a low-cost and high-throughput. One exciting prospect for the fabrication of nanogap devices is the use of additive manufacturing such as multilayer inkjet technology. In fact, just recently the group of Yakushenko reported the fabrication of submicron interelectrode distances using inkjet printing [10]. Here the gap size is controlled by the number of printed polystyrene nanosphere layers and in theory biofunctionalised inks could be directly integrated into the fabrication process. With further development this fabrication technique could operate in a roll-to-roll configuration.

As a concluding remark, although further work is required to improve interfacing for practical usage, two separate fabrication methods for the fabrication of large-area coplanar nanogap devices with close to ideal dual-plate geometry have been demonstrated. With some optimisation, the relative simplicity of the fabrication processes mean that they could be easily scaled towards mass-production. Nanogap devices are a promising platform for the direct electrochemical detection of biomolecules. By avoiding the use of time-consuming and expensive labelling techniques they are more amenable to low-cost point-of-care systems. The ability to operate the device in two modes, by performing either redox cycling or dielectric spectroscopy, offers a wider scope of detection schemes for applications in the fields of healthcare, food production, environmental monitoring and biodefence.

References

- [1] J. T. Nevill, D. Di Carlo, P. Liu, K. R. Jeong, and L. P. Lee. Detection of protein conformational changes with a nanogap biosensor. In *The 13th International Conference on Solid-State Sensors, Actuators and Microsystems, 2005. Digest of Technical Papers. TRANSDUCERS '05*, volume 2, pages 1668–1671. IEEE, 2005.
- [2] M. Yi, K. H. Jeong, and L. P. Lee. Theoretical and experimental study towards a nanogap dielectric biosensor. *Biosensors and Bioelectronics*, 20(7):1320–1326, 2005.
- [3] R. Hatsuki, A. Honda, M. Kajitani, and T. Yamamoto. Nonlinear electrical impedance spectroscopy of viruses using very high electric fields created by nanogap electrodes. *Frontiers in Microbiology*, 6:940, 2015.
- [4] A. K. Okay, O. Hanoglu, M. Yuksel, H. Acar, S. Sülek, B. Tekcan, S. Agan, N. Biyikli, and M. O. Guler. Using nanogap in label-free impedance based electrical biosensors to overcome electrical double layer effect. *Microsystem Technologies*, 23(4):889–897, 2017.
- [5] A. R. Kopf-Sill. Successes and challenges of lab-on-a-chip. *Lab on a Chip*, 2(3):42N–47N, 2002.
- [6] C. K. Fredrickson and Z. H. Fan. Macro-to-micro interfaces for microfluidic devices. *Lab on a Chip*, 4(6):526–533, 2004.
- [7] Y. Temiz, R. D. Lovchik, G. V. Kaigala, and E. Delamarche. Lab-on-a-chip devices: How to close and plug the lab? *Microelectronic Engineering*, 132:156–175, 2015.
- [8] A. C. Fischer, F. Forsberg, M. Lapis, S. J. Bleiker, G. Stemme, N. Roxhed, and F. Niklaus. Integrating MEMS and ICs. *Microsystems & Nanoengineering*, 1:15005, 2015.
- [9] H. van Heeren, R. Tantra, and P. Salomon. Microfluidic devices: a road forward by standardization of interconnects and classification. *Microfluidics and Nanofluidics*, 19(5):1203–1207, 2015.
- [10] N. Y. Adly, B. Bachmann, K. J. Krause, A. Offenhäusser, B. Wolfrum, and A. Yakushenko. Three-dimensional inkjet-printed redox cycling sensor. *RSC Advances*, 7(9):5473–5479, 2017.



Appendices

A Tried Fabrication Methods for Vertical Coplanar Nanogaps

A.1 Unexposed SU-8 as a sacrificial layer

SU-8 offers a wide range of advantageous mechanical, electrical and optical characteristics that make it an attractive material for use in microelectromechanical systems (MEMS). Another key benefit of SU-8 is that several individual layers can be consecutively spincoated and exposed before performing a single development step to fully cross-link the polymer. This technique has been previously reported by several groups [1–3] to create complex multi-layer structures that would be difficult, if not impossible to achieve with traditional processing.

Specifically, Chung and Allen demonstrated how by delaying the development step, uncross-linked SU-8 could be used as a sacrificial layer [4]. In their work they demonstrated 5-250 μm separation between a silicon substrate and suspended 3 mm \times 250 μm NiFe electrodes for the fabrication of torsional silicon oscillators. One important point is that below 65 °C the spincoated SU-8 provides a flat and stable surface for subsequent processing.

Figure A.1 outlines the fabrication approach, with the processing parameters provided in Table A.1. First, a 2.0 μm SU-8 2002 resist [MicroChem] is diluted using cyclopentanone to produce a 500 nm layer. This is spincoated on top of the lower electrode and partially exposed to define support blocks, leaving a central 50 μm \times 100 μm unexposed and uncross-linked region acting as the sacrificial layer. An Au layer is then thermally evaporated over the entire area, ensuring that the temperature is kept below 65 °C to prevent any cross-linking of the SU-8 layer. A thicker, >2 μm , SU-8 layer is then fully developed on top of the Au to provide an etch mask for patterning the upper electrode. This layer also acts to provide some structural support to the device, reducing the stress in the upper electrode. As the sacrificial layer is confined within a microchannel the device is left in MICROPOSIT™ EC Solvent 11 overnight to ensure that any remaining uncross-linked SU-8 is developed. Electrical connection to the top electrode is then made by piercing the top SU-8 layer.

Appendix A. Trialled Fabrication Methods for Vertical Coplanar Nanogaps

One of the problems with the process is that it was quite common for residues to be left within the microchannel, even after development overnight. This could have been due to partial cross-linking caused by poor contact during mask alignment. The top electrode was also prone to collapse and even when increasing the final SU-8 layer from 2 μm to 30 μm , the problem persisted.

One solution to help reduce collapse of the top electrode could be to reduce the distance between the support blocks. A sequence of such structures could then be fabricated on the same die to provide greater surface areas. In a similar vein, an array consisting of a large number of small support pillars could be fabricated to provide support. However, although this would provide planar diffusion of molecular species, the electromagnetic field would be somewhat more complex.

Table A.1: Process parameters for the fabrication of a vertical nanogap device using SU-8 as a sacrificial layer.

Step	Description
1a	Clean substrates: $\text{H}_2\text{SO}_4:\text{H}_2\text{O}_2$ (5:1, vol.), 10 min at RT, DI water rinse, N_2 dry
1b	Dehydration bake in oven, 30 min at 90 °C
1c	Spincoat 2.0 μm AZ [®] nLOF [™] 2070 (standard dilution), 5 s at 500 rpm, 100 rpm·s ⁻¹ , 30 s at 3000 rpm, 10,000 rpm·s ⁻¹
1d	Softbake on hotplate at 100 °C, 2 min at 110 °C
1e	Align lower electrode mask and expose for 10 s at 6.3 mW·cm ⁻² /60 mJ·cm ⁻² dose (365 nm) [Karl Süss MJB3]
1f	Post-exposure bake on hotplate, 1 min at 100 °C
1g	Manual agitation in AZ [®] 826 MIF developer, 50 s at RT
1h	Thermal evaporation of electrodes: Cr (20 nm, 0.4 nm·s ⁻¹) and Au (80 nm, 1.0 nm·s ⁻¹)
1i	Lift-off in MICROPOSIT [™] PR1165 Remover, 5 min at 60 °C with 30%-40% ultrasonic agitation
2a	Dilute SU-8 2002 using cyclopentanone (8:11, wt.) to form SU-8 2000.5 and spincoat, 5 s at 500 rpm, 100 rpm·s ⁻¹ , 30 s at 5000 rpm, 10,000 rpm·s ⁻¹
2b	Softbake on hotplate, 65 °C for 3 min
2c	Align first SU-8 mask and expose for 12.5 s at 6.3 mW·cm ⁻² /80 mJ·cm ² dose (365 nm) [Karl Süss MJB3]
2d	Post-exposure bake on hotplate, 65 °C for 3 min, ensuring layer is not exposed to UV
3a	Electron-beam evaporation of electrode layer (100 nm Au, 0.5 nm·s ⁻¹), maintaining temperature below 65 °C
3b	Spincoat thick SU-8 layer (SU-8 2002/2010/2030), 5 s at 500 rpm, 100 rpm·s ⁻¹ , 30 s at 3000 rpm, 10,000 rpm·s ⁻¹
3c	Softbake on hotplate, 65 °C for 60 s, ramping to 95 °C then holding at 95 °C for 60 s
3d	Align second SU-8 mask and expose to provide 100/125/155 mJ·cm ² dose (365 nm) [Karl Süss MJB3] for SU-8 2002/2010/2030, respectively
3e	Post-exposure bake on hotplate, 1 min at 65 °C then 3 min at 95 °C
3f	Manual agitation in MICROPOSIT [™] EC Solvent 11 for 60 s at RT
3g	Etch Au in KI:I ₂ :H ₂ O (4:1:80, vol.) for 120 s, quench and rinse in DI water
3h	Develop any remaining SU-8 in MICROPOSIT [™] EC Solvent 11 overnight
3i	Rinse with IPA, dry with N_2 and pierce SU-8 to expose contact pads

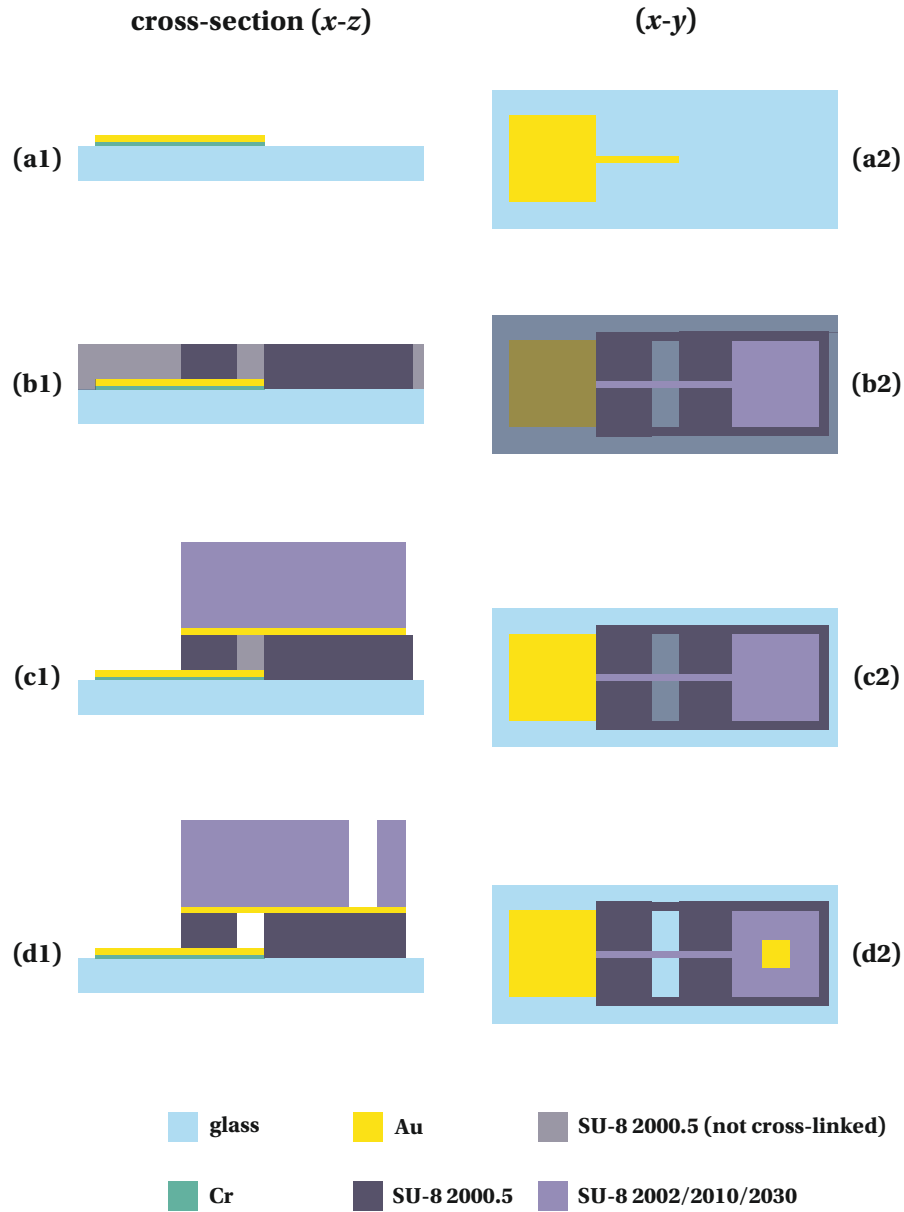


Figure A.1: Fabrication process based on SU-8 as a sacrificial layer. (a): First a lower metallic electrode is patterned using lift-off photolithography. (b): A diluted (500 nm) SU-8 layer is spincoated and exposed, but not fully cross-linked, acting as a sacrificial layer. (c): The top metallic electrode is ‘blanket’ deposited before patterning a thicker (2-30 μm) SU-8 layer that simultaneously acts as an etch mask for the top electrode as well as improving structural integrity. (d): Any remaining SU-8 that is not cross-linked (e.g. within the confined nanogap) is developed overnight.

A.2 SU-8 as an adhesive layer

Another trialled approach was to use SU-8 as an adhesive layer between two substrates patterned with electrodes. Figure A.2 shows the key steps of the attempted fabrication process and the processing parameters are provided in Table A.2. Two large (1.0 mm × 1.5 mm) central Au electrodes connected to two contact pads were optically patterned on ultra-flat quartz glass substrates. A 1 μm thick SU-8 film was then diluted from SU-8 2002 (2.0 μm) with cyclopentanone and spincoated on one of the substrates. The other substrate was then aligned and bonded under force and/or heat during one of the SU-8 cross-linking stages (*i.e.*, UV exposure, post-exposure bake, hardbake).

Devices bonded during the hardbake with an applied force of >2 kN qualitatively provided better results. However, even with some of the devices showing promising adhesion, many of them became separated when trying to make electrical connections. The adhesion was particularly vulnerable to shear stress. A Perspex[®] jig was used to try and reduce the number of failures, however, the large dimensions of the device mean that the resultant forces are relatively high. A redesign to bring the electrical contact pads closer towards the centre of the device may alleviate this issue.

It is important to highlight that when SU-8 is used as an adhesive layer the typical film thickness used for is around 10-100 μm [5–7]. In hindsight, a much thicker SU-8 film could be used to provide adhesion by elevating the lower electrode on the substrate. It would be relatively straightforward to first pattern an SU-8 block for the lower electrode to sit on. Any issue of adhesion between the SU-8 and metallic layer could be resolved with the use of a promoter such as 4-aminothiophenol (4-ATP) or Omnicoat[™] [MicroChem]. Using this approach, much thicker SU-8 layers could then be used to provide better adhesion. Consideration must be made for narrow channels (<200 μm) as the viscosity of SU-8 changes rapidly above the glass transition temperature (64 °C). Tuomikoski & Franssila investigated this issue and suggest that 68 °C may provide the optimal temperature as a compromise between successful bonding and minimal channel filling [6]. In their work they also suggest the use of ‘moats’ (*i.e.*, voids either side of the central structure) to reduce channel filling as well as provide improved resilience to failure by reducing stress in the SU-8 film.

Table A.2: Process parameters for the fabrication of a vertical nanogap device using SU-8 as an adhesive layer.

Step	Description
1a	Clean substrates: $\text{H}_2\text{SO}_4\text{:H}_2\text{O}_2$ (5:1, vol.), 10 min at RT, DI water rinse, N_2 dry
1b	Dehydration bake in oven, 30 min at 90 °C
1c	Spincoat 2.0 μm AZ [®] nLOF [™] 2070 (standard dilution), 5 s at 500 rpm, 100 rpm·s ⁻¹ , 30 s at 3000 rpm, 10,000 rpm·s ⁻¹
1d	Softbake on hotplate at 100 °C
1e	Align lower electrode mask and expose for 10 s at 6.3 mW·cm ⁻² /60 mJ·cm ⁻² dose (365 nm) [Karl Süss MJB3]
1f	Post-exposure bake on hotplate, 1 min at 100 °C
1g	Manual agitation in AZ [®] 826 MIF developer, 50 s at RT
1h	Thermal evaporation of electrode layer Cr (20 nm, 0.4 nm·s ⁻¹) and Au (80 nm, 1.0 nm·s ⁻¹)
1i	Lift-off in MICROPOSIT [™] PR1165 Remover, 5 min at 60 °C with 30%-40% ultrasonic agitation
2a	Clean sample in acetone then IPA, N_2 dry
2b	Dehydration bake on hotplate, 10 min at 200 °C
2c	Allow samples to cool to RT and use immediately
2d	Dilute SU-8 2002 using cyclopentanone (8:9, wt.) to form SU-8 2001 and spincoat on first substrate, 5 s at 500 rpm, 100 rpm·s ⁻¹ , 30 s at 5000 rpm, 10,000 rpm·s ⁻¹
2b	Softbake on hotplate for 3 min at 65 °C
2c	Align mask and expose for 15 s at 6.4 mW·cm ⁻² /100 mJ·cm ⁻² dose (365 nm) [Karl Süss MJB3]
2d	Post-exposure bake on hotplate for 3 min at 65 °C
3a	Align second substrate and apply force whilst heating on hot plate at 115 °C for 15 min

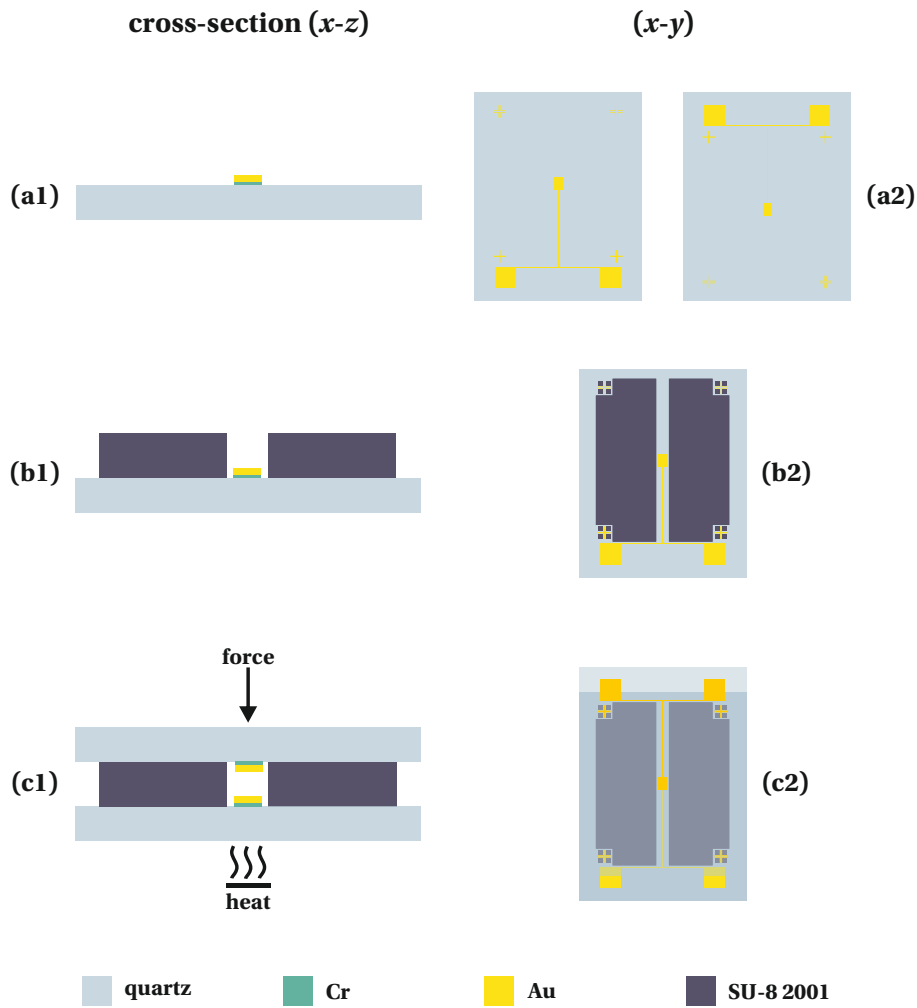


Figure A.2: Fabrication process based on SU-8 as an adhesive layer. (a): Metallic electrodes are first patterned on identical quartz substrates using lift-off photolithography. (b): A diluted ($1\ \mu\text{m}$) SU-8 layer is spincoated on one of the substrates and exposed to UV. (c): The second half of the device is aligned before applying force and/or heat during one of the cross-linking stages to bond the two halves.

B Tried Fabrication Methods for Horizontal Coplanar Nanogaps

B.1 Focused ion beam milling

Initially the fabrication process of the horizontal coplanar nanogap device was designed to include a single electron-beam lithography (EBL) step to pattern both the electrode and passivation layers. In this scheme the Ti/Au electrode layer was electron-beam evaporated on the glass substrate followed by atomic layer deposition (ALD) [Kurt J Lesker PVD75] of a TiO₂ passivation layer. A Ti hard mask was then patterned by lift-off using a ma-N 2403 negative tone EBL resist [MicroChem]. The Ti/Au/TiO₂ stack was then milled using a focused ion beam (FIB) [FEI Nova 200 NanoLab]. However, trials showed that the TiO₂ layer did not provide adequate isolation.

Figure B.1 outlines the revised process. The TiO₂ layer was substituted with an ≈ 80 nm SU-8 layer, etched using either reactive ion etching (RIE) [Figures B.2a & B.2b] or inductively-coupled plasma (ICP) RIE [Figures B.3a & B.3b] using the Ti hard mask. ICP was found to leave substantially less residue, likely due to the improved base pressure of the instrument. The undercut was estimated to be around 15 nm and 5 nm for the RIE and ICP-RIE processes, respectively. The Ti/Au layers were then milled using FIB through the Ti hard mask and underlying SU-8 layer.

Results showed that narrower trenches [Figure B.4] were not completely milled and the aspect ratio was restricted by the redeposition of milled material. Significant erosion was also evident at the edge of the mask layer. Varying the milling angle (0-40 °) and increasing the ion energy (0.2 kV to 1.0 kV) made little difference to improve the result. Removing the Ti hard mask after milling also presented several issues. Wet etching in HF:DI (1:1, vol.) was not sufficient to completely remove the layer, with the layer still providing a conducting electrical path. Attempts to remove any remaining Ti by FIB milling led to significant charging of the thin underlying SU-8 layer, eventually causing burning. For these reasons a two-stage lift-off strategy was adopted for further fabrication of horizontal coplanar devices.

Appendix B. Trialled Fabrication Methods for Horizontal Coplanar Nanogaps

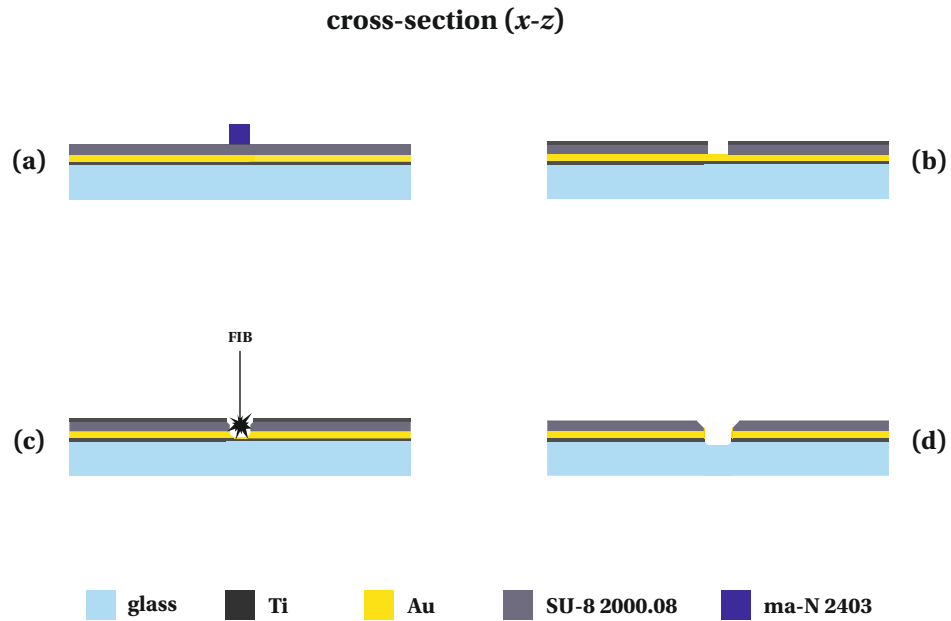


Figure B.1: Fabrication process based on FIB milling. (a): A ma-N 2403 resist is patterned by EBL on top of a Ti/Au/SU-8 stack. (b): A Ti hard mask is then patterned by lift-off and the exposed SU-8 dry etched using either RIE or ICP-RIE. (c): The top Ti layer and underlying SU-8 are used as a mask to mill a nanogap into the Ti/Au electrode layer. (d): After FIB milling the Ti hard mask is removed in diluted HF.

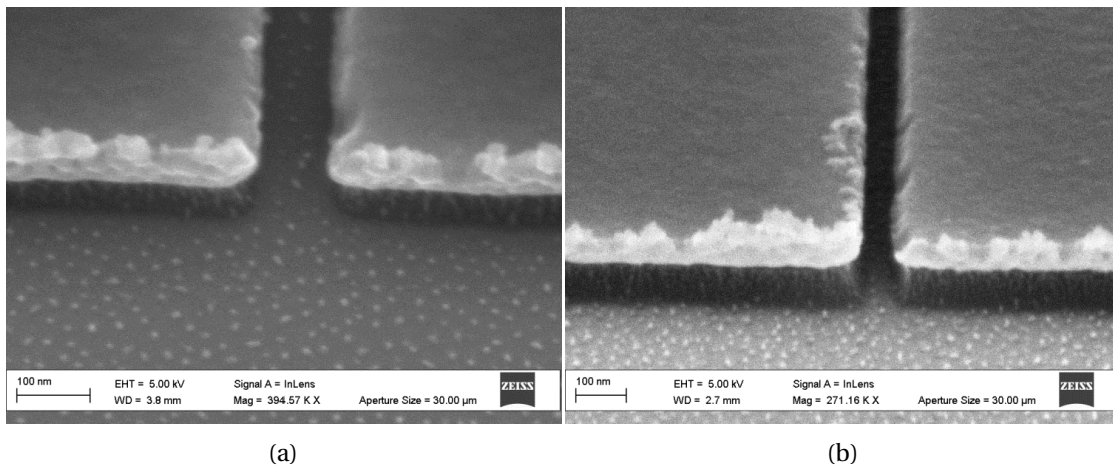


Figure B.2: SEM images showing the result of etching the SU-8 passivation layer with RIE for: (a) a wide channel and (b) a narrow channel.

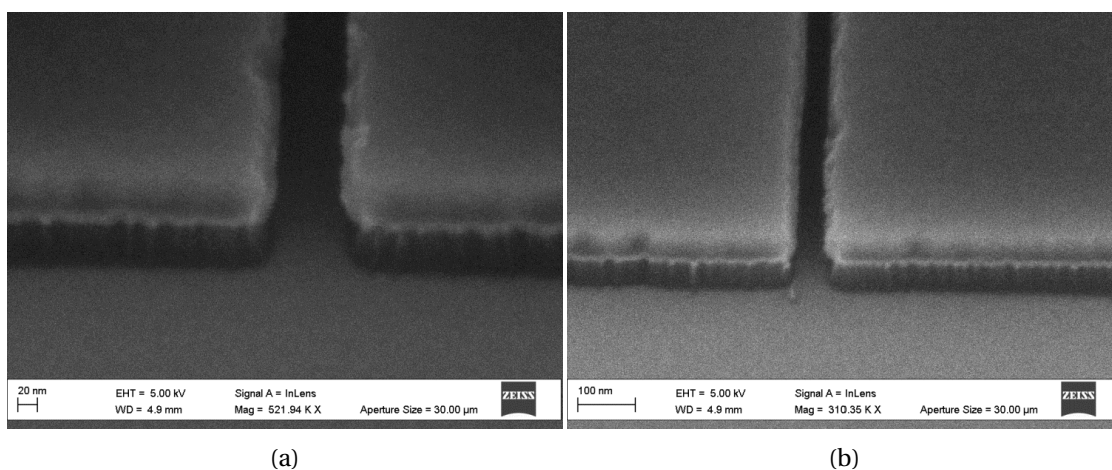


Figure B.3: SEM images showing the result of etching the SU-8 passivation layer with ICP-RIE for: (a) a wide channel and (b) a narrow channel.

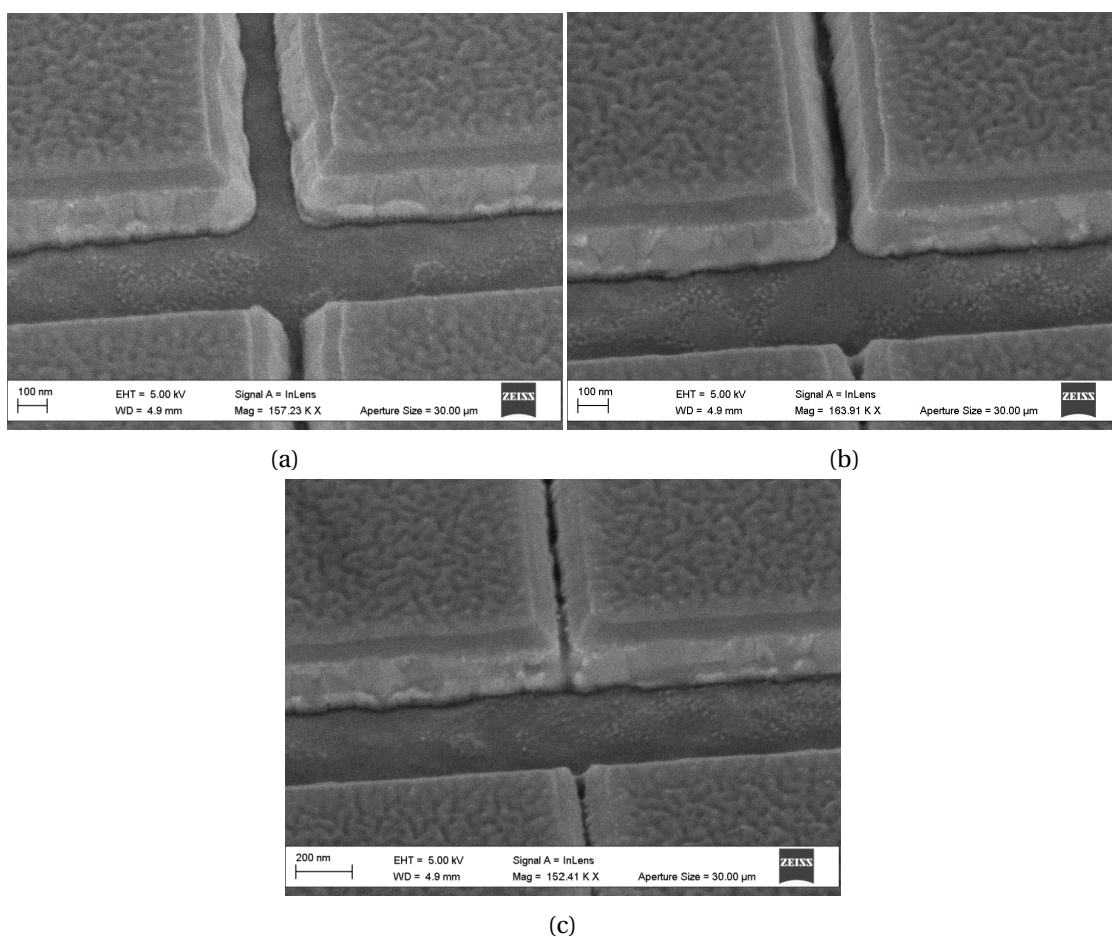


Figure B.4: SEM images showing the results of FIB milling for decreasing sizes of nanogaps.

Appendix B. Trialled Fabrication Methods for Horizontal Coplanar Nanogaps

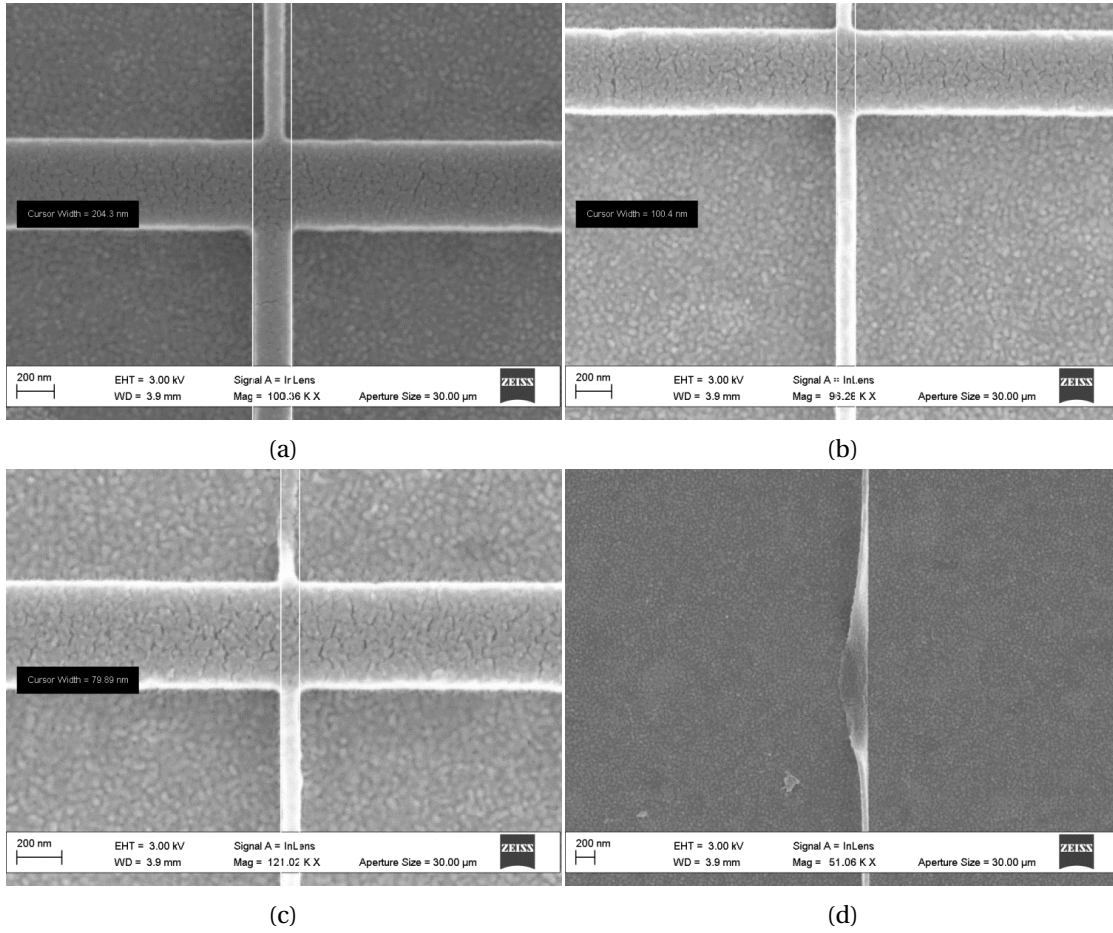


Figure B.5: SEM images showing the results of dose tests ($600 \mu\text{C}\cdot\text{cm}^{-2}$) for approximately (a) 200 nm, (b) 100 nm, (c) 80 nm and (d) 50 nm nanogaps.

B.2 Improving ma-N 2403/glass adhesion

During trials for the lift-off fabrication of the horizontal coplanar nanogap devices it became evident that the adhesion of the ma-N 2403 would be a limiting factor for the reducing the nanogap size. Results showed that pattern collapse would occur for ma-N 2403 for features <70 nm. Figure B.5 shows developed features of decreasing size, at a feature size of ≈ 50 nm the pattern collapses [Figure B.5d]. Increasing the dose was from $600 \mu\text{C}\cdot\text{cm}^{-2}$ to $1600 \mu\text{C}\cdot\text{cm}^{-2}$ led to improved line edge roughness for larger features and allowed smaller gaps, on occasion, to be achieved.

A diluted PMMA 950 k \overline{M}_w (2% anisole) (PMMA:anisole, 2:3, vol.) layer was trialled as an adhesion layer between the glass and ma-N 2403. This was spun at 6000 rpm for 40 seconds followed by a softbake on a hotplate at 200°C for 5 minutes. The ma-N 2403 electron-beam resist was then patterned as previously reported. However, after electron-beam exposure the PMMA was cross-linked under the ma-N 2403 leading to a 'halo' effect. Attempts to etch the

B.3. Patterning of a nanoimprint lithography silicon master

PMMA by ICP-RIE with O₂ chemistry were unsuccessful. Figure B.6a shows a microscope image of a large section of the nanogap serpentine. At this magnification the seriousness of the defect is not completely obvious. However, with increased zoom, Figure B.6b shows what appears to be cross-linking of the PMMA beneath the ma-N 2403 electron-beam resist.

Next a hexamethyldisilane (HMDS) priming step was tested by spincoating HMDS directly onto the dehydrated substrate. HMDS activates hydrophilic surfaces by binding its silicon atom with the oxidised surface and releasing ammonia to make the surface hydrophobic, thus improving resist adhesion. This was a complete failure, with the HMDS simply leaving the surface during spincoating; it may be that vapour application is required. Cationic priming agents such as SurPass 3000 [DisChem] would be more appropriate for application by spincoating. Finally a thin Cr layer (≈ 2.5 nm) was tested; this provided very good adhesion between the glass and ma-N 2403 allowing 50 nm features to be reliably patterned. An additional step is required to later remove this Cr layer and must provide significant undercut of the Ti/Au electrode layer.

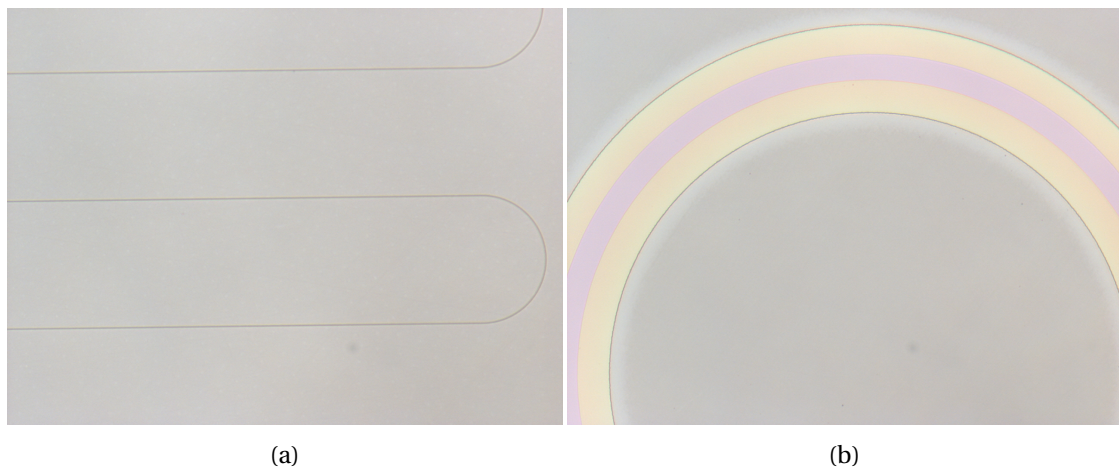


Figure B.6: Microscope images of: (a) the nanogap serpentine and (b) a zoomed view showing the 'halo' effect caused by cross-linking of the PMMA adhesion layer.

B.3 Patterning of a nanoimprint lithography silicon master

The process of nanoimprint lithography (NIL) was first reported in scientific literature by Stephen Chou's group at University of Minnesota in 1996 [8]. It provides a relatively low-cost and high-throughput method of creating nanometre scale features. The process does require a silicon master to be first patterned by electron-beam lithography, however this mould can then be used for a few thousand imprints. The process can be performed using a full wafer scheme and with the combination of other fabrication processes can be used to provide a wide variety of layer profiles.

Appendix B. Trialled Fabrication Methods for Horizontal Coplanar Nanogaps

A proposed NIL process is shown in Figure B.7. First an etch mask must be patterned by EBL, before dry etching the silicon wafer. It is critical that the profile is close to vertical to ensure that the intermediate stamp can be removed after curing, and also to provide a suitable profile for the following processes. The intermediate stamp is then used to imprint a bilayer consisting of an imprint resist on top of a dedicated 'lift-off' resist. The imprint resist can be either a UV- or thermal-sensitive resist and adopts the profile of the intermediate mould. After imprinting, the residual imprint resist is dry etched. Along with development conditions, this process provides the necessary undercut in the lift-off resist. The final step is to deposit a stack consisting of adhesion, electrode and passivation layers before performing lift-off to produce the nanogap geometry.

Possibly the most complex task is creating the silicon master. The electron-beam resist was swapped from ma-N 2403 to XR-1541-006 [Dow Corning], a hydrogen silsesquioxane (HSQ) negative tone resist ideal for patterning high resolution features with low line edge roughness. The final processing parameters are outlined in Table B.1. Initially MICROPOSIT™ MF-319 was used as a developer. Whilst this was acceptable for isolated features, it produced unsatisfactory results for dense features due to its low contrast. Using a 25% tetramethylammonium hydroxide (TMAH) aqueous solution provided improved results.

The patterned 200 nm serpentine is shown in Figure B.8 and measured as ≈ 167 nm. A series of 50 nm features including straight sections and arcs were also patterned and measured approximately 33 nm to 37 nm [Figure B.9]. The SEM images demonstrate the quality of the features that can be obtained with EBL patterning. The last step of the silicon master fabrication is to etch the silicon wafer using the electron-beam resist as a mask.

An initial ICP-RIE recipe developed by Hung *et al.* [9] for fabrication of highly ordered silicon nanowire arrays was adopted. In their work they demonstrated the fabrication of tall (400 nm to 1.3 μm) silicon pillars with sidewall angles between 88.4° and 90.6° . Grating structures with similar feature sizes to those on the mould were patterned by displacement Talbot lithography as test structures to check the etch recipe. The stack consisted of Si/ARC/ULTRA-*i* 123, with the 200 nm anti-reflective coating (ARC) etched by ICP-RIE with a CF_4 chemistry and the ULTRA-*i* 123 diluted from 800 nm to 400 nm prior to spincoating.

The features were developed in MEGAPOSIT™ MF CD-26 developer. Etching was performed using an Oxford Instruments PlasmaPro 100 ICP-RIE instrument. In order to create a stable plasma the RF power substantially increased from 9 W to 20 W. To bring the sidewall as close as possible to vertical (90°), the operating pressure was increased from 19 mTorr to 20 mTorr. A high degree of reflected power was recorded and even when tuning the capacitor field values ($C_1 = 51.5\%$, $C_2 = 17.5\%$) the reflected power could only be reduced from 100 W to 60 W.

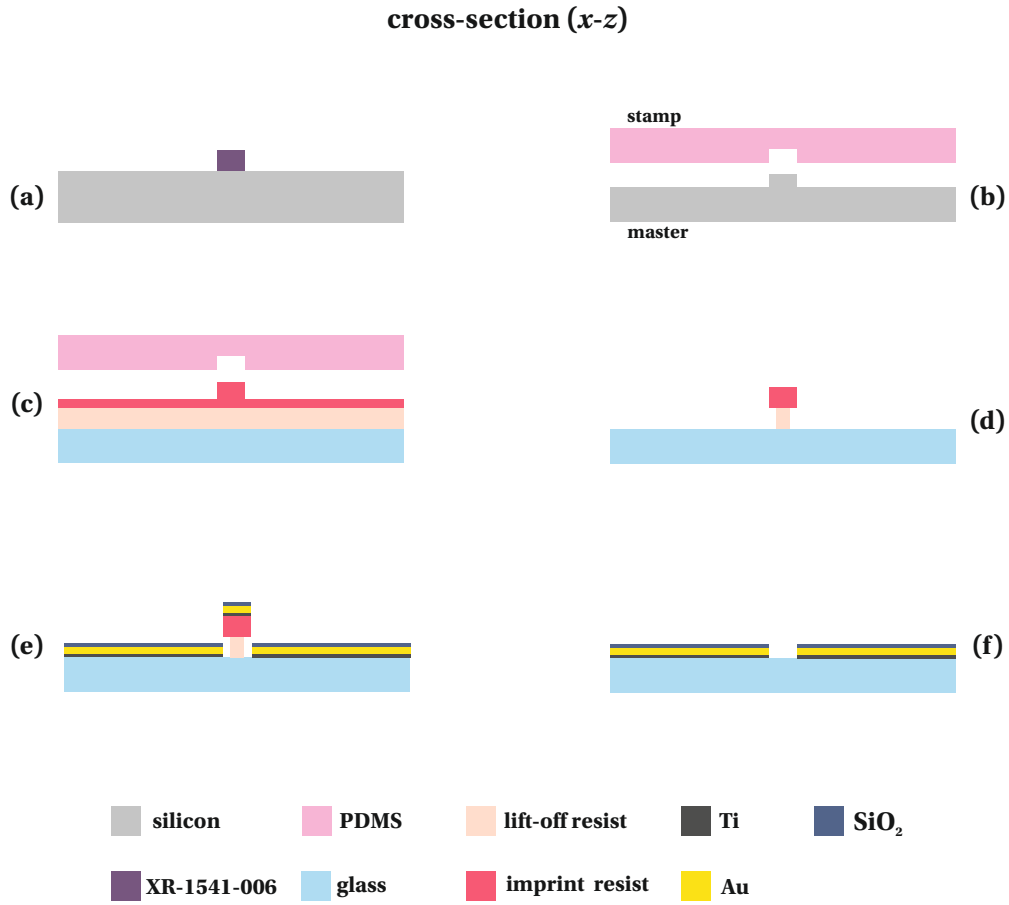


Figure B.7: Proposed nanoimprint lithography process. (a): First a XR-1541-006 resist is patterned using EBL to act as an etch mask. (b): The silicon is then dry etched and the resist removed to produce the master. An intermediate stamp is then created in PDMS (c): The PDMS stamp is then used to imprint a bilayer consisting of an imprint resist (*e.g.*, Mr-UVcur06 [micro resist technology]) and a lift-off resist (*e.g.*, PMGI/LOR [MicroChem]). (d): The residual resist is then removed using ICP/ICP-RIE with an O₂ chemistry whilst also generating the undercut required for lift-off. (e): A stack of Ti/Au/SiO₂ can then be deposited using electron-beam lithography without breaking vacuum. (f) Finally lift-off is performed in a suitable solvent (*e.g.* Remover PG [MicroChem]) to create the nanogap structure.

Appendix B. Trialled Fabrication Methods for Horizontal Coplanar Nanogaps

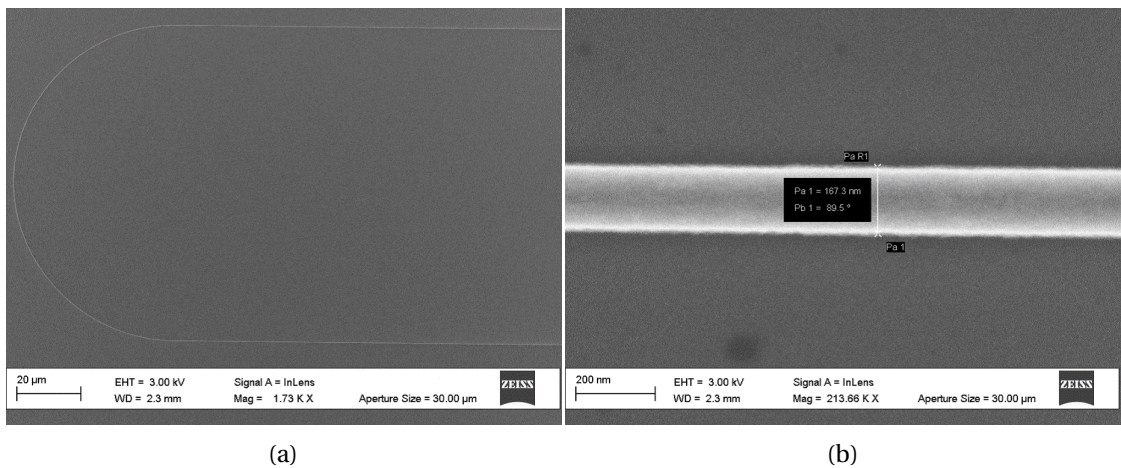


Figure B.8: SEM images showing: (a) two straight sections of the 200 nm nanogap serpentine connected by an arc and (b) measurement of the 200 nm nanogap serpentine.

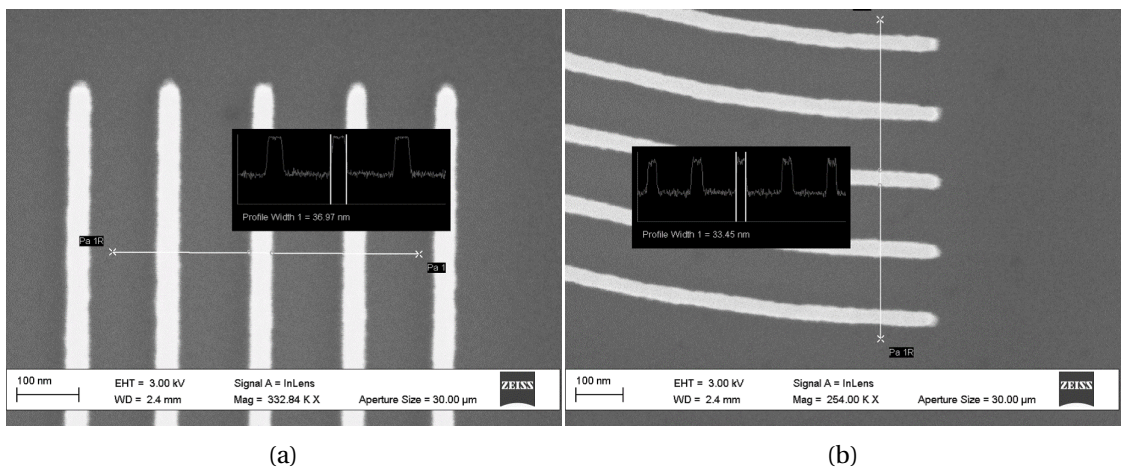


Figure B.9: SEM images showing measurement of (a) 50 nm straight sections and (b) 50 nm arcs.

Table B.1: Process steps for EBL patterning the NIL silicon master.

Step	Description
1a	Clean wafer: ultrasonic agitation in acetone then IPA, N ₂ dry
1b	UV-ozone treatment for 5 min
2a	Spincoat XR-1541-006 (≈ 110 nm), 5 s at 500 rpm, 100 rpm \cdot s ⁻¹ 2000 rpm for 60 s, 10,000 rpm \cdot s ⁻¹
2b	Softbake on hotplate, 2 min at 80 °C
3a	Electron-beam exposure, 100 kV, 1.5 nA beam current, 1200 $\mu\text{C}\cdot\text{cm}^{-2}$ dose [JEOL JBX-6300FS]
4a	Develop patterns in 25% TMAH, 30 s at RT
4b	DI water rinse, N ₂ dry

B.3. Patterning of a nanoimprint lithography silicon master

Table B.2: Optimised ICP-RIE parameters for etching vertical sidewalls in silicon.

Parameter	Reference value	Optimised value
Ar flow rate	20 SCCM	20 SCCM
SF ₆ flow rate	26 SCCM	26 SCCM
C ₄ F ₈ flow rate	54 SCCM	54 SCCM
He backing flow rate	—	5 SCCM
Operating pressure	19 mTorr	20 mTorr
Substrate temperature	—	0.0 °C
RF power	9 W	20 W
ICP power	800 W	800 W

C Simulation of the Horizontal Coplanar Nanogap Device

C.1 Electrostatics

Simulations were performed using the electrostatics interface of the AC/DC module in COMSOL Multiphysics® to provide an understanding of the electric fields for both the ideal geometry, with the top surface of the electrodes completely passivated and non-ideal geometry, with some portion of the passivation layer removed due to lateral etching during ICP-RIE. Contour plots show both the normalised electric potential and proportional electric field arrows. The streamline plots provide both normalised electric potential and the electric field lines.

In both cases the model simulates the electrostatics within the substrate (borosilicate), metallic electrode (Au), passivation layer (SU-8) and the sample medium (air/PBS). One of the electrodes is defined as a voltage terminal (with surface-applied potential) and the other as a ground. A relative permittivity constitution relation is selected to describe the properties of the medium, relating the electric displacement field \mathbf{D} [$\text{C}\cdot\text{m}^{-2}$] with the electric field \mathbf{E} [$\text{V}\cdot\text{m}^{-1}$], *i.e.*, $\mathbf{D} = \epsilon_0\epsilon_r\mathbf{E}$. The simulation then solves the static conditions for $\nabla\mathbf{D} = \rho$ and $\mathbf{E} = -\nabla V$, where ρ is the electric charge density [$\text{C}\cdot\text{m}^{-3}$] and V is the applied terminal voltage [V]. Both geometries are simulated in air [Figures C.1 & C.2] and in phosphate-buffered saline (PBS) Figures C.3 & C.4].

Table C.1: Parameters used for electrostatic simulations.

Material	ϵ_r	σ [$\text{S}\cdot\text{m}^{-1}$]
Air	1.0	—
Borosilicate	4.8	—
Au	6.9	45.6×10^6
PBS	80.0	1.5
SU-8	4.0	—

Appendix C. Simulation of the Horizontal Coplanar Nanogap Device

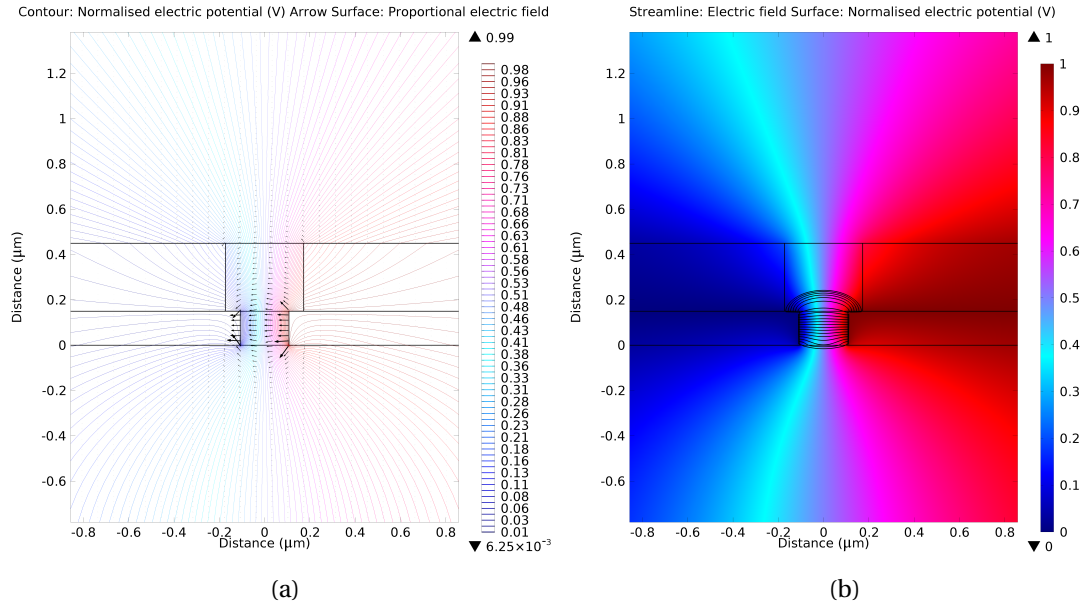


Figure C.1: Contour (a) and streamline (b) plots for the horizontal nanogap device with top surface of electrodes partially exposed in air.

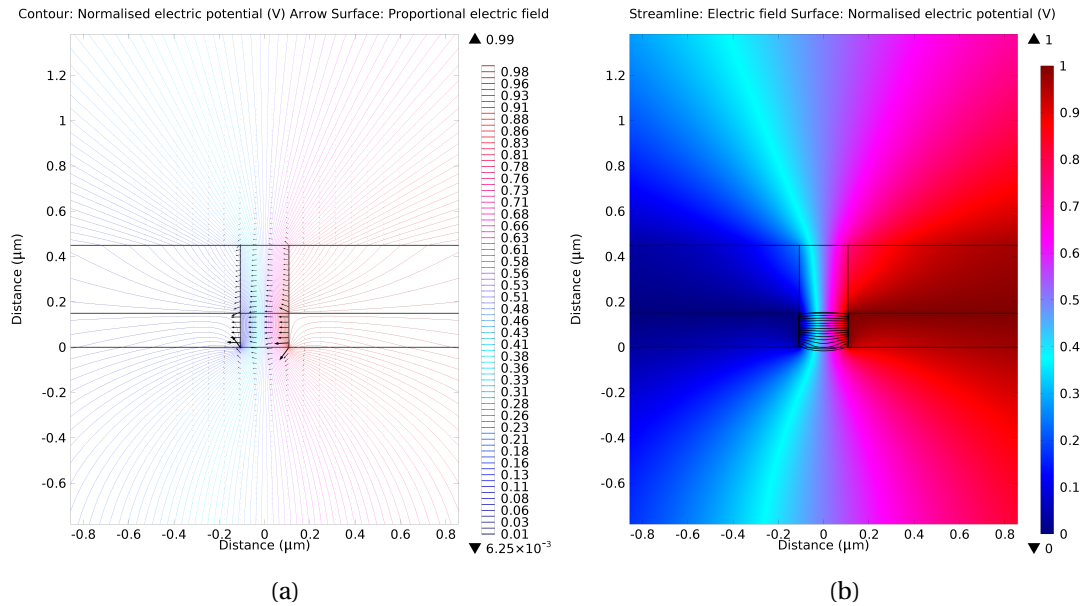


Figure C.2: Contour (a) and streamline (b) plots for the horizontal nanogap device with top surface of electrodes completely passivated in air.

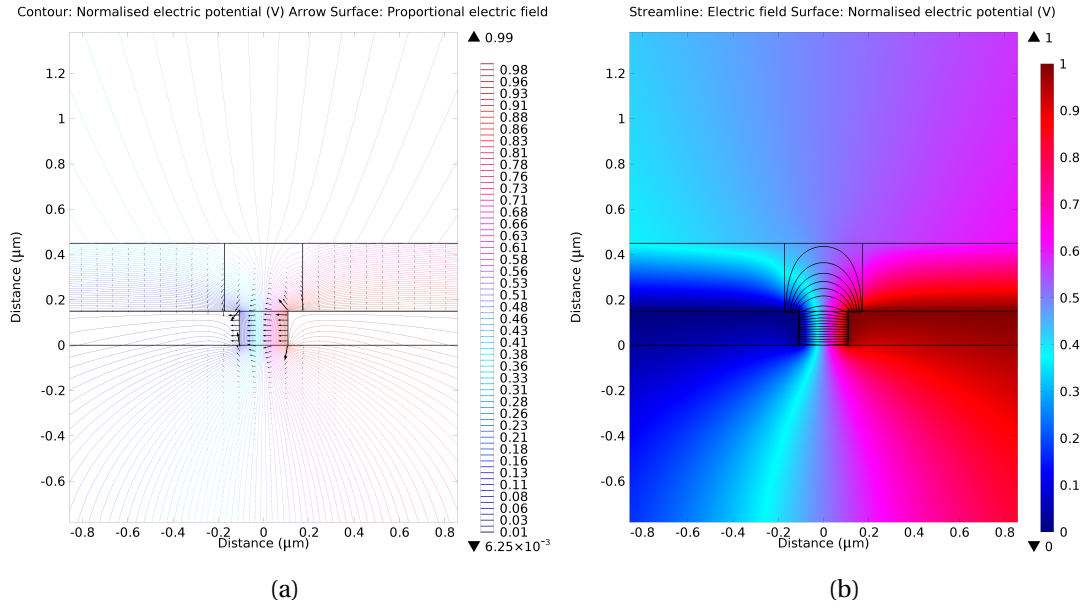


Figure C.3: Contour (a) and streamline (b) plots for the horizontal nanogap device with top surface of electrodes partially exposed in PBS.

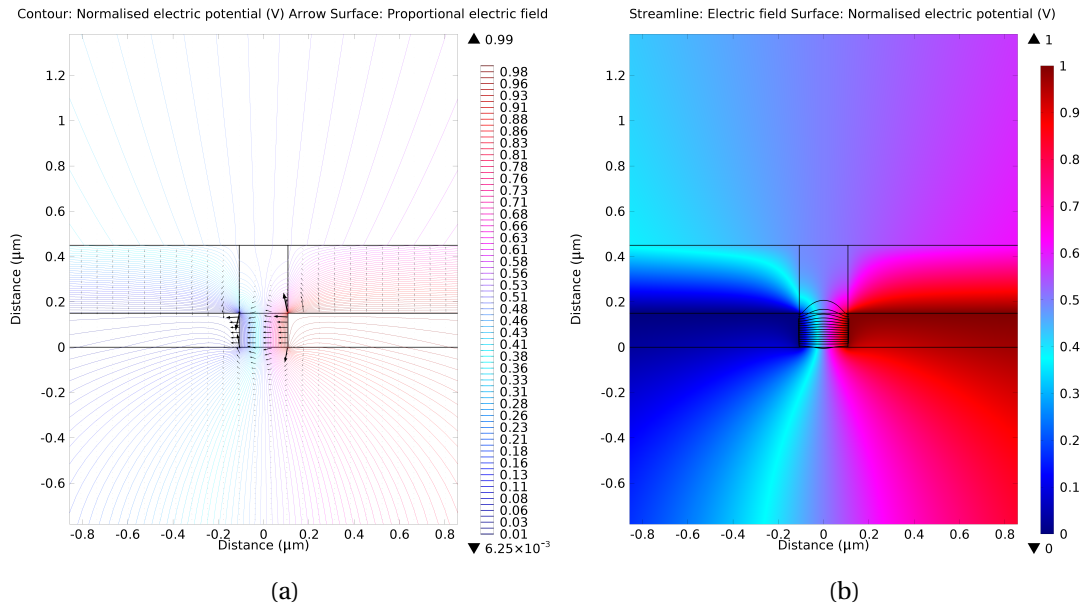


Figure C.4: Contour (a) and streamline (b) plots for the horizontal nanogap device with top surface of electrodes completely passivated in PBS.

C.2 Microfluidics

Flow velocities within the microfluidic serpentine were simulated using the laminar flow interface of the computational fluid dynamics module in COMSOL Multiphysics®. The boundary conditions used in the simulations were calculated by the Hagen–Poiseuille law [Equation 4.8]. Using a tube with an internal diameter of 50 μm and length of 0.25 m within the microfluidic network acts as a flow-limiting element. The hydraulic resistance R_h of this element dominates the flow through the series network and can be calculated as $R_h = \frac{8\mu l}{\pi r^4}$, where μ is the dynamic viscosity of the fluid [$\text{m}^2 \cdot \text{s}^{-1}$], l is the length of the tube [m] and r is the radius [m]. The flow can then be calculated by: $Q = \frac{\Delta P}{R_h}$, where Q is the volumetric flow rate [$\text{m}^3 \cdot \text{s}^{-1}$] and ΔP is the applied pressure difference [Pa]. Again, given that the hydraulic resistance of the horizontal coplanar nanogap device ($1.25 \times 10^{11} \text{ Pa} \cdot \text{s} \cdot \text{m}^{-3}$) is much smaller than that of the tubing ($1.63 \times 10^{15} \text{ Pa} \cdot \text{s} \cdot \text{m}^{-3}$), the total flow can be assumed to be controlled by the single hydraulic resistance. As the flow entering the device must equal the flow leaving the device the flow rate calculated by the Hagen–Poiseuille law makes a suitable boundary condition.

Flow rates ranging from $18.41 \text{ nL} \cdot \text{min}^{-1}$ to $1.29 \mu\text{L} \cdot \text{min}^{-1}$ were used based on using a Mitos Fluika low vacuum pump [Dolomite] generating 5 to 350 mbar below atmospheric pressure, respectively. At the upper values of flow rates the Reynolds number, defined as $\text{Re} = \frac{\rho \mathbf{u} \mathbf{L}}{\mu}$, where ρ is the density of the fluid [$\text{kg} \cdot \text{m}^{-3}$], \mathbf{u} is the velocity vector of the fluid [$\text{m} \cdot \text{s}^{-1}$], \mathbf{L} is the characteristic length [m] and μ is the dynamic viscosity of the fluid [Pa·s], approaches 1 for flow velocities within the serpentine. Therefore although the flow is laminar, a Stokes flow is not a suitable approximation and the inertial terms are retained.

Figure C.5a shows the central portion of the device, with the inlet/outlet funnels and serpentine visible. The mesh quality used for the simulation is depicted in Figure C.5b, which shows a zoomed area of the serpentine. Figures C.6a and C.6b then show the surface velocities within the microfluidic serpentine for flow rates of $18.4 \text{ nL} \cdot \text{min}^{-1}$ and $1.29 \mu\text{L} \cdot \text{min}^{-1}$, respectively. At the centre of the serpentine the velocity is typically around 10 times greater than the inlet velocity. For example, at a flow rate of $18.41 \text{ nL} \cdot \text{min}^{-1}$, the inlet velocity is $1.56 \times 10^{-4} \text{ m} \cdot \text{s}^{-1}$, whereas along the nanogap it varies between $1.29 \times 10^{-3} \text{ m} \cdot \text{s}^{-1}$ at the centre of a straight section to $1.33 \times 10^{-3} \text{ m} \cdot \text{s}^{-1}$ at the centre of an arc. Whilst the micro- and nanofluidic serpentes have a combined volume of $\approx 4 \text{ nL}$, the total volume of the microfluidic layer is $\approx 250 \text{ nL}$. This means that at low flow rates it can take considerable time ($> 10 \text{ min}$) for the volume to be exchanged. This could be quite easily rectified by simply reducing the size of the reservoirs. Alternatively, the inlet and outlet connections can be positioned as close as possible to the serpentine.

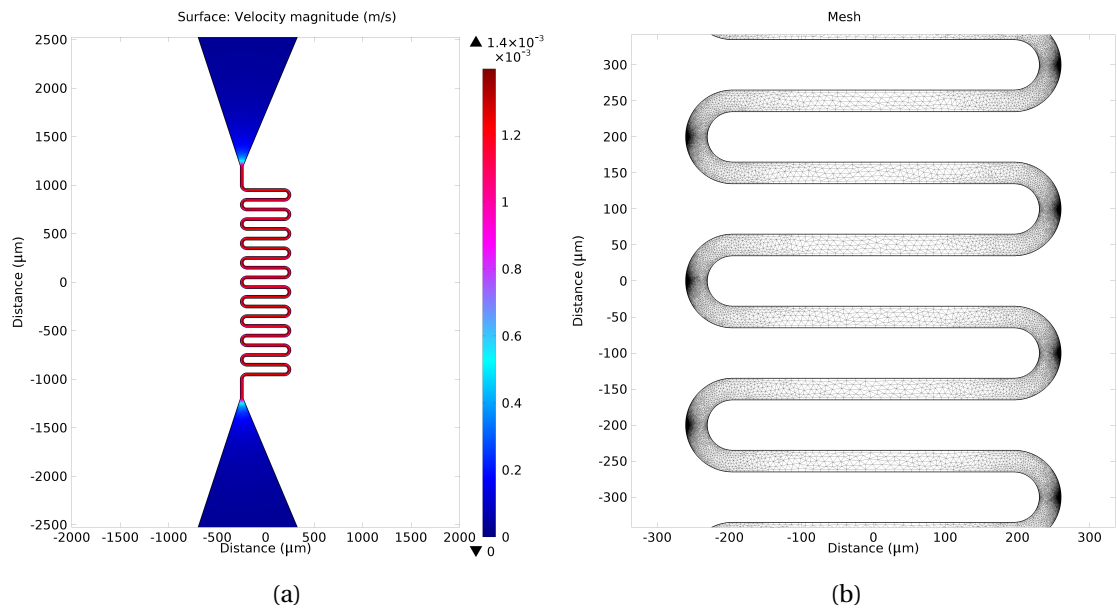


Figure C.5: Simulated surface velocities for (a) a flow rate of $18.41 \text{ nL} \cdot \text{min}^{-1}$ and (b) mesh used for the microfluidic simulations.

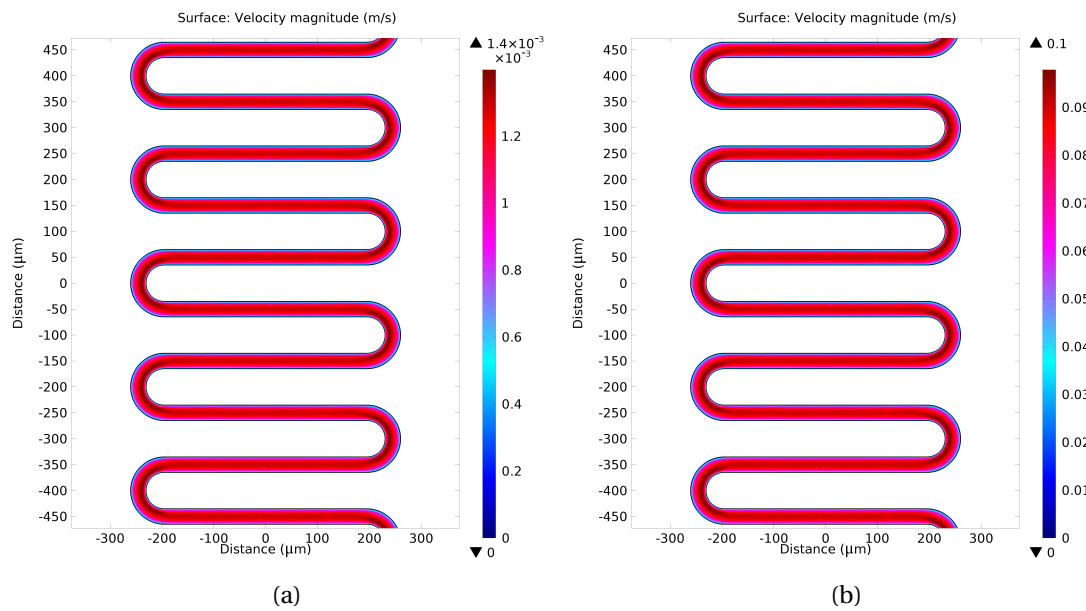


Figure C.6: Surface velocity plots for flow rates of (a) $18.41 \text{ nL} \cdot \text{min}^{-1}$ and (b) $1.29 \mu\text{L} \cdot \text{min}^{-1}$.

References

- [1] J. Carlier, S. Arscott, V. Thomy, J. C. Fourier, F. Caron, J. C. Camart, C. Druon, and P. Tabourier. Integrated microfluidics based on multi-layered SU-8 for mass spectrometry analysis. *Journal of Micromechanics and Microengineering*, 14(4):619–624, 2004.
- [2] B. Bohl, R. Steger, R. Zengerle, and P. Koltay. Multi-layer SU-8 lift-off technology for microfluidic devices. *Journal of Micromechanics and Microengineering*, 15(6):1125–1130, 2005.
- [3] A. Mata, A. J. Fleischman, and S. Roy. Fabrication of multi-layer SU-8 microstructures. *Journal of Micromechanics and Microengineering*, 16(2):276–284, 2006.
- [4] C. Chung and M. Allen. Uncrosslinked SU-8 as a sacrificial material. *Journal of Micromechanics and Microengineering*, 15(1):N1–N5, 2005.
- [5] R. J. Jackman, T. M. Floyd, R. Ghodssi, M. A. Schmidt, and K. F. Jensen. Microfluidic systems with on-line UV detection fabricated in photodefinable epoxy. *Journal of Micromechanics and Microengineering*, 11(3):263–269, 2001.
- [6] S. Tuomikoski and S. Franssila. Free-standing SU-8 microfluidic chips by adhesive bonding and release etching. *Sensors and Actuators A: Physical*, 120(2):408–415, 2005.
- [7] C. Pang, Z. Zhao, L. Du, and Z. Fang. Adhesive bonding with SU-8 in a vacuum for capacitive pressure sensors. *Sensors and Actuators A: Physical*, 147(2):672–676, 2008.
- [8] S. Y. Chou, P. R. Krauss, and P. J. Renstrom. Imprint Lithography with 25-Nanometer Resolution. *Science*, 272(5258):85–87, 1996.
- [9] Y.-J. Hung, S.-L. Lee, B. J. Thibeault, and L. A. Coldren. Fabrication of Highly Ordered Silicon Nanowire Arrays With Controllable Sidewall Profiles for Achieving Low-Surface Reflection. *IEEE Journal of Selected Topics in Quantum Electronics*, 17(4):869–877, 2011.

